Advancing Electrochemical Energy Systems with Electron Microscopy Approaches

A Dissertation

Presented to the Faculty of the Graduate School

of Cornell University

In Partial Fulfillment of the Requirements for the Degree of

Doctor of Philosophy

by

Yingchao Yu

May 2014

Advancing Electrochemical Energy Systems with Electron Microscopy Approaches

Yingchao Yu, Ph.D.

Cornell University 2014

ABSTRACT

Achieving a secure and sustainable energy future is one of the greatest scientific, technological and societal challenges of our time. The projected doubling of world energy consumption within the next 50 years, along with our current dependence on non-renewable fossil fuels, as well as the attendant detrimental effects on the environment that their utilization entails, point to the critical need of alternative energy sources as well as to the more efficient use of existing energy resources. The traditional fossil fuels such as coal, natural gas and oil rely heavily on the energy storage within the form of chemical bonds. A modern society must be able to store and convert large quantities of clean energy derived from solar, wind or other sustainable sources, as well as converting existing fossil fuels in a more efficient and sustainable way.

This PhD thesis focuses on the use and development of advanced (scanning) transmission electron microscopy techniques, especially *in-situ* methods, for energy applications. Specifically, the intent is to understand materials properties and reaction mechanisms of fuel cell catalysts and novel lithium-ion battery and lithium-sulfur electrode materials, so as to enhance the performance of practical devices. Three topics will be discussed (i) advanced electron microscopy for electrochemical energy storage and conversion systems: from *ex-situ* to *in-situ*; (ii) catalysts for proton exchange membrane (PEM) fuel cells; and (iii) materials for advanced lithium-sulfur batteries.

BIOGRAPHICAL SKETCH

Yingchao Yu was born in Lanzhou, China and is the son of Kai Yu and Bin Zhou. His passion in science was intrigued in high school when he studied for the National Chemistry Olympiad and was fully immersed in the kingdom of the microscopic world of life. He tapped into the world of chemistry after attending Xiamen University. Upon finishing his sophomore year, he encountered Prof. Zhong-Qun Tian and was fascinated by his pioneering research in electrochemical energy storage. He became a member of the group and conducted independent research in the field of surface enhanced Raman spectroscopy. In the senior year, he went to Uppsala University in Sweden as an exchange student. He joined Professor Leif Hammarström's research group and performed the undergraduate thesis research on dye-sensitized solar cells and their application for renewable energy.

In 2009, Yingchao entered Cornell and joined Professor Héctor D. Abruña's group as a doctoral candidate in the Department of Chemistry and Chemical Biology. Later he was co-advised by Professor David A. Muller in the Department of Applied and Engineering Physics. He carried out research in the mechanistic study of electrochemical energy systems using various material synthesis and characterization techniques, especially high resolution transmission electron microscopy. He has had the opportunities to work on several interesting systems such as fuel cells, lithium-ion batteries and lithium-sulfur batteries.

Apart from work, Yingchao also has diverse interests in sports. Being an avid runner, he holds the record of 100m race in the high school, and has completed the full 42km marathon in Xiamen. He also enjoys playing basketball, tennis and badminton.

Thank you my parents,

for giving me such wonderful life,

Thank you my wife,

for teaching me how to love and to be loved,

Thank you my friends,

for sharing tears and joys along my journey,

To my beloved grandfather and aunt,

may your souls rest in peace.

ACKNOWLEDGMENTS

I would like to specially thank Prof. Héctor D. Abruña for mentoring me over the last five years and giving me the opportunity to work in the fascinating world of electrochemistry. Besides his great personality, straight education and "tolerance" to my intellectual freedom, I can still vividly remember the 1st email he wrote to me, at his "working hour", or to be more specific, at 1 AM on Feb 18th, 2009:

"-Yingchao Yu: Thanks for your message. I have been out of town and just got back to Ithaca. I will check on the status of your application first thing in the morning. Let me know if you have any further questions. Cheers, HDA"

Five years have passed in one second. I am very grateful for his guidance that helps me grow not only as an independent researcher, but also as a complete person. I am lucky that I can learn from someone with brilliant knowledge, remarkable leadership, tireless working habit, and most important of all, the great personality that can magnetize the fellow students and co-workers together.

I would also like to thank Professor David A. Muller and Professor Francis J. DiSalvo for serving on my committee and provide insightful advice on my research projects. I would like to thank Professor David A. Muller specifically for welcoming me into his lab and collaborating with his students. I would like to acknowledge the many helpful members of the TEM facility at Cornell (Mr. John Grazul and Mr. Mick Thomas) for their assistance with data collection and processing.

I am lucky to be able to associate myself with the talented and hardworking members in the Abruña & Muller group. Dr. Deli Wang and Dr. Huolin Xin have

provided tremendous support in my earlier Ph.D. years that makes my research considerably more efficient and productive. I am greatly appreciated for their help during the early stage of my doctoral research and guiding me through the challenges and struggles.

Dr. Weidong Zhou, Ms. Megan Holtz, Dr. Hao Chen, Dr. Zichao Yang, Dr. Robert Hovden, Dr. William Baumgardner, Dr. Ye Zhu and Mr. Dong Ren, have all been wonderful friends and resourceful colleague throughout my doctoral research. We have all been there for each other and taught ourselves many tools and issues of electrochemistry and electron microscopy. They are dedicated scientists with intense curiosity and brilliant ideas and are great collaborators, as well as cheerful and companionable friends. They are always very kind and helpful about almost everything in life and science.

I would also like to thank my collaborators in the industrial world for the close collaboration. I thank Dr. Vic Liu from General Motors and Dr. John Damiano from Protochips Inc. for cherishing myself with wonderful ideas. Short as it was, I wholeheartedly cherish the precious memory of working with them. I also thank Prof. Masa-aki Haga, Dr. Jie Gao, Dr. Eric Rus, Dr. Hongsen Wang, Dr. Jimmy John, Dr. Julia A. Mundy, Dr. Hualei Qian, Dr. Michael A. Lowe, Dr. Stephen E. Burkhardt, Dr. Hongjun Chen, Ms. Qingyun Mao, Mr. Gabriel Rodriguez, Mr. Kenneth Hernandez, Mr. Sean Conte, Ms. Katie Silberstein, Ms. Tam Truong, Ms. Johary Rivera, Mr. Ryo Wakabayashi, Ms. Abby Van Wassen, Ms. Rebecca Potash, for their wonderful company and support during my Ph.D. career. I will never forget the many delightful times and fun activities we have done together. I would like to thank Dr. Michele Tague and Ms.

Nicole Ritzert in specific for arranging activities in the lab and maintaining it with good shape. I would also like to thank the other members of the Cornell community who provided me with generous support.

Last but not least, I thank my family: my parents, Mr. Yu Kai and Mrs. Zhou Bin, for giving me life in the first place, for educating me with aspects from both arts and science. Your love and support have helped me not only through graduate school, but also my life. I thank my maternal grandmother, Mrs. Yu Shaowen, for feeding my meals and taking care of almost everything since I was born. Nothing would be possible for my life without her support. I sincerely wish she can recover and walk again. I also thank my paternal grandparents, Professor Yu Jigang and Professor Lin Jiaying, for teaching me the importance of education. Most importantly, I thank my wife, Dr. Siyu Huang, for savoring the pain and joy with me over the past nine years, taking care of me through all those harrowing days and sleepless nights, and loved me unconditionally. Without her support, I can never imagine to complete this thesis in the dark night of cold Ithaca winter.

TABLE OF CONTENTS

LIST OF FIGURES

LIST OF TABLES

LIST OF ABBREVIATIONS

TEM, Transmission Electron Microscopy

EELS, Electron Energy Loss Spectroscopy

PEMFC, Proton Exchange Membrane Fuel Cell

ORR, Oxygen Reduction Reaction

EC, Ethylene Carbonate

DEC, Diethyl Carbonate

LiPF6, Lithium Hexafluorophosphate

LIB, Lithium Ion Battery

EV, Electric Vehicle

Li/S, Lithium Sulfur Battery

GO, Graphene Oxide

Amy, Amylopectin

PTFE, Poly-Tetrafluoroethylene

MWCNT, Multi-Walled Carbon NanoTube

HAADF, High Angle Annular Dark Field

BF, Bright Field

EDX, Energy Dispersive X-ray

XRD, X-Ray Diffraction

ADF, Annular Dark Field

STEM, Scanning Transmission Electron Microscopy

TGA, Thermal Gravimetric Analysis

LiTFSI, Lithium Bis (Trifluoromethanesulfonyl) Imide

DOL, 1,3-Dioxolane

DME, Dimethoxy Ethane

CHAPTER 1

INTRODUCTION

Section 1.1. Overview of Electrochemical Energy Storage and Conversion Systems

Among a variety of alternative energy conversion and storage technologies, fuel cells and lithium-ion batteries are of particular interest for the electrification of transportation as well as for grid applications. At the fundament level, both fuel cells and batteries are electrochemical devices, where the chemical reactions take place at an interface between an electron conductor (electrode) and ionic conductor (electrolyte). These electrochemical reactions involve electron transfer between the electrode and the electrolyte or species in solution. Thus, electrochemistry is the study of the interactions between electrical energy and chemical changes. [1, 2] While the field of electrochemistry covers a broad range of topics ranging from electrochemical phenomena, electrochemical devices, and electrochemical techniques, this thesis is mainly focused on understanding electrochemical devices such as fuel cells and batteries.

In electrochemical devices, electrical energy is generated by conversion of chemical energy via redox reactions at the anode and cathode. As the anode reactions usually take place at lower electrode potentials than at the cathode, the terms anode (or negative) and cathode (or positive) electrode are used to determine the voltage difference.

A fuel cell is an electric energy conversion device that coverts the chemical energy, normally in the form of hydrogen or small organic molecules, into electrical energy. As shown in Fig.1, normally fuel cells are composed of two electrodes, anode (where the fuel is oxidized) and the cathode (where the oxidant is reduced). By

transferring electrons during the oxidation-reduction reaction, chemical energy is converted into electrical energy. The most common type of fuel cell is the so called proton exchange membrane fuel cells (PEMFC), in which hydrogen fuel is oxidized at the anode and oxygen gas is reduced on the cathode. The major limitation of PEMFC is the high cost of the polymer membrane, which is made of proprietary Nafion®, and the cathode catalyst, which is primarily platinum. The object of academic research is to lower the loading of platinum by alloying with other transition metal(s). This approach could also improve of catalytic activity as well as enhancing durability.

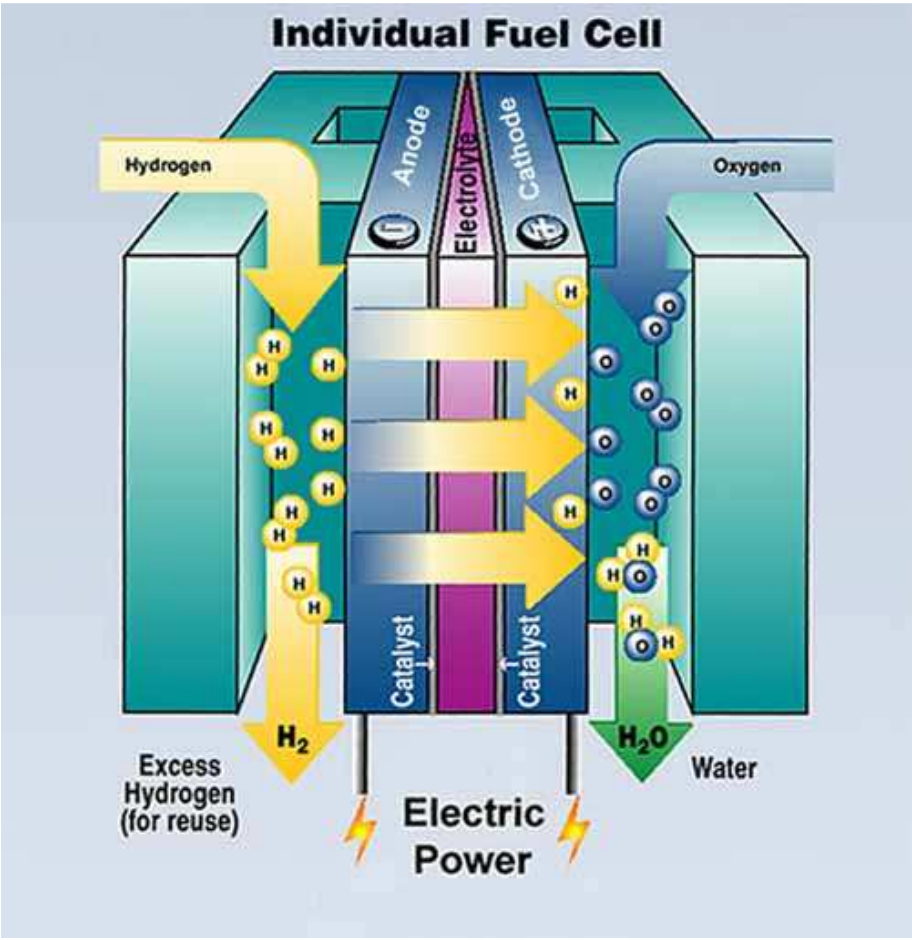

Fig.1.1 Schematic of a fuel cell. Figure reproduced from reference [3].

A lithium-ion battery is similar to a fuel cell, in that it also comprises an anode, cathode, electrolyte and membrane (Fig.2). The difference is that rather than supplying fuels externally, the battery can be charged and discharged (also known as “cycle”) within certain conditions. For example, a battery is self-contained and can be promoted to a higher energy state upon flowing of a positive current, or can be restored to its original discharged condition by an electric current flowing in the direction opposite to the flow of current when the cell is charged. The typical lithium-ion battery uses a lithium metal oxide as the cathode (i.e. $LiCoO_2$), a graphite/carbon as anode, $LiPF_6$ in a carbonate as electrolyte and a lithium-conducting polymer as separator (i.e. polyethylene). Lithium-ion batteries have been widely used as the major energy storage platform for consumer electronics and is being gradually used in electric vehicles and industrial level energy grid storage. Despite their wide application, today’s lithium-ion batteries still have limited energy density, precluding their application in long-range electric vehicles. Additionally, lithium-ion batteries commonly degrade significantly after 200-500 cycles, making longer term applications hard to implement.

A lithium sulfur battery is similar to a lithium-ion battery, with the exception that a sulfur-carbon composite is used as the cathode, metallic lithium is used as the anode, and LiTFSI in DOL/DME used as the electrolyte. Lithium-sulfur batteries have attracted much attention in recent years due to their high theoretical capacity of 1,672mAh g^{-1} and low cost. However, a rapid capacity fade is generally observed, attributed mainly to polysulfide dissolution and volume expansion. Although many strategies have been reported to prolong their cyclability, the high cost and complex preparation processes still preclude their practical application.

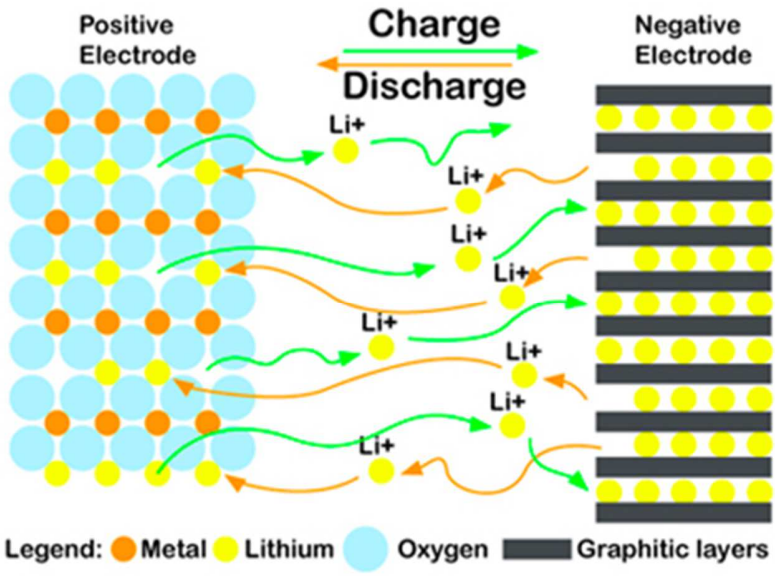

Fig. 2. Schematics of a lithium-ion battery. Figure reproduced from reference[4].

Section 1.2. Comparison of Different Systems

A fuel cell is an energy conversion system whereas a battery is an energy storage device. In the case of a fuel cell, it is an open system where the external sources such as hydrogens provide the energy. The reactions at the interfaces of cathodes and anodes are charge-transfer based. Therefore, the active masses undergoing the redox reactions are delivered from outside the cell, either from the environment, for example, oxygen from air, or from a tank, for example, fuels such as hydrogen. In the case of a battery, it is a closed system, where the anode and cathode are the charge-transfer medium and take an active role in the redox reactions as "active masses". Compared to fuel cells, batteries rely on the internal stored energy and utilized as the energy source for powering external devices.

A Ragone plot (energy density vs. power density) is typically used to compare the power and energy capabilities of common electrochemical devices[5]. As shown in Fig. 3, fuel cells can be considered to be high-energy systems, while batteries have higher power density but lower energy density. Lithium-metal batteries such as lithium-air and lithium-sulfur are considered hybrid systems of both batteries and fuel cells-they can provide improved energy density and therefore might be more suitable for applications where high energy is needed (Fig. 4). It is also noted that neither a fuel cell nor battery can match the characteristics of the internal combustion engine. High power and high energy can best be achieved when the available electrochemical power systems are hybrid. In such case, one would expect the fuel cell to provide high energy density while the battery can supply high power density needed to compete with the internal combustion engine.

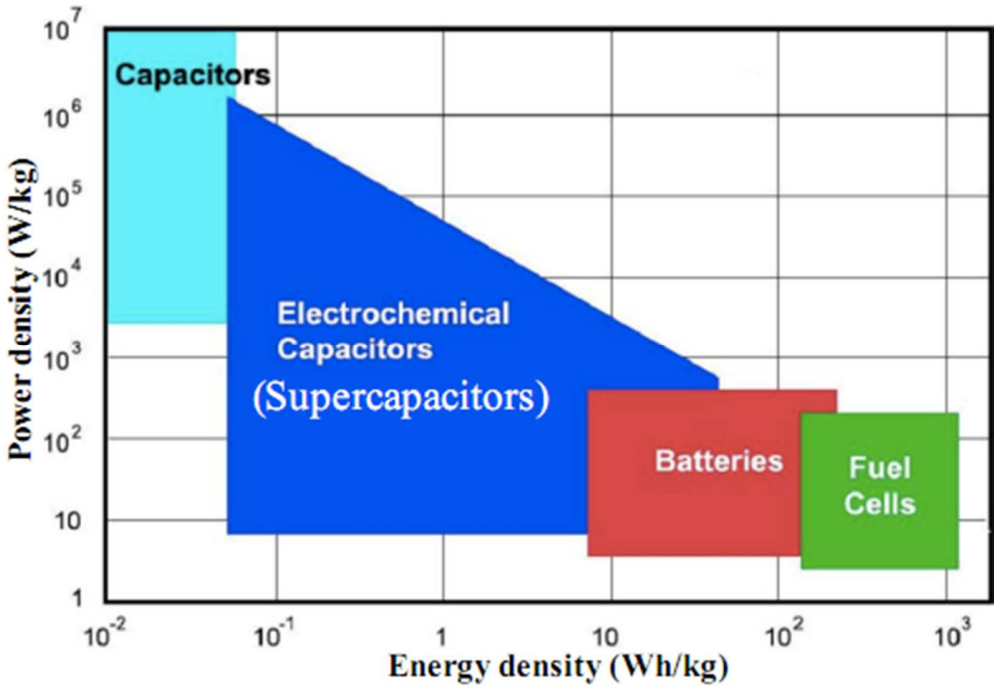

Fig.3 Ragone plot of different electrochemical energy storage and conversion devices. [5]

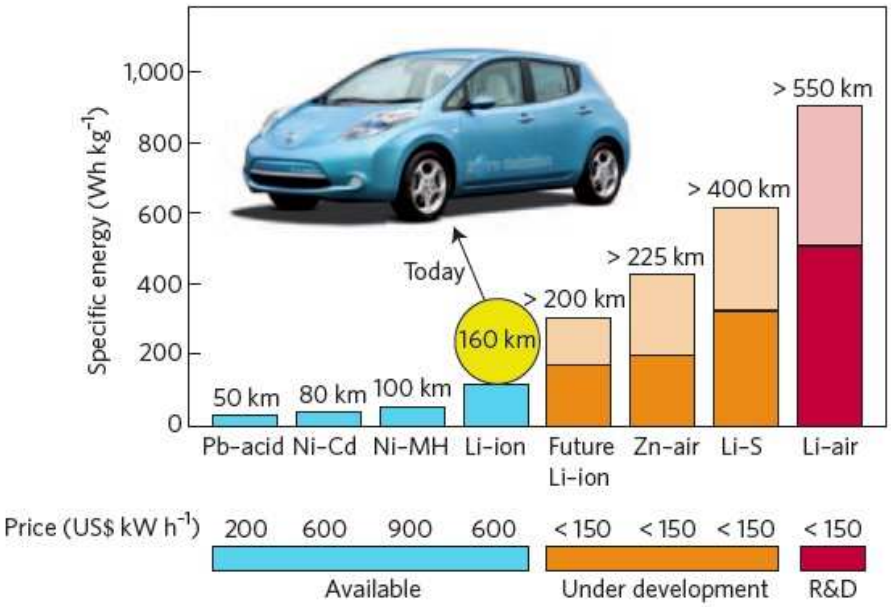

Fig. 4 Comparison of different energy storage devices and their projected ranges inside an electric vehicle, with cyan color representing available devices, yellow representing under development market and red representing R&D . Within the category of beyond “under development”, the light color represents potential energy density while the solid color is the achievable energy density. While the current electric vehicle can typically deliver a driving range of 160 km with energy density of 150 Wh/kg, Li-S batteries could potentially boost this driving range beyond 400 km with energy density of 600 Wh/kg. Figure reproduced from reference [6].

Both fuel cells and batteries are considered candidates for the replacement of traditional internal combustion engine with fossil fuels. Fuel cells generally provide higher energy density, demonstrating the required ~ 300 mile range for automotive applications.[7] However, the high cost and rapid degradation of platinum (Pt) catalysts are great challenges remaining to be solved. Research that enables a dramatic decrease of Pt cost or a prolonged cycle life of Pt catalyst is needed for the wide commercialization of fuel cells. Lithium-ion batteries generally have a higher power density but lower energy density, making them more suitable for small-vehicle, low-mileage-per-day electric vehicle applications. Research that enables battery electrode material with higher capacity, longer cycle life and faster charge-discharge rate will be essential for the wide acceptance of electric vehicles.

Section 1.3. New Insights from this thesis

This thesis is focused on the use and development of advanced scanning transmission electron microscopy techniques, especially *in-situ* methods, for energy applications. Specifically, the intent is to understand materials properties and reaction mechanisms of fuel cell catalysts and novel battery electrode materials. With the information obtained at the nanoscale (natural length scale for these applications), I have been able to demonstrate the performance improvement of fuel cells, lithium-ion batteries and lithium-sulfur batteries. More specifically, this thesis is divided into three main topics: (I) understanding the degradation mechanism of fuel cells and battery systems; (II) use the knowledge for the discovery and material characterization to design

better catalysts for fuel cells, and (III) advance the electrical energy storage characteristics for the lithium battery systems.

Section 1.4. Acknowledgements

The work presented in following chapters rely heavily on collaborative efforts. The fuel cell catalysts were synthesized Dr. Deli Wang (Abruña and DiSalvo group), Dr. Hao Chen (DiSalvo group), and also supplied by General Motors. The high resolution TEM was carried out in collaboration with Dr. Huolin Xin (Muller group) and Dr. Robert Hovden (Muller group). The *in-situ* TEM setup was designed in collaboration with Protochips Inc, while the experiment and data analysis were performed in collaboration with Ms. Megan Holtz (Muller group). The Fe_2O_3:Au catalysts were prepared by Dr. William Baumgardner (Hanrath group).

References

1. http://en.wikipedia.org/wiki/Electrochemistry.
2. Goodenough, J. B. *Energy & Environmental Science* **2014,** 7, (1), 14-18.
3. http://butane.chem.uiuc.edu/pshapley/Enlist/Labs/FuelCellLab/FuelCell.html.
4. http://www.snupeel.com/.
5. Winter, M.; Brodd, R. J. *Chemical Reviews* **2004,** 104, (10), 4245-4270.
6. BrucePeter, G.; FreunbergerStefan, A.; HardwickLaurence, J.; TarasconJean, M. *Nat Mater* **2012,** 11, (02), 172-172.
7. Wagner, F. T.; Lakshmanan, B.; Mathias, M. F. *J. Phys. Chem. Lett.* **2010,** 1, (14), 2204-2219.

CHAPTER 2

3-D TRACKING AND VISUALIZATION OF HUNDREDS OF Pt-Co FUEL CELL NANOCATALYSTS DURING ELECTROCHEMICAL AGING[*†]

Section 2.1. Introduction

Proton exchange membrane fuel cells (PEMFCs) represent an attractive energy conversion technology, which is also an environmentally-friendly alternative to the internal combustion engine used in automobiles[1, 2]. In a PEMFC, hydrogen fuel is oxidized at the anode and oxygen is reduced at the cathode to produce water and electricity. While the standard reduction potential of O_2 to H_2O is +1.23 V, the kinetics of the oxygen reduction reaction (ORR) are notoriously slow, giving rise to large overpotentials. As a result, much recent work has focused on the improvement of the cathode's electrocatalytic activity by synthesizing nanoparticles composed of platinum alloyed with a second element[3-6]. Among these, one of the most promising candidates is Pt_3Co, which has been shown both experimentally[7] and theoretically[8] to have a 2-4 fold enhancement in the ORR kinetics relative to pure Pt. However, the rapid degradation of the Pt_3Co nanocatalyst results in unacceptably short life times of the fuel cell[1]. To date, the cost and degradation of cathode catalyst are two of the major barriers for the commercialization of PEMFCs. Therefore, it is of great importance to understand the mechanisms of degradation of nanocatalyst particles during electrochemical aging in a fuel cell cathode. A great deal of past efforts have focused on the *ex-situ* study of the nanocatalyst after electrochemical aging in a membrane-electrode-assembly (MEA, the

---

[*] Produced with permission from Yingchao Yu, Huolin L. Xin, Robert M. Hovden, Deli Wang, Eric D. Rus, Julia A. Mundy, David A. Muller, Héctor D. Abruña. *Nano letters* 2012, 12 (9), 4417–4423. Copyright © 2012 American Chemical Society

[†] Author contribution: Y.Y and H.L.X designed, performed the experiment and analyzed the data. R.M.H, D.W, E.R.D, J.A.M helped to analyze the 3-D tomography data and interpreated the electrochemical measurement. D.A.M and H.D.A guided the work.

power generating component of a fuel cell) [9-11]. In these experiments, the MEA was sectioned for TEM analysis, making repeated observations on the same particles impossible. Consequently, particle trajectories were not available, making it difficult to unravel the concurrent coarsening effects of particle coalescence and Ostwald ripening[9-12]. In addition, particle-support interactions are also of great importance to the coarsening of the nanoparticles[13-15]. However, with 2-D images alone, one cannot determine how the catalyst particles are distributed on a 3-D fuel cell carbon support[16].

Section 2.2. Materials and Methods

Here we present a 3-D tomographic method that allows us to track, in 3-D, the trajectories and morphological changes of individual Pt-Co nanocatalyst particles on a fuel cell carbon support, before and after electrochemical aging via voltage sweeps. To achieve this, we carried out the electrochemical experiments directly on a TEM support grid[17-20]. In essence, a carbon-coated gold index grid was used as the working electrode in a three electrode electrochemical cell (Figure 1a). The fuel cell catalyst materials were deposited on the grid prior to the electrochemical experiments. The grid (Figure 1b) contained indexed windows, allowing us to perform electron tomography on exactly the same region of the catalyst material before (Figure 1c) and after (Figure 1d) aging, from which we were able to identify hundreds of nanoparticles in 3-D with precise one-to-one correspondence. This enabled us to study the coarsening evolution of the particles by tracking location changes on the support surface, observing changes in particle volume, and directly visualizing coarsening events. We found that, following extensive cycling of the Pt-Co catalysts under normal fuel cell operating conditions (voltage scan from +0.6 V to +1.0 V for 30,000 cycles), the coarsening could be mainly attributed to coalescence of the nanoparticles. Furthermore, the observed coalescence and movement of the nanocatalyst particles was found not to be the result of carbon support degradation, but rather due to the electrochemical cycling itself. In addition, in order to

detect changes in the near surface composition of the catalysts, we also performed atomic-scale electron energy loss spectroscopic (EELS) imaging of the nanoparticles,

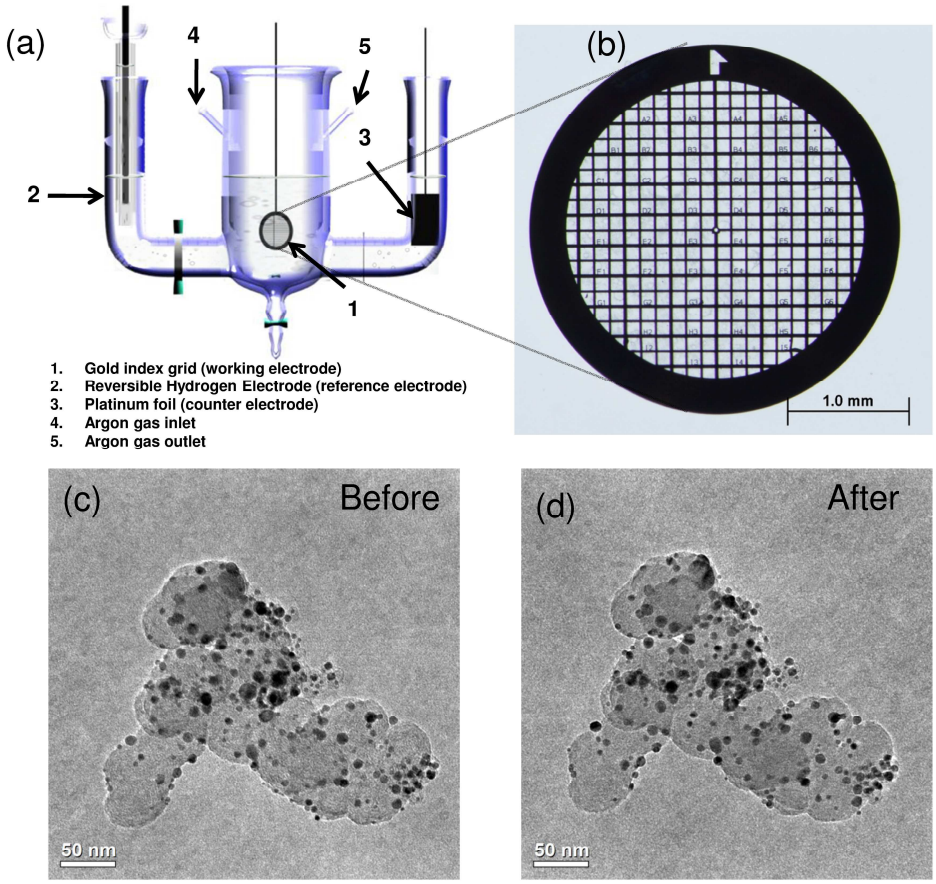

Figure 1. (a) Schematic of the three electrode electrochemical cell. **(b)** The carbon-coated gold finder grid. **(c)-(d)** Bright field TEM images of the same Pt-Co fuel cell material (metallic nanocatalyst loaded on 3-D carbon-black supports) identified before (c) and after (d) electrochemical aging.

from which we extracted the chemical composition of the near-surface volume of the particles after voltage cycling.

In our study, a carbon-coated gold TEM grid with indexed windows (Figure 1b) was chosen as the working electrode. The indexed windows facilitated the determination of locations of the same catalyst materials before and after the electrochemical aging (Figure 1c) in a three compartment electrochemical cell (Figure 1a). Gold grids were chosen because they are relatively inert over the potential range of interest. To demonstrate that the TEM grid is a reliable electrode, we characterized the grid from two aspects. First, Figure 1S (a) presents a comparison of the voltammetric profiles of a gold TEM grid and a gold disk electrode. Both profiles exhibited a Au-oxide reduction peak at approximately +1.2 V (vs. RHE)[‡], which was characteristic of a gold surface. The double-layer region exhibited a capacitive response, which indicated that the surface of the grid was free of contamination. Second, the cross-talk between the catalyst material and the electrode should be minimal under the electrochemical aging conditions of interest, i.e. between +0.6 V to +1.0 V in our experiments. Figure 1S (b) shows that, below +1.4 V, interference from the gold TEM substrate was not significant, demonstrating the electrochemical reliability of the grid. In addition to the cycling setup, it is crucial to choose the appropriate electrochemical aging method. In the case of platinum, previous studies have suggested that potential cycling is more damaging than holding the potential at a given value[21, 22] (Figure 2S), and that a triangular wave form is more damaging than a square wave[23]. Therefore, we chose to cycle the potential with a triangular wave, so as to introduce more severe aging effects to the electrocatalyst nanoparticles.

[‡] In the rest of the text, reported voltages are referenced to a RHE unless otherwise specified.

The aging experiment was performed at a scan rate of 50 mV/s, between +0.6 V to +1.0 V (vs. RHE), and a complete cycle from +0.05 V to +1.2 V was carried out immediately after each thousand cycles to determine the electrochemical surface area (ECSA) of the catalyst. The choice of aging window of +0.6 V to +1.0 V and 30,000 cycles is based on the US Department of Energy (DOE) accelerated stress test protocols for PEMFCs[24].

Section 2.3. Results and Discussions

The electrochemical aging results are shown in Figure 2a. Two key changes are highlighted by the blue and red dashed circles. First, the hydrogen adsorption peak at around +0.27 V in the anodic scan became sharper with aging. This sharpening effect was ascribed to the nanocatalyst surfaces becoming more Pt rich. The EELS spectrum analysis further confirmed such an assertion (vide-infra). Moreover, the hydrogen adsorption peaks at higher potential increased at the expense of those at lower potential. This is typically an indication of exposure of different facets after the electrochemical treatment[25]. The second feature to notice is the shift in the platinum oxide reduction peak at around +0.8 V to more positive values. To exclude the possibility that such a shift was due to the acid-leaching of cobalt, a set of control experiments was carried out on pure Pt nanocatalysts (i.e. no cobalt), as shown in Figure 3S. The results indicate that the positive shift of Pt oxide reduction peak could be observed both in Pt_3Co/C and Pt/C. Consequently, we ascribe the positive shift of the Pt-O reduction peak not due to Co leaching. It was speculated that such shift could be caused by the increase in the size of the nanoparticles, as it has been previously reported that a growth in the size of the nanoparticles is often accompanied by a shift in the Pt-O reduction peak[26, 27]. In our study, accompanied by the size increase of some nanoparticles, the overall surface area decreased, as suggested by the ECSA measurements in Figure 2b. The ECSA was calculated by determining the charges associated with the adsorption and desorption of

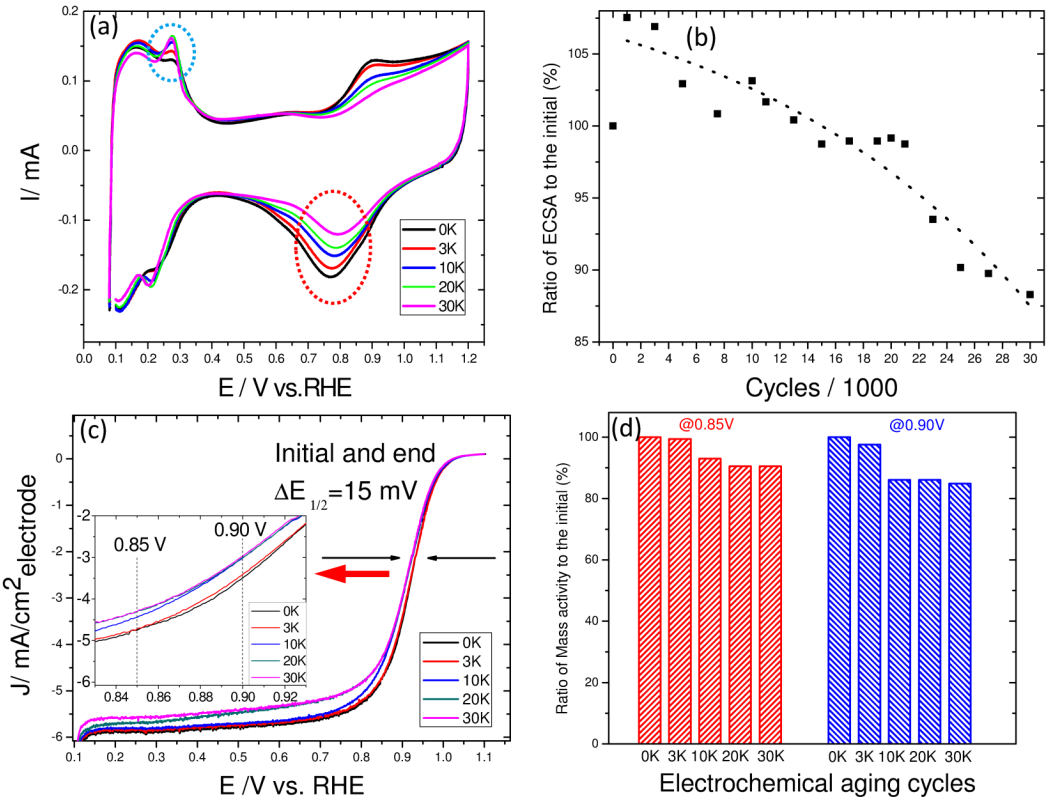

Figure 2. (a) Cyclic voltammogram (CV) of Pt_3Co/C nanocatalyst, before electrochemical aging (0K), and after 3000 (3K, 'K' represents 1000), 10K, 20K and 30K cycles (between +0.6 V and +1.0 V) in 0.1M $HClO_4$ at a scan rate of 50 mV/s. The blue dashed-circle highlights the sharpening of the H_2 adsorption peak at ~ +0.27 V. The hydrogen adsorption peaks at higher potential increase at the expense of those at lower potential. It is an indication of rearrangement between (100) and (111) facets[25]. The red dashed-circle highlights the shift of the Pt-O reduction peak to more positive potentials. **(b)** Plot of electrochemical surface area (ECSA) as a fraction of its initial value, as a function of the number of cycles, for experiments performed on a gold grid. **(c)** Polarization curves for the oxygen reduction reaction (ORR) during the aging process, in O_2 saturated 0.1M $HClO_4$ solution, at a scan rate of 5 mV/s. Inset is the magnification from +0.83 V to +0.93V. The shift in the potential at half maximum kinetic current ($\Delta E_{1/2}$) was 15 mV. **(d)** Percentile of mass activity calculated at +0.85 V (red) and +0.90 V (blue) compared to its initial value, during the aging process.

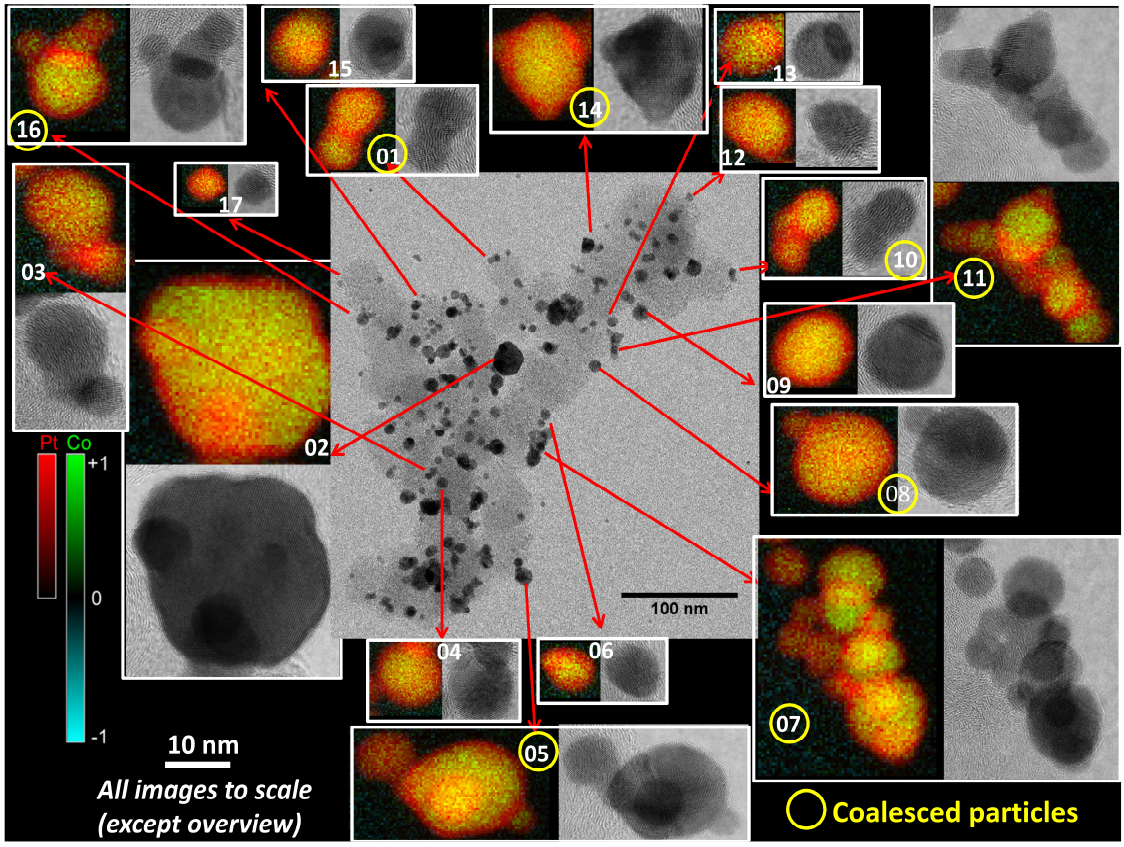

Figure 3. Pt_3Co/C nanocatalyst after electrochemical aging. The overall bright-field transmission electron microscopy (BF-TEM) image is shown in the center, with specific areas highlighted alongside Pt/Co chemical maps obtained by electron energy loss spectroscopy (EELS). The relative Pt concentration is shown in red and the Co concentration in green; yellow indicates a PtCo alloy. The arrow on the EELS map points out the position of the targeted particle from its carbon support. The yellow circle on the number indicates particles that were coalesced. All images (except the overview) are to the same scale for easy comparison.

hydrogen between +0.05 V and +0.40 V—assuming 0.21 mC/cm2 as the conversion factor for one monolayer of adsorbed hydrogen. Upon electrochemical aging, platinum was first oxidized to platinum oxide in the anodic scan (with an onset potential around +0.80 V), and the oxide was subsequently reduced back to platinum during the cathodic scan (with a peak potential at around +0.80 V). The dissolution-redeposition process results in a decrease in the ECSA28. At the end of the 30,000 cycles, the ECSA had dropped to around 87% of its initial value. This provides a direct indication of the overall changes in the surface area of the nanocatalysts.

The ORR polarization curves on the Pt_3Co/C nanocatalyst, before and after different extents of aging cycles, are shown in Figures 2c-d. The experiments were recorded on the same RDE electrode in an O_2-saturated 0.1 M $HClO_4$ solution at a rotation rate of 1600 rpm, after regular intervals of electrochemical aging. Metrics by which the activity of the nanocatalyst towards the ORR can be assessed include the potential at half maximum kinetic current ($E_{1/2}$), and the current at +0.85 V and +0.90 V. The last two can be used to evaluate the mass activity, by normalizing the kinetic current to the mass of the nanocatalyst on the electrode surface (Figure 3S for more detail). We found that the $E_{1/2}$ shifted in the negative direction by about 15 mV and that the mass activity at +0.85 V and +0.90 V decreased by 15 - 20% after 30,000 cycles of aging. Such a loss in ORR activity was consistent with the ECSA results. The degradation of the nanocatalyst was further confirmed by CO stripping (Figure 4S). The CO oxidation peak shifted to lower potentials, suggesting that the aging process resulted in an increase of the effective particle size. By comparing the integrated area of CO oxidation peak (Figure 4S), a 22% surface area loss was also observed, which was in agreement with the ECSA measurement.

Figures 5S-7S present bright-field TEM comparisons of the Pt-Co nanocatalyst materials. Owing to the labeled TEM tracing grid, it was possible to locate the same

areas before and after electrochemical aging. It has been reported that carbon corrosion can play an important role in the degradation of Pt-based nanocatalysts in an MEA[14, 15], in which the potential at the cathode could go significantly above +1.0 V, especially under hydrogen starvation conditions-so the carbon support can be oxidized. However, that was not the case in our study. In the three-electrode system employed, control of the potential upper limit during voltage cycling was accurate without ambiguity. As evident in Figures 6S-7S, the carbon support was stable over the cycling range of +0.6 V to +1.0 V. Thus, any coarsening of the nanoparticles cannot be related to carbon support corrosion. In addition, in order to eliminate the possibility that the coarsening may be caused by other effects, including electron beam damage, a control experiment (Figure 2S) was performed in which the potential was held constantly at +1.2 V for 16 hours, after the electrochemical aging. Virtually no change could be observed from both TEM and ECSA measurements. Thus, the coarsening events were attributed to the voltage cycling. In Figure 5S, the particles circled in yellow were suspected to have sintered during aging. To further confirm their chemical compositions, EELS mapping of those 17 spots, after electrochemical aging, was performed and the results are present in Figure 3. A Pt-rich shell was clearly observed, with an average shell thickness determined to be 0.85 ± 0.04 nm for single-core nanoparticles, and 0.93 ± 0.07 nm for multi-core nanoparticles. Both numbers correspond to a Pt shell thickness of 3-4 Pt monolayers (see Figure 8S for more details on determining the Pt shell thickness). When comparing this to our previous study[12] of the same nanocatalytst before electrochemical aging, where the average Pt shell thickness was determined to be 2-3 Pt monolayers, it was surprising that the Pt shell thickness did not grow beyond 2-3 monolayers. The voltage cycle range and the temperature of the aging conditions could explain this. Under the electrochemical aging conditions, Pt is first oxidized during the anodic scan and then reduced during the reverse cathodic scan. During such Pt

dissolution and redeposition, the Pt-Co alloy core is exposed to the acidic environment, allowing Co to be leached into the bulk solution. On the other hand, only Pt-O would be reduced back to Pt while Co was lost. Given enough time to reach equilibrium, the thickness of the Pt shell would reach a maximum value, which is likely to be determined by the voltage cycle range and temperature. Since the upper voltage limit in our experiment was precisely +1.0 V (but not +1.2 V or higher) and the experiment was carried out at room temperature (but not 80°C or higher), the aging conditions were milder than our previous approach[12]. These evidences were speculated to explain why the Pt shell thickness did not increase for more than 2-3 Pt monolayers. More importantly, EELS mapping is key for understanding how the Pt is redeposited, i.e., is the nanoparticle coarsening dominated by Ostwald ripening or coalescence? In Ostwald ripening, larger nanoparticles grow at the expense of smaller ones, with the small ones eventually being consumed. In such a scenario, a single-core particle should be expected[29, 30]. On the other hand in coalescence, two or more particles merge together to form a multi-core particle[29, 30]. Since only Pt should be able to redeposit over this potential range, the Pt-rich shell should be much thicker in Ostwald ripening when compared to coalescence. If Ostwald ripening played as a major part, then the shell thickness on multi-core particles should consequently be much larger than on single-core particles. However, as we determined in a statistical box plot (Figure 9S), no obvious difference in shell thickness between multi-core and single-core nanoparticles could be observed. Therefore, we conclude that the electrochemical aging in our study is mainly dominated by coalescence.

Taking advantage of the distinctive dissolution and redeposition properties of Pt and Co, we found that coalescence played a major role in the coarsening of the particles using atomic-scale chemical mapping. However, the trajectories of the coalesced particles were still missing, which made it difficult to understand the underlying driving

force(s) for this particular coarsening mechanism. To overcome this limitation, the electron tomography of a Pt-Co nanocatalyst region, obtained at the exactly same location both before and after electrochemical aging, is present in Figure 4. The area was chosen to be representative of a typical particle distribution and carbon support morphology (Figures 6S-7S). By overlaying the reconstructions before and after the aging, we can directly visualize particle movement and coalescence (Figures 4a-b, and Movie 1S). It is immediately evident that most particles did not move after aging, which was confirmed by comparing the volume distribution and nearest neighbor distances (Figure 10S). The mean particle radius, around 3.2 nm, also did not change significantly—any changes that may have occurred was within a thresholding error no more than one Pt monolayer (Figure 12S). The preservation of particle positions greatly facilitated accurate alignment of the reconstructions in 3-D. The large set of fiduciary particles enabled an alignment fine enough to detect even small movements (~1-2 nm) on the carbon support. A more dramatic example of particle migration is visualized in Figure 4f, where a nanocatalyst particle 'falls' from the negative curvature (summit) into the positive curvature (valley) of the carbon support. This movement is likely driven by maximizing the contact area with the carbon support. This is consistent with the electrochemical results (Figures 2a and 3S), which also suggest that the orientation of nanoparticle facets changed after aging. Tracking particles one-by-one, before and after electrochemical aging, also reveals the coarsening mechanisms in the system. We found that the majority of the coarsening events were caused by particle coalescence, as illustrated in Figures 4c-e. The particles were seen to both migrate and coalesce with adjacent particles. This is in contrast to Ostwald ripening, where the particles dissolve and uniformly redeposit onto larger particles nearby. After coalescence, there is a further diminution of surface area that takes place during the dissolution-redeposition process when the connection between the coalesced particles is rounded off to minimize

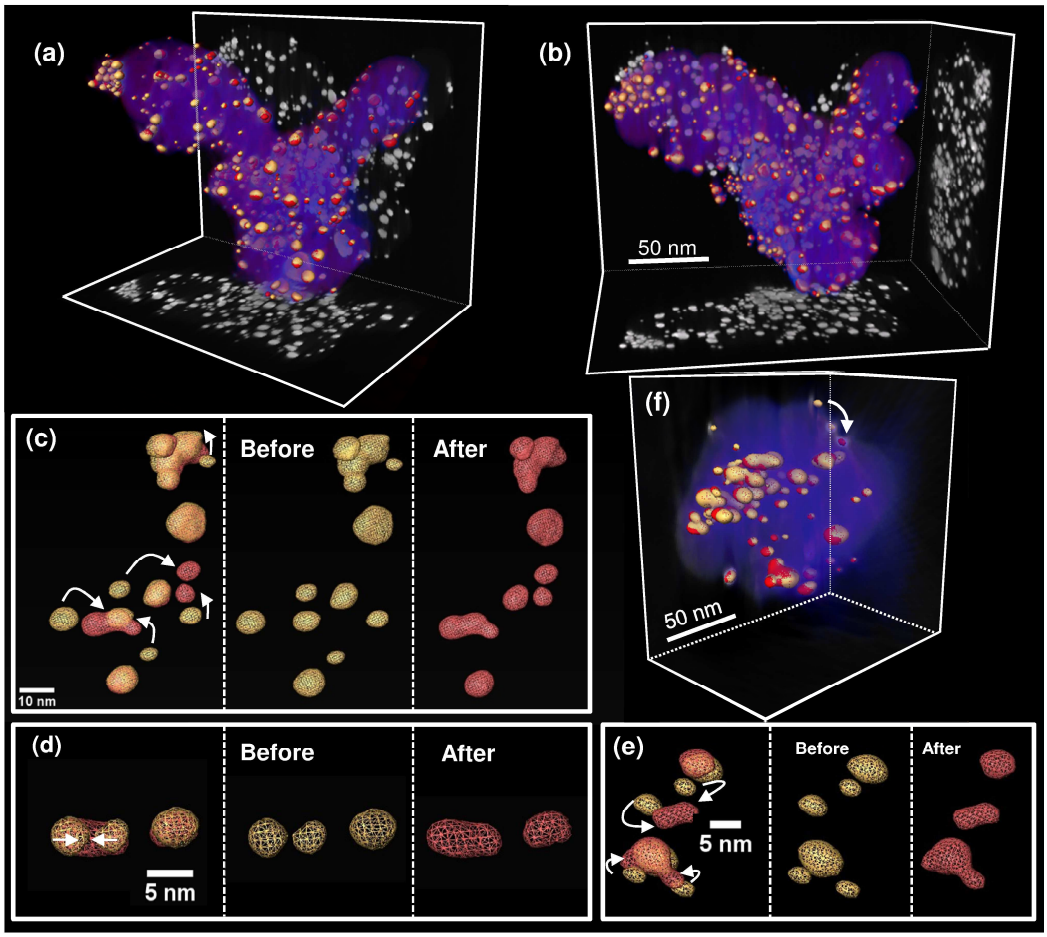

Figure 4. One-to-one correspondence of nanocatalyst particles before (*gold*) and after (*red*) electrochemical aging—same color scheme used in all figures. **(a)** 3-D reconstruction of nanocatalyst particles, on the carbon support (*violet*) with projected 2-D images shown at each side. (**b)** Alternate viewing angle. **(c,d,e)** Several instances of nanocatalyst particle coalescence and migration, with particle positions indicated by arrows. **(f)** One example of cropped volume from **(a,b)**, showing how one nanocatalyst particle moves into the positive curvature (valley) from the negative curvature (summit) of the catalyst support. The arrow points out the trajectory of the particle movement. Violet shading is the carbon support.

surface energy. This is best seen in Figure 4d, where two separate particles clearly merged uniformly. Such a result is in agreement with our previously proposed particle-particle-interaction between coalescence and Ostwald ripening[12]. It is important to note that isosurface[#] can sometimes be misleading with ill-chosen thresholds. Therefore, in this study, all coalescence events were verified with the volumetric reconstruction data (Figure 11S, Movie 2S and 3S). In Figures 11S(d)-(e), a gap seen between two particles suggests they were separate before aging, while the disappearance of such a gap confirms that the two particles were in contact with each other at the end of the cycles. This faithfully substantiates our visualization of nanoparticle coalescence in three-dimensions.

Although Ostwald ripening and coalescence might co-exist during electrochemical aging, it has been predicted that each of them would dominate at different potentials[23, 31]. At a higher cycling voltage (i.e. in MEA with hydrogen starvation), the Pt dissolution-redeposition was so severe that larger nanoparticles consumed smaller ones quickly. On the other hand, at a lower cycling voltage (i.e. our case), the migration of nanoparticles mainly took place to minimize the surface tension. One way to address the complex question would be to cycle the same nanoparticles to the potential higher than +1.4 V. However, under such conditions, our assumption regarding the gold TEM grid would no longer be valid.

Moreover, it has been reported that one of the coarsening mechanisms in Pt/Pt-alloy nanoparticle systems is carbon corrosion[18, 32, 33]. However, no obvious carbon degradation was observed in our study (Figures 6S and 7S). Possible explanations for

Isosurface represents points of constant value within a volume of space; it is a set of continuous function whose points group is in 3-D space (http://en.wikipedia.org/wiki/Isosurface)

the contrast with previous studies are two fold. First, in membrane electrode assembly (MEA) studies, the potential cycling window can be easily altered by hydrogen starvation and fuel cross-over. They can cause the potential at the cathode to be as high as +1.4V. However, in our well-defined three electrode electrochemical system, the control of the cycling window (+0.6 V to +1.0 V) is accurate. Therefore, the kinetics of carbon corrosion in this cycling window could indeed be very slow. However, we cannot completely rule out any early-stage inside-out corrosion of the carbon support that did not render an apparent change in the support morphology[14].

Section 2.4. Conclusion

In summary, we report for the first time a direct 3-D visualization of nanoparticle trajectories before and after electrochemical aging based on TEM grid indexing. The growth in the Pt shell thickness and observation of coalescence in 3-D could explain the decrease in electrochemically active surface area and loss of activity of Pt-Co nanocatalysts in fuel-cell cathodes. The simplicity and rigor of the three electrode system helps to rule out many factors that could take place in the MEA (such as hydrogen starvation), and therefore helps establish a direct correlation between ECSA and activity loss with the sintering behavior of nanocatalysts. The sintering processes were probed by atomic-scale chemical mapping and 3-D tomography. The majority of the coarsening events were determined to be coalescence, not Ostwald ripening. Moreover, the coalescence was not due to degradation of the carbon support, but rather due to the Pt dissolution-redeposition process and the curvatures on the carbon supports. Such findings suggest that minimization of particle movement can potentially slow down the coarsening of particles during the electrochemical aging. These studies will be of great help in the future design of an electrochemically durable fuel cell nanocatalyst and supports.

Supporting Information

The electrochemical and TEM characterizations of nanocatalyst, before and after aging, are available. Also included are three movies of nanoparticles on the carbon support. This material is available free of charge via the Internet at http://pubs.acs.org.

REFERENCES

1. Mathias, M. F.; Makharia, R.; Gasteiger, H. A.; Conley, J. J.; Fuller, T. J.; Gittleman, C. I.; Kocha, S. S.; Miller, D. P.; Mittelsteadt, C. K.; Xie, T.; Yan, S. G.; Yu, P. T. *Electrochem. Soc. Interface* **2005,** 14, 24-35.
2. Stamenkovic, V. R.; Fowler, B.; Mun, B. S.; Wang, G. F.; Ross, P. N.; Lucas, C. A.; Markovic, N. M. *Science* **2007,** 315, 493-497.
3. Gupta, G.; Slanac, D. A.; Kumar, P.; Wiggins-Camacho, J. D.; Kim, J.; Ryoo, R.; Stevenson, K. J.; Johnston, K. P. *The Journal of Physical Chemistry C* **2010**.
4. Mazumder, V.; Chi, M.; More, K. L.; Sun, S. *Journal of the American Chemical Society* **2010**.
5. Zhou, Y.; Neyerlin, K.; Olson, T. S.; Pylypenko, S.; Bult, J.; Dinh, H. N.; Gennett, T.; Shao, Z.; O'Hayre, R. *Energy & Environmental Science* **2010**.
6. Wang, C.; van der Vliet, D.; More, K. L.; Zaluzec, N. J.; Peng, S.; Sun, S.; Daimon, H.; Wang, G.; Greeley, J.; Pearson, J.; Paulikas, A. P.; Karapetrov, G.; Strmcnik, D.; Markovic, N. M.; Stamenkovic, V. R. *Nano Letters* **2010**, null-null.
7. Stamenkovic, V. R.; Mun, B. S.; Arenz, M.; Mayrhofer, K. J. J.; Lucas, C. A.; Wang, G.; Ross, P. N.; Markovic, N. M. *Nat Mater* **2007,** 6, (3), 241-247.

8. GreeleyJ; Stephens, I. E. L.; Bondarenko, A. S.; Johansson, T. P.; Hansen, H. A.; Jaramillo, T. F.; RossmeislJ; ChorkendorffI; Nørskov, J. K. *Nat Chem* **2009,** 1, (7), 552-556.

9. Stanis, R. J.; Kuo, M. C.; Rickett, A. J.; Turner, J. A.; Herring, A. M. *Electrochimica Acta* **2008,** 53, (28), 8277-8286.

10. Sugawara, S.; Maruyama, T.; Nagahara, Y.; Kocha, S. S.; Shinohra, K.; Tsujita, K.; Mitsushima, S.; Ota, K. *Journal of Power Sources* **2009,** 187, (2), 324-331.

11. Chen, S.; Gasteiger, H. A.; Hayakawa, K.; Tada, T.; Shao-Horn, Y. *J. Electrochem. Soc.* **2010,** 157, (1), A82-A97.

12. Xin, H.; Mundy, J.; Cabezas, R.; Fitting-Kourkoutis, L.; Muller, D.; Liu, V.; Zhang, J.; Subramanian, N.; Makharia, R.; Wagner, F. *Microscopy and Microanalysis* **2010,** 16, (SupplementS2), 104-105.

13. Shao-Horn, Y.; Sheng, W. C.; Chen, S.; Ferreira, P. J.; Holby, E. F.; Morgan, D. *Topics in Catalysis* **2007,** 46, (3-4), 285-305.

14. Liu, Z. Y.; Brady, B. K.; Carter, R. N.; Litteer, B.; Budinski, M.; Hyun, J. K.; Muller, D. A. *J. Electrochem. Soc.* **2008,** 155, (10), B979-B984.

15. Schulenburg, H.; Schwanitz, B.; Linse, N.; Scherer, G. n. G.; Wokaun, A.; Krbanjevic, J.; Grothausmann, R.; Manke, I. *The Journal of Physical Chemistry C* **2011,** 115, (29), 14236-14243.

16. Midgley, P. A.; Dunin-Borkowski, R. E. *Nat Mater* **2009,** 8, (4), 271-280.

17. Hartl, K.; Hanzlik, M.; Arenz, M. *Energy & Environmental Science* **2011,** 4, (1), 234-238.

18. Liu, Z. Y.; Zhang, J. L.; Yu, P. T.; Zhang, J. X.; Makharia, R.; More, K. L.; Stach, E. A. *J. Electrochem. Soc.* **2010,** 157, (6), B906-B913.

19. Mayrhofer, K. J. J.; Meier, J. C.; Ashton, S. J.; Wiberg, G. K. H.; Kraus, F.; Hanzlik, M.; Arenz, M. *Electrochemistry Communications* **2008,** 10, (8), 1144-1147.

20. Mayrhofer, K. J. J.; Ashton, S. J.; Meier, J. C.; Wiberg, G. K. H.; Hanzlik, M.; Arenz, M. *Journal of Power Sources* **2008,** 185, (2), 734-739.

21. Darling, R. M.; Meyers, J. P. *J. Electrochem. Soc.* **2003,** 150, (11), A1523-A1527.

22. Mathias, M. F.; Makharia, R.; Gasteiger, H. A.; Conley, J. J.; Fuller, T. J.; Gittleman, C. J.; Kocha, S. S.; Miller, D. P.; Mittelsteadt, C. K.; Xie, T.; Yan, S. G.; Yu, P. T. *Electrochem. Soc. Interface* **2005,** 14, (3), 24-35.

23. Kinoshita, K.; Lundquist, J. T.; Stonehart, P. *Journal of Electroanalytical Chemistry and Interfacial Electrochemistry* **1973,** 48, (2), 157-166.

24. Strasser, P.; Koh, S.; Anniyev, T.; Greeley, J.; More, K.; Yu, C.; Liu, Z.; Kaya, S.; Nordlund, D.; Ogasawara, H.; Toney, M. F.; Nilsson, A. *Nature Chemistry* **2010,** 2, (6), 454-460.

25. Cerviño, R. M.; Triaca, W. E.; Arvia, A. J. *Electrochimica Acta* **1985,** 30, (10), 1323-1327.

26. Frelink, T.; Visscher, W.; van Veen, J. A. R. *Journal of Electroanalytical Chemistry* **1995,** 382, (1-2), 65-72.

27. Peuckert, M.; Yoneda, T.; Betta, R. A. D.; Boudart, M. *J. Electrochem. Soc.* **1986,** 133, (5), 944-947.

28. Rinaldo, S. G.; Stumper, J. r.; Eikerling, M. *The Journal of Physical Chemistry C* **2010,** 114, (13), 5773-5785.

29. Bowker, M. *Nat Mater* **2002,** 1, (4), 205-206.

30. Campbell, C. T.; Parker, S. C.; Starr, D. E. *Science* **2002,** 298, (5594), 811-814.

31. Adzic, R.; Büchi, F. *Springer Science and Business Media* **2009,** 7.

32. Ball, S. C.; Hudson, S. L.; Thompsett, D.; Theobald, B. *Journal of Power Sources* **2007,** 171, (1), 18-25.

33. Xu, F.; Wang, M.-x.; Liu, Q.; Sun, H.-f.; Simonson, S.; Ogbeifun, N.; Stach, E. A.; Xie, J. *J. Electrochem. Soc.* **2010,** 157, (8), B1138-B1145.

CHAPTER 3

COALESCENCE IN THE THERMAL ANNEALING OF NANOPARTICLES: AN *IN-SITU* STEM STUDY OF THE GROWTH MECHANISM OF ORDERED Pt-Fe NANOPARTICLES IN A KCl MATRIX[*†]

Section 3.1. Introduction

With potential applications in ultrahigh-density magnetic recording media and high-performance nano-composite magnets, ferromagnetic PtFe nanoparticles and thin films with small particle sizes, narrow size distributions, and optimized compositions are of great interest.[1-5] In contrast to PtFe alloys, the atomically-ordered intermetallic structure is ferromagnetic and shows large uniaxial magnetocrystalline anisotropy and good chemical stability. The PtFe nanoparticles are usually synthesized by a liquid phase reduction of metal cation precursors, during which different long chain surfactant molecules are used to protect the particles from aggregation as well as to control grain growth and particle size.[1, 6-9] The as-synthesized nanoparticles are reported to have a disordered face-centered cubic (FCC) structure and are superparamagnetic at room temperature. In contrast, PtFe nanoparticles of the ordered tetragonal (FCT) structures are ferromagnetic at room temperature. To prepare such ordered particles, annealing at moderate temperatures (up to 600 ^{o}C) is necessary.[1, 9] At these temperatures, the surfactant molecules decompose to form carbonaceous residues and the particles coarsen and agglomerate in an uncontrolled manner.[9] Different post-synthetic approaches have been developed to prepare ferromagnetic

---

[*] Produced with permission from Hao Chen, Yingchao Yu, Huolin L. Xin, Kathryn A. Newton, Megan E. Holtz, Deli Wang, David A. Muller, Héctor D. Abruña, and Francis J. DiSalvo, (2012), *Chemistry of Materials*, 2013, 25 (8), 1436–1442.

† H.C. and Y.Y. contributed equally to this work. H.C. and Y.Y. designed, performed and analyzed the majority data of the experiments presented. H.L.X, K.A.N, M.E.H. and D.W. helped to analyze the data. D.A.M., H.D.A. and F.J.D. guided the work.

PtFe nanoparticles without forming aggregates. For example, the as-synthesized nanoparticles can be coated either with SiO_2 or MgO before thermal annealing, and the protecting oxide layer is then removed after the ordered tetragonal phase is formed. These methods involve multiple steps, including nanoparticle synthesis by hot injection (200 ^oC ~ 300 ^oC) with long-chain capping ligands and a separate oxide coating step.[9, 10]

Section 3.2. Materials and Methods

Synthesis of PtFe Np-KCl matrix. All the chemicals were purchased from STREM Chemicals Inc. or otherwise listed individually. The synthesis was carried as follows: 0.08 mmol $PtCl_4$, 0.08 mmol $FeCl_3$ and 2.24 mmol LiCl were weighed out in an argon filled glovebox and dissolved in 25 mL THF by stirring. 3.5 mL reducing agent KEt_3BH (1M Sigma-Aldrich) was mixed with THF to form a 10 mL solution. Then, the precursor solution was drawn up into a syringe and injected into the reducing agent solution under vigorous stirring. The mixed solutions immediately (within seconds) formed an opaque black solution. The solution was then transferred to a centrifuge tube, sealed and brought out of the box and centrifuged at 5000 rpm for 5 min. The clear supernatant was decanted off and the precipitate was subsequently washed three times with THF and hexanes without air exposure. The product was then dried under vacuum for 2 hours and transfer back into the Ar glovebox.

Annealing procedure to achieve the ordered intermetallic phase. The PtFe-KCl powder was placed into silica tubes in an argon filled glovebox, which were then transferred to a Schlenk / vacuum line and sealed under vacuum. The sample was then heated to 600 ^oC at a rate of 100 ^oC per hour and annealed at 600 ^oC for 12 hours.

STEM (scanning transmission electron microscopy) and EELS (electron-energy loss spectroscopy) measurement. The high resolution STEM images and EELS maps were acquired on a 5^{th}-order aberration-corrected scanning transmission electron

microscope (Nion UltraSTEM) operated at 100 kV, with a convergence angle α_{max} = ~30 mrad. With the setup, atomic-resolution imaging and EELS mapping are achieved routinely.[26]

In-situ STEM measurement. The *in-situ* heating experiments were obtained on a Schottky-field-emission-gun Tecnai F20 scanning transmission electron microscope (STEM) operated at 200 keV. A high-angle annular dark field detector provided an incoherent projection image of the specimen with a signal intensity proportional to the amount of material and its atomic number, which is also known as Z-contrast. The *in-situ* heating substrate (E-AHA21) and the heating TEM holder (Aduro System) are manufactured by Protochips, Inc. The heating chip contains a resistive ceramic membrane so the set temperature can be attained less than a second, after changing the set point. The calibration of temperatures was performed by using a thermo-camera prior to the experiment, and the stability of temperature was determined to be +/- 1^{o}C.

X-Ray diffraction. Powder X-ray diffraction (XRD**)** data were measured using Cu Kα radiation on a Rigaku *Ultima IV* diffractometer equipped with a theta-theta goniometer, a sealed-tube solid-state generator, and a D/TeX Ultra Imaging detector.

Particle size statistics. The edges of particles were outlined based on the intensity contrast of particles (brighter) and background (darker) from the STEM image. The areas (S) of the segmented 2D projection of nanoparticles were then used to represent particle sizes and the diameters in figure 4f were back calculated by solving for effective diameter, *d*, in $\pi*(d/2)^2 = S$. A detailed description of this method is shown in figure S5.

Robustness of the size measurements. To evaluate the robustness of the particle size measurement, two independent measurements of different number**s** of nanoparticles were conducted at each temperature frame and showed similar size distribution. As shown in figure S7, The shapes of histograms from the two data

sets match each other, indicating good precision of the particle size measurement at the areas analyzed.

Section 3.3. Results and Discussion

Synthesis of ferromagnetic PtFe nanoparticles. Here, we report on a study of the mechanism of particle growth and ordering during annealing of samples that are prepared through a one-pot scalable synthesis and stabilization method, resulting in ferromagnetic PtFe nanoparticles. The general strategy of this method is shown in figure 1. Instead of separate synthesis and protection steps, a nanoparticle-KCl (Np-KCl) matrix is formed in a simple room temperature liquid phase reduction in THF (equation 1). A detailed synthesis and thermal annealing procedure is shown in the method section.

$$PtCl_4 + FeCl_3 + 33LiCl + 40KEt_3BH \rightarrow$$

$$PtFe + 40KCl + 3.5H_2 + 7Et_3B + 33LiEt_3BH \qquad (1)$$

The THF-insoluble KCl by-product forms a matrix that protects the nanoparticles from sintering during thermal annealing up to 600 °C and that can be removed under mild conditions. This approach can be generalized to the scalable synthesis of other transition-metal/Pt intermetallic nanoparticles (e.g. Pt_3Fe, Pt_3Mn, Pt_2CoFe, PtNi), also allowing small particle sizes to be synthesized, and such nanoparticles are being considered as fuel cell catalysts.[11]

Samples of Np-KCl assemblies were annealed for 12 hours at 400 ^oC and 600 ^oC, respectively. As expected, the average composition of an ensemble of nanoparticles in an area of 500 nm by 500 nm obtained by Energy-dispersive X-ray spectroscopy (EDX) for Pt:Fe is typically 50:50 (±3%) and uniform throughout the sample (figure S1).

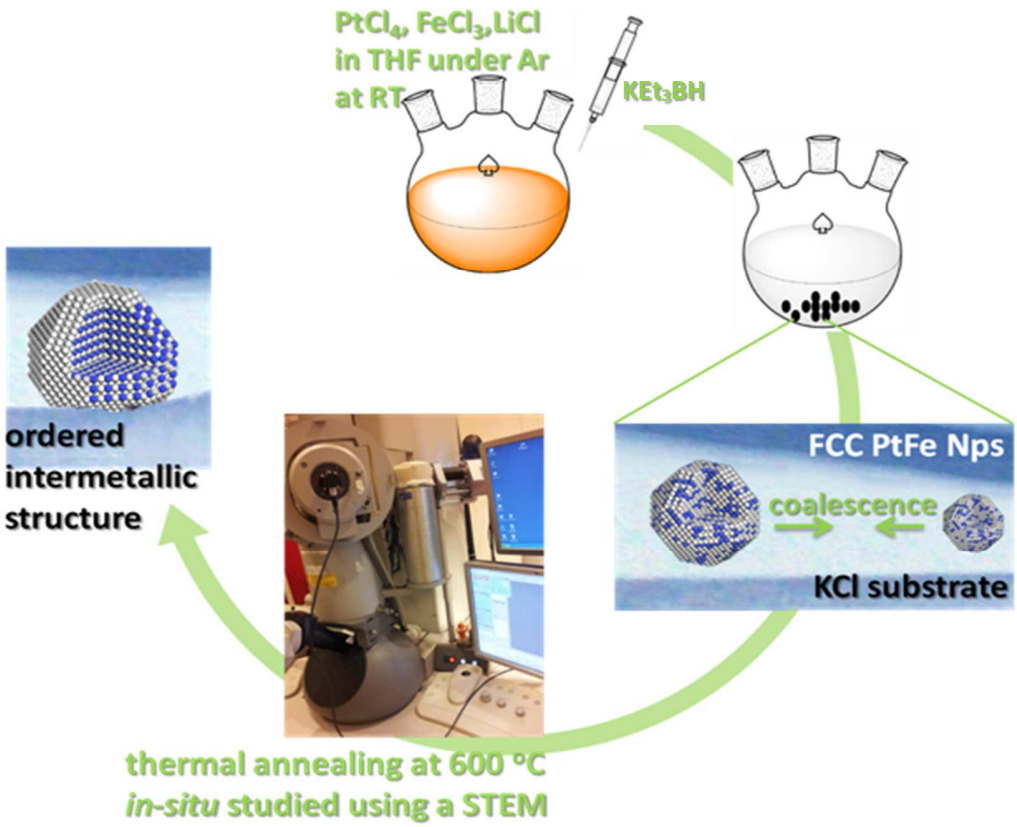

Figure 1. PtFe nanoparticles are formed in a rapid, room temperature, solution-based reduction of their chloride precursors by using KEt_3BH as reducing agent and THF as the solvent. Since the by-product KCl is not soluble in THF, the newly formed PtFe nanoparticles are protected by the KCl matrix. A thermal annealing process converts the FCC PtFe to the ordered intermetallic structure. An *in-situ* study of the annealing process showed that coalescence of nanoparticles is the main mechanism for particle sintering on or in the KCl matrix.

Characterization of the intermetallic structure. As shown in the X-ray diffraction (XRD) pattern (figure 2a), the as-synthesized PtFe nanoparticles are essentially amorphous or have very small domain sizes. After annealing at 400 ^{o}C for 12 hours under vacuum, the PtFe nanoparticles remain in an alloy FCC structure. However, after increasing the annealing temperature to 600 °C for 12 hours, the ordered tetragonal phase is obtained. The observation of ordering peaks, such as the expected weak (001), (110) and (201) peaks, demonstrates that the desired ordered intermetallic phase is formed. The average domain size and average particle size have increased to 5 nm (figure S2). With comparable domain and particle sizes, there are still fewer internal grain boundaries than the external surfaces. Grain boundary planes are expected to become more important as the sintering becomes more pronounced, but for the annealing conditions identified here these effects are still quite small. The regime studied here would be best described as the initial stages of sintering, as there are fewer grain boundary planes than external surfaces.

Magnetic measurements at room temperature of the PtFe-40KCl (mole ratio of PtFe to KCl matrix is 1: 40) annealed at 400 ^{o}C, taken in a Quantum Design superconducting quantum interference device (SQUID – Model Quantum Design MPMS-XL7), exhibit superparamagnetic behavior (figure 2b). In summary, XRD and magnetic data clearly show that annealing at 400 ^{o}C for 12 hours did not convert the FCC PtFe to the ordered intermetallic tetragonal structure. In contrast, PtFe-40KCl annealed at 600 ^{o}C for 12 hours is ferromagnetic with a coercivity of almost 1 T at 300K. A saturation magnetization of 29 emu per gram of PtFe is observed (figure 2b). In comparison, the saturation magnetization of Fe metal is 220 emu per gram. The smaller moment of PtFe is due, in part, to the small particle sizes, the dilution of Fe by nonmagnetic Pt, and the much larger mass of Pt related to Fe. Previous authors have reported values as high as 56 emu per gram for 7 nm diameter PtFe particles.[9]

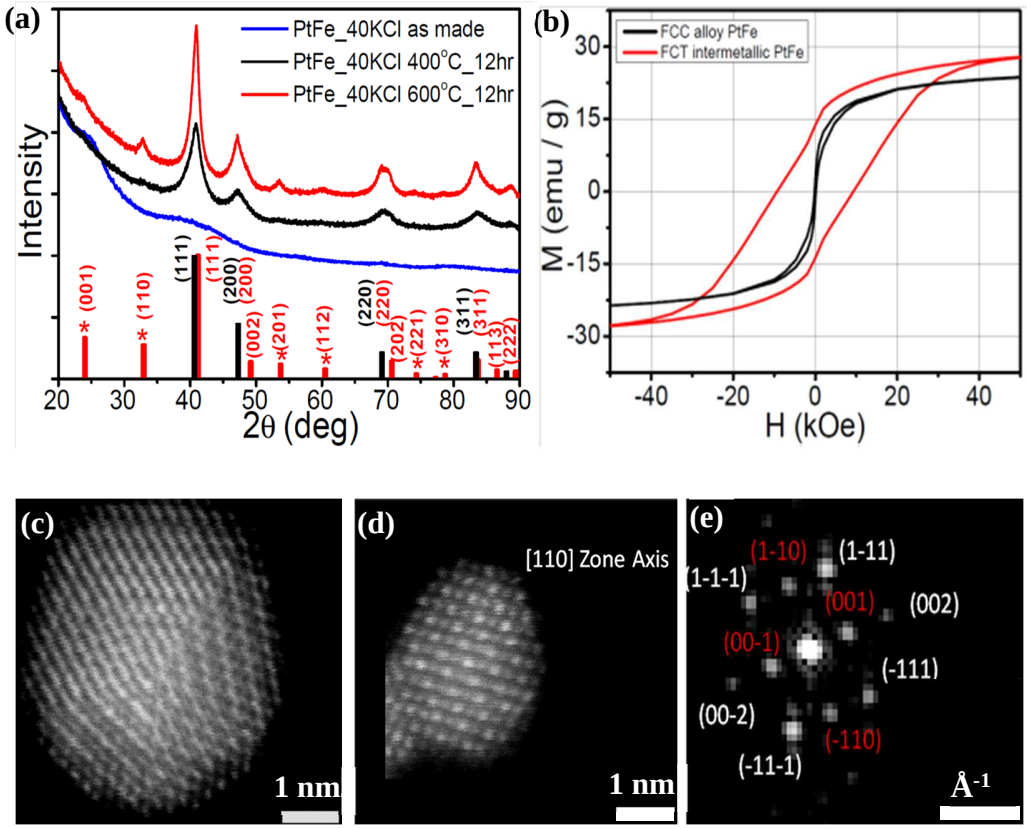

Figure 2. (a) XRD patterns of PtFe from a PtFe-40KCl matrix with no thermal annealing (blue) and annealed for 12 hours at 400 °C (black) and 600 °C (red), respectively. After annealing the PtFe-40KCl matrix for 12 hours, the KCl matrix is removed in an ethylene glycol and water solution, and the PtFe nanoparticles are deposited directly on suspended carbon black particles (Vulcan XC-72). The peak positions for the disordered alloy phase (PDF#030659122) and intermetallic phase (PDF# 030659121) of PtFe are shown at the bottom as black and red tick marks, respectively. The superlattice peaks from ordering are marked with *. **(b)** SQUID data of hysteresis loops of the PtFe nanoparticles obtained after the thermal annealing of the PtFe-40KCl complex at 400 °C (black) and 600 °C (red) for 12 hours under vacuum. **(c)-(d)** HAADF-STEM images of the annealed intermetallic nanoparticles. Due to the atomic number 'Z contrast' of the HAADF signal, the Pt shows up as much brighter than the Fe signal. The STEM images show periodic changes of brighter and darker columns of atoms, indicating the presence of the ordering structure on the zone axis observed. **(d)** The ordered intermetallic structures viewed on [110] zone axis, where periodic arrays of brighter and darker atoms present Pt and Fe, respectively. **(e)** Diffractogram of (d) showing superlattice peaks such as the {001} and {110} marked with red.

After thermal annealing a PtFe-40KCl sample at 600 ^{o}C for 12 hours to achieve the ordered intermetallic phase, the KCl matrix was removed, and the particles were bound to a Vulcan carbon support by mixing the support and matrix in an ethylene glycol and water solution at room temperature. Atomic-resolution high-angle annular dark field (HAADF) STEM images of the annealed nanoparticles were taken. As shown in figure 2c-d, due to the atomic-number 'Z contrast' of the HAADF signal, the Pt shows up as much brighter than the Fe signal. The STEM images show periodic changes of brighter and darker columns of atoms, which suggests the ordering of the two elements in the nanoparticles, indicating the presence of the ordering structure on the zone axis observed.[12] Shown in figure 2d, an intermetallic nanoparticle is observed on the [110] zone axis. The intermetallic structure can also be realized by the appearances of the superlattice planes in the electron diffraction pattern of a single crystal domain. Shown in figure 2e is the diffractogram from figure 2d with the superlattice spacings marked in red. Spacings of 3.7 Å and 2.7 Å are measured for the {001} and {110} superlattice spots, respectively, and match with the bulk PtFe intermetallic structure. These data confirm the formation of an ordered intermetallic phase after thermal annealing at 600 ^{o}C.

We have also determined the composition of individual annealed nanoparticles by performing electron-energy loss spectroscopy (EELS) imaging. An on-axis intermetallic nanoparticle is shown in figure 3a. The Fe signal is extracted using a power-law background fit

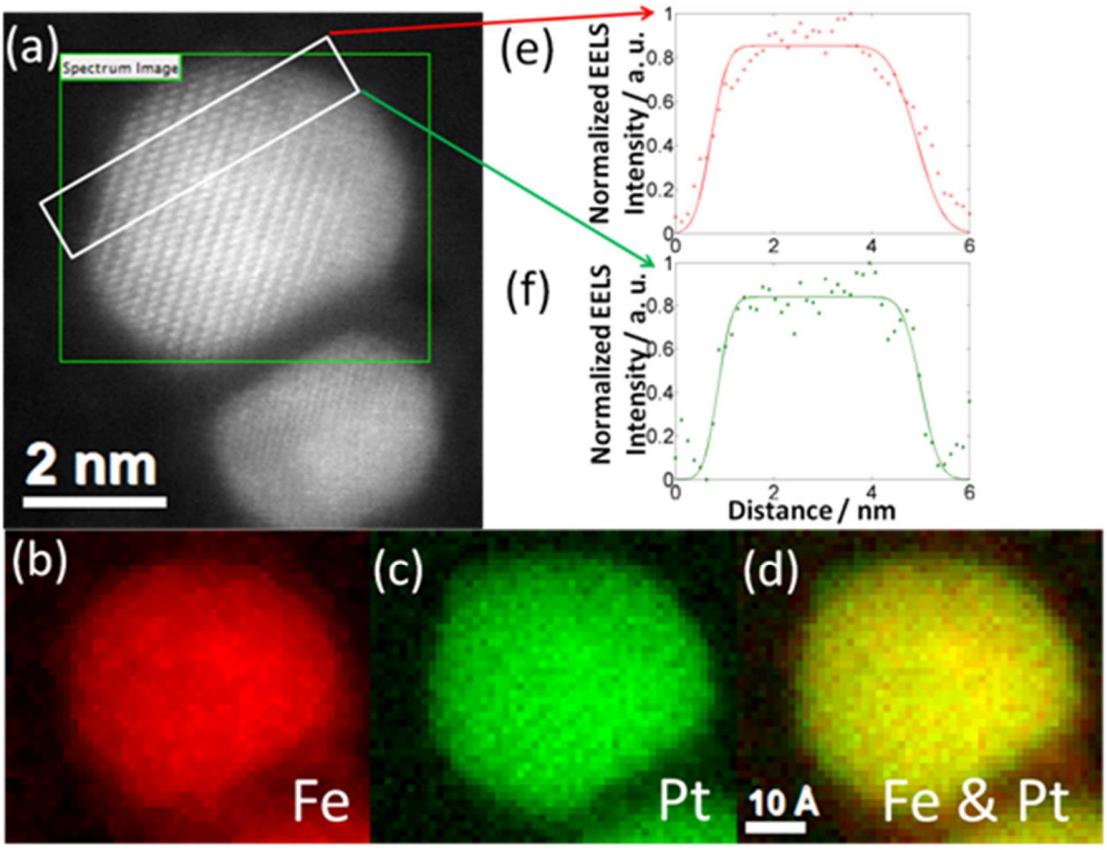

Figure 3. STEM-EELS analysis of PtFe nanoparticles. **(a)** HAADF-STEM image, with highlighted EELS spectrum images shown in **(b)** Fe-$L_{2,3}$ edge, extracted by power-law background fit; **(c)** Pt-N_3 edge, extracted after 20 iterations of MCR (multivariate curve resolution) and **(d)** composite of Fe and Pt. The line profiles of **(e)** Fe and **(f)** Pt show homogenous distributions of Fe and Pt, without any obvious core-shell structure, within the experimental resolution of less than one atomic layer. The best-fit lines are extrapolated by using two error functions and the distance is calculated based on the full width at half maximum of the best-fit line.

on the Fe-$L_{2,3}$ edge, since the peaks have a distinct and abrupt onset. However, since the broad Pt-M and Pt-N edges have delayed onsets, we used the MCR (multivariate curve resolution)method to extract the Pt-N_3 edge, although background subtraction still works well for the higher-energy Pt-M edge. Details and tests of the reliability of this approach for analyzing the Pt-N_3 edge can be found in previous publications[13, 14] and their supplements. The EELS study suggested a homogenous distribution of Fe and Pt, with no obvious phase segregation within the experimental precision of less than one atomic layer (figure 3b-d). To quantitatively evaluate whether a core-shell structure exists, EELS line profiles were obtained (figure 3f), and the full width at half maximum (FWHM) of the projected Fe and Pt mass profiles were extracted. The difference between the FWHM of the Pt and Fe signals is less than one atomic layer, indicating no obvious core-shell formation. Such homogeneity is also expected since the thermal annealing was performed under vacuum rather than in a reducing environment, such as hydrogen. Under a hydrogen atmosphere, Pt usually segregates to the surface in order to lower the surface energy through the formation of relatively strong Pt-H bonds.[15]

The STEM images of the as-prepared disordered FCC and ordered tetragonal PtFe nanoparticles in the KCl matrix are shown in figure S2. The KCl matrix of the as-prepared PtFe-40KCl showed a BET surface area of 54.1 m^2/g with a domain size of 77 nm (figure S4). The as-prepared PtFe nanoparticles average less than 2 nm in diameter. Even after thermal annealing at 600 ^oC for 12 hours, the KCl matrix protects the nanoparticles from significant large-scale aggregation (figure S2b and S2c). Nonetheless, the particles have grown in diameter by factors of 2 to 3, compared to the as-prepared sample (figure S2a).

In-situ observation of annealing by STEM. To better understand this dynamic growth process, an *in-situ* STEM annealing study of the Np-KCl assembly on a heated

substrate was undertaken.[16, 17] Since the nanoparticles are formed in or on the KCl, the Np-KCl assembly was transferred onto the heating grid in an Ar-protected atmosphere, preventing any interference from air. During imaging, the sample was heated to 400 ^{o}C and then to 500 ^{o}C, holding for c.a. two hours (figure 5a). Nanoparticle sintering was observed during the heat treatment (figures 4-5).

In general, there are two competing mechanisms in the sintering process, namely Ostwald ripening and coalescence.[18, 19] Ostwald ripening is caused by the exchange of atoms, one at a time, with larger particles growing and smaller particles continuously shrinking in size. Coalescence is the result of the motion of the nanoparticles themselves. In Ostwald ripening, the larger particles grow at the expense of the smaller ones; hence, as the size distribution evolves, it is expected to have a bias toward larger diameters. However, such distributions can only be observed if sufficient time is allowed for the particles to grow to about 10 times their initial diameter, such that any history of the initial distribution is lost.[20, 21] Coalescence, in contrast, is the merging of two nanoparticles. Studies have suggested that a log-normal distribution should result from coalescence.[22-25] To determine the dominant growth mechanism, we followed the time evolution of the particle positions and sizes over the same area of the PeFe-KCl assembly under thermal annealing up to 600 ^{o}C (figure 4a-d and movie S1). We found that most coarsening events occurred primarily through the motion of the nanoparticles in or on the KCl matrix, which suggests that coalescence is the main coarsening mechanism. In addition, the particle size distribution of over four hundred nanoparticles in the same area, at different temperatures, was measured *in-situ* (figure 4e). As the temperature increased, the mean diameter of the particles became larger, along with a broadening of the size distribution.[22-25] The size distribution is plotted in figure 4f, and fits well to the log-normal distribution that is consistent with coalescence. To illustrate the coalescence

process, the evolution of several particles was shown in figure 4g. Nanoparticles, instead of atoms, diffuse in or on the KCl matrix and coalesce to form bigger particles.

Although the size distribution is consistent with the existence of coalescence, the size distribution alone is not sufficient to eliminate the occurrence of Ostwald ripening, whose ideal distribution will not be apparent unless the average diameter is increased by a factor of 10. The heating temperature was then increased to 600 ^{o}C and held there to address this problem. We tracked the size and positions of individual particles in a selected area during a more detailed time series, instead of relying solely on the size distribution.

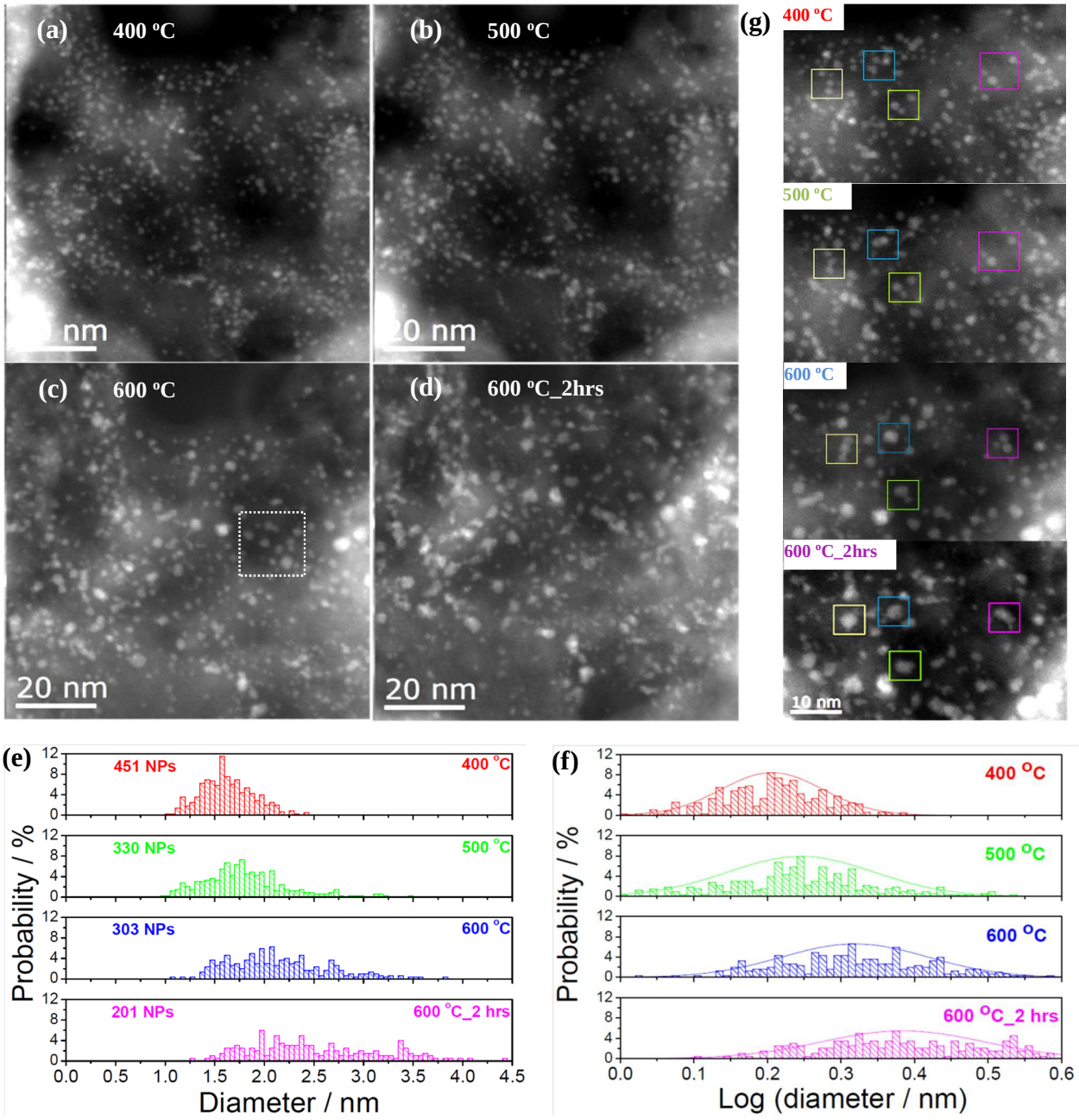

Figure 4. HAADF-STEM images of one representative area during the *in-situ* heating experiment. **(a)** 400°C; **(b)** 500°C; **(c)** 600°C; **(d)** 600°C and after 2 hours; **(e)** Statistical histogram of size distribution in (a)-(d); **(f)** Log scale of size distribution, fitted with a log-normal distribution. The maintenance of such a log-normal distribution is consistent with coalescence. **(g)** Zoomed in images of (a)-(d). The evolution of four particles has been tracked with changes in temperature, showing that coalescence is the main mechanism for particle growth.

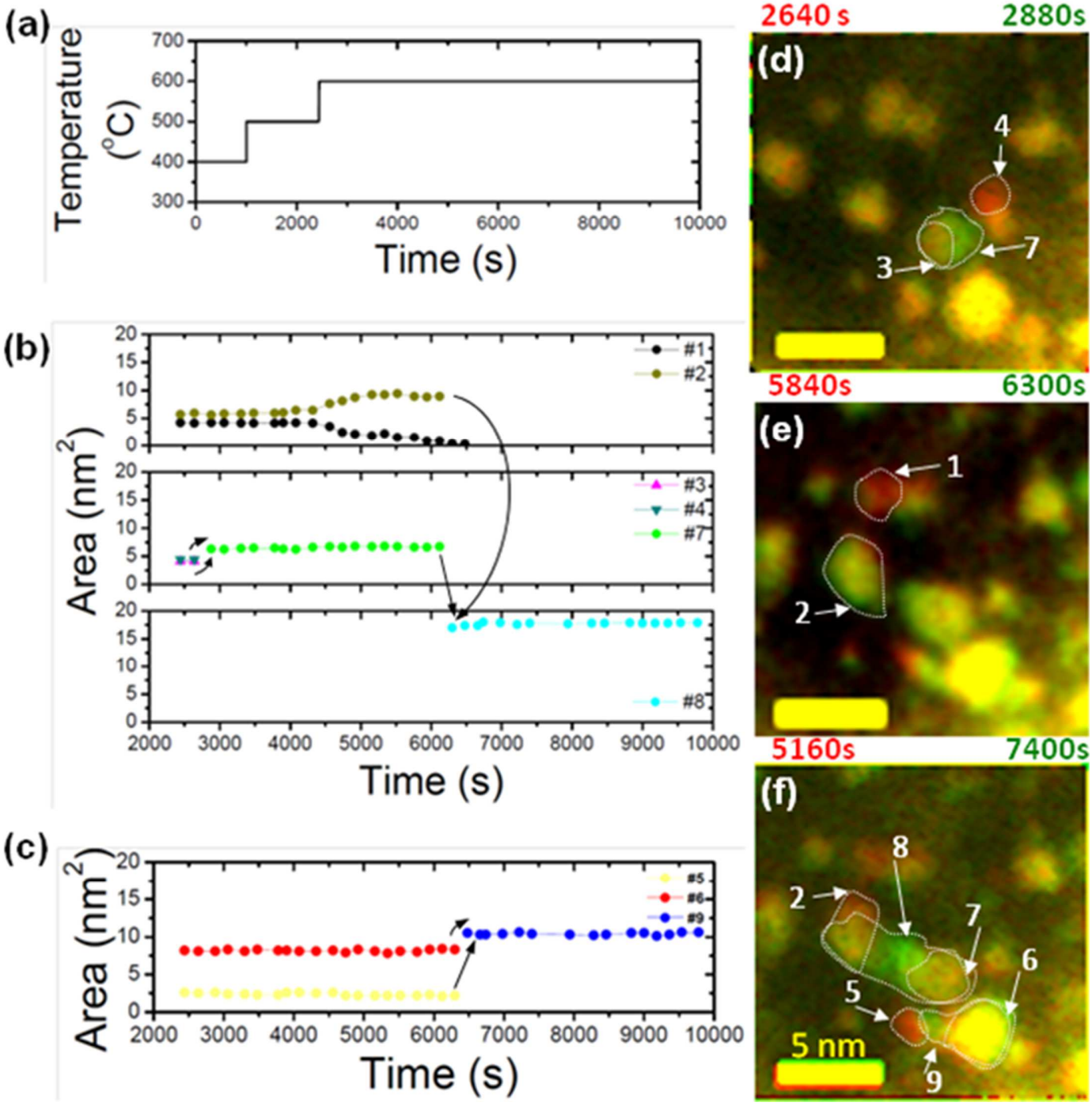
(a)
Temperature (°C)
Time (s)
(b)
Area (nm²)
#1
#2
#3
#4
#7
#8
Time (s)
(c)
Area (nm²)
#5
#6
#9
Time (s)
2640 s
2880s
(d)
4
3
7
5840s
6300s
(e)
1
2
5160s
7400s
(f)
8
2
7
6
5
9
5 nm

Figure 5. (a) Plot of grid temperature *versus* real time during the *in-situ* heating experiment. The sample was heated to 600 ^{o}C at 2442 s and kept at that temperature for two hours. An isolated area, marked in figure 4(c), has been imaged every 3 minutes to track the change of particle sizes. **(b)** and **(c)** Particle sizes *versus* real time. To better illustrate the subtle changes in particle sizes, we have segmented the nanoparticles with polygons, which are also for area estimation. A detailed example is shown in figure S5. **(d)-(f)** Video images of corresponding particles in (b) and (c) showing the particle growth pathways. A more comprehensive movie showing this particular area can be found in movie S2. The images are colored with red (for before i.e. t-1) and green (for after, i.e. t) corresponding to different time frames labeled on the top. If the particles did not move, a yellow color is expected. If the particles disappeared from one location, a red color is expected at the original location. If the particles migrated or are newly formed, a green color is expected at the new location. Ostwald ripening occurred in **(d)** from particles # 1 to # 2. Coalescence took place in **(e**) with the formation of particle # 7 from # 3 and # 4. Two other cases of coalescence can be seen in **(f)** where the formation of # 9 is from the migration and sintering of # 5 and # 6, and formation of # 8 is from # 2 and # 7. In 150 total particles, 22 instances of coalescence and only 4 instances of Ostwald ripening were observed.

Figure 5a presents a plot of the grid temperature *versus* real time. The area shown in figure 4c was imaged every 3 minutes at 600 ^{o}C for two hours. In a region of 150 nanoparticles, 22 instances of coalescence *versus* 4 instances of Ostwald ripening were counted. As an example, a selected area, which is circled in figure 4c, is shown in figure 5d and movie S2. In the initial stages of coalescence, the particles are not all round or oval in shape. To better illustrate the subtle changes in particle sizes, we measured the projected areas of the nanoparticles to represent the particle sizes. This assumes that the third, projected dimension, does not deviate significantly in scale from the other two dimensions (A more detailed method is included in figure S5). To eliminate the influence of particles that are outside the observed area, the sizes of particles closest to the target particles were measured and showed no significant changes (figure S6). The particle sizes in the observed area are shown in figures 5b and 5c. Shown in figure 5d-f are the images of the selected area at specific times. The corresponding particles are marked in the images. Coalescence of particles was observed and dominated the particle growth process. Note the formation of particle #7 from particles #3 and #4 at 2880 s, the formation of particle #8 from particle #7 and #2 at 7400 s, and the formation of particle #9 from #5 and #6 at 7400 s. A common pattern has been observed for these coalescence events, in which two particles diffuse toward each other and subsequently merge. Ostwald ripening was also observed in a few instances as well. The gradual size increase of particle #2 and size decrease of

particle #1 evidence a clear pattern for ripening. As mentioned previously, there were very few Ostwald ripening events (4 incidences out of 150 particles) compared to coalescence events (22 incidences out of 150 particles).

The different shapes of nanoparticles are also an indication of the sintering mechanism. When Ostwald ripening occurs, as for particles #1 and #2 in figure 5, the shapes before and after are closer to round or oval. This can be understood in terms of the exchange of individual atoms between particles. Individual atoms, that attach to each particle are more likely to locate at sites that minimize the overall surface/volume ratio (which, in turn, minimizes the surface energy), while particles are most likely to detach from sites that maximize overall surface/volume ratio. The end result is a tendency toward more rounded particles. This process is isotropic in nature and thus should not lead to any preferential shape. However, this is not the case for coalescence. The joining of two or more nanoparticles will occur when the two particles first touch, initially leading to elongated structures. If the particles have different orientations, then a grain boundary will be created where the particles touched. After significant surface diffusion, a rounder shape evolves to lower the energy of the system. As an example, in figure 4g, several particles that display this elongated shape are highlighted. However, like other TEM/STEM studies, this *in-situ* STEM study is based on a 2D projection of Np-KCl matrix during thermal annealing. Based solely on one projected image, it is almost impossible to distinguish if the two nanoparticles overlap or sinter. However, in this study, since the videos recorded contain multiple snapshots at different temperatures and times, it is sometimes possible to distinguish particle overlap from sintering by their relative motions. One example can be seen in figure 5d and movie S2, where the yellow colored nanoparticle below # 4 can be categorized as an overlapping rather than a sintered one.

Section 3.4. Conclusion

PtFe ordered intermetallic nanoparticles have been synthesized by a Np-KCl matrix method, and the coarsening mechanism during thermal annealing has been studied by *in-situ* STEM heating. The motivation for our work was to reach the ordered phase without significant particle aggregation or growth in average particle size, which would dramatically limit their utility in proposed applications. The *in-situ* STEM studies allowed us to individually track the growth and motion of particles during thermal annealing of the Np-KCl assemblies. This study shows that encasing nanoparticles in a KCl matrix significantly slows agglomeration and particle size growth. Based on these observations, we conclude that coalescence is the dominant mechanism of nanoparticle growth in the KCl matrix at the temperatures studied. It is expected that this approach can be generalized to study other nanoparticle-substrate systems.

Supporting Information Available: The synthesis method and TEM characterization of nanocatalyst particles, before and after annealing, are available on line at http://pubs.acs.org free of charge. Also included is a movie of the thermal annealing of nanoparticles on the KCl matrix.

REFERENCES

1. Sun, S. H.; Murray, C. B.; Weller, D.; Folks, L.; Moser, A., Monodisperse FePt Nanoparticles and Ferromagnetic FePt Nanocrystal Superlattices. *Science* **2000**, 287, 1989-1992.

2. Kuo, C. M.; Kuo, P. C.; Wu, H. C., Microstructure and Magnetic Properties of $Fe_{100-X}Pt_x$ Alloy Films. *J. Appl. Phys.* **1999**, 85, 2264-2269.

3. Watanabe, M.; Nakayama, T.; Watanabe, K.; Hirayama, T.; Tonomura, A., Microstructure and Magnetic Properties of High-Coercive Fe-Pt Alloy Thin Films. *Mater. Trans., JIM* **1996**, 37, 489-493.

4. Weller, D.; Doerner, M. F., Extremely High-Density Longitudinal Magnetic Recording Media. *Annu. Rev. Mater. Sci.* **2000**, 30, 611-644.

5. Bader, S. D., Colloquium: Opportunities in Nanomagnetism. *Rev. Mod. Phys.* **2006**, 78, 1-15.

6. Chen, M.; Liu, J. P.; Sun, S. H., One-Step Synthesis of FePt Nanoparticles with Tunable Size. *J. Am. Chem. Soc.* **2004**, 126, 8394-8395.

7. Elkins, K. E.; Vedantam, T. S.; Liu, J. P.; Zeng, H.; Sun, S. H.; Ding, Y.; Wang, Z. L., Ultrafine FePt Nanoparticles Prepared by the Chemical Reduction Method. *Nano Lett.* **2003**, 3, 1647-1649.

8. Sun, S. H.; Anders, S.; Thomson, T.; Baglin, J. E. E.; Toney, M. F.; Hamann, H. F.; Murray, C. B.; Terris, B. D., Controlled Synthesis and Assembly of FePt Nanoparticles. *J. Phys. Chem. B* **2003**, 107, 5419-5425.

9. Kim, J. M.; Rong, C. B.; Liu, J. P.; Sun, S. H., Dispersible Ferromagnetic FePt Nanoparticles. *Adv. Mater.* **2009**, 21, 906-909.

10. Yamamoto, S.; Morimoto, Y.; Tamada, Y.; Takahashi, Y. K.; Hono, K.; Ono, T.; Takano, M., Preparation of Monodisperse and Highly Coercive $L_{1(0)}$-FePt

Nanoparticles Dispersible in Nonpolar Organic Solvents. *Chem. Mater.* **2006**, 18, 5385-5388.

11. Chen, H.; Wang, D.; Yu, Y.; Newton, K. A.; Muller, D. A.; Abruña, H.; DiSalvo, F. J., A Surfactant-Free Strategy for Synthesizing and Processing Intermetallic Platinum-Based Nanoparticle Catalysts. in preperation.

12. Delalande, M.; Guinel, M. J. F.; Allard, L. F.; Delattre, A.; Le Bris, R.; Samson, Y.; Bayle-Guillemaud, P.; Reiss, P., $L_{1(0)}$ Ordering of Ultrasmall FePt Nanoparticles Revealed by TEM in Situ Annealing. *J. Phys. Chem. C.* **2012**, 116, 6866-6872.

13. Yu, Y.; Xin, H. L.; Hovden, R.; Wang, D.; Rus, E.; Mundy, J. A.; Muller, D. A.; Abruña, H. D., 3-D Tracking and Visualization of Hundreds of Pt-Co Fuel Cell Nanocatalysts During Electrochemical Aging. *Nano Lett.* **2012**, Article ASAP. DOI:10.1021/nl203920s.

14. Xin, H. L.; Mundy, J. A.; Liu, Z.; Cabezas, R.; Hovden, R.; Kourkoutis, L. F.; Zhang, J.; Subramanian, N. P.; Makharia, R.; Wagner, F. T.; Muller, D. A., Atomic-Resolution Spectroscopic Imaging of Ensembles of Nanocatalyst Particles across the Life of a Fuel Cell. *Nano Lett.* **2012**, 12, 490-497.

15. Yin, Y. D.; Rioux, R. M.; Erdonmez, C. K.; Hughes, S.; Somorjai, G. A.; Alivisatos, A. P., Formation of Hollow Nanocrystals through the Nanoscale Kirkendall Effect. *Science* **2004**, 304, 711-714.

16. Chang, S. L. Y.; Barnard, A. S.; Dwyer, C.; Hansen, T. W.; Wagner, J. B.; Dunin-Borkowski, R. E.; Weyland, M.; Konishi, H.; Xu, H., Stability of Porous Platinum Nanoparticles: Combined in-Situ TEM and Theoretical Study. *J. Phys. Chem. Lett.* **2012**, 3, 1106-1110.

17. Delalande, M. l.; Guinel, M. J. F.; Allard, L. F.; Delattre, A.; Le Bris, R. m.; Samson, Y.; Bayle-Guillemaud, P.; Reiss, P., L_{10} Ordering of Ultrasmall Fept

Nanoparticles Revealed by Tem in Situ Annealing. *J. Phys. Chem. C* **2012**, 116, 6866-6872.

18. Bowker, M., Surface Science - the Going Rate for Catalysts. *Nat. Mater.* **2002**, 1, 205-206.

19. Campbell, C. T.; Parker, S. C.; Starr, D. E., The Effect of Size-Dependent Nanoparticle Energetics on Catalyst Sintering. *Science* **2002**, 298, 811-814.

20. Karnesky, R. A.; Isheim, D.; Seidman, D. N., Direct Measurement of Two-Dimensional and Three-Dimensional Interprecipitate Distance Distributions from Atom-Probe Tomographic Reconstructions. *Appl. Phys. Lett.* **2007**, 91, 013111

21. Sudbrack, C. K.; Ziebell, T. D.; Noebe, R. D.; Seidman, D. N., Effects of a Tungsten Addition on the Morphological Evolution, Spatial Correlations and Temporal Evolution of a Model Ni-Al-Cr Superalloy. *Acta Mater.* **2008**, 56, 448-463.

22. Granqvist, C. G.; Buhrman, R. A., Size Distributions for Supported Metal-Catalysts - Coalescence Growth Versus Ostwald Ripening. *J. Catal.* **1976**, 42, 477-479.

23. Lifshitz, I. M.; Slyozov, V. V., The Kinetics of Precipitation from Supersaturated Solid Solutions. *J. Phys. Chem. Solids* **1961**, 19, 35-50.

24. Boyer, P.; Meunier, M., Modeling Solvent Influence on Growth Mechanism of Nanoparticles (Au, Co) Synthesized by Surfactant Free Laser Processes. *J. Phys. Chem. C* **2012**, 116, 8014-8019.

25. Lee, D.; Choi, M., Coalescence Enhanced Synthesis of Nanoparticles to Control Size, Morphology and Crystalline Phase at High Concentrations. *J. Aerosol Sci.* **2002**, 33, 1-16.

26. Muller, D. A.; Kourkoutis, L. F.; Murfitt, M.; Song, J. H.; Hwang, H. Y.; Silcox, J.; Dellby, N.; Krivanek, O. L., Atomic-scale chemical imaging of composition and bonding by aberration-corrected microscopy. *Science* **2008**, 319, 1073-1076.

CHAPTER 4

NANOSCALE IMAGING OF LITHIUM INO DISTRIBUTION DURING *IN SITU* OPERATION OF BATTERY ELECTRODE AND ELECTROLYTE[*†]

Section 4.1. Introduction

The integration of renewable, and often intermittent, energy sources such as solar and wind into the energy landscape, as well as the electrification of transportation, requires dramatic advances in electrical energy conversion and storage technologies including fuel cells, batteries and supercapacitors.[1, 2] Advancing our understanding necessitates the development of experimental tools capable of *operando* characterization that can discern mechanisms of operation and degradation in the native operating environment. Energy storage materials, such as battery electrodes, often display inhomogeneous behavior on the nanoscale.[3] Thus, the most illuminating and useful characterization methods are those capable of providing detailed mechanistic information of charge/discharge dynamics of *individual* grains and particles. TEM investigations specialize in revealing structural and compositional information with nanoscale spatial resolution and sub-second temporal resolution. Unfortunately, conventional TEM is not compatible with studies of many electrochemical energy storage processes because they occur in liquid environments. Recently, the development of TEM holders that encapsulate thin liquid layers promise

---

[*] Produced with permission from Megan E. Holtz, Yingchao Yu, Deniz Gunceler, Jie Gao, Ravishankar Sundararaman, Kathleen A. Schwarz, Tomás A. Arias, Héctor D. Abruña, David A. Muller, *Nano Letters*, 2014, 14 (3), 1453–1459. Copyright © 2014 American Chemical Society.

[†] M.E.H. and Y.Y. contributed equally to this work. D.A.M., H.D.A., Y.Y., and M.E.H. designed the electrochemical TEM experiment. M.E.H. and Y.Y. performed the experiments. M.E.H. analyzed the data. D.G. and R.S., supervised by T.A., designed and performed JDFT calculations to analyze the solution intensity, with discussions with K.A.S. J.G. synthesized the particles. The manuscript was written with contributions from all authors.

in situ imaging and spectroscopy on the nanoscale.[4-8] Incorporating electrodes[9, 10] enables *in situ* imaging of electrochemical processes,[11-13] including electrodeposition[9] and dendrite growth.[14] However, quantitative electrochemistry in the electron microscope remains a major challenge. Here we develop broadly-applicable, *quantitative* electrochemistry in a liquid cell TEM holder that can be correlated with microstructure and local electronic structure changes during operation, even for surface-sensitive catalysts such as those used in fuel cells. To follow the underlying ion redistributions, we demonstrate a method for spectroscopic imaging of nanoscale processes during electrochemical operation and follow the charging and discharging dynamics of a battery electrode.

The lithium-ion battery is a particularly promising candidate for electric vehicle and energy storage applications.[1, 15-18] A key mechanistic aspect in the performance of lithium-ion battery electrodes is how the lithium ions intercalate and deintercalate from the electrode during cycling. Here, as a demonstration of tracking lithiation and degradation in an *in situ* battery in the TEM, we studied the cathode material $LiFePO_4$, which has surged in interest due to its attractive capacity, ability to sustain high charging and discharging rates, abundance, low toxicity, relative operational safety, and low cost.[17, 19] There is much discussion in the literature on the mechanism of lithiation and delithiation,[3, 17, 20-27] with evidence of a two-phase reaction or a metastable solid solution.[17, 25] Within the two-phase reaction pathway, there are different theories for the propagation of lithiation, one of which suggests concurrent transformation[23, 28] and the other particle-by-particle intercalation.[21, 24, 27, 29] Some disagreement may be attributed to many-particle effects, where bulk measurements (both *in situ* and *ex situ*) convolve signals from the entire area of the electrode probed.[3] *Ex situ* studies are inherently compromised by removal of the particles from their native – and often reactive – environment, which leads to

questions of relaxation or reactions caused by the foreign surroundings. In this study, we probe, in real time, the evolution of individual grains and nanoparticles of $LiFePO_4$ in the native environment of a battery in a liquid cell TEM. Particles are seen to delithiate, one at a time, in a mosaic fashion, with most particles either lithium-rich or lithium-poor. We are also able to directly image the phase transformations and see different delithiation mechanisms in neighboring particles, and have observed core-shell structures and anisotropic growth in different particles within the same agglomerate on the electrode.

TEM detection of lithium through a liquid is difficult, because lithium is a weak elastic scatterer and multiple scattering from the liquid overwhelms the inelastic core-loss signal in electron energy-loss spectroscopy (EELS). In this work, we successfully observed the lithiation state by valence energy-filtered TEM (EFTEM), which probes the low-energy regime (~1-10 eV), and allows us to work in thicker liquid layers than core-level spectroscopy.[6] Valence EELS can provide electronic structure information, allowing us to track battery charging and discharging as ions are being transferred between electrode and electrolyte. This method is analogous to observing color changes in optical spectroscopy during battery cycling on the micron scale,[30, 31] except that valence EFTEM achieves nanometer resolution. While electronic structure features in the lithiated and delithiated electrode are have been well documented,[32] identifying electronic structure fingerprints in the solution is less well explored because there are many solvated species in solution that are difficult to distinguish. Here we employed *ab initio* theory to calculate optical gaps of solvated species.[33] We took solution effects into account with a hybrid functional[34] including a nonlinear description of the polarization response of the surrounding liquid,[35] which gives a more physical model of bound solvent charges near the solute than linear models. For the first time, we applied this technique to calculate excited electronic

states and found quantitative matches to experimental excitation energies. By combining electrochemistry in the TEM with valence spectroscopic imaging and theory, we were able to identify the lithiation state of the electrode *and* electrolyte during *in situ* operation.

Section 4.2. Materials and Methods

We use a liquid cell holder developed by Protochips using chips we designed to mimic a typical electrochemical cell (Figure 1a-b). The tip of the holder is a microfluidic flow cell with silicon nitride viewing membranes that confine a liquid, shown in cross section in Figure 1a. Figure 1b illustrates the top chip, with three patterned electrodes optimized for electrochemical cycling and imaging. Traditional silicon-processing methods use a chromium adhesion layer and gold electrodes. However, chromium diffuses rapidly through gold (especially at grain boundaries) and can affect and even dominate the electrochemical signal. In addition, high-atomic-number electrode materials such as Pt and Au obscure imaging. Instead, we used a carbon working electrode which only weakly scatters electrons and is commonly used in bulk electrochemistry, and titanium adhesion layers under platinum reference and counter electrodes.

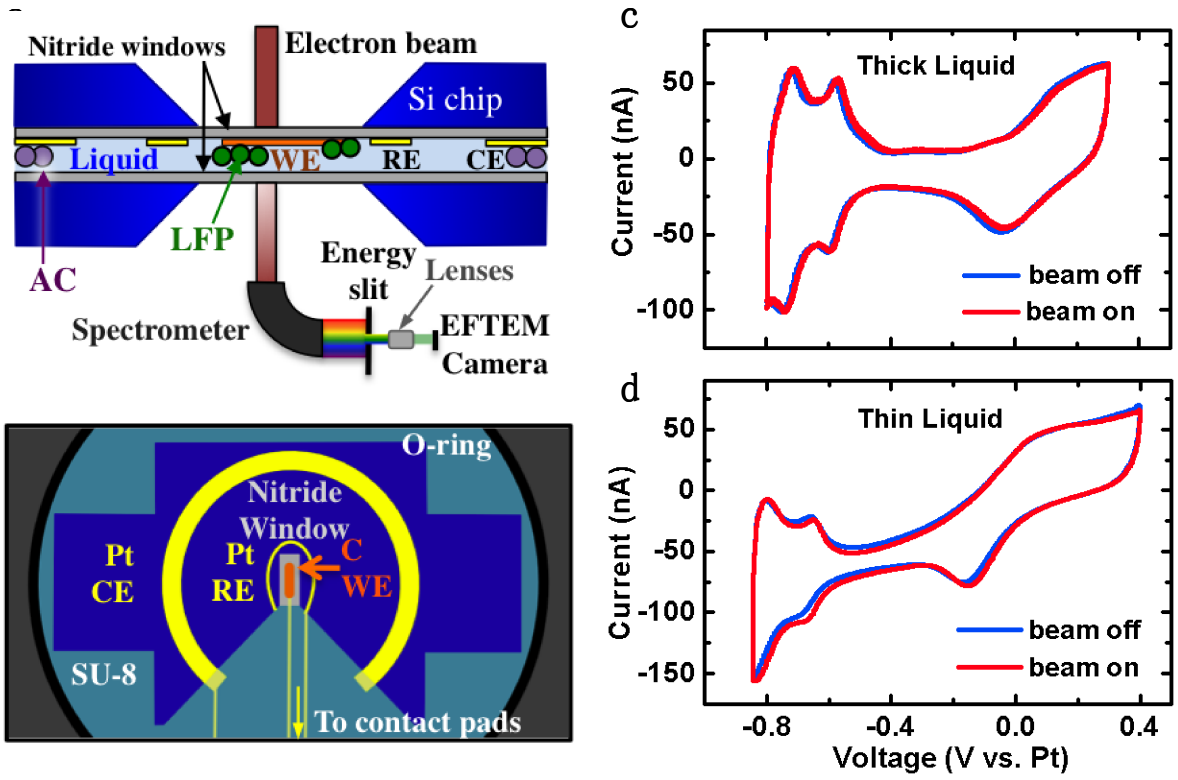

Figure 1. Schematic of the *in situ* electrochemistry TEM holder and electrochemical data. (a) Cross-sectional view of the holder, with silicon nitride membranes encapsulating a fluid layer. The working electrode (WE), made of carbon, lies in the viewing window, with $LiFePO_4$ (LFP) nanoparticles deposited on top. The platinum counter electrode (CE) is coated with an excess of activated carbon (AC). In EFTEM mode, energies are selected by a slit to be imaged. (b) Schematic of the top chip, with three patterned electrodes: a carbon WE on the viewing membrane, Pt RE (not used here) and Pt CE. The connection leads are covered by SU8, and the contact pads to the holder do not contact the liquid, so as to minimize electrochemical activity outside the viewing window. The chips exhibited electrochemical activity qualitatively similar to that of an *ex situ* microelectrode, as shown for the Pt cyclic voltammetry (CV) in (c) and in (d). In extremely thin liquid layers (~150 nm) the voltammetric profile exhibits a significant ohmic drop as seen in (d).

This allows us to image through the electrode with little loss in spatial resolution and contrast, which is dominated by scattering in the liquid, instead. As a practical matter, and discussed below, spatial resolution is often limited by the low doses needed to control radiation damage than by beam spreading in the cell.

To demonstrate that *in situ* electrochemistry reproduces well-established criteria, we performed cyclic voltammetry of a film of platinum, shown in Figure 1c-d, in the TEM. This control experiment represents a test case for quantitative electrochemistry, since the features are surface effects, including hydrogen adsorption and desorption (at negative potentials) and oxide formation and reduction (at positive potentials) which are very sensitive to contaminants at the sub-monolayer level. The *in situ* electrochemistry reproduced the characteristic voltametric profile of a polycrystalline platinum electrode at an appropriate current scale, regardless of the electron beam. In thin liquid layers, the ohmic drop in the solution becomes significant, as evidenced by the slanted curve in Figure 1d. This implies an inherent compromise between the highest spatial resolution imaging and quantitative electrochemistry. Accounting for ohmic drops in solution, this setup replicates results of a conventional electrochemical cell while obtaining nanometer resolution.

Section 4.3. Results and Discussions

Having established the electrochemical performance of the TEM holder, we studied $LiFePO_4$, a widely used Li-ion cathode material, in 0.5 M Li_2SO_4 aqueous electrolyte. The *ex situ* characterization of the $LiFePO_4$ is discussed in the Supporting Information Section 1. Because aqueous electrolytes have safety benefits over organic-based electrolytes, such as the commonly used carbonates, and due to its high abundance, low weight and non-toxicity, researchers have considered aqueous electrolytes in addition to the more traditional carbonates.[36] We find the use of an

aqueous electrolyte to be practical for technique development as carbonates are more viscous than aqueous electrolytes, leading to higher flow pressures and potentially more window breakages. In the event of electrolyte leakage, aqueous liquids will dissipate quickly while carbonate electrolytes lead to contamination of the microscope column.

To elucidate the lithiation mechanism we must examine how the lithium ions intercalate into/out of the electrode. In the TEM, lithiation can be tracked by morphological changes or structural changes using electron diffraction,[21, 37] although morphology does not give chemical maps and diffraction spots are quickly obscured in thicker liquid films. As a light element, lithium scatters electrons weakly, making elastic imaging challenging, and the energy-dispersive X-ray signal for lithium has too low an energy to enable detection. Instead, we tracked the lithiation state of the battery using EELS, which offers chemical fingerprints (core-loss EELS) and electronic structure information (valence EELS). Yet, using EELS to identify lithium in liquids presents two obstacles. First, EELS is degraded by multiple scattering events in thick liquids.[6] Second, the lithium-K edge resides at 54 eV and is lost in the superimposed bulk plasmon of the thick films of liquid. As a consequence, previous liquid cell studies have performed their lithium edge spectroscopy separately and *ex situ*.[38] Additionally, the lithium-K edge overlaps with many transition metal M edges such as iron.[39] This makes core-loss EELS of the lithium practically impossible to detect in the liquid cell TEM.

Valence EELS, which interrogates electronic structure, can detect the state of lithiation of battery electrodes in liquid electrolytes. During discharge and charge, lithium ions move in and out of the electrode, filling and emptying valence bands, thereby changing the electronic structure. These electronic structure shifts are accessible by optical spectroscopy, where lithiation has been observed on the micron

scale in electrodes as they change color as a function of their state of lithiation.[30, 31] Valence EELS surveys the same electronic levels as ultraviolet-visible (UV-VIS) spectroscopy. Optical absorption spectra track the imaginary part of the energy-dependent dielectric constant, Im(ε), and the electron energy-loss function in EELS is proportional to $Im(\varepsilon)/[Re(\varepsilon)^2 + Im(\varepsilon)^2]$. An advantage of valence EELS is its high spatial resolution, which is ultimately limited to the nanoscale by the delocalization of the low-energy excitations.[40] While delocalization prevents atomic-resolution valence EFTEM studies, resolution in the liquid environment is often more strongly limited by multiple scattering or by the low-dose imaging conditions required. Valence EELS provides strong signals due to large scattering cross sections and low background from the liquid. The electronic structure shift usually occurs where the electrolyte is stable, at energies below its optical gap (~6-7 eV) where the electrolyte is transparent. Taking advantage of the electronic structure shifts in battery electrodes during cycling is a practical method to track the lithiation state.

The spectroscopic characteristics of the battery cathode $LiFePO_4$ and electrolyte 0.5 M Li_2SO_4/H_2O are shown in Figure 2. The monochromated valence EELS of dry $LiFePO_4$ is shown in Figure 2a. There is a fingerprint of the delithiated $FePO_4$ at 5 eV, which is not present in the lithiated $LiFePO_4$. This corresponds to the electronic structure shift in $FePO_4$ as it lithiates to $LiFePO_4$. As lithium ions interact with the Fe-3d bands, the corresponding peak at 5 eV disappears.[32, 41] Thus, this peak enables quick spectroscopic mapping of the state of lithiation.[42]

Figure 2b presents the UV-VIS spectra of 0.5 M Li_2SO_4 electrolyte, and for comparison 0.5 M H_2SO_4 and water. There is a peak in the 0.5 M Li_2SO_4 solution at 6.2 eV, not present in sulfuric acid or water. Because of the alkaline pH of the Li_2SO_4 electrolyte (pH ca. 8), there is a very low concentration of protonated species. Using equilibrium constants we can identify the predominant solvated species in solution as:

0.74 M Li^+, 0.26 M $LiSO_4^-$, 0.24 M SO_4^{2-}, with less than 10^{-5} M of LiOH, HSO_4^- and $LiHSO_4$. We uniquely identified that the absorption peak at 6.2 eV in the electrolyte is due to solvated $LiSO_4^-$ using *ab initio* theory. Because electronic screening from the surrounding electrolyte shifts the optical gaps of the relevant species on the same order as their separations (~1 eV), we developed a novel *ab initio* approach to calculate excited states while accounting for the surrounding liquid. We employed joint density-functional theory (JDFT) to compute the electronic structure information of solvated species in thermodynamic equilibrium with a liquid environment.[33] Using a hybrid functional for the solute[34] and a nonlinear description of the polarization response of the surrounding liquid,[35] this approach yielded an *ab initio* optical gap of solvated $LiSO_4^-$ of 6.3 eV, in excellent agreement with experimental absorption peak at 6.2 eV. Thus, the presence of this peak indicates a lithiated solution. Other solvated species in the solution have peaks at higher energies, which are

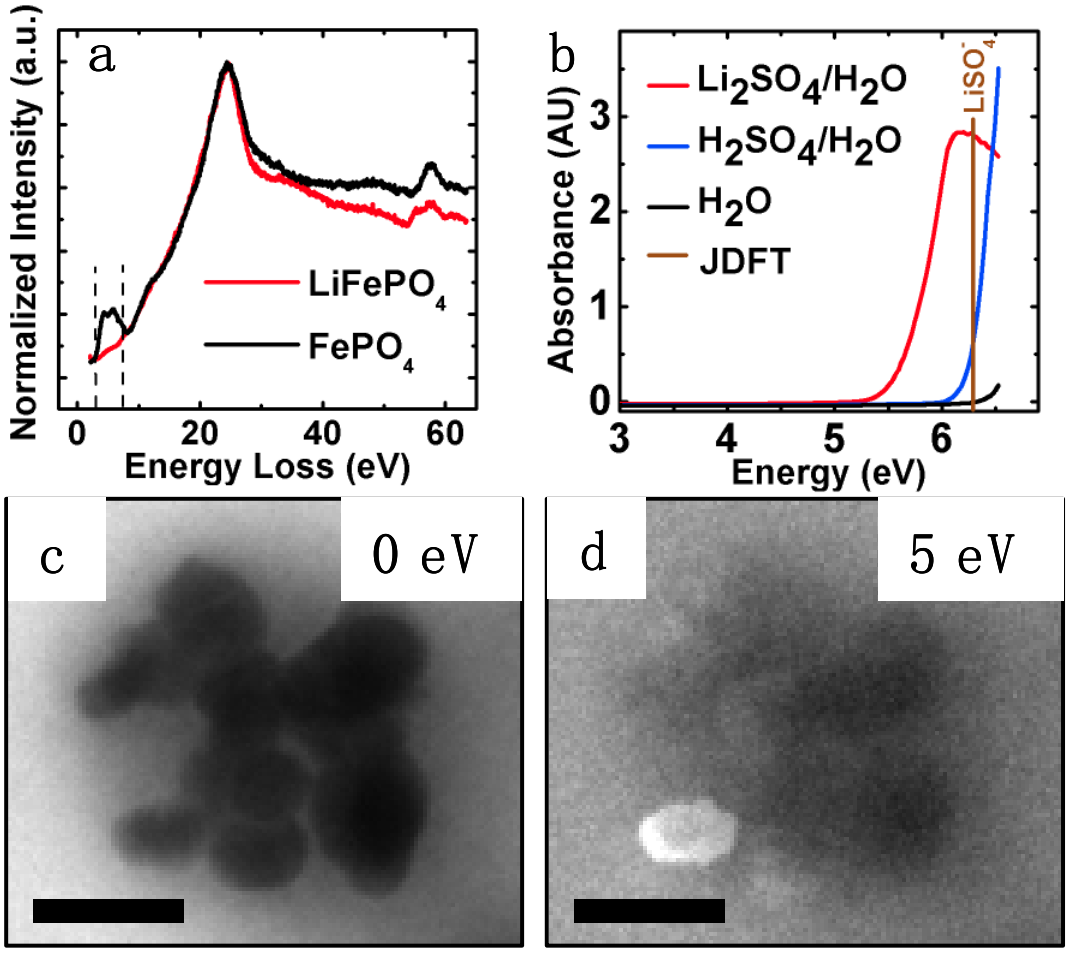

Figure 2. Spectroscopy of $LiFePO_4$ and the delithiated counterpart $FePO_4$ and the Li_2SO_4 aqueous electrolyte. (a) Monochromated EELS, with an energy resolution of 0.2 eV, of a dry sample shows a peak at 5 eV for $FePO_4$ but not for $LiFePO_4$. (b) UV-VIS spectra of the electrolyte 0.5 M Li_2SO_4/H_2O, 0.5 M H_2SO_4/H_2O, and pure water. There is an absorption peak at 6 eV for the Li_2SO_4 solution. The JDFT calculated gaps of the solvated species in solution indicate that the 6 eV peak is caused by $LiSO_4$ EFTEM of $LiFePO_4$ in 0.5 M Li_2SO_4/H_2O with a 5 eV energy slit around (c) 0 eV where the liquid dominates the signal and the particles look fairly homogeneous, showing no diffraction contrast, and at (d) 5 eV, which highlights the $FePO_4$. Scale bar is 200 nm. Using the 5 eV EFTEM image we can locate delithiated regions.

discussed and tabulated in the Supporting Information Section 2. This theory shows remarkable agreement with experiment, and has been repeated for other solvated ions measured by UV-VIS, see Supporting Information Section 2. In the 5 eV EFTEM images we have two fingerprints: one of the delithiated cathode material $FePO_4$ at 5 eV, and one for the lithiated liquid electrolyte at 6.2 eV.

We used EFTEM to obtain spectroscopic mapping of the 5 eV signal with a 5 eV wide slit (energy range from 2.5 to 7.5 eV), which captured the state of lithiation of both the particle and the solution. The 0 eV and 5 eV spectroscopic images of $LiFePO_4$ particles in a 200 nm thick 0.5 M Li_2SO_4 electrolyte are shown in Figure 2c-d, respectively. In the elastic 0 eV EFTEM image, the particles appear fairly homogeneous with no evident diffraction contrast. In the 5 eV EFTEM image, the delithiated regions of the particles are brighter, enabling us to differentiate delithiated and lithiated particles rapidly on the nanoscale. The solution has a high intensity, indicating a lithiated solution, as as would be expected. Our convergence and collection angles are relatively large, which minimizes diffraction contrast. We can estimate the extent of the diffraction contrast, which is an elastic effect, by examining the elastic only (0 eV) EFTEM images that are recorded interlaced with the 5 eV images. We see little diffraction contrast in the cathode material, but a high level of contrast in the 5 eV image. Hence, we conclude that the contrast changes are due to chemical and not to diffraction contrast. We used electron beam conditions that minimized beam interactions in a control experiment, where irradiation without cycling had no apparent affect on morphology or composition (Supporting Information Figure 3). Another control experiment with the same electron beam conditions showed similar effects over the entire electrode, not just in the region imaged (Supporting Information Figure 4). This method of EFTEM enables rapid

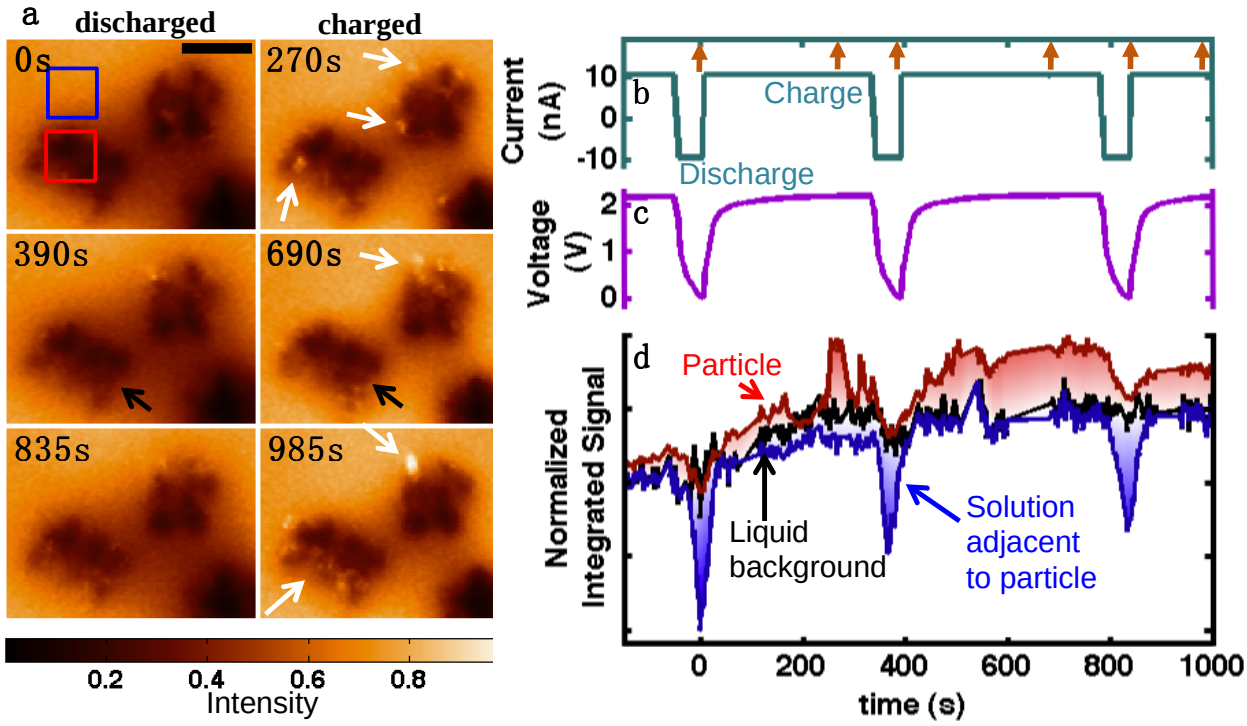

Figure 3. *In situ* charging and discharging of the cathode material $LiFePO_4$ in 0.5 M Li_2SO_4 aqueous electrolyte. (a) 5eV spectroscopic EFTEM images of charging and discharging at indicated times. Scale bar is 400 nm. Bright regions are delithiated $FePO_4$ and dark regions are $LiFePO_4$. There are more bright regions of $FePO_4$ at the end of charge cycles and less during the discharges. White arrows point towards "bright" charged particles while black arrows point towards "dark" discharged particles. (b) Current profile corresponding to 10C. Time = 0 s corresponds to the start of our study, which began on the third charge cycle (not on the first) after assembly. Arrows on the top axis indicate the times of the images shown in (a). The corresponding voltage profile is in (c), using the activated carbon counter electrode also as reference. (d) Integrated intensity over various regions, tracking with the voltage profile, from the regions shown by the boxes in (a). The solution becomes very dark during discharges and returns to the background level during charge. Regions of the particle are seen to light up and disappear, potentially due to delithiating and fracturing off of the particle cluster. During times when no imaging occurred, the data are linearly extrapolated, and for comparison the intensity is brought to the same level by subtraction.

(second-long) mapping of the nanoscale lithium distribution in both the electrode and the electrolyte.

Having an electrochemical cell for the TEM and a technique to observe the lithiation state, we assembled an *in situ* battery using an activated carbon anode, 0.5 M Li_2SO_4 aqueous electrolyte, and a $LiFePO_4$ cathode. We imaged at 5 eV with a 5 eV wide energy window to track the state of lithiation (Figure 3a, Supporting Information Movie 1) and recorded electrochemical data (Figure 3b-c) simultaneously. Figure 3b shows the current profile (applied current was ±10 nA) applied between the anode and cathode. From an estimate of the amount of active material present on the electrode and the specific capacity from *ex situ* aqueous studies (31 mAh/g, Supporting Information Figure 1), this corresponds approximately to a charge/discharge rate of about 10 C (time to charge or discharge to theoretical capacity is $1/10^{th}$ of an hour or 6 minutes). Figure 3c shows the resulting voltage profile between the anode and cathode. Because the potential difference for the deintercalation (intercalation) of lithium ions between $LiFePO_4$ and $FePO_4$ is 1 V,[43] charging (discharging) occurs within the potential range of our experiment. Since we are charging above 1.2 V, it is possible that there could be gaseous evolution. However, given that at the electrodes employed the overpotentials for hydrogen and oxygen evolution are large, we do not feel that under these experimental conditions that this is a concern. The rapid cycling rate (10C) enabled multiple charge-discharge cycles to be acquired in the course of the experiment and decreased the electron beam exposure time.

There are clear differences in the 5 eV spectroscopic images between the charged (Figure 3a, right) and the discharged state (Figure 3a, left) in both the particles and the solution. In the charged state, compared to the discharged state, particles show more bright regions - indicated by white arrows - corresponding to delithiated $FePO_4$. Additionally, the cluster of particles is overall brighter in the

charged image, especially around the edges of the cluster, than in the discharged image, as marked by black arrows. The brightest particles may correspond to completely delithiated $FePO_4$, whereas the overall slight increase in intensity in the particles may indicate partially delithiated particles. On discharge, these bright regions of $FePO_4$ disappear, transitioning back to $LiFePO_4$. If we spatially integrate the 5 eV EFTEM intensity over a cluster of particles, inside the region of the red box in Figure 3d. we see an average increase in intensity on charge and a decrease on discharge. The intensity of the particles in Figure 3d was raised to the background level of the solution. Radiation damage is expected to be irreversible and uncorrelated with voltage cycle, and the appearance of the bright regions of $FePO_4$ and lithiated solution is repeatable/reproducible and correlated with charge state, indicating that the electron beam did not cause the observed responses. This demonstrates tracking of the lithiation state of battery electrodes at the nanoscale.

We next examined the 5 eV EFTEM intensity in the solution adjacent to the particles. There is a local decrease in intensity in the solution surrounding the particles during discharge, which can be seen in Figure 3a. The spatially integrated signal from the solution adjacent to the particle (blue) drops dramatically during discharge, plotted in Figure 3d. Far away from the particles, the intensity in the solution remains relatively constant (black trace). From UV-VIS measurements and JDFT calculations, the bright intensity in the solution is caused by $LiSO_4^-$. As the particles lithiate during discharge, the adjacent solution becomes depleted of Li^+ and $LiSO_4^-$, causing the drop in the 5 eV signal. The profile of the intensity drop matches that of a diffusional concentration profile (Supporting Information Figure 2), supporting that it is due to depletion of species near the electrode. Additionally, the intensity change appears in the inelastic but not in the elastic images, indicating a chemical change. We thus observe the expected delithiation of the solution in the 5 eV EFTEM images as the

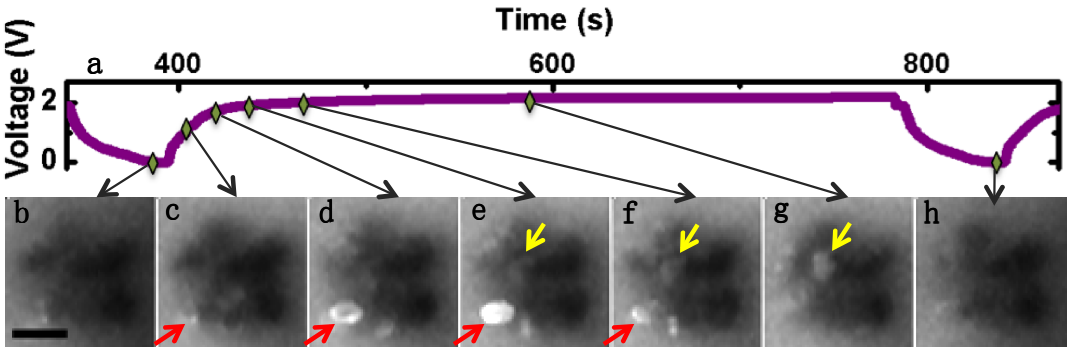

Figure 4. Temporal evolution of a $LiFePO_4/FePO_4$ cluster during one charge/discharge cycle. The voltage profile is shown in (a), corresponding to the second imaged cycle (fourth cycle after assembly). The 5 eV EFTEM image in (b) is for the completely discharged state, with a scale bar of 200 nm. At the bottom of (c) and (d) we see the emergence of core-shell structures. In (d) a bright particle appears with a core-shell structure that fills in brighter in (e), and partially disappears in (f). More regions of bright $FePO_4$ develop in (g), and the particle returns to the discharged state in (h) where it is darker. In general, images taken for the charged state (d-g) have more bright regions than the images taken in the discharged state, (a) and (h), which have significantly more dark sections. Red arrows indicate particles delithiating by a core-shell pathway and yellow arrows indicate delithiation propagating from left to right through the particle.

particles are being lithiated. Thus, valence EFTEM can track the lithium ions in the particles and solution during battery cycling.

With the capability to locate ions at the nanoscale, we explored the mechanism of lithiation and delithiation of individual cathode nanoparticles. There are several proposed mechanisms of lithiation for $LiFePO_4$,[21, 23-25, 44] which have been reported to depend on particle size, coating, synthesis methods, charging rate and other experimental conditions.[45] These methods typically rely on bulk particle analysis which convolutes the effects of many particles.[3]

We observed the evolution of many individual particles under high rate conditions in aqueous solution. The evolution of one cluster of particles is shown in Figure 4, corresponding to the voltage profile in Figure 4a. In Figure 4b the cell is discharged, and the particles and solution are dark, corresponding to a lithiated particle and a delithiated solution. During charge, the red arrows track the evolution of an individual particle. In Figure 4c, the start of nucleation is seen. In Figure 4d, we see a core-shell type structure, which completely transforms into $FePO_4$ in Figure 4e. In Figure 4f, the particle appears to have mostly fractured off. We track the evolution of a representative particle denoted by the yellow arrows, where the edge of the particle transitions to $FePO_4$, and the delithiation front propagates anisotropically across the particle until it is completely delithiated in Figure 4g. We return to the discharged state in Figure 4h, and the bright regions disappear, converting to $LiFePO_4$.

The delithiation of individual particles as seen in Figure 3a and in Figure 4 demonstrates slow nucleation during the transformation, indicating particle-by-particle delithation. Growth of the phase is also slow enough for us to image (Figure 4) and we see particles that are not fully transformed – in contrast with the “domino cascade” model that predicts the full transformation of individual particles once nucleated. We observed core-shell structures, but more commonly delithiation started at an edge and

then moved through the rest of the particle supporting anisotropic growth. Also, stronger regions of delithiation are seen on the edges of agglomerates, where the particle may be in better electrical contact with the current collector. However, the same particles are not always the active ones. The kinetics are consistent with a diffusional response (Supporting Information Figure 3), which is not surprising, considering the high cycling rate and thin liquid layer. Strikingly, the particles exhibit an inhomogeneous response at the nanoscale and many of the particles are inactive at any moment in time. This inhomogeneous response is likely a characteristic of the kinetics and the mechanism of Li-ion insertion and de-insertion associated with multi-particle polycrystalline $LiFePO_4$, and similar inhomogeneity has been noted *ex situ* by scanning transmission x-ray spectroscopy at much lower (40 nm) spatial resolution.[29] This highlights the advantages of nanoscale imaging during cycling, as bulk analysis can rarely deconvolve these effects.

We observe degradation mechanisms in the $LiFePO_4$ particles during the course the rapid charge/discharge cycles. We see gradual mass loss of the $LiFePO_4$ throughout the experiment from our observations from elastic 0 eV EFTEM images (20% particle area diminution in 5 cycles). The fracturing and mass loss were observed in a control experiment to occur over the entire electrode, even where it was not exposed to the electron beam during cycling (Supporting Information Figure 4). This is consistent with our observations in the 5 eV EFTEM images during cycling. As particles delithiated, they often disappeared from the field of view, followed by the formation of another delithiated region – seen in Figure 4e and 4f, and in Supporting Information Video 1. An plausible explanation is that as the particles delithiate, and given the rapid cycling (10C) conditions, lattice strain causes regions to physically detach from the particle and float away in the solution. In fact, fracturing has been observed in *ex situ* studies.[20, 46] After fracturing, a fresh surface of $LiFePO_4$ is

exposed, enabling further delithiation, as found in Sn(II) oxide by *in situ* x-ray tomography.[47]

Section 4.4. Conclusion

This work demonstrates the unique ability of liquid cell *in situ* TEM coupled with spectroscopy and theory to observe the lithium insertion and de-insertion dynamics and degradation of $LiFePO_4$ in real time. These techniques may provide valuable insights into operation and other degradation pathways in a wide range of electrical energy conversion and storage devices such as batteries, fuel cells and supercapacitors.

Supporting Information Available: methods, *ex situ* material testing, supporting video and further discussion of ion transport in electrolyte and JDFT, and description of beam damage control experiments. This material is available free of charge via the Internet at http://pubs.acs.org.

REFERENCES

1. Tarascon, J. M.; Armand, M. *Nature* **2001,** 414, (6861), 359-367.

2. Whittingham, M. S. *Proceedings of the Ieee* **2012,** 100, 1518-1534.

3. Malik, R.; Abdellahi, A.; Ceder, G. *Journal of the Electrochemical Society* **2013,** 160, (5), A3179-A3197.

4. de Jonge, N.; Ross, F. M. *Nat. Nanotechnol.* **2011,** 6, (11), 695-704.

5. Yuk, J. M.; Park, J.; Ercius, P.; Kim, K.; Hellebusch, D. J.; Crommie, M. F.; Lee, J. Y.; Zettl, A.; Alivisatos, A. P. *Science* **2012,** 336, (6077), 61-64.

6. Holtz, M. E.; Yu, Y.; Gao, J.; Abruña, H. D.; Muller, D. A. *Microsc. microanal.* **2013,** 19, (4), 1027-35.

7. Jungjohann, K. L.; Evans, J. E.; Aguiar, J. A.; Arslan, I.; Browning, N. D. *Microsc. microanal.* **2012,** 18, (3), 621-627.

8. Zheng, H. M.; Smith, R. K.; Jun, Y. W.; Kisielowski, C.; Dahmen, U.; Alivisatos, A. P. *Science* **2009,** 324, (5932), 1309-1312.

9. Williamson, M. J.; Tromp, R. M.; Vereecken, P. M.; Hull, R.; Ross, F. M. *Nat. Mater.* **2003,** 2, (8), 532-536.

10. Grogan, J. M.; Bau, H. H. *J. Microelectromech. Syst.* **2010,** 19, (4), 885-894.

11. Unocic, R. R.; Adamczyk, L. A.; Dudney, N. J.; Alsem, D. H.; Salmon, N. J.; More, K. L. *Microsc. microanal.* **2011,** 17, ((Suppl 2)), 1564-1565.

12. Huang, J. Y.; Zhong, L.; Wang, C. M.; Sullivan, J. P.; Xu, W.; Zhang, L. Q.; Mao, S. X.; Hudak, N. S.; Liu, X. H.; Subramanian, A.; Fan, H.; Qi, L.; Kushima, A.; Li, J. *Science* **2010,** 330, (6010), 1515-1520.

13. Liu, X. H.; Zhang, L. Q.; Zhong, L.; Liu, Y.; Zheng, H.; Wang, J. W.; Cho, J.-H.; Dayeh, S. A.; Picraux, S. T.; Sullivan, J. P.; Mao, S. X.; Ye, Z. Z.; Huang, J. Y. *Nano Letters* **2011,** 11, (6), 2251-2258.

14. White, E. R.; Singer, S. B.; Augustyn, V.; Hubbard, W. A.; Mecklenburg, M.; Dunn, B.; Regan, B. C. *ACS Nano* **2012,** 6, (7), 6308-17.

15. Dahn, J. R.; Zheng, T.; Liu, Y. H.; Xue, J. S. *Science* **1995,** 270, (5236), 590-593.

16. Whittingham, M. S. *Science* **1976,** 192, (4244), 1126-1127.

17. Padhi, A. K.; Nanjundaswamy, K. S.; Goodenough, J. B. *Journal of the Electrochemical Society* **1997,** 144, (4), 1188-1194.

18. Herle, P. S.; Ellis, B.; Coombs, N.; Nazar, L. F. *Nat. Mater.* **2004,** 3, (3), 147-152.

19. Chen, J. J.; Whittingham, M. S. *Electrochemistry Communications* **2006,** 8, (5), 855-858.

20. Chen, G. Y.; Song, X. Y.; Richardson, T. J. *Electrochem. Solid State Lett.* **2006,** 9, (6), A295-A298.

21. Brunetti, G.; Robert, D.; Bayle-Guillemaud, P.; Rouviere, J. L.; Rauch, E. F.; Martin, J. F.; Colin, J. F.; Bertin, F.; Cayron, C. *Chemistry of Materials* **2011,** 23, (20), 4515-4524.

22. Jones, J. L.; Hung, J. T.; Meng, Y. S. *J. Power Sources* **2009,** 189, (1), 702-705.

23. Laffont, L.; Delacourt, C.; Gibot, P.; Wu, M. Y.; Kooyman, P.; Masquelier, C.; Tarascon, J. M. *Chemistry of Materials* **2006,** 18, (23), 5520-5529.

24. Delmas, C.; Maccario, M.; Croguennec, L.; Le Cras, F.; Weill, F. *Nat. Mater.* **2008,** 7, (8), 665-671.

25. Sharma, N.; Guo, X. W.; Du, G. D.; Guo, Z. P.; Wang, J. Z.; Wang, Z. X.; Peterson, V. K. *J. Am. Chem. Soc.* **2012,** 134, (18), 7867-7873.

26. Malik, R.; Zhou, F.; Ceder, G. *Nat. Mater.* **2011,** 10, (8), 587-590.

27. Dreyer, W.; Jamnik, J.; Guhlke, C.; Huth, R.; Moskon, J.; Gaberscek, M. *Nat. Mater.* **2010,** 9, (5), 448-453.

28. Badi, S.-P.; Wagemaker, M.; Ellis, B. L.; Singh, D. P.; Borghols, W. J. H.; Kan, W. H.; Ryan, D. H.; Mulder, F. M.; Nazar, L. F. *Journal of Materials Chemistry* **2011,** 21, (27), 10085-10093.

29. Chueh, W. C.; El Gabaly, F.; Sugar, J. D.; Bartelt, N. C.; McDaniel, A. H.; Fenton, K. R.; Zavadil, K. R.; Tyliszczak, T.; Lai, W.; McCarty, K. F. *Nano Letters* **2013,** 13, (3), 866-872.

30. Harris, S. J.; Timmons, A.; Baker, D. R.; Monroe, C. *Chem. Phys. Lett.* **2010,** 485, (4-6), 265-274.

31. Patel, M. U. M.; Demir-Cakan, R.; Morcrette, M.; Tarascon, J. M.; Gaberscek, M.; Dominko, R. *Chemsuschem* **2013,** 6, (7), 1177-1181.

32. Kinyanjui, M. K.; Axmann, P.; Wohlfahrt-Mehrens, M.; Moreau, P.; Boucher, F.; Kaiser, U. *J. Phys.-Condes. Matter* **2010,** 22, (27), 275501.

33. Sundararaman, R.; Letchworth-Weaver, K.; Arias, T. A. JDFTx.

34. Ernzerhof, M.; Scuseria, G. E. *J. Chem. Phys.* **1999,** 110, (11), 5029-5036.

35. Gunceler, D.; Letchworth-Weaver, K.; Sundararaman, R.; Schwarz, K. A.; Arias, T. A. *Modelling and Simulation in Materials Science and Engineering* **2013,** 21, (7), 074005.

36. Wang, Y. G.; Yi, J.; Xia, Y. Y. *Adv. Energy Mater.* **2012,** 2, (7), 830-840.

37. Wang, C.-M.; Xu, W.; Liu, J.; Zhang, J.-G.; Saraf, L. V.; Arey, B. W.; Choi, D.; Yang, Z.-G.; Xiao, J.; Thevuthasan, S.; Baer, D. R. *Nano Letters* **2011,** 11, (5), 1874-1880.

38. Gu, M.; Parent, L. R.; Mehdi, B. L.; Unocic, R. R.; McDowell, M. T.; Sacci, R. L.; Xu, W.; Connell, J. G.; Xu, P.; Abellan, P.; Chen, X.; Zhang, Y.; Perea, D. E.;

Evans, J. E.; Lauhon, L. J.; Zhang, J.-G.; Liu, J.; Browning, N. D.; Cui, Y.; Arslan, I.; Wang, C.-M. *Nano Letters* **2013**.

39. Moreau, P.; Boucher, F. *Micron* **2012,** 43, (1), 16-21.

40. Muller, D. A.; Silcox, J. *Ultramicroscopy* **1995,** 59, (1-4), 195-213.

41. Sigle, W.; Amin, R.; Weichert, K.; van Aken, P. A.; Maier, J. *Electrochem. Solid State Lett.* **2009,** 12, (8), A151-A154.

42. Moreau, P.; Mauchamp, V.; Pailloux, F.; Boucher, F. *Appl. Phys. Lett.* **2009,** 94, (12), 123111.

43. Luo, J. Y.; Cui, W. J.; He, P.; Xia, Y. Y. *Nat. Chem.* **2010,** 2, (9), 760-765.

44. Ramana, C. V.; Mauger, A.; Gendron, F.; Julien, C. M.; Zaghib, K. *J. Power Sources* **2009,** 187, (2), 555-564.

45. Zhang, W. J. *J. Power Sources* **2011,** 196, (6), 2962-2970.

46. Wang, D. Y.; Wu, X. D.; Wang, Z. X.; Chen, L. Q. *J. Power Sources* **2005,** 140, (1), 125-128.

47. Ebner, M.; Marone, F.; Stampanoni, M.; Wood, V. *Science* **2013,** 342, (6159), 716-720.

CHAPTER 5

NANOPARTICLE METAMORPHOSIS: AN *IN-SITU* HIGH TERMPERATURE TEM STUDY OF THE STRUCTURAL EVOLUATION OF HETEROGENEOUS Au: Fe_2O_3 NANOPARTICLES[*†]

Section 5.1. Introduction

The ability to control structure and composition at the nanoscale has generated opportunities to create novel materials with properties by design. Concurrent advances in synthesis,[1] characterization[2] and computational modeling[3] of nanoparticles (NPs) with precise size,[4] shape,[5,6] and composition have provided valuable scientific insights and improved our understanding of fundamental structure property relationships.[7-10] Moreover, the successful application of NPs as building blocks in a variety of prototype devices has underscored their immense potential in emerging nanotechnologies.[11,12]

Heterogeneous NPs combining multiple functionalities of dissimilar materials have emerged as versatile materials with novel properties emerging from complementary and synergistic interactions among the nanostructures components. A variety of core/shell,[13,14] dot/rod[15,16] and Janus-like[17] heterostructures have been created and demonstrated to exhibit unique optoelectronic[18,19], catalytic[20,21], and biomedical[22] properties. While highly promising, many basic thermodynamic and

[*] Produced with permission from William J. Baumgardner, Yingchao Yu, Robert Hovden, Shreyas Honrao, Richard G. Hennig, Héctor D. Abruña, David A. Muller and Tobias Hanrath. Unpublished result.

[†] W.J.B. and Y.Y. contribute equally to this work. The synthesis and casting of binary NP assemblies, and in-situ XRD was carried out by W.J.B. The design and characterization using in-situ STEM (including EDX, EELS), post-data analysis and manuscript writing are performed by Y.Y. and W.J.B.. H.D.A, D.A.M and T.H guide the experiment as well as revising the paper.

kinetic aspects governing the formation of heterostructured NPs remain poorly understood, which renders progress largely empirical.

Thin film growth and epitaxial techniques established for planar surfaces present interesting analogies to the growth of heterostructured NPs. In planar geometries, the formation of islands (*i.e.,* Volmer-Weber or Stranski–Krastanov growth) or conformal layer-by-layer (*i.e.,* Frank-van der Merwe growth) is well understood and depends on the chemical potential of the deposited layers. The emergence of nanostructured materials introduces the question of how these concepts and fundamental relationships apply in the case of thin layer growth in nanostructured systems, *e.g.* on the curved surface of a spherical NP. In light of growing interest in heterostructured nanomaterials, addressing this knowledge gap could provide the most valuable insights. Specifically, we need to understand how thermodynamic and kinetic aspects of the formation relate to the structure of the thin shell formed on the surface of colloidal NPs.

Size-effects are known to significantly alter the physical and electronic properties of single component NPs; however, the impact of size on phase behavior of heterogeneous NPs is less well understood. The sensitive relationship between the structure of heterogeneous NPs and their properties provides strong motivation to better understand and ultimately control their formation. Fusing dissimilar NPs under controlled conditions is an advantageous approach to study these processes in detail. To a first approximation, homogeneous and heterogeneous NP fusion can be described in terms of the average Gibbs free energy change associated with the NP surface energy. However, this simplification fails to capture complexities that arise from faceting of the NP surface and variations in the atomic composition of the core relative to the surface. These size-dependent effects may introduce significant perturbations relative to the known phase equilibrium of the corresponding bulk materials.

In-situ transmission electron microscopy (TEM) at variable temperatures, detailed in this paper, allowed us to directly monitor the NP fusion in real time and to establish the size-dependent phase behavior of heterogeneous NPs. *In-situ* X-ray diffraction (XRD) experiments confirmed similar trends in thin films of NPs. Using Au and Fe_2O_3 NPs as a model system, we demonstrate the evolution of structure and composition of heterogeneous Au:Fe_2O_3 particles at elevated temperatures. Based on the detailed *in-situ* structure analysis presented in this paper, we submit the hypothesis that the heterogeneous fusion of Fe_2O_3 and Au particles can be explained by the sequence of events illustrated in Fig. 1. First, Au, from a smaller NP, spreads across the surface of a partially reduced hematite particle. The amount of Au in the initial fusion product is insufficient to form a monolayer. Upon further addition Au NPs, the Au:Fe surface alloy layer transforms into a well-defined core/shell structure. Experimental insights, detailed below, allowed us to establish a temperature-dependent phase diagram of Au and Fe_2O_3 NPs to illustrate the complex interplay of NP composition, morphology, temperature, and size.

The large difference in melting points makes Au and Fe_2O_3 NPs an advantageous model system for the present study. The smaller Au NPs (6.6 nm diameter) melt in the range of 850-900˚C, which is lower than that of the bulk value due to the contributions of surface energy described by the Gibbs-Thomson effect.[23] The larger Fe_2O_3 NPs (15 nm diameter), on the other hand, exhibit minimal melting point reduction and are expected to melt near their bulk value of 1566˚C. We deliberately focused on NPs of different diameters for two reasons: first, as a means to favor heterogeneous sintering through Ostwald ripening; the process by which larger particles (*i.e.,* Fe_2O_3) grow at the expense of smaller ones (*i.e.,* Au) to lower surface free energy;[24] and secondly, to form thin films of the material from the smaller Au NP

(lower surface energy) spread across the surface of the larger Fe_2O_3 NP (with larger surface energy).

Disordered films of Au and Fe_2O_3 NPs were formed by drop-casting a dilute suspension of Au and Fe_2O_3 NPs (ratio 1:1) onto a heating chip. We studied a field of view with a diverse range of local NP stoichiometries and morphologies to gain insights into NP sintering behavior as a function of local nanoscale environment rather than bulk composition. TEM images of the starting materials as well as detailed size analysis are provided in the supplementary materials (Fig. S1).

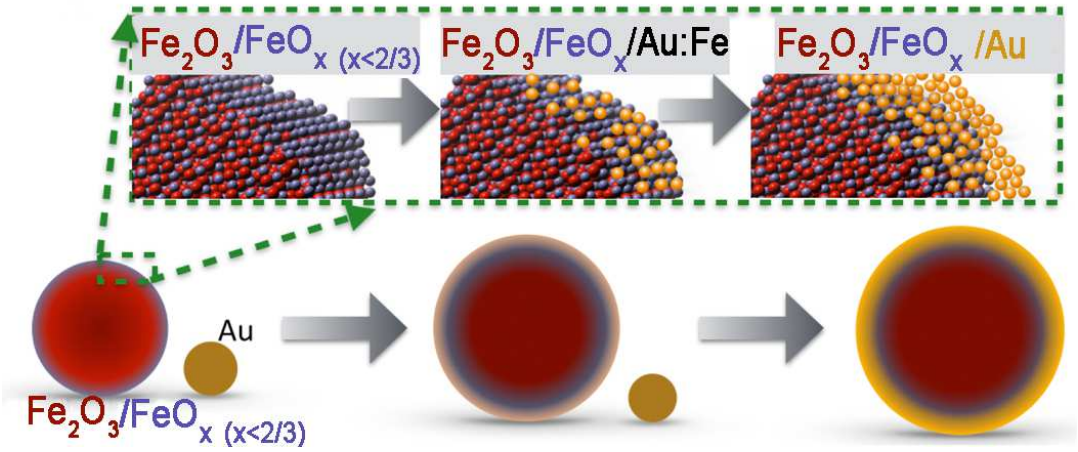

Fig. 1. Schematic illustration of heterogeneous Au / Fe_2O_3 NP fusion. Au dissolves into the Fe-rich surface layer to form a Fe_2O_3/Au:Fe surface-alloyed structure. Further addition of Au leads to the formation of a phase segregated Au shell.

Section 5.2. Materials and Methods

Fig. 2 summarizes *in-situ* TEM observation of the evolution of NP structure and morphology during the heating experiment. We heated the NP film from room temperature to 900˚C over the course of four hours (a detailed temperature profile is provided in the supplementary materials, Fig. S4) and monitored structural changes of the binary NP film in real time using high angle annular dark-field scanning transmission electron microscopy (HAADF-STEM). *In-situ* TEM studies with extended beam exposure times must be performed with careful attention to the possibility of beam damage effects. Based on a detailed analysis of the electron beam dosage and careful control experiments detailed in the supplementary materials, we can confidently conclude that irradiation-induced artifacts are not a factor in the experimental observations detailed below. All experiments were captured in video, excepting only short recesses to capture stills and perform elemental analysis by EDX. Due to Z-contrast from the incoherent signal from HAADF-STEM imaging[25] Au is expected to be about 10 times brighter than Fe and O. We included several movies of the NP fusion events in the supplementary materials (see movies S1-S3).

Section 5.3. Results and Discussion

For temperatures up to 450˚C, the particles appeared stable and we did not observe any NP fusion. At 500˚C, the film morphology changed dramatically and Au NPs fused with Fe_2O_3. Our detailed *in-situ* observations revealed three remarkable trends: (1) during fusion, NP heterostructures undergo fluid shape transformations at temperatures several hundred degrees below their size-reduced melting point; (2) heterogeneous fusion of Au and Fe_2O_3 NPs is significantly favored over homogeneous fusion of either Au or Fe_2O_3 particles; (3) the structure of heterogeneously sintered Au:Fe_2O_3 NPs evolves from a particle with uniform contrast to a phase segregated (Janus or core/shell) morphology upon addition of further Au. Below, we discuss each

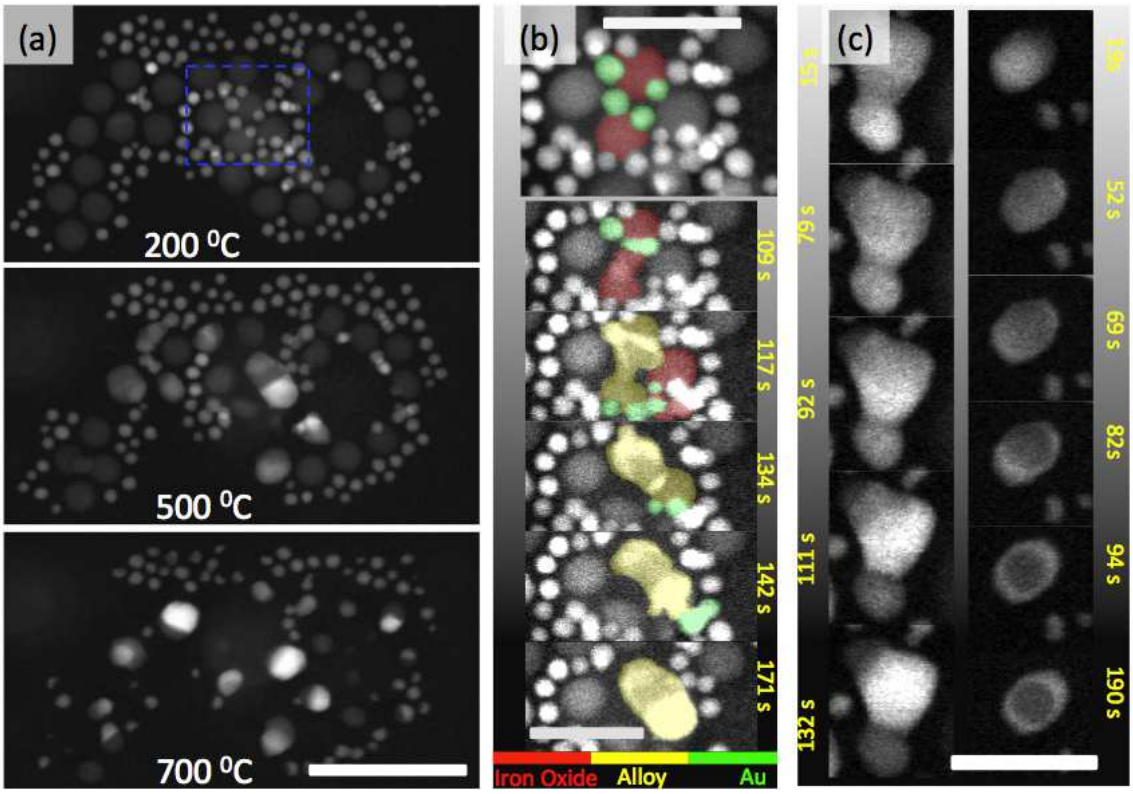

Fig. 2. *In-situ* HAADF-STEM images acquired during the thermal annealing experiment. (a) Video stills of two regions of the NP sample at 500^0C, forming alloy NPs. In the stills, particles that are taking part in the next fusion event are colored, red for iron oxide, green for gold, and yellow for composite particles. (b) Overview of the primary viewing region at 200, 500 and 700^0C. C) (c) Video snapshots of particles undergoing a phase transition from alloy to phase segregated at 650^0C (left) and from alloy to core/shell at 750^0C (right). All scale bars represent 50 nm.

of these observations in the context of underlying energetic and kinetic factors driving the transformation of particle shape and composition.

As shown in the movies S1 and S2, the heterogeneous Au/Fe_2O_3 fusion leads to structures that rapidly deform in a fluid fashion. Fig. 2b provides several snapshots illustrating the dynamics of the quasi-fluid particle fusion. Careful analysis of the video data shows that particles formed by heterogeneous fusion of Au and Fe_2O_3 NPs often appear to be 'activated' for a period of approximately 60 seconds, participating in a rapid series of subsequent fusion events. Remarkably, this quasi-fluid fusion occurs at temperatures approximately 1000˚C below the expected melting point of Fe_2O_3 NPs. Detailed structural analysis (*vide infra*) confirms that the core of the fused Au:Fe_2O_3 particle maintains the hematite crystal structure.

The fluid-like deformation of NP particles during the fusion event is intriguing and uncharacteristic of crystalline particles. Nearby NPs, that were not involved in the fusion, remained relatively stationary. The physical process that initiates the apparently spontaneous fusion is not yet fully understood but may be related to phase transitions in the iron oxide particles. Variable-temperature XRD experiments (see supplementary materials, Fig. S6) revealed a maghemite-to-hematite phase transition to occur near 500˚C – the same temperature at which we observe the initiation of heterogeneous NP fusion events. Further investigation is required to understand the possible role of the lattice structure transformation in initiating the NP fusion.

Heterogeneous fusion of Au and Fe_2O_3 NPs is significantly favored over homogeneous fusion of either Au or Fe_2O_3 NPs based on extensive *in-situ* TEM observations. We interpret the preference for heterogeneous fusion in context of the change in Gibbs free energy. In the case of homogeneous fusion of two similar NPs the Gibbs energy change is given by $dG = \sigma dA$. Similarly, the Gibbs free energy change associated with the heterogeneous fusion, *e.g.* Au and Fe_2O_3, is given by

$dG = \sigma_1 dA_1 + \sigma_2 dA_2 + \sigma_{12} dA_{12}$, where σ presents the corresponding surface or interface energy and dA_1, dA_2, and dA_{12} present the change of the Au, Fe_2O_3 NPs surface area and the Au/Fe_2O_3 interface, respectively. Based on the observed preference for heterogeneous fusion at 500˚C, we can infer that the adhesion energy of Au on Fe_2O_3 is larger than the surface energy of Au, specifically $\sigma_{12} > (1+\phi)\sigma_1$ where ϕ is a geometric factor accounting for the radius of the two NPs involved in the fusion (see supplementary materials). The preference for heterogeneous fusion of Au and Fe_2O_3 on a TEM grid is consistent with previous reports of Au/Fe_2O_3 NP heterostructures formed via coalescence of colloidal particles in a heated suspension.[26]

The sequence of structural transformations of heterogeneous Au:Fe_2O_3 NPs fusion products from initial structures with uniform contrast to phase segregated particles merits more detailed discussion. Fig. 2c illustrates how a fused particle with initially homogeneous contrast evolves to phase segregate into bright (Au-rich) and dark (Au-lean) regions at 650˚C over the course of about 2 minutes. The right panel illustrates the transformation of a fused particle with uniform contrast into a well-defined core/shell structure at 750˚C. At the highest temperatures (800^0C), nearly all NPs redistributed their contrast to form a core/shell morphology. We observed this to be the final transient state before the particles decomposed and were subsequently lost to the vacuum of the instrument. Collectively, these observations illustrate the complexity of shape and composition transformations of heterogeneous NPs. We investigated the temperature-dependent evolution of composition and structure using a suite of characterization techniques including electron energy loss spectroscopy (EELS), energy dispersive X-ray spectroscopy (EDX) and X-ray diffraction (XRD).

In-situ EDX analysis during the course of the annealing experiment provides important insights into the evolution of the composition of the sintered NPs. NPs with a uniform contrast exhibited a homogenous distribution of Fe and Au measured across

the particle (Fig. 3a-d). If the NP fusions were approximated as a constant volume process, spreading a 6.6 nm diameter Au particle across the surface of a 15 nm Fe_2O_3 particle would yield an Au layer with a thickness of approximately 0.2 nm. This thickness is too small to form a coherent film of pure gold.[27] Based on the isochoric model, we calculated that approximately 7 Au NPs would be required to form a coherent 1nm thick Au shell (see supplementary materials Fig. S8).

To explain the uniform contrast of the fused Au:Fe_2O_3 particles, we formulated several alternative hypotheses. First, the uniform contrast could be interpreted as a homogeneous $Au_xFe_yO_z$ alloy NP. In the bulk, such alloys have not been reported. We discarded the possibility of a homogeneous $Au_xFe_yO_z$ alloy on the basis of highly unfavorable energetics. Density-functional theory calculations (see supplementary materials) showed that formation energies for Au within the hematite lattice were in excess of 1.8 eV. As a second hypothesis, we considered the possibility that the uniform contrast in the fused NP may be due to phase segregation in the direction of the beam, *i.e.* with the gold rich region either at the top (towards the electron beam), or bottom of the particle. In projection, this would look similar to an even distribution of gold throughout the particle. Such a structure could be driven by an energetic preference for Au wetting of the Fe_2O_3 of the particle as opposed to the silicon carbide (SiC_x) substrate. However, this interpretation fails to fully explain the size and shape changes of the particles, as well as the liquid-like behavior. In particular, particle deformation to initiate the event, and movement across the substrate cannot be explained with the interpretation as a particle with vertical phase segregation.

The third alternative interpretation of the uniform contrast is as a thin Au-Fe alloy layer coating the surface of the fused particle; we refer to these structures as surface alloy nanoparticles (sa-NP). At 500˚C, the bulk solubility of Au in Fe is less than 1 at. % whereas the solubility of Fe in Au is near 15 at%.[28] To better understand

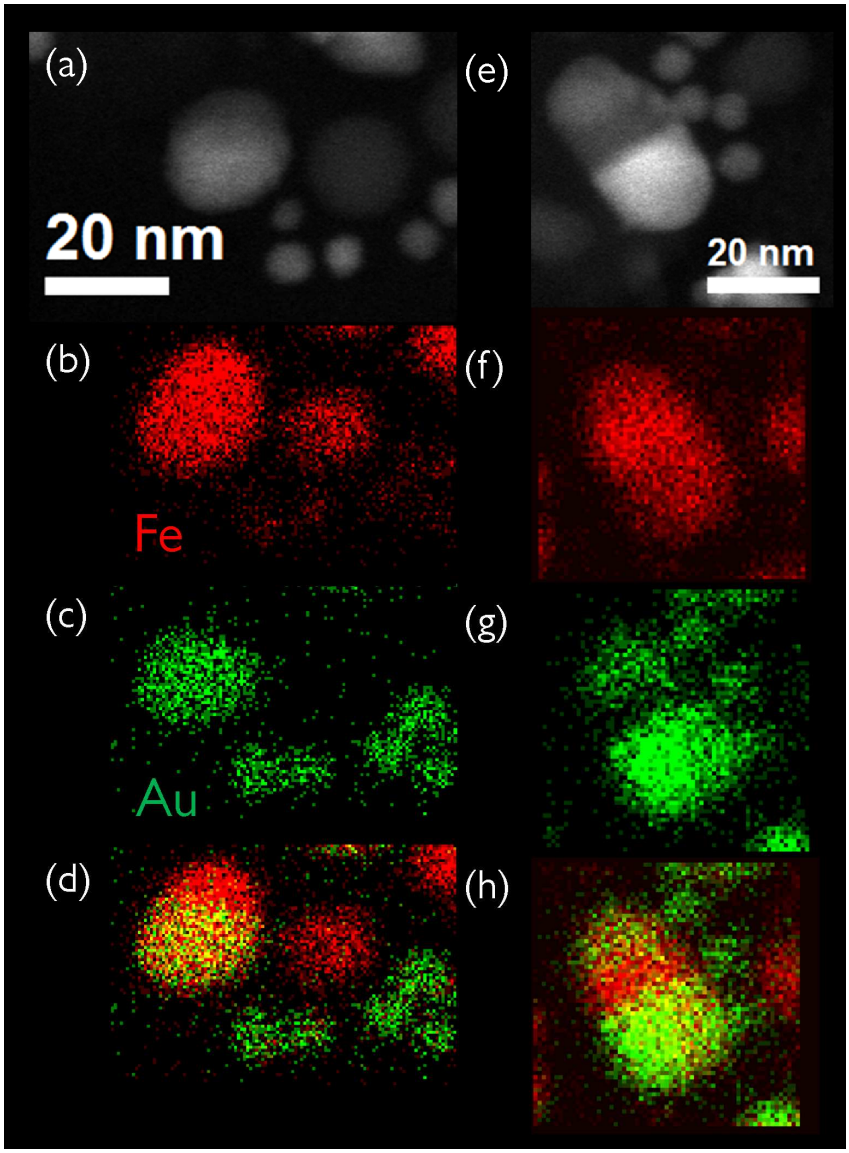

Fig. 3. Compositional analysis of surface alloy (sa-NP) and phase-segregated (ps-NP) structures. (a) HAADF-STEM image of a region composed of alloy particles, and its corresponding EDX mapping of (b) Fe, in red; (c) Au, in green; (d) composite of both. (e)-(h) represents a different location comprised of a phase-segregated structure.

the structure of the fused heterogeneous NP and to test the hypothesis of Au-Fe surface alloys, we performed a detailed analysis of structure and composition of the fused particles as discussed below.

NPs with clearly discernible phase segregation in the brightness of HAADF-STEM images exhibit a different compositional profile. EDX analysis of phase-segregated nanoparticles (ps-NP) revealed a clear segregation of the gold distribution within the particle, consistent with the distribution of the bright contrast (Fig. 3e-h). Interestingly, by comparing the O:Fe ratio in the EDX spectrum of the fused and unfused particles, we observe a relative decrease in the ratio of the fused NP relative to the starting material (see supplementary materials Fig. S11). We point to this comparison of composition as an indication that NPs with a lower O:Fe ratio (*i.e.* Fe-rich stoichiometry) are more likely to sinter. This trend further supports the hypothesis of the role of a Fe-rich surface layer in initiating the heterogeneous NP fusion.

The peculiar NP fusion and metamorphosis motivates the study of the evolution of the NP composition in real time. Unfortunately, time-resolved EDX analysis is impractical given the long acquisition time for the spectra (*e.g.*, 200 s for Fig. 3). We resolved this limitation by calibrating the contrast in the HAADF-STEM images relative to the composition of the particles determined from EDX based on the Z contrast in HAADF-STEM imaging.[25] This approach provided detailed, real-time insights into the concurrent shape and composition changes during NP sintering, allowing us to connect the contrast redistributions we observed in STEM to chemical changes in the compositional distribution of the particle itself. Specifically, the metamorphosis from sa-NPs to ps-NPs commonly observed above 600^0C was indicative of migration and segregation of gold atoms on the particle surface that could be detected in real time (Fig. 2e, Movies 2S-3S).

To provide a quantitative description of NP fusion at elevated temperatures, we analyzed STEM video data to determine the specific phase behavior of individual particles within the sample as a function of composition (percentage of Au and Fe_2O_3), temperature, morphology (uniform or phase segregated) and size (diameter). To obtain this information, we performed a geometric analysis to approximate the atomic composition of each individual NP at the beginning of the experiment. We carefully tracked the video data frame-by-frame and catalogued each NP fusion event (see supplementary materials Fig. S12). Using this approach, we determined the composition of new sa-NPs or ps-NPs based on the composition of the precursor particles from which it formed.

To estimate the inhomogeneity in atomic distribution, and hence, phase of each particle, we indexed the contrast histogram of each NP. Using the correlation between HAADF contrast and atomic distribution established by EDX above, we measured the standard deviation of contrast within each stable NP at each temperature, with higher values indicating more diverse contrast values and hence phase segregated NPs morphology. Finally, we tabulated the comparative 'size' of the particle as the cubed root of the total number of atoms within each particle (a detailed description of the methodology is provided in the supplementary information).

Fig. 4 summarizes the phase behavior of Au:Fe_2O_3 NPs as a function of composition, temperature, and particle size as the parameters. In the diagram, each data point represents a specific particle that was tracked throughout the experiment. All particles within the viewing region were included. The color of the point corresponds to the phase of the NP (sa-NP red, ps-NP blue and core/shell NP in grey), determined by the method described above. The diameter of the point is proportional to the NP diameter. The abscissa and ordinate are the particle composition, and the temperature at which it was observed to be stable, respectively.

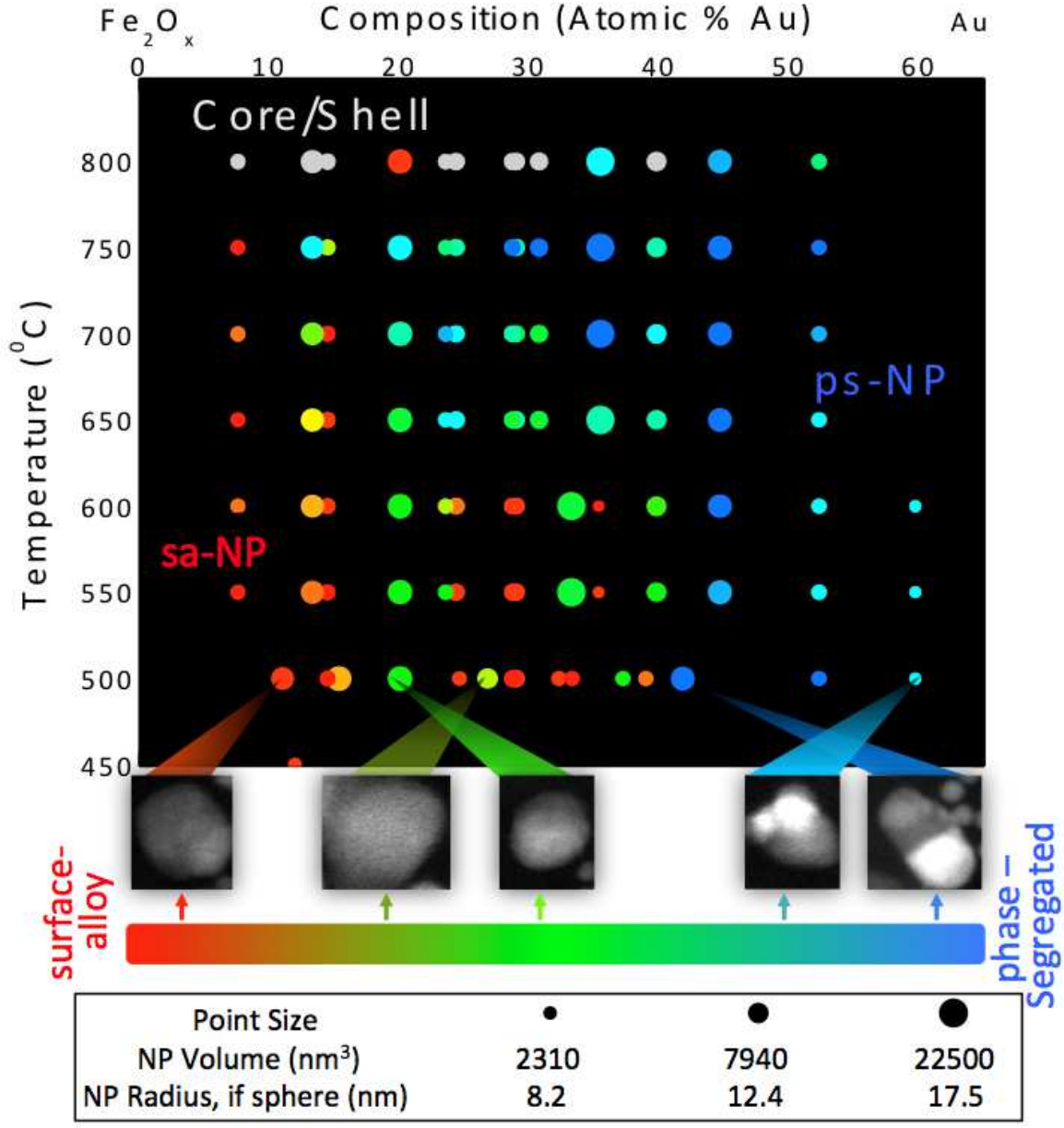

Fig. 4. A phase diagram of composite particles made of Fe_2O_3 and Au. Each point corresponds to a specific particle present in the video data. The composition is estimated by observing fusion events in the real time video. The color of the data point corresponds to its degree of phase segregation, as estimated by the standard deviation of the contrast within the particle. The size of the point is proportional to the cubed root of the number of atoms estimated to be within the particle.

The phase diagram illustrates a number of important trends. The sa-NPs with uniform image contrast are generally more common with lower gold content (*i.e.*, towards the left of the phase diagram) and at lower temperatures. Phase segregation appears to be more likely in larger fused particles compared to smaller particles with similar overall composition. This trend is corroborated by basic geometric arguments of the isochoric core/shell mode detailed in the supplementary materials. For a given composition, larger particles formed by the fusion of multiple Fe_2O_3 and Au NPs will exhibit a relatively thicker shell. Comparison of the experimental data summarized in the phase diagram (Fig.4) and the theoretical model suggest that a shell thickness of approximately 2 nm is required to observe phase segregation in heterogeneous NPs. To the best of our knowledge, this is the first observation and analysis of analogous Stranski–Krastanov growth on the surface of spherical NPs (see supporting information, Fig. S9).

The formation of sa-NPs naturally leads to questions about the chemical and structural nature of the heterogeneous NP surface. We investigated the core electron-bonding environment of the Fe atoms within the alloy using electron energy loss spectroscopy (EELS) (Fig.5a-c). We acquired EELS spectra of Au, Fe_2O_3, sa-NP, and ps-NPs at 550^0C (see supplementary materials, Fig.S15, S16). While the Au signature is too broad to reveal fine structure, the Fe-L edge signal confirmed the hematite-like valence of the Fe_2O_3 particles. In sa-NPs, we observed a 0.4 eV redshift in the Fe-L_3 peak and a 1.0 eV redshift in the Fe-L_2 peak, indicating an overall reduction in the Fe oxidation state upon alloying. The ps-NPs displayed similar shifts in the Fe-L edge absorptions at the gold rich edges of the particle compared to the gold deficient sections. EELS data confirm that the formation of sa-NPs causes a change in the chemical and bonding environment of the Fe atoms compared to pure Fe_2O_3, resulting in an average decrease in the Fe oxidation state.

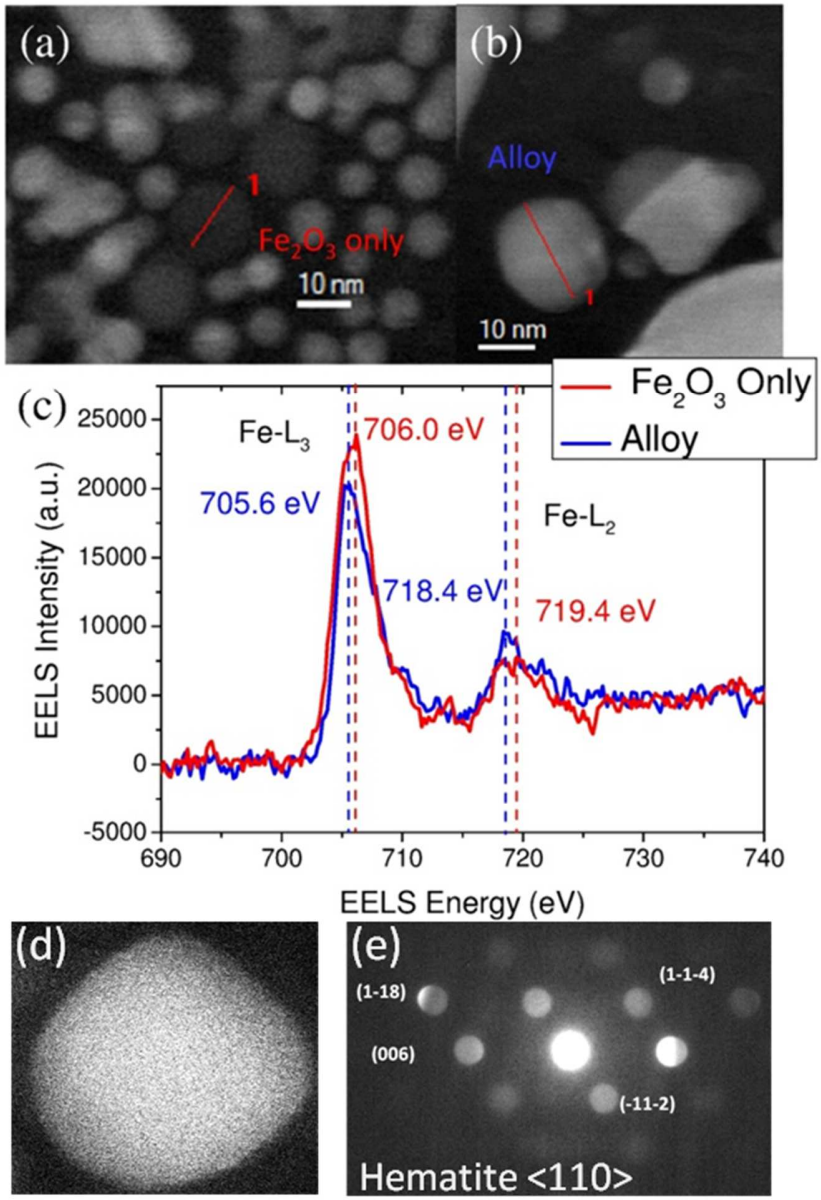

Fig. 5. *In-situ* EELS and nanodiffraction at 550 ^{0}C. (a) STEM image of an Fe_2O_3 particle. (b) STEM image of a sa-NP. (c) Fe L edge EELS spectra of particles in (a) and (b). (d) STEM image of sa-NP. (e) Indexed diffractograms of particle (d). The spots index to the hematite <110> zone axis.

We applied STEM nanodiffraction to gain detailed insights into the structure of the NPs. Analysis of the diffraction patterns of sa-NPs revealed their crystalline hematite Fe_2O_3 structure with small strains in the angles or spacing of the diffraction disks (Fig.5d-e and supplementary materials Fig. S19). In the case of ps-NPs, we observed different diffraction patterns based on the region of the particle that was being measured. In addition, real-space atomic-resolution images also confirm that the products after the heterogeneous sintering – ps-NPs and core/shell NPs – still have crystalline structure, with no noticeable amorphous structure on any particle that is reasonably steady after the sintering (see supplementary materials, Fig. S18).

In-situ variable-temperature XRD measurements corroborated that the structural evolution of Au:Fe_2O_3 NPs described above is not unique to thin films on TEM supports but also occurs on thin films prepared on arbitrary substrates (see supplementary materials Fig. S6). XRD revealed hysteresis in reflection of the (104) spacing of the hematite crystal when cycled from ambient temperature to 1000˚C. Control experiments with neat hematite NPs showed no hysteresis. The lattice expansion relative to the bulk is attributed to a reduction of surface energy accompanying the formation evolution from surface-alloy, to phase-segregated and ultimately core/shell metamorphs detailed above. Interestingly, the Fe_2O_3 NPs contained a mixture of small domain hematite and maghemite crystals, which transformed into single crystal hematite between 500 and 550 °C (see supplementary materials Fig.S6). The maghemite-to-hematite phase transition may play a key role in the initiation of the NP fusion observed in our experiments. Further studies are required to test this conjecture.

Section 5.4. Conclusion

We have investigated the rich phase diagram of a binary NP assembly. In the Au/Fe_2O_3 system, we found that heterogeneous fusion readily occurred at elevated

temperatures, resulting in new crystalline particles with a surface-alloyed or phase-segregated morphology. Further increases in temperature caused nearly all sa-NPs to transform into ps-NPs, either through additional Au fusing with the particle or temperature induced segregation of the Au. As the temperature increased further, the NPs formed an unstable core/shell phase before sublimation within the vacuum. Using these data, we were able to produce the first ever individual-particle nano-sized binary phase diagram combining information on composition, temperature, and particle size. From this diagram we obtained information about the stable compositions and sizes of this new, bulk-forbidden phase and provided a blueprint for how to construct similar diagrams for new systems. These observations prompt many other exciting opportunities: What other phases might be possible, how might they be used, and what are the physical processes governing their formation? In answering these questions, the field is poised to greatly expand the functional materials library and broaden our knowledge of chemistry at the nanoscale.

REFERENCES

(1) Wang, X.; Zhuang, J.; Peng, Q.; Li, Y. A General Strategy for Nanocrystal Synthesis. *Nature* **2005**, *437*, 121–124.

(2) Murray, C.; Kagan, C.; Bawendi, M. Synthesis and Characterization of Monodisperse Nanocrystals and Close-Packed Nanocrystal Assemblies. *Annual Review of Materials Science* **2000**, *30*, 545–610.

(3) Derlet, P. Atomistic Simulations as Guidance to Experiments. *Scripta Materialia* **2003**, *49*, 629–635.

(4) Puntes, V.; Krishnan, K.; Alivisatos, A. Colloidal Nanocrystal Shape and Size Control: the Case of Cobalt. *Science* **2001**, *291*, 2115–2117.

(5) Yu, W. W.; Wang, Y. A.; Peng, X. Formation and Stability of Size-, Shape-, and Structure-Controlled CdTe Nanocrystals: Ligand Effects on Monomers and Nanocrystals. *Chem Mater* **2003**.

(6) Xia, Y.; Xiong, Y.; Lim, B.; Skrabalak, S. E. Shape-Controlled Synthesis of Metal Nanocrystals: Simple Chemistry Meets Complex Physics? *Angew Chem Int Edit* **2009**, *48*, 60–103.

(7) Podsiadlo, P.; Krylova, G.; Lee, B.; Critchley, K.; Gosztola, D. J.; Talapin, D. V.; Ashby, P. D.; Shevchenko, E. V. The Role of Order, Nanocrystal Size, and Capping Ligands in the Collective Mechanical Response of Three-Dimensional Nanocrystal Solids. *J Am Chem Soc* **2010**, *132*, 8953–8960.

(8) He, Y.; Miao, Y.; Li, C.; Wang, S.; Cao, L.; Xie, S.; Yang, G.; Zou, B.; Burda, C. Size and Structure Effect on Optical Transitions of Iron Oxide Nanocrystals. *Phys Rev B* **2005**, *71*, 125411.

(9) Luther, J. M.; Law, M.; Song, Q.; Perkins, C. L.; Beard, M. C.; Nozik, A. J. Structural, Optical, and Electrical Properties of Self-Assembled Films of PbSe

Nanocrystals Treated with 1,2-Ethanedithiol. *ACS Nano* **2008**, *2*, 271–280.

(10) Smith, A. M.; Nie, S. Semiconductor Nanocrystals: Structure, Properties, and Band Gap Engineering. *Accounts of Chemical Research* **2010**, *43*, 190–200.

(11) Gur, I.; Fromer, N.; Geier, M.; Alivisatos, A. Air-Stable All-Inorganic Nanocrystal Solar Cells Processed From Solution. *Science* **2005**, *310*, 462–465.

(12) Mcdonald, S. A.; Konstantatos, G.; Zhang, S.; Maiti, N.; Klem, E. J. D.; Levina, L.; Sargent, E. H. Solution-Processed PbS Quantum Dot Infrared Photodetectors and Photovoltaics. *Nat Mater* **2005**, *4*, 138–142.

(13) Li, J. J.; Wang, Y. A.; Guo, W.; Keay, J. C.; Mishima, T. D.; Johnson, M. B.; Peng, X. Large-Scale Synthesis of Nearly Monodisperse CdSe/CdS Core/Shell Nanocrystals Using Air-Stable Reagents via Successive Ion Layer Adsorption and Reaction. *J Am Chem Soc* **2003**, *125*, 12567–12575.

(14) Kim, J.; Kim, H. S.; Lee, N.; Kim, T.; Kim, H.; Yu, T.; Song, I. C.; Moon, W. K.; Hyeon, T. Multifunctional Uniform Nanoparticles Composed of a Magnetite Nanocrystal Core and a Mesoporous Silica Shell for Magnetic Resonance and Fluorescence Imaging and for Drug Delivery. *Angew Chem Int Edit* **2008**, *47*, 8438–8441.

(15) Milliron, D.; Hughes, S.; Cui, Y.; Manna, L.; Li, J.; Wang, L.; Alivisatos, A. Colloidal Nanocrystal Heterostructures with Linear and Branched Topology. *Nature* **2004**, *430*, 190–195.

(16) Mokari, T.; Banin, U. Synthesis and Properties of CdSe/ZnS Core/Shell Nanorods. *Chem Mater* **2003**, *15*, 3957–3962.

(17) Du, J.; O'Reilly, R. K. Anisotropic Particles with Patchy, Multicompartment and Janus Architectures: Preparation and Application. *Chemical Society Reviews* **2011**, *40*, 2402–2416.

(18) Zhu, H.; Song, N.; Lian, T. Wave Function Engineering for Ultrafast Charge Separation and Slow Charge Recombination in Type II Core/Shell Quantum Dots. *J Am Chem Soc* **2011**, *133*, 8762–8771.

(19) Zhang, L.; Blom, D. A.; Wang, H. Au–Cu 2O Core–Shell Nanoparticles: a Hybrid Metal-Semiconductor Heteronanostructure with Geometrically Tunable Optical Properties. *Chem Mater* **2011**, *23*, 4587–4598.

(20) Schubert, M. M.; Plzak, V.; Garche, J.; Behm, R. J. Activity, Selectivity, and Long-Term Stability of Different Metal Oxide Supported Gold Catalysts for the Preferential CO Oxidation in H2-Rich Gas - Springer. *Catalysis Letters* **2001**, *76*, 143–150.

(21) Andreeva, D.; Tabakova, T.; Idakiev, V.; Christov, P.; Giovanoli, R. Au/A-Fe 2 O 3 Catalyst for Water–Gas Shift Reaction Prepared by Deposition–Precipitation. *Applied Catalysis A: General* **1998**, *169*, 9–14.

(22) Li, C.; Chen, T.; Ocsoy, I.; Zhu, G.; Yasun, E.; You, M.; Wu, C.; Zheng, J.; Song, E.; Huang, C. Z.; et al. Gold-Coated Fe 3O 4Nanoroses with Five Unique Functions for Cancer Cell Targeting, Imaging, and Therapy. *Adv. Funct. Mater.* **2013**, n/a–n/a.

(23) Junggoo Lee, J. L. T. T. A. H. M. In Situatomic-Scale Observation of Melting Point Suppression in Nanometer-Sized Gold Particles. *Nanotechnology* **2009**, *20*, 475306.

(24) Voorhees, P. W. The Theory of Ostwald Ripening. *J Stat Phys* **1985**, *38*, 231–252.

(25) Jesson, D. E.; Pennycook, S. J. Incoherent Imaging of Crystals Using Thermally Scattered Electrons. *Proc R Soc Lon Ser-A* **1995**, *449*, 273–293.

(26) Park, H.-Y.; Schadt, M. J.; Wang; Lim, I.-I. S.; Njoki, P. N.; Kim, S. H.; Jang, M.-Y.; Luo, J.; Zhong, C.-J. Fabrication of Magnetic Core@Shell Fe

Oxide@Au Nanoparticles for Interfacial Bioactivity and Bio-Separation. *Langmuir* **2007**, *23*, 9050–9056.

(27) Chaurasia, H. K.; Voss, W. A. G. Ultra-Thin Conducting Films of Gold on Platinum Nucleating Layers. *Nature* **1974**, *249*, 28–29.

(28) Okamoto, H.; International, A. Phase Diagrams of Binary Gold Alloys; Asm Intl, 1987.

CHAPTER 6

TURNING ORR ACTIVITY VIA CONTROLLABLE DEALLOYING: A MODEL STUDY OF ORDERED CU_3PT/C INTERMETALLIC NANOCATALYSTS[*†]

Section 6.1. Introduction

Proton exchange membrane fuel cells (PEMFCs) have long been considered as a potential green alternative to internal combustion engines used in automotive and stationary applications due to the potential for high efficiencies (as they are not limited by the Carnot cycle) and zero carbon dioxide emissions, when hydrogen is the fuel.[1,2] One of the major limitations for commercialization of this technology is the high cost of Pt, which is used as the electrocatalyst in the anodes and cathodes of fuel cells. Numerous studies have been dedicated to screening more efficient electrocatalytic materials, especially for lowering the precious metal loading and improving the sluggish kinetics of the oxygen reduction reaction (ORR) at the cathode. Early studies focused on lowering cost and improving ORR activity by alloying Pt with some 3*d* transition metals (i.e. Pt-M alloys, where M=Fe, Co, Ni, V, etc.), [3-9] and the activities of these materials have been found to be about 2-4 times greater than pure Pt for the ORR[8, 10-14]. Other approaches have included Pt monolayer catalysts on nanoparticles of other metals or metal oxides,[15-17] and different single crystal planes, such as Pt(110)[18], Pt(100)[18], and $Pt_3Ni(111)$[19] etc.

---

[*] Deli Wang, Yingchao Yu, Huolin L. Xin, Robert Hovden, Peter Ercius, Julia A. Mundy, Hao Chen, Jonah H. Richard, David A. Muller, Francis J. DiSalvo, and Héctor D. Abruña, (2012), *Nano Letters*, 2012 (10) 5230. Copyright © 2012 American Chemical Society.

[†] D.W. and Y.Y. contributed equally to this work. D.W. and Y.Y. designed, performed and analyzed the majority data of the experiments presented. H.L.X, R.H., P.E. contributed to EELS and 3-D work. J.A.M., H.C. and J.H.R. contributed in analyzing the data. D.A.M., H.D.A. and F.J.D. guided the work.

Recently, dealloyed Pt bimetallic nanoparticles, especially Pt-Cu alloy nanoparticles, have attracted attention as electrocatalyts for the ORR.[20-25] It has been shown that by using electrochemical methods, Cu is removed from the alloy surface layers, forming a Pt-rich core-shell nanostructure, which exhibits enhanced ORR activity when compared to pure Pt nanoparticles.[22-24] Most previous studies have focused on Pt-based alloy nanoparticles, in which the lack of an ordered structure makes it more challenging to produce a specific atomic-level morphology and surface structure.[26, 27] Here we explore ordered intermetallic Cu_3Pt/C nanoparticles as a promising type of a low Pt-content electrocatalyst, which can be prepared using a simple impregnation-reduction method followed by a high temperature post-treatment. Two dealloying methods were examined to enhance the ORR activity—namely, electrochemical and chemical leaching. The morphology and atomic-scale elemental distribution of the as-prepared and dealloyed nanoparticles were determined using atomic-resolution electron energy loss spectroscopic (EELS) imaging in a 5^{th}-order aberration-corrected scanning transmission electron microscope (STEM) equipped with an electron energy loss spectrometer (EELS). Using atomic-scale EELS mapping, we found that both Pt and Cu are distributed relatively uniformly in the as-prepared particles, and that the surfaces do not show significant preferential segregation. After electrochemical dealloying, a ~1 nm Pt-rich shell is formed enclosing an ordered Cu_3Pt intermetallic core. The ordered core strains the Pt shell, which is known to enhance the electrocatalytic activity towards the ORR.[7] Unlike electrochemical dealloying, however, chemical leaching gave rise to a ‘spongy’ structure with no apparent remaining ordered intermetallic structure, which was further verified by a 3-D tomographic reconstruction. This study reveals the correlations among the dealloying treatments, the resulting atomic-scale chemical structure and ORR activity.

Section 6.2. Materials and Methods

Carbon-supported Cu_3Pt intermetallic nanoparticles with ten percent Pt by weight, 10wt%, were prepared via a two-step route (Figure S1.). First, the Cu_3Pt/C nanoparticles were pre-prepared using an impregnation-reduction method, in which the H_2PtCl_6 and $CuCl_2$ precursors (previously adsorbed on the Vulcan XC-72 support) were reduced under flowing H_2 in a tube furnace at 300 ^oC. The sample was then annealed at 1000 ^oC in a tube furnace under flowing H_2 to form an ordered intermetallic phase.

Section 6.3. Results and Discussions

Figure 1 shows the X-ray diffraction (XRD) patterns of the samples and the standard powder diffraction files (PDF). When annealed at 300 ^oC, two types of diffraction peaks were present: broad peaks with characteristic at 2θ values of 41, 48, 70 ^{o} and sharp ones at 2θ values of 43, 50, 74 ^{o}. The broad diffraction peaks were at higher angles, compared to pure Pt, because the lattice contracts when Cu atoms are incorporated into the Pt lattice to form a $PtCu_x$ alloy. The sharp diffraction peaks, corresponding to metallic Cu, indicate that not all of the Cu was alloyed with Pt under the experimental conditions employed. On the other hand, the single phase, ordered intermetallic Cu_3Pt, formed after the as-prepared $PtCu_x$-Cu/C nanoparticles were heat-treated at 1000^{o}C (Figure 1). The XRD pattern showed pronounced (100) and (110) super-lattice peaks, characteristic of a well-ordered, intermetallic phase, and all the diffraction peak positions were consistent with the standard PDF card of the Cu_3Pt intermetallic phase (PDF card #03-065-3247). We also performed an *in-situ* TEM heating experiment to monitor changes to the as prepared (at 300 ^oC) $PtCu_x$-Cu nanoparticles upon annealing at higher temperatures (Figure S2). After heating at 1000 ^oC, the large Cu particles decreased in size and disappeared, while the smaller particles of $PtCu_x$ grew concomitantly larger.

EDX and EELS elemental mapping are invaluable tools for understanding the composition and morphology of Pt-bimetallic nanoparticles.[22, 28-31] Figures 2a-b show the STEM-EELS images of a Cu_3Pt/C nanoparticle, while the EELS mappings of Cu and Pt are shown in Figures 2b-d. The images indicate that there is no phase segregation of Cu and Pt in the core, while one to two monolayers of Cu are

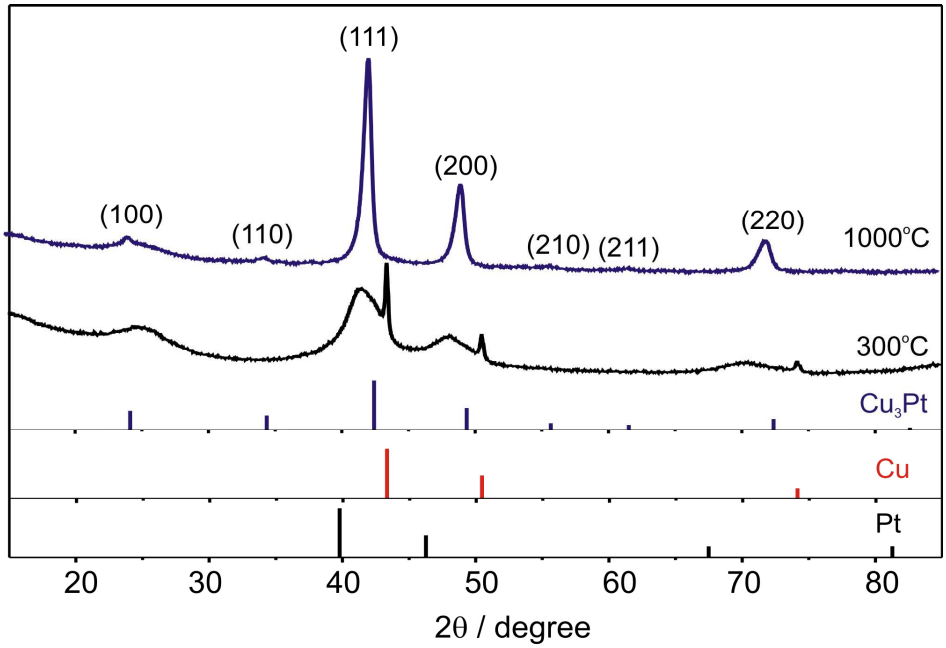

Figure 1. XRD patterns of Cu_3Pt/C prepared at 300ºC and after 1000ºC heat-treatment. Below are the peak positions of standard pure metallic Pt, Cu and intermetallic Cu_3Pt.

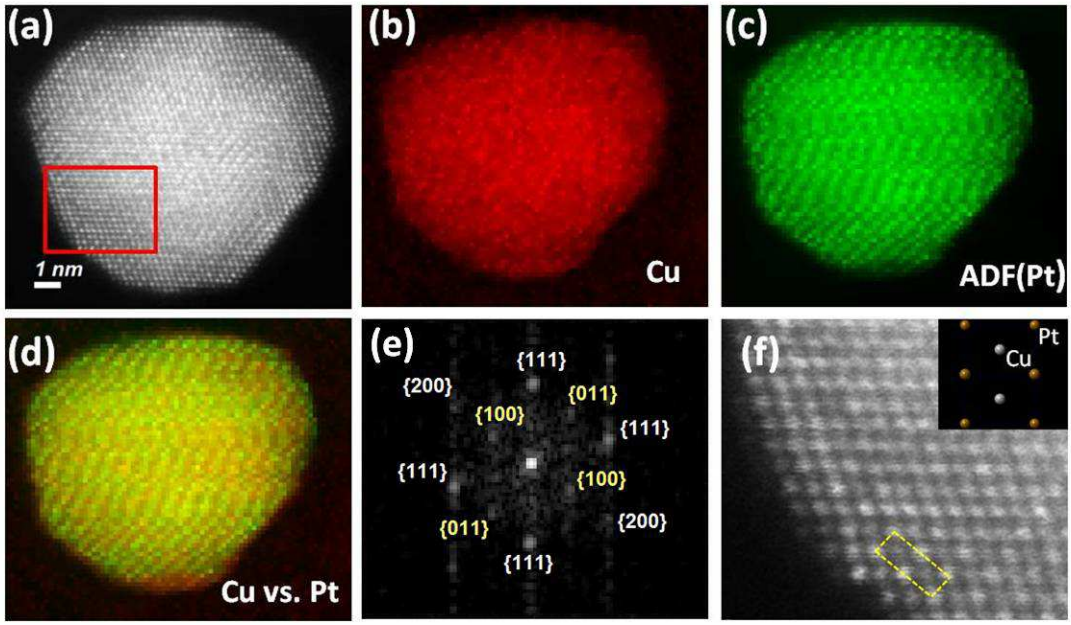

Figure 2. (a) ADF-STEM images of a [011] oriented Cu_3Pt/C intermetallic nanoparticle; (b) 2-D EELS map of Cu-$L_{2,3}$ edge; (c) Simultaneously recorded ADF image, which represents signals from Pt due to 'Z-contrast'; (d) Composite Cu vs. Pt map, showing a homogenous distribution of Pt and Cu; (e) FFT of (a), with {100} peak indicating formation of intermetallic structure; (f) A crop of the super lattice feature from (a), with four Pt atoms (brighter) around each Cu atom (darker). The matching theoretical model of ordered intermetallic Cu_3Pt is shown in the inset of (f).

segregated on four facets, while others are Pt-Cu alloy terminated. Evidence of Cu on the surface could also be found in the CV (cyclic voltammetric) testing in Figure 3a, *vide infra*. The FFT analysis (Figure 2e) exhibited three groups of diffraction peaks, {111}, {100}, and {200} which are in agreement with the XRD results. The strong intensity of the {100} and {110} peaks is evidence of the existence of an ordered structure across the selected region. The 'Z-contrast' image obtained with an annular dark field (ADF) was used to differentiate between columns of Pt and Cu atoms in appropriately oriented particles. The ADF detector collects elastically scattered electrons with an intensity that is 5-7 times higher for Pt than for Cu, allowing the differentiation of Pt and Cu atoms based on the intensities in a ADF-STEM image.[32] The box in Figure 1f demonstrates that there are periodic square arrays of four Pt atoms around each Cu atom, which is consistent with the ordered structure (inset in Figure 2f). All of these observations unambiguously indicate the formation of ordered intermetallic Cu_3Pt nanoparticles.

Two methods were used to dealloy the Cu_3Pt/C intermetallic nanoparticles. In the first, the potential applied to the Cu_3Pt/C intermetallic nanoparticles was cycled between +0.05 V and +1.0 V (figures 3a-b). The first 5 cycles exhibited no clear hydrogen adsorption/desorption peaks between +0.05 and +0.3 V, indicating that the surface is not Pt-rich. In addition, at the second cycle, it was apparent that some Cu had dissolved into the solution during the first anodic scan, as indicated by the small bulk Cu oxidation peak at around +0.3 V, and the broad peak between +0.3 V to +0.9 V due to the under potential deposition of Cu. In the cathodic scan, Cu was re-deposited on the nanoparticles, as evidenced by the three peaks at +0.6 V, +0.35 V and +0.25 V. As the cycling continued, the Cu peaks gradually decreased and hydrogen adsorption/desorption features emerged, and became well-defined after 50 cycles, indicating that the surface had become Pt-rich. In addition, both the onset potential and

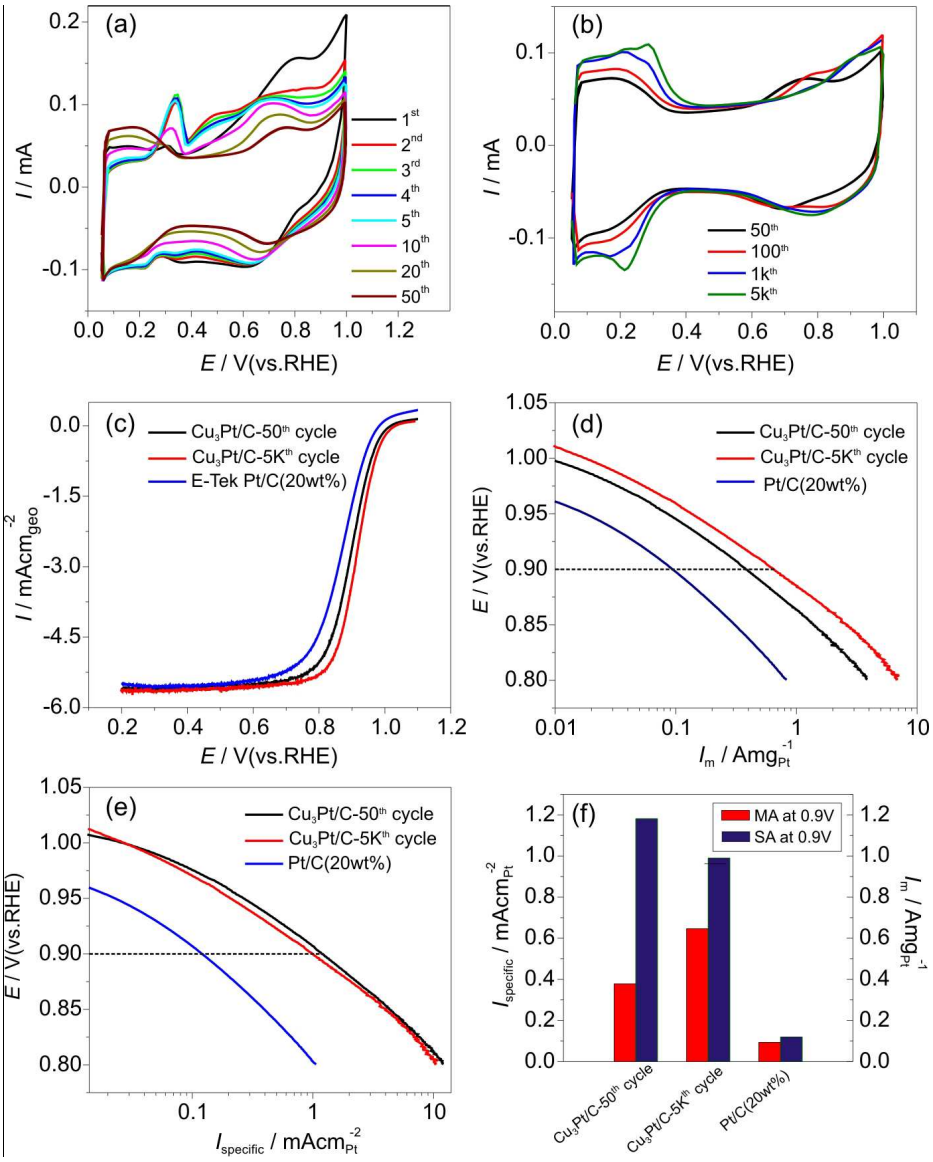

Figure 3. (a,b) Cyclic voltamograms of Cu_3Pt/C ordered intermetallic nanoparticles during electrochemical dealloying in 0.1 M $HClO_4$, at a scan rate of 50 mVs^{-1}. Color coded legends indicate the cycle number. (c) ORR polarization curves in O_2-saturated 0.1 M $HClO_4$ at a rotation rate of 1600 rpm and a scan rate of 5 mVs^{-1}, (d,e) Pt mass and area specific activities at +0.9V, respectively. (f) Summary of mass and specific activities for the ORR.

the peak potential of the Pt oxide reduction shifted in positive direction with cycling, reflecting a decrease in the adsorption strength of the oxygen-containing species on the electrode surface, which is key for enhancing the ORR activity. [33, 34]

After rinsing the electrode and placing it in fresh, O_2-saturated electrolyte, the electrocatalytic activity for ORR of electrochemically dealloyed Cu_3Pt/C intermetallic nanoparticles was investigated by linear sweep voltammetric (LSV) scans using a rotating disk electrode (RDE) (Figure 3c). Compared to Pt/C catalyst nanoparticles, the ORR polarization curves of dealloyed Cu_3Pt/C intermetallic nanoparticles exhibited onset and half wave potentials that were 40 mV more positive after 50 potential cycles, and even more positive (for a total about of 50 mV) after 5,000 cycles. The Pt mass activity at +0.9 V was determined to be 0.38 and 0.65 A/mg_{Pt} after 50 and 5,000 cycles, respectively. These values are about five and seven times higher than that of the Pt/C catalyst (Figure 3d, f). The specific activity (current per unit surface area of Pt as determined by hydrogen adsorption) also showed a one order of magnitude increase (Figure 3e) relative to Pt/C. The current density was obtained by normalizing the kinetic current to the Pt surface area which was calculated by integrating the coulometric charge associated with the adsorption and desorption of hydrogen between +0.05 and +0.40 V, using a conversion factor of 200 μCcm^{-2} for the adsorption of a monolayer of hydrogen (The value of 200 μCcm^{-2} was recently proposed by Feliu et al.[35, 36]). Such enhanced activity could be ascribed to two reasons (1) the formation of a large number of active sites after dealloying (Figure 3b) and (2) the modification of the electronic structure of Pt. Both effects would affect the bonding energy between Pt and oxygen-containing species (Figure 3b).

Figures 4a-b show a pair of overview STEM images of Cu_3Pt/C intermetallic nanoparticles after electrochemical dealloying. The images show that a majority of the particles are still well-dispersed on the carbon support. One representative

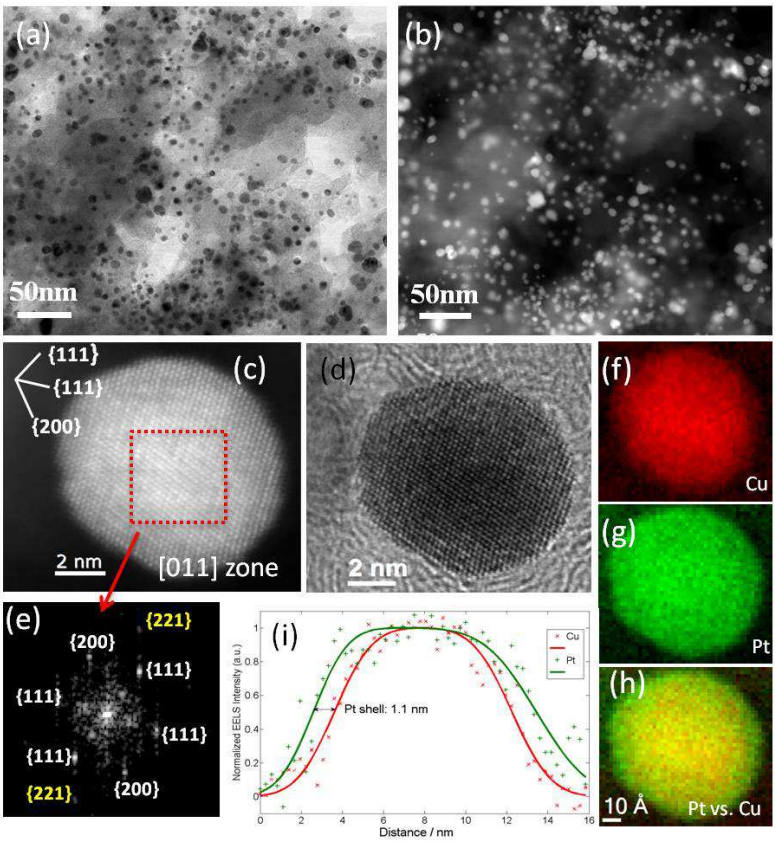

Figure 4. (a,b) BF and ADF-STEM overview images of Cu_3Pt/C intermetallic nanoparticles after electrochemical dealloying; (c,d) Atomic-resolution HAADF-STEM and BF images of one nanoparticle along [011] zone axis, showing an ordered intermetallic structure in the highlighted region; (e) FFT of highlighted area from (c), with superlattice peaks in red; (f) EELS mapping of Cu $L_{2,3}$ edge; (g) EELS mapping of Pt N_3 edge, after 20 iterations of MCR (multivariate curve resolution) analysis (a comparison on the reliability of such method is in figure S6); (h) Combination of (f) and (g), showing Pt shell; (i) Line profiles of Pt and Cu, with a quantitatively determined 1.1 nm Pt shell.

nanoparticle was investigated by atomic resolution imaging (figures 4c-d). The intermetallic core structure was preserved after the electrochemical dealloying treatment, as seen from the ADF-STEM images (figures 4c-d), and the FFT indicates the presence of superlattice peaks such as {221} (figure 4e). The surface of this nanoparticle is Pt-rich, as demonstrated by EELS mapping (Figures 4f-h), and consistent with the cyclic voltammetric measurements. Since the Cu-$L_{2,3}$ edge has very distinct features and an abrupt onset, a linear combination of power-law background subtraction method was used[37] (Figure 4f) to separate out the Cu edge. On the other hand, the delayed onset for Pt-N and Pt-M edges is highly sensitive to errors in the power-law background subtraction. To map Pt concentrations accurately (Figure 4g), the MCR (multivariate curve resolution) method was carried out on the Pt-N edge (the evaluation of such method is presented in Figure S6 and can also be found in a previous publication[28]). This method enables a clear determination of the Pt-shell thickness to be about 1 nm (Figure 4i).

Chemical dealloying of the Cu_3Pt/C ordered intermetallic nanoparticles was carried out by immersing the sample in 1 M HNO_3 for 2 days under continuous magnetic stirring. XRD showed that after chemical dealloying, all the peaks became weaker and their peak positions shifted to lower angles, although still not as low as the peak positions of pure Pt (Figure S3), indicating the partial, but not total, removal of the Cu from the bulk of the Cu_3Pt/C ordered intermetallic nanoparticles. The super lattice peaks characteristic of the ordered intermetallic structures at around 24^o and 34^o are almost invisible, indicating that a disordered Pt_xCu alloy formed after chemical dealloying. The overview of BF and ADF-STEM images (Figures 5a) show that the particles are well distributed on the carbon support. The speckle patterns in the Z-contrast (ADF-STEM) images (Figures 5a (right) and 5b) of the chemically dealloyed particles indicate that the particles may have developed a porous structure. However,

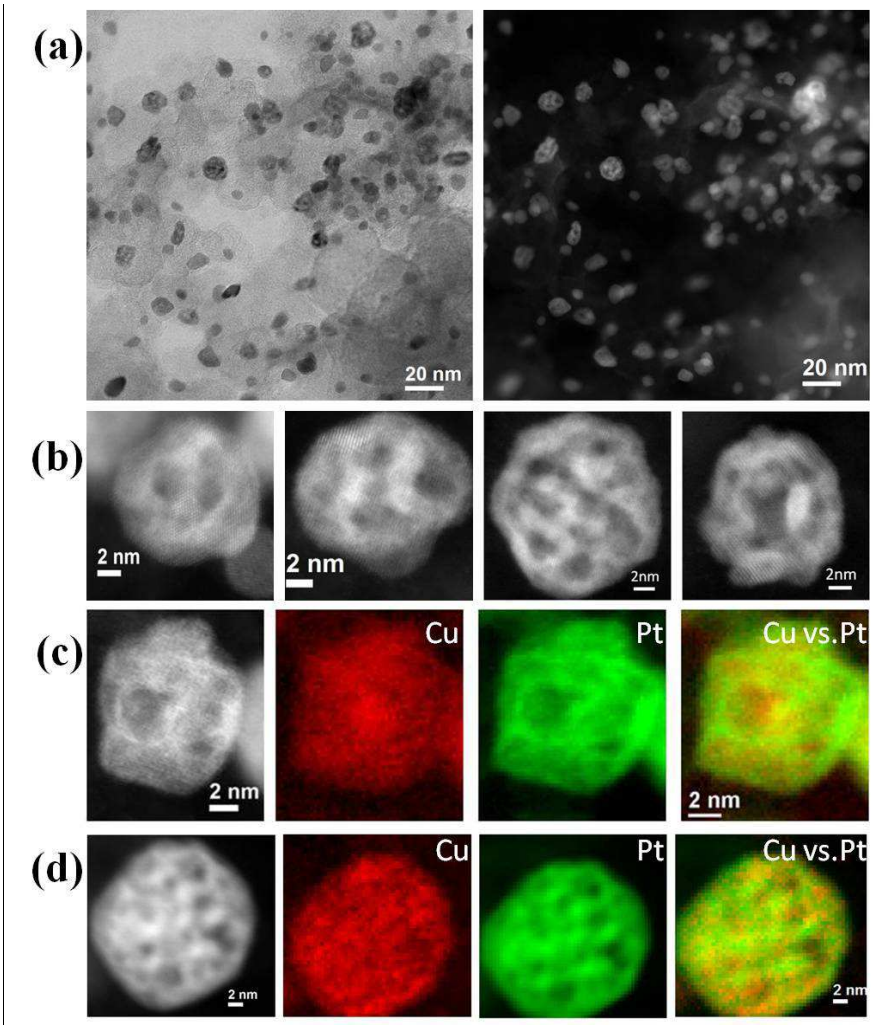

Figure 5. (a) BF (left) and ADF-STEM (right) overview images of Cu_3Pt/C intermetallic nanoparticles after chemical dealloying; (b) Atomic-resolution BF-STEM image of four 'spongy' nanoparticles; (c,d) EELS mapping of Cu $L_{2,3}$ edge and simultaneously recorded Pt $M_{4,5}$ edges and combination of Cu and Pt maps, showing two nanoparticles of approximately 10 and 20 nm, respectively.

the origin of the dark spots in the projected Z-constrast images could either reflect Cu-rich volumes (Cu scatters less than Pt) or voids/divots (deficiency of both Pt and Cu). The presence of Cu-rich volumes, nonetheless, can be excluded by our chemical mapping of the particles (Figure 5c and d). From a comparison of the Z-contrast dark spots and the Cu and Pt elemental maps, there does not appear to be any correlation. Thus, although a bit speculative on our part, we believe that the dark features in the image represent voids in the naoparticles, consistent with a spongy structure. To directly visualize the three-dimensional porous network formed after chemical dealloying, we performed ADF-STEM 3-D tomography of 'spongy' nanoparticles. The reconstructed porous structures are visualized in Figure 6. Two differential viewing angles are provided (Figures 6a,b) with two arrows indicating channels connecting to the exterior surfaces. The internal porous network is visualized from consecutive cross-sectional images through the 3-D reconstruction of the nanoparticle (Figure 6c). It demonstrates the internal nanoporosity of the nanoparticles and a dramatic increase in the surface-to-volume ratio after the chemically dealloying process. The formation of the 'spongy' structures is likely due to the Kirkendall effect—the diffusion rates of Pt and Cu are different in the alloy—similar to the previously reported hollow-structure formation.[38]

To evaluate the effects of size on the morphology of chemically dealloyed nanoparticles,[39] we analyzed the size distributions of 'spongy' nanoparticles (Figure 7). Since only a fraction of the nanoparticles are on the same focal plane from the HAADF-STEM image (Figure 5a), analyzing nanoparticles from these images will introduce inaccuracies, especially when many of the pores are almost invisible, if not on focus. Therefore, we have carried out an experiment in which we take 34 consecutive images at different defocus; a procedure that has been previously reported to be more accurate for analyzing nanoparticle size distribution.[40] By extend depth of

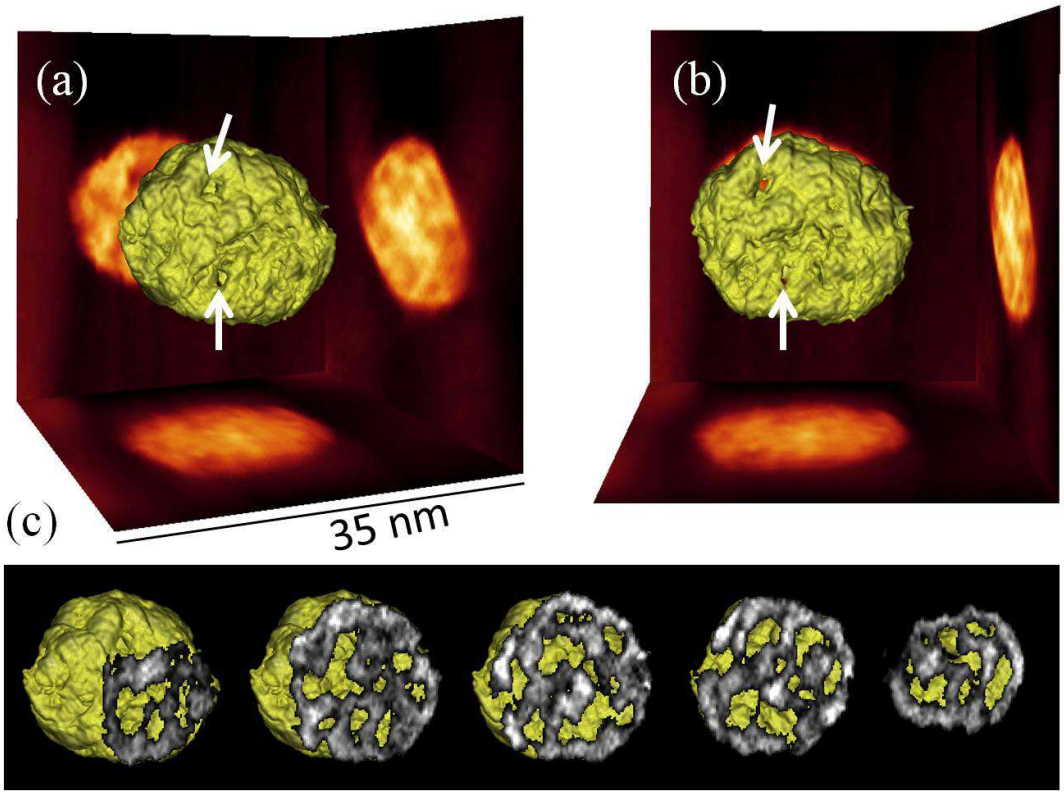

Figure 6. (a,b) 3-D tomographic reconstruction of a chemically dealloyed nanoparticle ('spongy'), at two different viewing directions. The arrows indicate channels connecting to the exterior surfaces. (c) A series of consecutive slices through the isosurfaces of such nanoparticle, showing the porous networks.

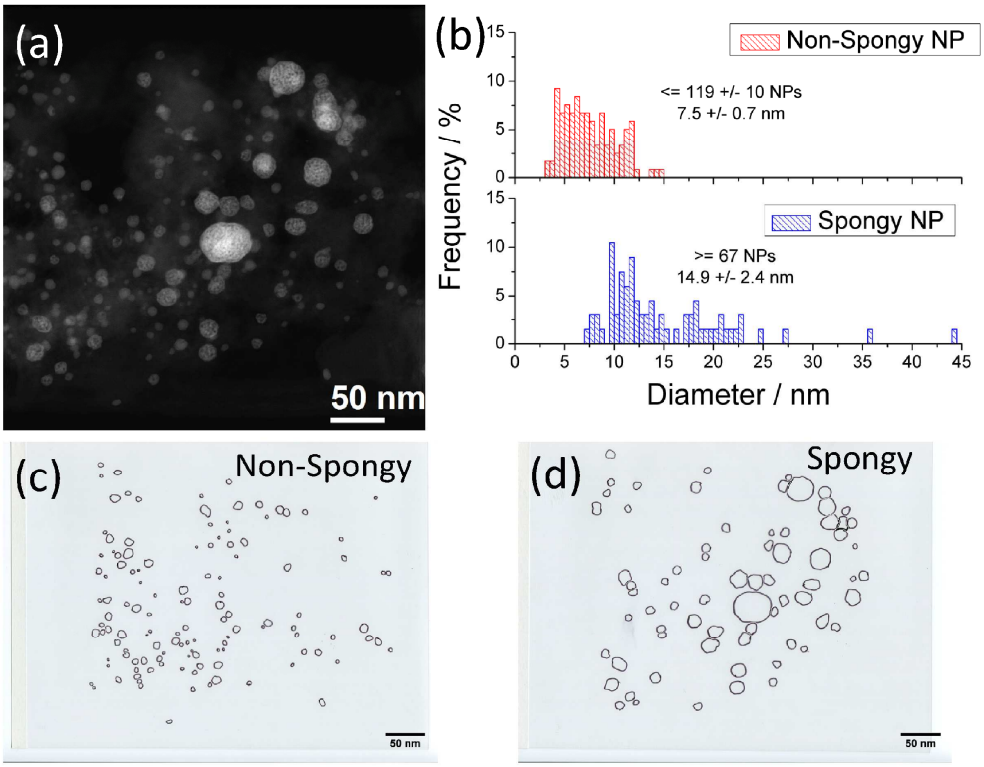

Figure 7. (a) Extend depth of field reconstruction of 34 through-focal series of the dealloyed spongy Pt-Cu nanoparticles, with most nanoparticles reconstructed at the same focal plane; (b) Size distributions of non-spongy and spongy nanoparticles, with error bars of mean diameter corresponding to three standard errors of the mean; (c)-(d) Masks for analyzing the size distribution. Each of the 34 through-focal frames is checked to categorize the spongy and non-spongy nanoparticles. However, due to the limitation of spatial resolution, we cannot eliminate errors of placing spongy ones into the non-spongy category. Therefore, we report the upper limit of non-spongy nanoparticles and the lower limit of spongy nanoparticles, assuming the confidence interval in the number of non-spongy nanoparticles is dominated by Poisson counting statistics. It is clear that larger nanoparticles are more likely to form a spongy structure.

field reconstruction,[41] most nanoparticles are present on the same focal plane (Figure 7a). The size distribution of such an image is shown in Figure 7b, where the 'non-spongy' nanoparticles have a mean diameter of 7.5 ± 0.7 nm while the 'spongy' ones are 14.9 ± 2.4 nm. We checked the accuracy of the method by hand-segmentation of non-spongy and spongy particles separately (Figure 7c-d). However, due to the limitation of spatial resolution, it is possible that we might pick (place) some 'spongy' ones into the 'non-spongy' category. The analysis of such error is propagated by reporting the upper bound of the number of 'non-spongy' ones and the lower bound for the 'spongy' ones. As Figure 5a shows, after chemically dealloying, only the larger size nanoparticles have evolved into porous structures, while most smaller ones remain 'non-spongy'. In the case of Pt-Cu binary materials, since Cu is more soluble than Pt upon electrochemical cycling, a vacancy is expected in the bulk, if a Pt-rich shell is formed on the surface, so as to slow further diffusion. A 'spongy' structure could evolve when the etching rate of Cu is comparable to the surface diffusion rate of Pt.[28, 42] However, if the diffusion length (where Pt is redeposited on the surface) is larger than the particle size, a 'spongy' structure would not be expected.[28, 39, 42] This explains why many smaller nanoparticles have remained 'non-spongy' after chemical dealloying, and in turn, illustrates the importance of using through-focal ADF-STEM imaging series and EELS mapping to confirm the existence of porous structures. Similar results have been recently reported in a study of the size dependence of structure and morphology in dealloyed bimetallics in which it was shown that nanopores or hollows were not observerd when the particle size was below 5 nm, while multiple core-shell structures formed when the particle size ranged up to 20 nm.[39]

We compared the ORR activity of 'spongy' Pt_xCu/C nanoparticles with Pt/C. As shown in Figure 8, the as-prepared 'spongy' particles (denoted as the "no cycling" sample) exhibited higher onset and half wave potentials than pure Pt. The half-wave potential was about 50 mV more positive than Pt. It has been reported that such hollow structures are not stable under fuel cell operating conditions.[38,43] However, after 50 cycles, the ORR mass activity of the 'spongy' nanoparticles grew by a factor of 1.6; and was even slightly higher after 5,000 cycles. These data suggest that by tuning the atomic and/or electronic structures, one can achieve improved electrocatalytic activity for the ORR (Figure 8a). The CVs (Figure 8b) reveal a large hydrogen adsorption/desorption region in the first cycle, but without well-resolved peaks. The hydrogen peaks decreased in amplitude with potential cycling, but were almost constant after 50 cycles. In addition, two well-defined peaks appeared, indicating the presence of several Pt surface structures. This suggests that the Pt surface structure was established from the topmost layers during potential cycling. Chemical leaching gave rise to disordering of the previously ordered intermetallic nanoparticles so that the resulting surfaces would be anticipated to have more defects such as steps and kinks. With electrochemical cycling, Pt atoms associated with these defects might be able to re-arrange due to electrochemical dissolution and re-deposition, which may explain the appearance of the well-defined hydrogen adsorption/desorption features. This phenomenon might also lead to a change in the adsorption of oxygen-containing species and affect the ORR activity accordingly. The mass activities at +0.90 V of the 'spongy' nanoparticles were found to be 0.35, 0.58 and 0.64 Amg^{-1}_{Pt} with no potential cycling, after 50 cycles and 5,000 cycles, respectively. The corresponding specific activities were measured to be 0.38, 0.91, and 1.1 $mAcm^{-2}_{Pt}$. The 'spongy' structures were stable even after 5,000 potential cycles, which can be seen from the STEM images (Figure S4) showing that most of the

‘spongy’ structures were preserved after 5,000 potential cycles. The chemically leached nanoparticles exhibited better electrocatalytic activity, just after leaching, than the electrochemically treated nanoparticles after 50 cycles, as can be ascertained from Figure S5. The half-wave potential of the ‘spongy’ product was about 20 mV more positive than the electrochemically leached product (Figure S5) and the mass activity at 0.9 V was about 1.5 times higher, although the specific activity is slightly less (Figure S5).

The higher mass activity of chemically dealloyed nanoparticles (‘spongy’) could be attributed, at least in part, to the increased surface area resulting from nano-voids formed after chemical leaching. We have investigated the nature of such enhancement from two aspects. First, by comparing the CVs presented in figures 3b and 8b, we can see that the areas corresponding to hydrogen adsorption/desorption regions are higher for chemically dealloyed nanoparticles than for electrochemically dealloyed ones, indicating that the chemically dealloyed samples present a higher electrochemical surface area (ECSA). Second, we performed high-resolution chemical mapping and 3-D reconstruction of the chemically dealloyed nanoparticles (Figure 5 and Figure 6). The results showed that the nanoparticles developed a nonporous structure after chemical dealloying. This porous structure dramatically increased the surface-to-volume ratio which, in turn ,increased the electrocatalytic activity towards the ORR.

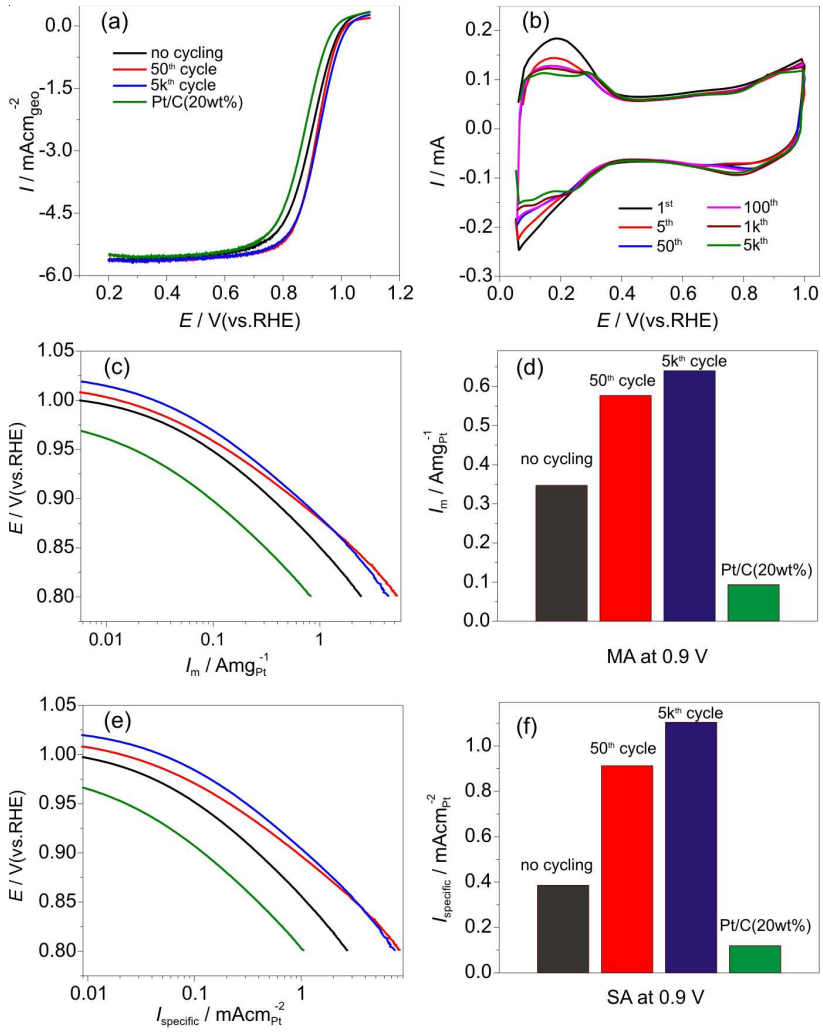

Figure 8. (a) ORR polarization curves of chemically leached nanoparticles after different potential cycles (0.05-1.0 V vs. RHE) in O_2-saturated 0.1 M $HClO_4$, at a rotation rate of 1600 rpm and a scan rate of 5 mVs^{-1}. (b) Cyclic voltammograms of chemically leached nanoparticles after different potential cycles (0.05-1.0 V vs. RHE) in 0.1 M $HClO_4$, at a scan rate of 5 mVs^{-1}. Color coded legend indicates the cycle number. (c,d) Pt mass activities for the ORR at +0.9 V. (e,f) Specific activities for the ORR at +0.9 V.

Section 6.4. Conclusion

In conclusion, ordered Cu_3Pt intermetallic electrocatalyst nanoparticles have been successfully prepared and electrochemically activated via two dealloying methods. Sub-Ångstrom resolution EELS-STEM imaging indicated that the electrochemical treatment resulted in a 3-5 monolayer Pt-rich shell, which enhanced the ORR activity. Furthermore, the chemically leached samples ('spongy' nanoparticles), showed both higher activity and durability for the ORR. Since most electrocatalysts yield a lower catalytic activity after extensive electrochemical aging, it is important to note that the 'spongy' nanoparticles behaved differently with their ORR activity actually improving by electrochemical cycling, at least up to 5,000 cycles. Without the aid of surfactants or capping ligands, the methods reported here offer morphology control and new opportunities for preparing durable, active and low Pt-loading electrocatalysts, which are crucial for the wide commercialization of PEMFCs.

Supporting Information Paragraph. More experimental details, material characterizations, additional figures (Figures S1-S6). This material is available free of charge via the Internet at http://pubs.acs.org.

REFERENCES

1. Debe, M. K. *Nat. Mater.* **2012,** 486, 9.
2. Steele, B. C. H.; Heinzel, A. *Nature* **2001,** 414, (6861), 345-352.
3. Wu, J. B.; Zhang, J. L.; Peng, Z. M.; Yang, S. C.; Wagner, F. T.; Yang, H. *J. Am. Chem. Soc.*

   2010, 132, (14), 4984-4985.
4. Maillard, F.; Dubau, L.; Durst, J.; Chatenet, M.; Andre, J.; Rossinot, E. *Electrochem. Commun.*

   2010, 12, (9), 1161-1164.
5. Jeon, M. K.; Zhang, Y. A.; McGinn, P. J. *Electrochim. Acta* **2010,** 55, (19), 5318-5325.
6. Bogdanovskaya, V. A.; Tarasevich, M. R.; Kuznetsova, L. N.; Zhutaeva, G. V.; Lozovaya, O. V.

   Russ. J. Electrochem. **2010,** 46, (8), 925-933.
7. Qian, Y. D.; Wen, W.; Adcock, P. A.; Jiang, Z.; Hakim, N.; Saha, M. S.; Mukerjee, S. *J. Phys.*

   Chem. C **2008,** 112, (4), 1146-1157.
8. Yano, H.; Kataoka, M.; Yamashita, H.; Uchida, H.; Watanabe, M. *Langmuir* **2007,** 23, (11),

   6438-6445.
9. Antolini, E.; Salgado, J. R. C.; Gonzalez, E. R. *J. Power Sources* **2006,** 160, (2), 957-968.
10. Mukerjee, S.; Srinivasan, S.; Soriaga, M. P.; McBreen, J. *J. Phys. Chem.* **1995,** 99, (13), 4577-

4589.

11. Malheiro, A. R.; Perez, J.; Villullas, H. M. *J. Electrochem. Soc.* **2009,** 156, (1), B51-B58.
12. Wang, C.; Wang, G.; van der Vliet, D.; Chang, K.-C.; Markovic, N. M.; Stamenkovic, V. R.

    Phys. Chem. Chem. Phys. **2010,** 12, (26), 6933-6939.
13. Wu, J.; Zhang, J.; Peng, Z.; Yang, S.; Wagner, F. T.; Yang, H. *J. Am. Chem. Soc.* **2010,** 132,

    (14), 4984-4985.
14. Antolini, E.; Passos, R. R.; Ticianelli, E. A. *Electrochim. Acta* **2002,** 48, (3), 263-270.
15. Adzic, R. R.; Zhang, J.; Sasaki, K.; Vukmirovic, M. B.; Shao, M.; Wang, J. X.; Nilekar, A. U.;

    Mavrikakis, M.; Valerio, J. A.; Uribe, F. *Top. Catal.* **2007,** 46, (3-4), 249-262.
16. Sasaki, K.; Adzic, R. R. *J. Electrochem. Soc.* **2008,** 155, (2), B180-B186.
17. Sasaki, K.; Zhang, L.; Adzic, R. R. *Phys. Chem. Chem. Phys.* **2008,** 10, (1), 159-167.
18. Stamenkovic, V.; Markovic, N. M.; Ross, P. N. *J. Electroanal. Chem.* **2001,** 500, (1-2), 44-51.
19. Stamenkovic, V. R.; Fowler, B.; Mun, B. S.; Wang, G.; Ross, P. N.; Lucas, C. A.; Markovic, N.M. *Science* **2007,** 315, (5811), 493-497.
20. Mani, P.; Srivastava, R.; Strasser, P. *J. Power Sources* **2011,** 196, (2), 666-673.
21. Oezaslan, M.; Strasser, P. *J. Power Sources* **2011,** 196, (12), 5240-5249.
22. Strasser, P.; Koh, S.; Anniyev, T.; Greeley, J.; More, K.; Yu, C.; Liu, Z.; Kaya, S.; Nordlund, D.;

    Ogasawara, H.; Toney, M. F.; Nilsson, A. *Nat.e Chem.* **2010,** 2, (6), 454-460.

23. Koh, S.; Strasser, P. *J. Am. Chem. Soc.* **2007,** 129, (42), 12624-12625.

24. Srivastava, R.; Mani, P.; Hahn, N.; Strasser, P. *Angew. Chem. Int. Ed.* **2007,** 46, (47), 8988-
8991.

25. Cui, C.; Li, H.-H.; Liu, X.-J.; Gao, M.-R.; Yu, S.-H. *ACS Catal.* **2012**, 462 (6), 916-924.

26. Casado-Rivera, E.; Volpe, D. J.; Alden, L.; Lind, C.; Downie, C.; Vázquez-Alvarez, T.; Angelo, C. D.; DiSalvo, F. J.; Abruña, H. D. *J. Am. Chem. Soc.* **2004,** 126, (12), 4043-4049.

27. Sanabria-Chinchilla, J.; Abe, H.; DiSalvo, F. J.; Abruña, H. D. *Surf. Sci.* **2008,** 602, (10), 1830-1836.

28. Xin, H. L.; Mundy, J. A.; Liu, Z.; Cabezas, R.; Hovden, R.; Kourkoutis, L. F.; Zhang, J.;
Subramanian, N. P.; Makharia, R.; Wagner, F. T.; Muller, D. A. *Nano Lett.* **2011,** 12, (1), 490-
497.

29. Wang, D.; Xin, H. L.; Yu, Y.; Wang, H.; Rus, E.; Muller, D. A.; Abruna, H. D. *J. Am. Chem.*
Soc. **2010,** 132, (50), 17664-17666.

30. Yu, Y. X., H. L.; Hovden, R.;Wang, D.; Rus, E.; Mundy, J. A.; Muller, D. A.; Abruna, H. D.
Nano Lett. **2011,** DOI: 10.1021/nl203920s.

31. Carlton, C. E.; Chen, S.; Ferreira, P. J.; Allard, L. F.; Shao-Horn, Y. *J. Phys. Chem. Lett.* 3, (2), 161-166.

32. Crewe, A. V.; Wall, J.; Langmore, J. *Science* **1970,** 168, (3937), 1338-1340.

33. Markovic, N. M.; Ross, P. N. *Surf. Sci. Rep.* **2002,** 45, (4-6), 121-229.

34. Mukerjee, S.; Srinivasan, S.; Soriaga, M. P.; McBreen, J. *J. Phys. Chem.* **1995,** 99, (13), 4577-
4589.
35. Vidal-Iglesias, F. J.; Aran-Ais, R. M.; Solla-Gullon, J.; Herrero, E.; Feliu, J. M. *Acs Catal.* **2011,**
2, (5), 901-910.
36. Chen, Q.-S.; Solla-Gullon, J.; Sun, S.-G.; Feliu, J. M. *Electrochim. Acta* **2010,** 55, (27), 7982-
7994.
37. Cueva, P., Hovden,R., Mundy, J. A., Xin, H. L., Muller, D. A. *Micros. Microanal.* **2012**, DOI:
http://dx.doi.org/10.1017/S1431927612000244.
38. Chen, H. M.; Liu, R.-S.; Lo, M.-Y.; Chang, S.-C.; Tsai, L.-D.; Peng, Y.-M.; Lee, J.-F. *J. Phys.*
Chem. C **2008,** 112, (20), 7522-7526.
39. Oezaslan, M.; Heggen, M.; Strasser, P. *J. Am. Chem. Soc.* **2011,** 134, (1), 514-524.
40. Hovden, R.; Xin, H. L.; Muller, D. A. *Micros. Microanal.* **2011,** 17, (01), 75-80.
41. Forster, B.; Van de Ville, D.; Berent, J.; Sage, D.; Unser, M. *Microsc. Res. Tech.* **2004,** 65, (1-2),
33-42.
42. Erlebacher, J.; Aziz, M. J.; Karma, A.; Dimitrov, N.; Sieradzki, K. *Nature* **2001,** 410, (6827),
450-453.
43. Peng, Z.; Wu, J.; Yang, H. *Chem.Mater.* **2010,** 22, (3), 1098-1106.

CHAPTER 7

STRUCTURALLY ORDERED INTERMETALLIC PLATINUM-COBALT CORE-SHELL NANOPARTICLES WITH ENHANCED ACTIVITY AND STABILITY AS OXYGEN REDUCTION ELECTROCATALYSTS[*†]

Section 7.1. Introduction

To enhance and optimize nanocatalyst performance and durability for the oxygen reduction reaction (ORR) in fuel cell applications, we look beyond Pt-Metal disordered alloys and describe a new class of Pt-Co nanocatalysts comprised of ordered Pt_3Co intermetallic cores with a 2-3 atomic-layer thick platinum shell. These nanocatalysts exhibited over 200% increase in mass activity and over 300% increase in specific activity when compared to the disordered Pt_3Co alloy nanoparticles as well as Pt/C. To date, this mass activity for the ORR is the highest among the Pt-Co systems reported in the literature under similar testing conditions. Stability tests showed a minimal loss of activity after 5,000 potential cycles and the ordered core-shell structure was maintained virtually intact as established by atomic-scale elemental mapping. The high activity and stability are attributed to the Pt-rich shell, and the stable intermetallic Pt_3Co core arrangement. These ordered nanoparticles provide a new direction for catalyst performance optimization for next-generation fuel cells.

---

[*] Produced with permission from Deli Wang1 Huolin L. Xin, Robert Hovden, Hongsen Wang, Yingchao Yu, David A. Muller, Francis J. DiSalvo and Héctor D. Abruña, *Nature Materials* 12, 81–87 (2013). Copyright © 2013 Nature Publishing Group

[†] D.W. and H.L.X. conceived and designed the experiments. D.W. performed synthesis and electrochemical characterizations. H.L.X. performed STEM and EELS mapping experiments. D.W. and H.L.X. wrote the manuscript with assistance from R.H. D.W. and H.L.X. contributed equally to this work. R.H. participated in analysis of the data. All authors discussed results and commented on the manuscript.

The sluggish kinetics of the oxygen reduction reaction (ORR) at the cathode is one of the key challenges for the commercial viability of proton exchange membrane fuel cells (PEMFCs)[1-4] especially for transportation applications. In this regard, it is of great interest to explore more active catalysts, with superior performance and durability, than the traditionally employed carbon supported Pt (Pt/C) nanoparticles. Considerable progress has been made on Pt-based bi- and tri-metallic electrocatalysts such as alloying Pt with 3d-transition metals, including Fe[5-10], Co[5, 11-15], Ni[5, 13, 14, 16, 17], Cu[18-20], Cr[13, 21]and Mn[22, 23] etc. Other approaches have included monolayer coating of Pt on suitable metal nanoparticles[24-26], and dealloying of binary/ternary nanocatalysts[18-20, 27]. Most recently, the use of perovskites[28], Co_3O_4 nanocrystals grown on graphene oxide[29], and carbon nanotube-graphene complexes[30] have been suggested. Among these catalysts, Pt-Co systems have received considerable attention because of their relatively high ORR activity[5] and stability in acidic environments[7, 31]. However,

previous studies have mainly focused on the disordered Pt-Co alloy catalysts, with only limited reports on structurally ordered intermetallic Pt-Co nanocatalysts[32, 33]. The lack of interest in the ordered phase can be attributed to the previously reported low activity of ordered Pt-Co catalysts[32] and concerns about particle sintering during the high temperature annealing that is generally necessary to obtain ordered phases. However, ordered intermetallic phases, with definite composition and structure, provide predictable control over structural, geometric, and electronic effects not afforded by the widely studied alloys[33-36]. Here, we demonstrate that core-shell structured Pt-Co nanoparticles, composed of Pt_3Co ordered intermetallic cores with 2-3-atomic-layer Pt

shells (Pt_3Co@Pt), can be prepared by a facile method. The Pt shell is strained to the ordered intermetallic core, which has an 0.8% smaller lattice constant than the disordered alloy. These particles exhibited the highest Pt mass activities for the ORR among Pt-Co systems reported in the literature under similar testing conditions (Supplementary Fig. S1) and with greatly enhanced durability, making them promising candidates for next generation PEMFCs.

Section 7.2. Materials and Methods

Sample preparation. The carbon supported Pt/C and Pt_3Co/C nanoparticles were prepared using an impregnation method. In a typical synthesis, 53.3 mg of $H_2PtCl_6 \cdot 6H_2O$ and 8.2 mg of $CoCl_2 \cdot 6H_2O$ were dissolved in deionized water, and 78 mg of Vulcan XC-72 carbon support were dispersed in it. After ultrasonic blending for 30 min, the suspension was heated under magnetic stirring to allow the solvent to evaporate and to form a smooth, thick slurry. The slurry was dried in an oven at 60 ^oC. After being ground in an agate mortar, the resulting dark and free-flowing powder was heated in a tube furnace at 150 ^oC under flowing H_2/N_2 for 2 h. Finally, the powder was cooled to room temperature under N_2. The as-prepared Pt_3Co/C catalysts were then annealed at 400 ^oC and 700 ^oC under an H_2 atmosphere for 2 h. These samples are denoted as Pt_3Co/C-400 and Pt_3Co/C-700, respectively.

Characterization. The as-prepared catalysts were characterized by powder X-ray diffraction using a Rigaku® Ultima VI diffractometer, and diffraction patterns were collected at a scanning rate of 5 ^{o}/min and with a step of 0.02 ^{o}. TEM was performed using

a Shottky-field-emission-gun Tecnai F20 operated at 200 kV. The electron energy loss spectroscopic (EELS) maps were acquired on a 5th-order aberration-corrected scanning transmission electron microscope (Cornell Nion UltraSTEM) operated at 60 kV (α_{max} = ~30 mrad). Under such conditions, a real space resolution of 1.3 Å[37] and a reciprocal space information transfer, up to 1.18 Å can be routinely achieved. The method of extracting Pt and Co maps from the EELS spectroscopic images are described in the previous publication[15]. The atomic-resolution annular dark-field STEM (ADF-STEM) images were recorded with this machine operated at 100 kV (α_{max} = 27.8 mrad). Sub-angstrom resolution is achievable at these operating conditions.

Particle size distributions were made from ADF-STEM images. Due to the limited depth of field of the aberration corrected microscope, extended depth of field techniques were used to obtain a single projection image with all particles in focus[38]. The particles were hand segmented to determine particle areas from the projection image and diameters were estimated by assuming a spherical particle geometry.

Electrochemical testing. Electrochemical experiments were carried out in 0.1 M $HClO_4$ at room temperature using a Solartron model 1280 B electrochemistry station employing the analog sweep mode. Working electrodes were prepared by mixing the catalyst with Nafion (0.05 wt % Nafion dissolved in ethanol) solution. The mixture was sonicated and about 5.0 µL were applied onto a glassy carbon disk. After solvent evaporation, a thin layer of Nafion-catalyst-Vulcan ink remained on the GC surface to serve as the working electrode. The Pt loading on the RDE was calculated as 17.7 μg_{Pt} cm^{-2}. A Pt wire was

used as the counter electrode and a reversible hydrogen electrode (RHE), in the same electrolyte as the electrochemical cell, was used as the reference electrode. All potentials are referred to RHE, and the readout currents were recorded without any iR drop correction during the measurements. Since we use a Luggin capillary type RHE, the ohmic drop in the solution is negligible. For the electrochemical surface area (ECSA) study, cyclic voltammetry (CV) was conducted over the potential range of +0.05 V to +1.00 V at a scan rate of 50 mVs^{-1} in 0.1 M $HClO_4$. ECSA values were calculated by integrating the area under the curve for the hydrogen adsorption/desorption region between +0.05 and +0.40 V for the reverse sweep in the CV and using a conversion factor of 200 μCcm^2, according to recent results from Feliu. [39, 40]. The oxygen reduction reaction (ORR) polarization curves were obtained by sweeping the potential from +0.20 to +1.10 V at a scan rate of 5 mV s^{-1} and at a rotation rate of 1600 rpm. The kinetic current (I_k) can be calculated using the Koutecky–Levich equation which is expressed by

$$I = \frac{1}{I_k} + \frac{1}{I_d} \quad (1)$$

where I is the measured current and I_d the diffusion limited current.

The I_d term can be obtained from the Levich equation:

$$I_d = 0.62nFAD^{2/3}\upsilon^{-1/6}\omega^{1/2}C_{O_2} \quad (2)$$

where n is the number of electrons transferred; F is Faraday's constant (96,485 C mol^{-1}); A is the area of the electrode (0.196 cm^2); D is the diffusion coefficient of O_2 in 0.1 M $HClO_4$ solution (1.93×10^{-5} cm^2 s^{-1}); υ is the kinematic viscosity of the electrolyte (1.01×10^{-2} cm^2 s^{-1}); ω is the angular frequency of rotaion, $\omega=2\pi f/60$, f is the RDE rotation rate in rpm and C_{O2} is the concentration of molecular oxygen in 0.1 M $HClO_4$ solution (1.26×10^{-6} mol cm^{-3})."

Section 7.3. Results and Discussions

The structures of the carbon supported Pt_3Co nanoparticles (Pt_3Co/C) were controlled by pre-treatment of the as-prepared Pt_3Co/C, which was, in-turn synthesized using an impregnation-reduction method [41-45], at different temperatures under a flowing H_2/N_2 mixed gas atmosphere. As shown in the X-ray diffraction (XRD) pattern of Fig. 1a, the sample, after pre-treatment at 400 ^oC (denoted as Pt_3Co/C-400) showed typical Pt face-centered-cubic (fcc) features. The broad peak at around 25^o is attributed to the carbon support. The other four diffraction peaks are consistent with those of pure Pt metals with an fcc structure, corresponding to the (111), (200), (220) and (311) planes. The peak positions are shifted to higher angles, relative to Pt/C, indicating that Co is incorporated into the Pt fcc structure to form an alloy phase with a concomitant lattice contraction. We will use the Pt_3Co/C-400 sample as a reference for the traditional, disordered Pt_3Co catalysts. After heat-treatement at 700 ^oC (denoted as Pt_3Co/C-700), the XRD pattern showed pronounced (100) and (110) peaks characteristic of an ordered, intermetallic Pt_3Co phase and an additional 0.8% lattice contraction (Table 1). The lattice parameter, calculated from the (220) diffraction peak position, and the average particle size, calculated using the full width at half maximun of the (220) diffraction and the Debye-Scherrer equation, are presented in Table 1.

Table 1. XRD and E-Chem results of Pt/C and Pt_3Co/C

sample	Particle size/nm	Lattice parameter/nm	$E_{1/2}$/V[‡]	MA*@0.9V /mAμg^{-1}	I_k[§] @0.9V /mAcm^{-2}
Pt/C	4.4 ± 0.5	0.3916	0.875	0.06	0.09
Pt_3Co-400	4.8 ± 1	0.3873	0.918	0.16	0.31
Pt_3Co-700	7.2 ± 1	0.3841	0.945	0.52	1.10

[‡] for ORR at RT, 0.1 M $HClO_4$, 1600 rpm, 5 mVs^{-1}. * Mass activity. [§] Specific activity.

Bright-field (BF) and annular dark-field (ADF) images of Pt_3Co/C-700 simultaneously acquired in a 5^{th}-order aberration-corrected scanning transmission electron microscope (STEM) operated at 60 kV are presented in the supplementary information (Figs. S2 and S4). The images demonstrate that the majority of the particles stay well dispersed on the Vulcan carbon support after the 700 ^oC heat treatment. The particle size distribution, calculated from more than 150 nanoparticles, shows that the mean particle size is about 5 nm in diameter (Supplementary Fig. S3[38]), which is slightly smaller than the value calculated from XRD because XRD gives volume-weighted measurements which tend to overestimate the geometric particle size [46]. In the center of Fig. 1b, a 5-nm Pt_3Co nanoparticle is viewed along the [001] zone axis. Due to the unique super periods that are not present in the disordered alloy phase, the presence of the $L1_2$ ordered intermetallic structure in Pt_3Co can be directly identified from atomic-resolution ADF-STEM images (Supplementary Fig. S5). For example, along the [001] axis, the projected $L1_2$ unit cell is composed of a periodic square array of pure Co columns surrounded by Pt columns at the edges and corners of each unit cell (Figs. 1b and d). Because ADF-STEM images reflect the Z-contrast of materials [47], the Pt columns will have an intensity higher than that of the Co columns (Figs. 1d and e). This differs from the disordered alloy phase which has all columns with equal intensity and lacks the (001) super period (Supplementary Fig. S5). Therefore, from the qualitative agreement of the simulation (Fig. 1e) with the experimental ADF-STEM image of the center particle in Figs. 1b and d, we confirm that the bulk of the nanoparticle is $L1_2$ ordered. It should also be noted that the first 2-3 atomic layers on the {100} facets—as indicated by the yellow arrows in Fig. 1b—appear free of the ordered super-lattice structure. Our

image simulations indicate that they are likely pure Pt planes (Figs. 1f and g). For detailed information on the simulation, see Supplementary Fig. S6 in the supporting information. We will later demonstrate (vide infra) by 2-D atomic-scale aberration-corrected chemical mapping, that they are, in fact, Pt surface segregation layers, rather than a disordered Pt_3Co.

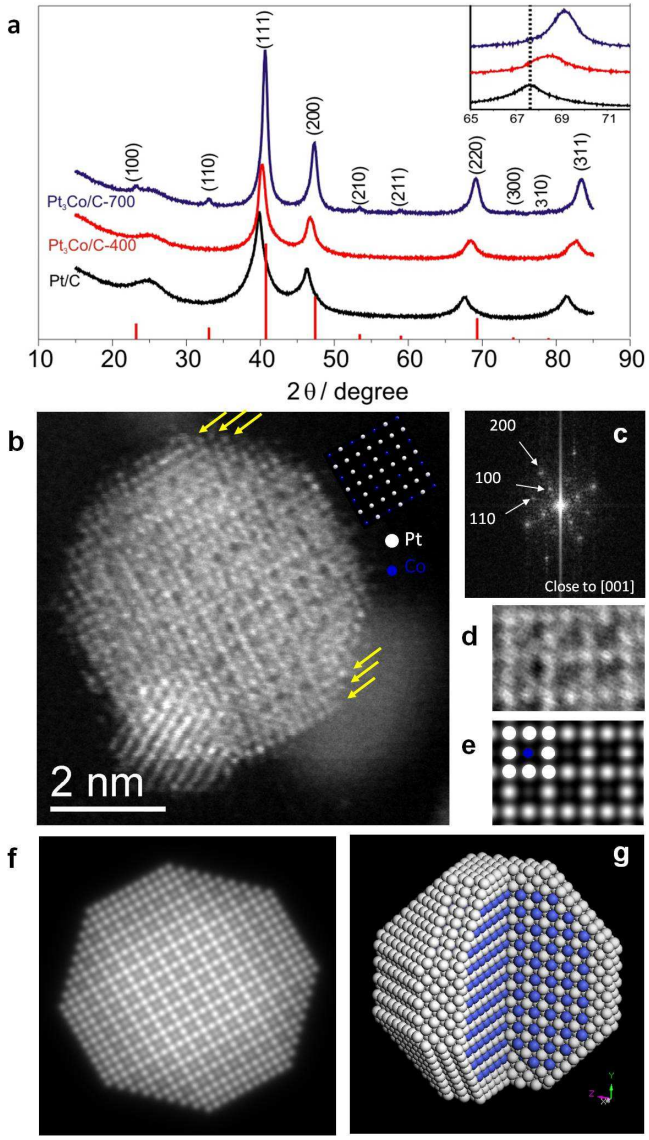

Figure 1 | X-ray diffraction and HAADF-STEM images. a, XRD patterns of Pt/C, Pt_3Co/C-400, and Pt_3Co/C-700. The inset in Fig. 1a shows the enlarged region of the Pt (220) diffraction peaks. The red lines indicate the peak positions of the intermetallic Pt_3Co reflections (PDF card # 04-004-5243). **b,** Atomic-resolution ADF-STEM image of Pt_3Co/C-700 after Richardson-Lucy deconvolution (for details see Supplementary Fig. S5). A smaller particle (lower left) overlaps the larger particle in projection. The inset shows the projected unit cell along the [001] axis. **c,** Diffractogram of the center particle in Fig. 1b. **d**, A crop of the super lattice feature from Fig. 1b. **e,** The simulated ADF-STEM image of $L1_2$ ordered Pt_3Co along [001] by a simple incoherent linear imaging model. **f**, Multislice simulated ADF-STEM (100 kV, probe forming angle=27.8 mrad, ADF collection angles=98-295 mrad) image of the idealized nanoparticle as shown in Fig. 1b. **g,** The idealized atomic structure of the Pt_3Co core-shell nanoparticle.

The chemical microstructure of the surface of the Pt-rich Pt_3Co/C-700 nanoparticles was examined using electron energy loss spectroscopic mapping employing a 5th-order berration-corrected STEM operated at 60 kV[15, 48, 49]. Fig. 2a shows the ADF-STEM image of a Pt_3Co/C-700 nanoparticle that was spectroscopically imaged. Figs. 2b and c show the Pt and Co projected distributions within the particle. The Pt (red) vs. Co (green) composite image (Fig. 2d) indicates that the Pt_3Co core (yellow) is surrounded by a pure Pt shell. However, the outside of the particle is decorated by a small amount Co/Co oxide. The Co/Co oxides will not affect the electrocatalytic activity of these particles because they quickly dissolve in acid conditions. Fig. 2e shows the line extracted from the Pt and Co maps across the facet indicated by the arrows. It can be seen that the Pt shell thickness is about 0.5 nm, which is 2-3 atomic layers, in agreement with our ADF analysis in Fig. 1 and Supplementary Fig. S7.

The polarization curves for the ORR obtained with Pt/C, Pt_3Co/C-400, and Pt_3Co/C-700 electrocatalysts as thin-films on a rotating disk electrode (RDE) in an O_2-saturated 0.1 M $HClO_4$ solution at 1600 rpm are shown in Fig. 3a. All electrodes were pre-treated by cycling the potential between +0.05 and +1.00 V at a sweep rate of 50 mVs^{-1} for 50 cycles in order to remove surface contamination prior to the ORR activity testing. We can see from Fig. 3a that both Pt_3Co/C-400 and Pt_3Co/C-700 have similar ORR onset potentials, which is nearly 50 mV higher than for Pt/C. At higher overpotentials, the current reaches its diffusion-limited value, ~5.6 $mAcm^{-2}$. At lower overpotentials (+0.80 V to +1.00 V), the current approaches the mixed regime. In this region, the half-wave potential of an ORR polarization curve, $E_{1/2}$, is often used to evaluate the electrocatalytic activity of a catalyst. As listed in Table 1, the half wave potential, $E_{1/2}$,

increased in the sequence: Pt/C < Pt_3Co/C-400 < Pt_3Co/C-700. The Pt_3Co/C-700 showed a dramatic positive shift in $E_{1/2}$ of ~70 mV relative to Pt/C. These data show that the intermetallic phase of Pt_3Co/C-700 exhibits dramatic activity improvements over Pt/C and disordered Pt_3Co/C-400 alloy catalysts. For a better understanding of the observed catalytic activities of the synthesized electrocatalysts for the ORR, the mass activities (MA) and specific activity (SA) at +0.85 and +0.90 V were calculated based on the ORR polarization curves and the amount of Pt or electrochemical surface area (ECSA) of Pt on the electrodes. The kinetic current (I_k) can be calculated using the Koutecky–Levich equation[50] which is expressed by

$$I = \frac{1}{I_k} + \frac{1}{I_d} \qquad (1)$$

where I is the measured current and I_d is the diffusion limited current.

The I_d term can be obtained from the Levich equation:

$$I_d = 0.62nFAD^{2/3}\upsilon^{-1/6}\omega^{1/2}C_{O_2} \qquad (2)$$

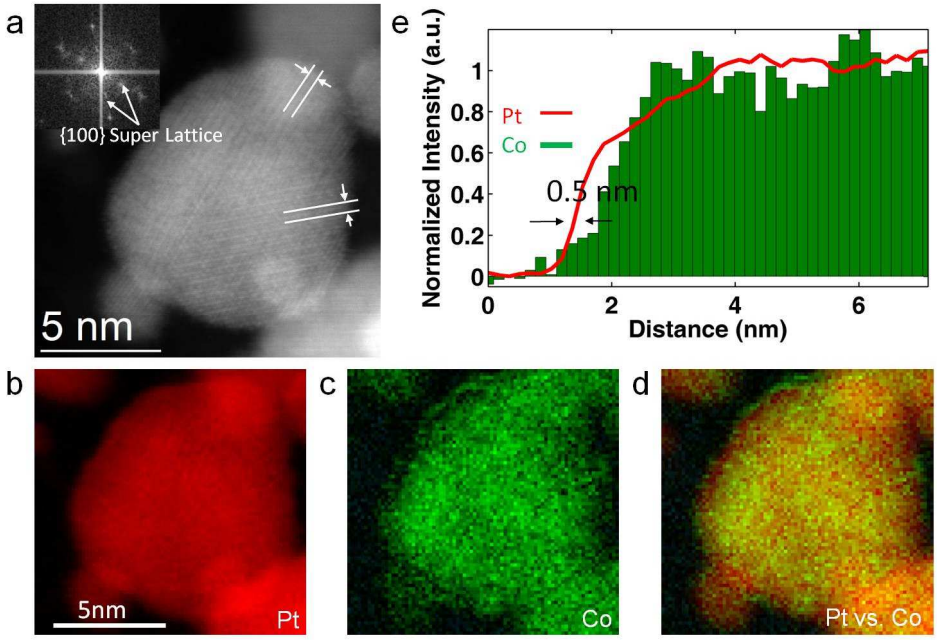

Figure 2 | ADF-STEM image of one nanoparticle and elemental mapping. **a**, ADF-STEM image of a Pt_3Co/C-700 nanoparticle; 2-D EELS map of **b,** Pt and **c,** Co along with the **d**, composite Pt vs. Co map. **e,** line profiles extracted from Fig. 2b and c across the facet indicated by the arrows showing that the Pt shell is ~0.5 nm thick.

Fig. 3b shows the rotation-rate-dependent current-potential curves of the Pt_3Co/C-700 nanoparticles (similar curves for the Pt/C nanoparticles are given in the Supplementary Information, Supplementary Fig. S8). The number of electrons transferred (*n*) was calculated to be ~ 4.0 at 0.8 – 0.9V from the slopes of the Koutecky–Levich plots, indicating the nearly complete reduction of O_2 to H_2O on the surface of Pt_3Co/C-700 nanoparticles. The mass activity comparison of Pt/C, Pt_3Co/C-400, Pt_3Co/C-700 at +0.85 and +0.90 V is shown in Fig. 3c, where one can see that Pt_3Co/C-700 exhibits much higher mass activity than pure Pt and Pt_3Co/C-400. Compared with the mass activity of Pt-Co/C systems tested under similar conditions at +0.90 V reported in the literature, our Pt_3Co/C-700 catalyst exhibits one of the highest electrocatalytic activities for the ORR (Supplementary Fig. S1 and Table S1). Fig. 3d compares the specific activity (I_k) towards the ORR for Pt/C, Pt_3Co/C-400, and Pt_3Co/C-700 electrodes. The I_k was obtained by normalizing the kinetic current to the electrochemical surface area (ECSA) which was calculated by measuring the charge associated with the adsorption of hydrogen H_{ads} (Q_H) between +0.05 and +0.40 V (Supplementary Fig. S9) and assuming a conversion factor of 200 μCcm^{-2} for the adsorption of a monolayer of hydrogen. (The value of 200 μCcm^{-2} was recently proposed by Feliu et al.[39, 40].) The measured currents were also corrected for mass transport to obtain the true kinetic currents. At +0.9 V, the specific activity of Pt_3Co/C-700 was 1.1 $mAcm^{-2}{}_{Pt}$, which is much higher than pure Pt and Pt_3Co/C-400 (Table 1, Supplementary information).

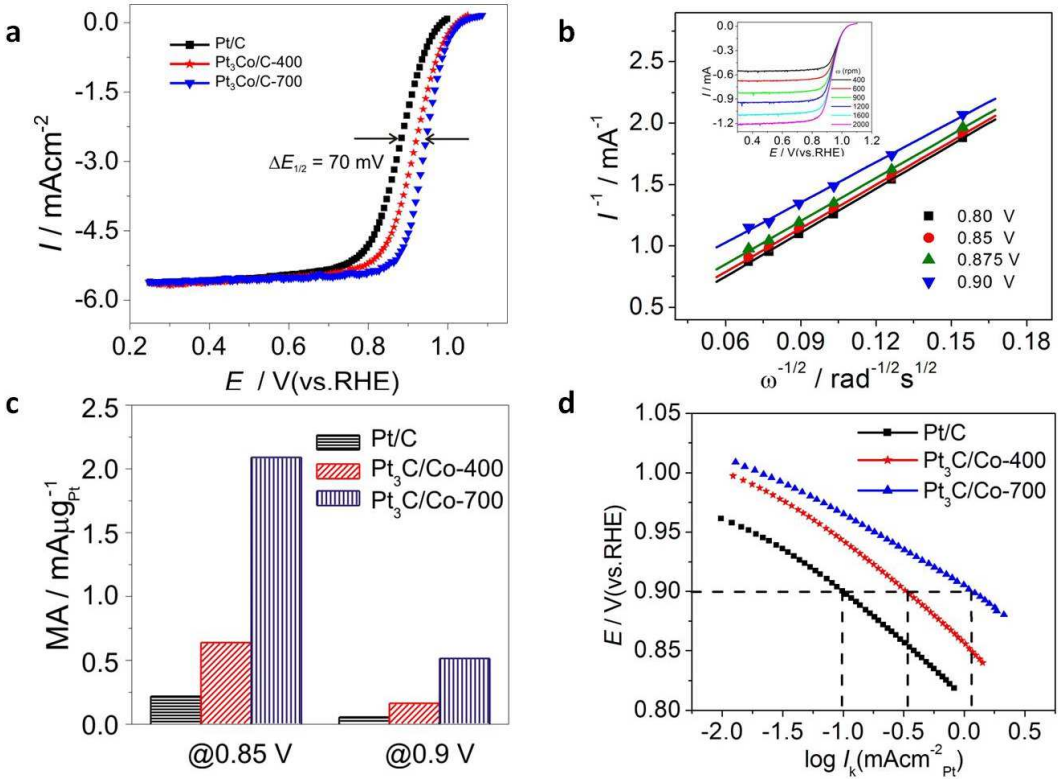

Figure 3 | Electrochemical characterization. a, ORR polarization curves for Pt/C, Pt_3Co/C-400 and Pt_3Co/C-700 in O_2-saturated 0.1 M $HClO_4$ at room temperature, Rotation rate, 1600 rpm; Sweep rate, 5 mVs^{-1}. **b,** The Koutecky–Levich plots from ORR data forn Pt_3Co/C-700 at different potentials. The inset in b shows the rotation-rate-dependent current-potential curves. **c,** Comparison of mass activities for Pt/C, Pt_3Co/C-400 and Pt_3Co/C-700 at 0.85 and 0.9 V. **d**, Comparison of specific activities (I_k).

The durability of the catalysts was evaluated by potential cycling between +0.05 and +1.00 V for 5,000 cycles in an N_2- saturated 0.1 M $HClO_4$ solution at a scan rate of 50 mVs^{-1}. The cyclic voltammograms (CVs) of Pt_3Co/C-400 and Pt_3Co/C-700 nanoparticles obtained after 2, 100, 500, 2000, and 5000 cycles are shown in Fig. 4a and b. For the Pt_3Co/C-400 nanoparticles, there were no well-defined hydrogen adsorption/desorption peaks after the first 100 cycles (See also the Supplementary Fig. S10). With continued cycling, the hydrogen adsorption/desorption peaks, as well as the Pt oxides reduction peaks become prominent (Fig. 4a). This suggests that, in the beginning, the behavior of the Pt_3Co/C-400 nanoparticles was dominated by the Pt-Co alloy and that cobalt was gradually leached away leaving a Pt-rich surface. However this was not the case for Pt_3Co/C-700 nanoparticles. Even the second CV cycle exhibited two prominent hydrogen adsorption/desorption peaks, along with the Pt oxides formation/reduction peaks (Fig. 4b) indicating that the Pt_3Co/C-700 nanoparticle surfaces were Pt-rich right after preparation. The peak currents increased slightly with potential cycling (Fig. 4b) indicating that some Co/Co oxides on the catalyst surface dissolved with potential cycling, exposing additional Pt on the surface. This result agrees with our ADF-STEM and STEM-EELS images that indicate there is a small amount of Co/Co oxides decorating the Pt-rich surface of the Pt_3Co/C-700 nanoparticles. The ECSAs of Pt_3Co/C-400 and Pt_3Co/C-700, after a given number of potential cycles, are shown in Fig. 4c. It can be seen that both Pt_3Co/C-400 and Pt_3Co/C-700 show an increased ECSA in the first few cycles, which could exhibited attributed to surface roughening and removal of contaminants from the sample surface, since the hydrogen adsorption/desorption peaks became more prominent. The ECSA of Pt_3Co/C-400 reached

a maximium value after 500 cycles, then decreased rapidly with additional cycling. After 5,000 cycles, the ECSA had decayed by about 30% of its maximum value. However, for the Pt_3Co/C-700 catalyst, the ECSA increased by about 20% after 2,000 cycles, and then stabilized. After 5,000 potential cycles, the Pt_3Co/C-400 catalyst showed a degradation of more than 30 mV in its half wave potential, $E_{1/2}$ (Fig. 4d), while the degradation of the Pt_3Co/C-700 catalyst was much lower, with less than a 10 mV negative shift in the half wave potential, indicating that the structurally ordered intermetallic Pt_3Co/C was much more durable and stable than the disordered Pt_3Co/C alloy. In addition, most of the particles were still well-dispersed on the carbon support (Supplementary Fig. S11). The structural stability of Pt_3Co/C-700 nanoparticles after 5,000 electrochemical cycles was verified by ADF-STEM images and EELS elemental mapping (Fig. 5). As shown in Fig. 5a, although some of the particles coalesced and/or aggregated (a), the Pt-riched shell (b,c,d) and ordered intermetallic core (a,e) structure were preserved. Compared with the ADF-STEM images and EELS elemental mapping of Pt_3Co/C-700 nanoparticles before potential cycling (Fig. 2), there are no Co/Co oxides left on the surface and the Pt rich shell can be clearly seen (Fig. 5b, c, and d).

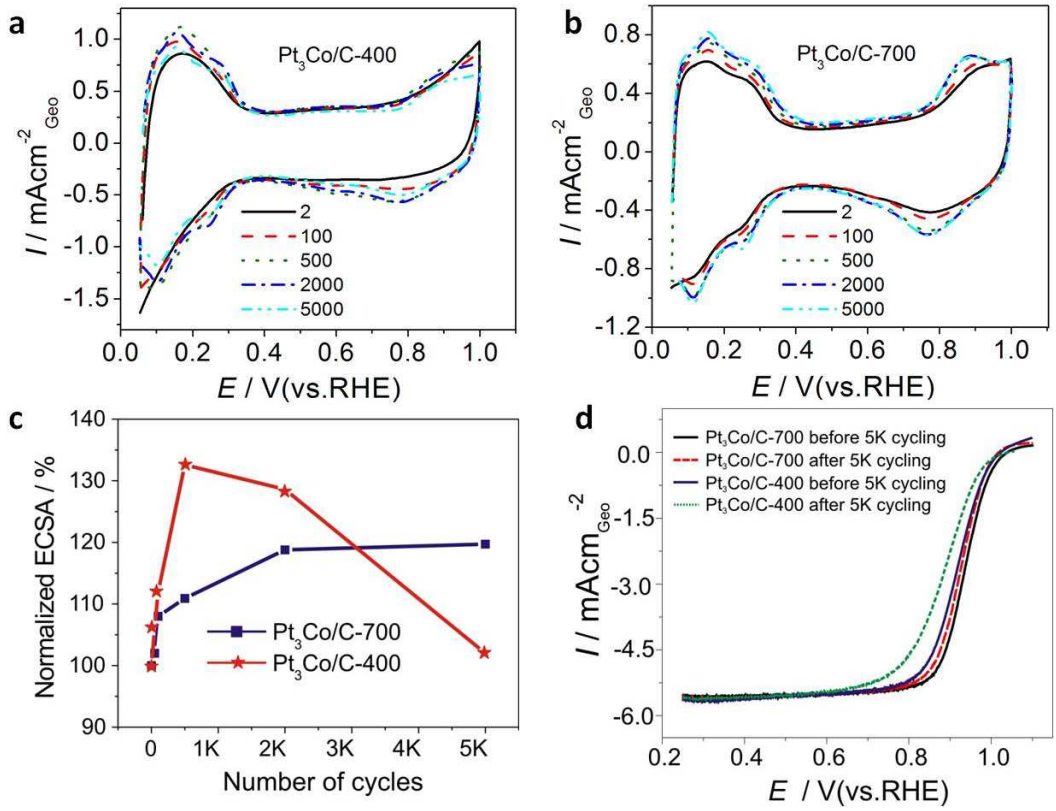

Figure 4 | Characterization of the surface area changes and stability for ORR. a, CV curves of Pt_3Co/C-400 and **b,**Pt_3Co/C-700 nanoparticles in N_2-purged 0.1 M $HClO_4$ solution after different potential cycles, at room temperature, at a scan rate of 5 mVs^{-1}. **c,** Electrochemical surface area (ECSA) as a function of the number of CV cycles for Pt_3Co/C-400 and Pt_3Co/C-700 catalysts. **d**, Comparative ORR activities of Pt_3Co/C-400 and Pt_3Co/C-700 catalysts before and after 5000 potential cycles.

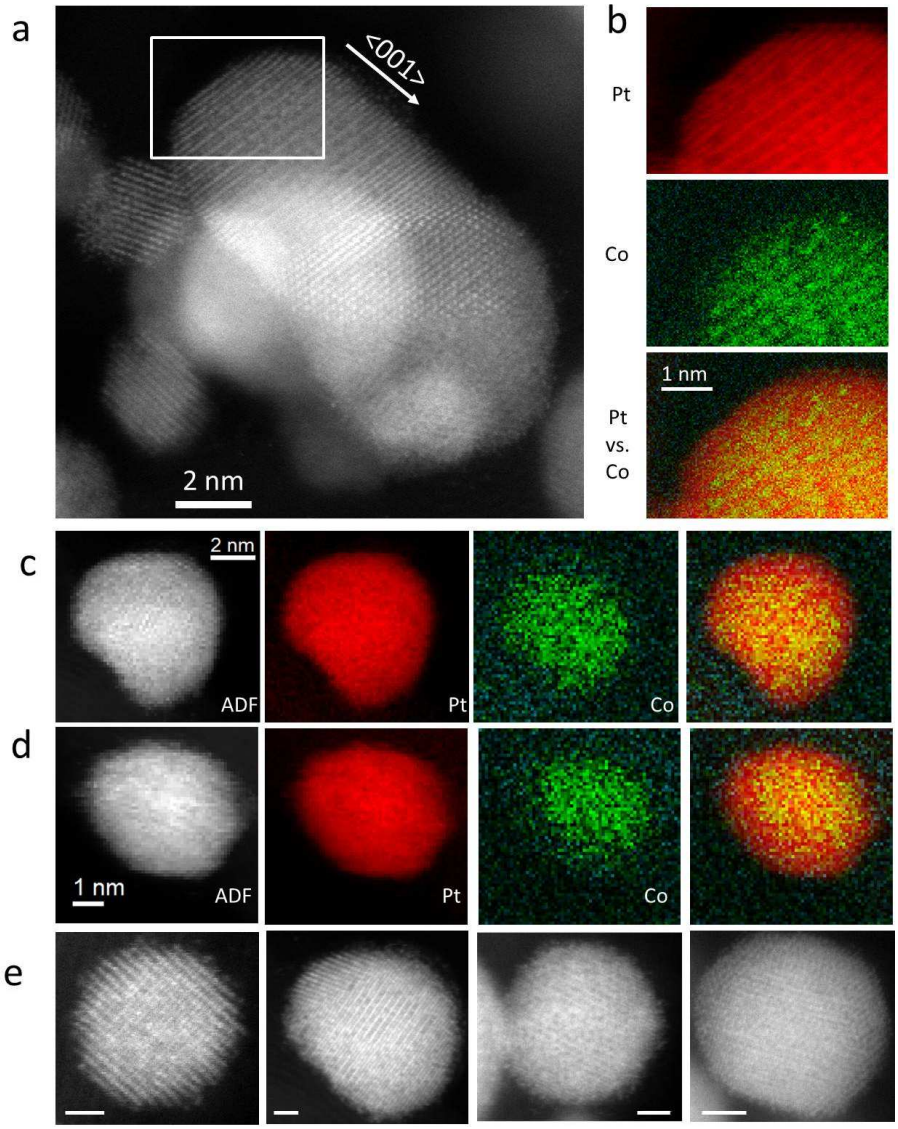

Figure 5 | Structural stability. a, ADF-STEM image of a Pt_3Co/C-700 nanoparticles after 5,000 electrochemical cycles. **b,** EELS maps of Pt, Co and the composite Pt vs. Co map from the selected region in **a**. **c**,**d,** two more particles and their Pt, Co elemental mapping to show the Pt-riched shell and PtCo intermetallic core after electrochemical cycling. **e**, Additional particles to demonstrate that the ordered structure is maintained after electrochemical cycling. All the scale bars are 1nm.

Section 7.4. Conclusion

In summary, this work presents a new kind of electrocatalyst for the ORR, composed of ordered, intermetallic core-shell Pt_3Co@Pt/C nanoparticles. These nanoparticles are more active and durable than the disordered Pt_3Co/C alloy and could represent the next-generation ORR electrocatalyst for fuel cells applications. The high activity and durability of the electrocatalyst for the ORR can be ascribed to the Pt-rich shell and the stable intermetallic Pt, Co arrangement in the core. This study provides a new design strategy for preparing fuel cell catalysts with both excellent electrocatalytic activity and stability.

Supporting Information

Supplementary information accompanies this paper at www.nature.com/naturechemistry. Reprints and permission information is available online at http://npg.nature.com/reprints.

REFERENCES

1. Debe, M. K. Electrocatalyst approaches and challenges for automotive fuel cells. *Nat. Mater*. **486**, 9 (2012).
2. Gasteiger, H. A. & Markovic, N. M. Just a dream-or future reality? *Science* **324**, 48-49 (2009).
3. Greeley, J. et al. Alloys of platinum and early transition metals as oxygen reduction electrocatalysts. *Nat. Chem.* **1**, 552-556 (2009).
4. Shao, M. H., Shoemaker, K., Peles, A., Kaneko, K. & Protsailo, L. Pt monolayer on porous Pd-Cu alloys as oxygen reduction electrocatalysts. *J. Am. Chem. Soc.* **132**, 9253-9255 (2010).
5. Stamenkovic, V. R. et al. Trends in electrocatalysis on extended and nanoscale Pt-bimetallic alloy surfaces. *Nat. Mater.* **6**, 241-247 (2007).
6. Yano, H., Kataoka, M., Yamashita, H., Uchida, H. & Watanabe, M. Oxygen reduction activity of carbon-supported Pt-M (M = V, Ni, Cr, Co, and Fe) alloys prepared by nanocapsule method. *Langmuir* **23**, 6438-6445 (2007).
7. Antolini, E., Salgado, J. R. C. & Gonzalez, E. R. The stability of Pt-M (M = first row transition metal) alloy catalysts and its effect on the activity in low temperature fuel cells - A literature review and tests on a Pt-Co catalyst. *J. Power Sources* **160**, 957-968 (2006).
8. Rao, C. V. & Viswanathan, B. ORR activity and direct ethanol fuel cell performance of carbon-supported Pt-M (M = Fe, Co, and Cr) alloys prepared by polyol reduction method. *J. Phys. Chem. C* **113**, 18907-18913 (2009).
9. Kim, J., Lee, Y. & Sun, S.H. Structurally ordered FePt nanoparticles and their enhanced catalysis for oxygen reduction reaction. *J. Am. Chem. Soc.* **132**, 4996-4997 (2010).
10. Malheiro, A. R., Perez, J. & Villullas, H.M. Well-alloyed PtFe/C Nanocatalysts of controlled composition and same particle size: oxygen reduction and methanol tolerance. *J. Electrochem.Soc.* **156**, B51-B58 (2009).
11. Stamenkovic, V. R., Mun, B. S., Mayrhofer, K. J. J., Ross, P. N. & Markovic, N.M. Effect of surface composition on electronic structure, stability, and electrocatalytic properties of Pt-transition metal alloys: Pt-skin versus Pt-skeleton surfaces. *J. Am. Chem. Soc.* **128**, 8813-8819 (2006).
12. Hwang, S. J. et al. Ternary Pt-Fe-Co Alloy electrocatalysts prepared by electrodeposition: lucidatEing the roles of Fe and Co in the oxygen reduction reaction. *J. Phys. Chem. C* **115**, 2483-2488.
13. Min, M. K., Cho, J. H., Cho, K. W. & Kim, H. Particle size and alloying effects of Pt-based alloy catalysts for fuel cell applications. *Electrochim. Acta* **45**, 4211-4217 (2000).
14. Stamenkovic, V., Schmidt, T. J., Ross, P. N. & Markovic, N. M. Surface composition effects in electrocatalysis: Kinetics of oxygen reduction on well-defined Pt3Ni and Pt3Co alloy surfaces. *J. Phys. Chem. B* **106**, 11970-11979 (2002).
15. Xin, H. L. *et al.* Atomic-resolution spectroscopic imaging of ensembles of nanocatalyst particles across the life of a fuel cell. *Nano Letters* **12**, 490-497 (2012)
16. Wu, J. B. et al. Truncated octahedral Pt3Ni oxygen reduction reaction electrocatalysts. *J. Am. Chem. Soc.***132**, 4984-4985 (2010).

17. Zhang, J., Yang, H. Z., Fang, J. Y. & Zou, S. Z. Synthesis and oxygen reduction Aactivity of shape-controlled Pt_3Ni nanopolyhedra. *Nano Lett.* **10**, 638-644 (2010).
18. Strasser, P. et al. Lattice-strain control of the activity in dealloyed core-shell fuel cell catalysts. *Nat. Chem.* **2**, 454-460 (2010).
19. Mani, P., Srivastava, R. & Strasser, P. Dealloyed Pt-Cu core-shell nanoparticle electrocatalysts for use in PEM fuel cell cathodes. *J. Phys. Chem. C* **112**, 2770-2778 (2008).
20. Srivastava, R., Mani, P., Hahn, N. & Strasser, P. Efficient oxygen reduction fuel cell electrocatalysis on voltammetrically dealloyed Pt-Cu-Co nanoparticles. *Angew. Chem. Int. Ed.***46**, 8988-8991 (2007).
21. Jeon, M. K., Zhang, Y. A. & McGinn, P. J. A comparative study of PtCo, PtCr, and PtCoCr catalysts for oxygen electro-reduction reaction. *Electrochim. Acta* **55**, 5318-5325 (2010).
22. Mukerjee, S., Srinivasan, S., Soriaga, M. P. & McBreen, J. Role of structural and electronic-properties of Pt and Pt alloys on electrocatalysis of oxygen reduction- an in-situ XANES and EXAFS investigation. *J. Electrochem.Soc.* **142**, 1409-1422 (1995).
23. Kang, Y. & Murray, C. B. Synthesis and electrocatalytic properties of cubic Mn-Pt nanocrystals (nanocubes). *J. Am. Chem. Soc.* **132**, 7568-7569 (2010).
24. Gong, K. P., Su, D. & Adzic, R. R. Platinum-monolayer shell on $AuNi_{0.5}Fe$ nanoparticle core electrocatalyst with high activity and stability for the oxygen reduction reaction. *J. Am. Chem. Soc.* **132**, 14364-14366 (2010).
25. Sasaki, K. et al. Core-protected platinum monolayer shell high-stability electrocatalysts for fuel-cell cathodes. *Angew. Chem. Int. Ed.* **49**, 8602-7 (2010).
26. Wang, J. X. et al. Oxygen Reduction on well-defined core-shell nanocatalysts: particle size, facet, and Pt shell thickness effects. *J. Am. Chem. Soc.* **131**, 17298-17302 (2009).
27. Neyerlin, K. C., Srivastava, R., Yu, C. F. & Strasser, P. Electrochemical activity and stability of dealloyed Pt-Cu and Pt-Cu-Co electrocatalysts for the oxygen reduction reaction (ORR). *J. Power Sources* **186**, 261-267 (2009).
28. Suntivich, J. et al. Design principles for oxygen-reduction activity on perovskite oxide catalysts for fuel cells and metal–air batteries. *Nat. Chem.* **3**, 546-550 (2011).
29. Liang, Y. et al. Co_3O_4 nanocrystals on graphene as a synergistic catalyst for oxygen reduction reaction. *Nat. Mater.* **10**, 780-786 (2012).
30. Li, Y. et al. An oxygen reduction electrocatalyst based on carbon nanotube-graphene complexes. *Nat. nanotech.* **7**, 394-400 (2012).
31. Li, X., Colon-Mercado, H. R., Wu, G., Lee, J.-W. & Popov, B. N. Development of method for synthesis of Pt-Co cathode catalysts for PEM fuel cells. *Electrochem. Solid-State Lett.* **10**, B201-B205 (2007).
32. Watanabe, M., Tsurumi, K., Mizukami, T., Nakamura, T. & Stonehart, P. Activity and stability of ordered and disordered Co-Pt alloys for phosphoric acid fuel cells *J. Electrochem.Soc.* **141**, 2659-2668 (1994).
33. Koh, S., Toney, M. F. & Strasser, P. Activity-stability relationships of ordered and disordered alloy phases of Pt_3Co electrocatalysts for the oxygen reduction reaction (ORR). *Electrochim. Acta* **52**, 2765-2774 (2007).

34. Liu, Z. F., Jackson, G. S. & Eichhorn, B. W. PtSn Intermetallic, Core-shell, and alloy nanoparticles as CO-tolerant electrocatalysts for H_2 oxidation. *Angew. Chem. Int. Ed.***49**, 3173-3176 (2010).
35. Ji, X. L. et al. Nanocrystalline intermetallics on mesoporous carbon for direct formic acid fuel cell anodes. *Nat. Chem.* **2**, 286-293 (2010).
36. Ghosh, T., Vukmirovic, M. B., DiSalvo, F. J. & Adzic, R. R. Intermetallics as novel supports for Pt monolayer O_2 reduction electrocatalysts: potential for significantly improving properties. *J. Am. Chem. Soc.* **132**, 906-907 (2010).
37. Wang, D., Zhuang, L. & Lu, J. T. An alloying-degree-controlling step in the impregnation synthesis of PtRu/C catalysts. *J. Phys. Chem. C* **111**, 16416-16422 (2007).
38. Wang, D. L., Lu, S. F. & Jiang, S. P. Pd/HPW-PDDA-MWCNTs as effective non-Pt electrocatalysts for oxygen reduction reaction of fuel cells. *Chem. Commun.* **46**, 2058-2060 (2010).
39. Wang, D. L., Lu, S. F. & Jiang, S. P. Tetrahydrofuran-functionalized multi-walled carbon nanotubes as effective support for Pt and PtSn electrocatalysts of fuel cells. *Electrochim. Acta* **55**, 2964-2971 (2010).
40. Wang, D. L. et al. Highly stable and CO-tolerant $Pt/Ti_{0.7}W_{0.3}O_2$ electrocatalyst for proton-exchange membrane fuel cells. *J. Am. Chem. Soc.* **132**, 10218-10220 (2010).
41. Wang, D. L. et al. Pt-decorated PdCo@Pd/C Core-Shell Nanoparticles with enhanced stability and electrocatalytic activity for the oxygen reduction reaction. *J. Am. Chem. Soc.* **132**, 17664-17666 (2010).
42. Hovden, R., Xin, H. L. & Muller, D. A. Extended depth of field for high-resolution scanning transmission electron microscopy. *Micros. Microanal.* **17**, 75-80 (2011).
43. Warren, R. X-ray Diffraction. Dover Publications (1990).
44. Crewe, A. V., Wall, J. & Langmore, J. Visibility of single atoms. *Science* **168**, 1338-1340 (1970).
45. Muller, D. A. et al. Atomic-scale chemical imaging of composition and bonding by aberration-corrected microscopy. *Science* **319**, 1073-1076 (2008).
46. Kourkoutis, L. F. et al. Atomic-resolution spectroscopic imaging of oxide interfaces. *Philos. Mag.* **90**, 4731-4749.
47. Bard, A. J. & Faulkner, L. R. Electrochemical methods: fundamentals and applications. *John Wiley* (2001).
48. Vidal-Iglesias, F. J., Aran-Ais, R. M., Solla-Gullon, J., Herrero, E. & Feliu, J. M. Electrochemical characterization of shape-controlled Pt nanoparticles in different supporting electrolytes. *Acs Catal.* **2**, 901-910 (2011).
49. Chen, Q.-S., Solla-Gullon, J., Sun, S.-G. & Feliu, J. M. The potential of zero total charge of Pt nanoparticles and polycrystalline electrodes with different surface structure: The role of anion adsorption in fundamental electrocatalysis. *Electrochim. Acta* **55**, 7982-7994 (2010).
50. Huang, P. Y. et al. Grains and grain boundaries in single-layer graphene atomic patchwork quilts. *Nature* **469**, 389-392 (2011).

1. Debe, M. K. *Nature Materials* **2012,** 486, 9.
2. Gasteiger, H. A.; Markovic, N. M. *Science* **2009,** 324, (5923), 48-49.
3. Greeley, J.; Stephens, I. E. L.; Bondarenko, A. S.; Johansson, T. P.; Hansen, H. A.; Jaramillo, T. F.; Rossmeisl, J.; Chorkendorff, I.; Norskov, J. K. *Nature Chemistry* **2009,** 1, (7), 552-556.
4. Shao, M. H.; Shoemaker, K.; Peles, A.; Kaneko, K.; Protsailo, L. *Journal of the American Chemical Society* **2010,** 132, (27), 9253-9255.
5. Stamenkovic, V. R.; Mun, B. S.; Arenz, M.; Mayrhofer, K. J. J.; Lucas, C. A.; Wang, G. F.; Ross, P. N.; Markovic, N. M. *Nature Materials* **2007,** 6, (3), 241-247.
6. Yano, H.; Kataoka, M.; Yamashita, H.; Uchida, H.; Watanabe, M. *Langmuir* **2007,** 23, (11), 6438-6445.
7. Antolini, E.; Salgado, J. R. C.; Gonzalez, E. R. *Journal of Power Sources* **2006,** 160, (2), 957-968.
8. Rao, C. V.; Viswanathan, B. *Journal of Physical Chemistry C* **2009,** 113, (43), 18907-18913.
9. Kim, J.; Lee, Y.; Sun, S. H. *Journal of the American Chemical Society* **2010,** 132, (14), 4996-4997.
10. Malheiro, A. R.; Perez, J.; Villullas, H. M. *Journal of the Electrochemical Society* **2009,** 156, (1), B51-B58.
11. Stamenkovic, V. R.; Mun, B. S.; Mayrhofer, K. J. J.; Ross, P. N.; Markovic, N. M. *Journal of the American Chemical Society* **2006,** 128, (27), 8813-8819.
12. Hwang, S. J.; Yoo, S. J.; Jang, S.; Lim, T.-H.; Hong, S. A.; Kim, S.-K. *Journal of Physical Chemistry C* 115, (5), 2483-2488.
13. Min, M. K.; Cho, J. H.; Cho, K. W.; Kim, H. *Electrochimica Acta* **2000,** 45, (25-26), 4211-4217.
14. Stamenkovic, V.; Schmidt, T. J.; Ross, P. N.; Markovic, N. M. *Journal of Physical Chemistry B* **2002,** 106, (46), 11970-11979.
15. Xin, H. L.; Mundy, J. A.; Liu, Z.; Cabezas, R.; Hovden, R.; Kourkoutis, L. F.; Zhang, J.; Subramanian, N. P.; Makharia, R.; Wagner, F. T.; Muller, D. A. *Nano Letters* **2012,** 12, (1), 490-497.
16. Wu, J. B.; Zhang, J. L.; Peng, Z. M.; Yang, S. C.; Wagner, F. T.; Yang, H. *Journal of the American Chemical Society* **2010,** 132, (14), 4984-4985.
17. Zhang, J.; Yang, H. Z.; Fang, J. Y.; Zou, S. Z. *Nano Letters* **2010,** 10, (2), 638-644.
18. Strasser, P.; Koh, S.; Anniyev, T.; Greeley, J.; More, K.; Yu, C. F.; Liu, Z. C.; Kaya, S.; Nordlund, D.; Ogasawara, H.; Toney, M. F.; Nilsson, A. *Nature Chemistry* **2010,** 2, (6), 454-460.
19. Mani, P.; Srivastava, R.; Strasser, P. *Journal of Physical Chemistry C* **2008,** 112, (7), 2770-2778.
20. Srivastava, R.; Mani, P.; Hahn, N.; Strasser, P. *Angewandte Chemie-International Edition* **2007,** 46, (47), 8988-8991.
21. Jeon, M. K.; Zhang, Y. A.; McGinn, P. J. *Electrochimica Acta* **2010,** 55, (19), 5318-5325.
22. Mukerjee, S.; Srinivasan, S.; Soriaga, M. P.; McBreen, J. *Journal of the Electrochemical Society* **1995,** 142, (5), 1409-1422.
23. Kang, Y.; Murray, C. B. *Journal of the American Chemical Society* 132, (22), 7568-+.
24. Gong, K. P.; Su, D.; Adzic, R. R. *Journal of the American Chemical Society* **2010,** 132, (41), 14364-14366.
25. Sasaki, K.; Naohara, H.; Cai, Y.; Choi, Y. M.; Liu, P.; Vukmirovic, M. B.; Wang, J. X.; Adzic, R. R. *Angew Chem Int Ed Engl* **2010,** 49, (46), 8602-7.
26. Wang, J. X.; Inada, H.; Wu, L. J.; Zhu, Y. M.; Choi, Y. M.; Liu, P.; Zhou, W. P.; Adzic, R. R. *Journal of the American Chemical Society* **2009,** 131, (47), 17298-17302.

27. Neyerlin, K. C.; Srivastava, R.; Yu, C. F.; Strasser, P. *Journal of Power Sources* **2009,** 186, (2), 261-267.
28. Suntivich, J.; Gasteiger, H. A.; Yabuuchi, N.; Nakanishi, H.; Goodenough, J. B.; Shao-Horn, Y. *Nat Chem* **2011,** 3, (7), 546-550.
29. Liang, Y.; Li, Y.; Wang, H.; Zhou, J.; Wang, J.; Regier, T.; Dai, H. *Nature Materials* **2012,** 10, (10), 780-786.
30. Li, Y.; Zhou, W.; Wang, H.; Xie, L.; Liang, Y.; Wei, F.; Idrobo, J.-C.; Pennycook, S. J.; Dai, H. *Nature nanotechnology* **2012,** 7, (6), 394-400.
31. Li, X.; Colon-Mercado, H. R.; Wu, G.; Lee, J.-W.; Popov, B. N. *Electrochemical and Solid State Letters* **2007,** 10, (11), B201-B205.
32. Watanabe, M.; Tsurumi, K.; Mizukami, T.; Nakamura, T.; Stonehart, P. *Journal of the Electrochemical Society* **1994,** 141, (10), 2659-2668.
33. Koh, S.; Toney, M. F.; Strasser, P. *Electrochimica Acta* **2007,** 52, (8), 2765-2774.
34. Liu, Z. F.; Jackson, G. S.; Eichhorn, B. W. *Angewandte Chemie-International Edition* **2010,** 49, (18), 3173-3176.
35. Ji, X. L.; Lee, K. T.; Holden, R.; Zhang, L.; Zhang, J. J.; Botton, G. A.; Couillard, M.; Nazar, L. F. *Nature Chemistry* **2010,** 2, (4), 286-293.
36. Ghosh, T.; Vukmirovic, M. B.; DiSalvo, F. J.; Adzic, R. R. *Journal of the American Chemical Society* **2010,** 132, (3), 906-907.
37. Huang, P. Y.; Ruiz-Vargas, C. S.; van der Zande, A. M.; Whitney, W. S.; Levendorf, M. P.; Kevek, J. W.; Garg, S.; Alden, J. S.; Hustedt, C. J.; Zhu, Y.; Park, J.; McEuen, P. L.; Muller, D. A. *Nature* **2011,** 469, (7330), 389-392.
38. Hovden, R.; Xin, H. L.; Muller, D. A. *Microscopy and Microanalysis* **2011,** 17, (1), 75-80.
39. Chen, Q.-S.; Solla-Gullon, J.; Sun, S.-G.; Feliu, J. M. *Electrochimica Acta* **2010,** 55, (27), 7982-7994.
40. Vidal-Iglesias, F. J.; Aran-Ais, R. M.; Solla-Gullon, J.; Herrero, E.; Feliu, J. M. *Acs Catalysis* **2011,** 2, (5), 901-910.
41. Wang, D.; Zhuang, L.; Lu, J. T. *Journal of Physical Chemistry C* **2007,** 111, 16416-16422.
42. Wang, D. L.; Lu, S. F.; Jiang, S. P. *Chemical Communications* **2010,** 46, (12), 2058-2060.
43. Wang, D. L.; Lu, S. F.; Jiang, S. P. *Electrochimica Acta* **2010,** 55, (8), 2964-2971.
44. Wang, D. L.; Subban, C. V.; Wang, H. S.; Rus, E.; DiSalvo, F. J.; Abruna, H. D. *Journal of the American Chemical Society* **2010,** 132, (30), 10218-10220.
45. Wang, D. L.; Xin, H. L.; Yu, Y. C.; Wang, H. S.; Rus, E.; Muller, D. A.; Abruna, H. D. *Journal of the American Chemical Society* **2010,** 132, (50), 17664-17666.
46. Warren, R. **1990**.
47. Crewe, A. V.; Wall, J.; Langmore, J. *Science* **1970,** 168, (3937), 1338-1340.
48. Muller, D. A.; Kourkoutis, L. F.; Murfitt, M.; Song, J. H.; Hwang, H. Y.; Silcox, J.; Dellby, N.; Krivanek, O. L. *Science* **2008,** 319, (5866), 1073-1076.
49. Kourkoutis, L. F.; Xin, H. L.; Higuchi, T.; Hotta, Y.; Lee, J. H.; Hikita, Y.; Schlom, D. G.; Hwang, H. Y.; Muller, D. A. *Philosophical Magazine* 90, (35-36), 4731-4749.
50. Bard, A. J. F., L.R. *John Wiley* **2001**.

CHAPTER 8

YOLK-SHELL STRUCTURE OF POLYANILINE COATED SULFUR FOR LITHIUM-SULFUR BATTERIES[1][2]

Section 8.1. Introduction

The widespread usage of portable electronic devices and the rapid growth of electric vehicles require the development of next generation batteries with higher capacity and energy density. Among all rechargeable batteries, the Lithium-Sulfur (Li-S) cell is one of the most promising candidates due to (1) it's high theoretical capacity of 1672 mAh g^{-1}, which is over 5 times that of currently used transition metal oxide cathode materials; (2) it's low cost and abundant resources of sulfur; (3) non-poisonous and environmentally benign.[1-5] Despite these advantages, the practical application of Li-S cells is still limited mainly due, at least in part, to: (1) the low conductivity of sulfur (5×10^{-30} S cm^{-1} at 25 ^{0}C); (2) the dissolution of polysulfides and the resulting shuttling effect in the charge-discharge process; (3) the volumetric expansion during the discharge of the cell.[4-8] While the dissolution of polysulfides is the hardest problem to overcome, these issues are often accompanied with each other. Therefore, a systematic material design strategy intended to prevent polysulfide dissolution, might address this problem.

---

[1] Produced with permission from Weidong Zhou, Yingchao Yu, Hao Chen, Francis J. DiSalvo and Héctor D. Abruña, *Journal of the American Chemical Society.*, 2013, *135* (44), 16736–16743. Copyright © 2013 American Chemical Society.

[2] W.Z. and Y.Y. contributed equally to this work. W.Z. synthesized the sample, Y.Y. performed the microscopy imaging. W.Z. and Y.Y. designed and analyzed the battery testing. H.C. helped to perform the sysnthesis. H.D.A. and F.J.D. guided the work.

The high capacity and cycling ability of sulfur arises from the electrochemical cleavage and reformation of sulfur-sulfur bonds in cathode, which is believed to proceed in two steps. First, the reduction of sulfur to lithium higher polysulfides (Li_2S_n, $4 \leq n \leq 8$) followed by further reduction to lithium lower polysulfides (Li_2S_n, $1 \leq n \leq 3$).[6-8] The higher polysulfides are easily dissolved into the organic liquid electrolyte, enabling them to penetrate through the polymer separator and react with the lithium metal anode, leading to the loss of sulfur active materials. Even if some of the dissolved polysulfides could diffuse back to the cathode during the recharge process, the sulfur particles formed on the surface of the cathode are electrochemically inactive owing to the poor conductivity. Such a degradation path, leads to poor capacity retention, especially during the long cycling (i.e. more than 100 cycles).

Efforts to trap the sulfur have mainly focused on the use of mesoporous carbons to absorb polysulfides through weak intermolecular interactions[9-17] and physically encapsulating sulfur particles with conducting polymers[18-24] or graphite carbon[25-29]. The mesoporous carbon/sulfur composites are often prepared *via* the sulfur vapor impregnation into conductive mesoporous carbons, which show obvious advantage on their high conductivity and large surface area due to the small pores size and large overall pore volume. However, if the sulfur can diffuse into the small pores of the mesoporous carbons, it also could diffuse out theoretically, considering the fact that the sulfur can still be accessed by an electrolyte for a long term. Although the weak interactions between sulfur and the mesopores could alleviate the dissolution of polysulfides in the short term, the polysulfides could still eventually be dissolved. This is likely the reason why extended cycle life (>100 cycles) tests, with stable capacity retention and high Coulombic efficiency, are rarely reported for this type of composite. On the other hand, the methodology of core-shell composites adopts the reverse order, in which, sulfur nanoparticles are first prepared

and then coated with a conductive polymer or graphite carbon. While, this method could provide for the long term retention of sulfur, the large volumetric expansion of sulfur during lithiation renders the protective coating layer susceptible to cracking or even breaking, resulting in the loss of polysulfides. In this respect, Cui and coworkers pioneered the concept of forming a yolk-shell structure, to adjust the amount of sulfur encapsulated inside the TiO_2 shell, by leaching only a fraction of the encapsulated sulfur using organic solvents.[30] This approach greatly improved the confinement of sulfur, resulting a long-term cycling performance for Li/S batteries. Despite the promising progress, some issues remain, for example, the electrolyte might still dissolve away additional polysulfides considering the fact that toluene could dissolve out the sulfur during the preparation of this system. It is difficult to control the amount of sulfur leached out while maintaining a uniform distribution of leaching percentage across an entire array of nanoparticles. The insulating nature of the TiO_2 shell in the electrochemical window of 1.5 to 3.0V *vs* Li can limit the actual capacity of the sulfur. Another innegligible phenomenon in Li/S batteries is that polyvinylidene fluoride (PVDF) dissolved in N-methyl-2-pyrrolidone (NMP) was generally employed as the binder. However, NMP could dissolve sulfur out of the pre-constructed nanostrucutures and the evaporation of NMP under vacuum could also cause related environmental problems.[31]

Section 8.2. Materials and Methods

Material Synthesis

$Na_2S_2O_3$ (2.37 g) in 50 ml water was slowly added into the diluted sulfuric acid solution (500ml, 3mM) containing 1% (weight ratio) of polyvinylpyrrolidone (PVP, Mw~40,000). After stirring for 2hours at room temperature, the sulfur particles were collected by centrifugation and re-dispersed into 300ml aqueous solution of PVP (1%). 200mg aniline and 10ml sulfuric acid (1M)

was added into the above emulsion. 0.5g ammonium persulphate in 30ml water was added in dropwise under nitrogen flow at 0^0C. After stirring at 0^0C for 24hours, the polyaniline coated sulfur particles were collected by centrifugation and dried under vacuum overnight. To prepare the sulfur-polyaniline yolk-shell structures, the powder of the core-shell particles was sealed into a glass tube filled with argon and heated to 180^0C for 12hours.

Electrochemical Measurement

To prepare the cathodes, sulfur based materials were first mixed with carbon black and polytetrafluoroethylene (PTFE) binder (80:15:5 by weight) through ground in mortar. The mixture was then roll-pressed to produce electrode films with an average sulfur loading of 4mg cm^{-2}, which were heated at 50^0C for 12 hours under vacuum before using to fabricate the coin cells. 2032 type coin cells were fabricated in an argon filled glove box using lithium foil as the anode and TFSI (1M in DOL/DME) as the electrolyte. The sulfur contents of S-Pani core-shell and yolk-shell in the whole cathode films were calibrated to be 65.6% and 46.4%, respectively.

Material Characterization

Powder X-ray diffraction (XRD) was performed by using a Rigaku® Ultima VI diffractometer, and diffraction patterns were collected at a scanning rate of 5 °/min and with a step of 0.02 °. Electron microscopy imaging was carried out using a Schottky-field-emission-gun Tecnai F20 scanning transmission electron microscope (STEM) operated at 200 keV. A high-angle annular dark field detector provided an incoherent projection image of the specimen with a signal intensity proportional to the amount of material and its atomic number, which is also known as Z-contrast. The energy dispersive x-ray (EDX) analysis was per-formed in F20 using an Oxford detector, at a beam current of about 1 nA. An EDX resolution of 1-5 nm is routinely achieved on this setup. Sulfur was not found to sublime into vacuum within the electron microscope under the testing conditions, likely due to the core-shell or yolk-shell structure, which protects sulfur against sublimation.

Section 8.3. Results and Discussions

In this paper, sulfur-polyaniline(S-Pani) core-shell and yolk-shell nano-architectures have been prepared, tested and compared. They exhibited different cycling stability especially in prolonged cycling performance. The yolk-shell nano-composite was prepared through a heating treatment of core-shell composite and was found to provide higher capacity retention owing to its unique morphology that encapsulated the sulfur inside the polymer shells with buffer void. The advantage of yolk-shell structures lies in the presence of internal void space to accommodate the volumetric expansion of sulfur during lithiation, thus preserving the structural integrity of the shell while minimizing polysulfide dissolution. With the help of this yolk-shell structure, the capacity of Li/S batteries could be stabilized at 765 mAh g^{-1} at 0.2 C and 628 mAh g^{-1} at 0.5 C after 200 cycles.

The S-Pani core-shell structure was synthesized as shown in Figure 1. First, the mono-dispersed sulfur nanoparticles were prepared through the reaction of sodium thiosulfate with acid (HCl, HCOOH and H_2SO_4 were tested) in the presence of 1% (weight ratio) of polyvinylpyrrolidone (PVP, Mw~40000).[32,33] The freshly prepared sulfur particles were then dispersed in an aqueous solution of aniline and diluted sulfuric acid under strong stirring. The polyaniline coated sulfur could be obtained through oxidation with ammonium persulphate at 0^oC for 24 hours.[34,35] The scanning electron microscopy (SEM) image in Figure 1 shows uniform spherical nanoparticles prepared using H_2SO_4 as the acid source, with averaging diameter about 348±20 nm. When HCl and HCOOH were employed as the acid sources, the obtained nanoparticles showed not only larger but also ununiformed nanoparticles, as shown in the Supporting Information(SI) Figure S1. Comparisons of maximum particle size obtained in the

presence of 1% PVP show the following order: H_2SO_4 < HCOOH < HCl. The surface of S-Pani particles appears to be very rough, with many nanoparticles protruding on the surface (SI, Figure S2), which can be attributed to the cross aggregation of polyaniline chains. The high angle annular dark field and bright field scanning transmission electron microscopy (HAADF-STEM, BF-STEM) images indicated that sulfur nanoparticles were uniformly encapsulated inside the polyaniline shell. From the contrast variation in Figure 2a-b, the polyaniline shell was measured to be about 15 nm, whereas the sulfur core was about 300 nm. Energy dispersive x-ray (EDX) elemental mapping confirmed that the core of the particle in Figure 2b was sulfur, along with overlaying carbon and nitrogen signals from coating polyaniline shells (Figure 2c). The EDX spectrum displayed a very strong sulfur peak, which was over ten-fold higher in peak intensity relative to carbon, as shown in Figure 2d. The X-ray diffraction (XRD) data of this S-Pani core-shell structure only gave the well matched signals of orthorhombic sulfur, as shown in the Figure S3 of SI, indicating the polyaniline was amorphous. Thermogravimetric analysis (TGA) showed that about 82 wt% of sulfur was incorporated in the S-Pani composite (SI, Figure S4). Compared with recent reports on the polymer coated sulfur composites,[21,22,36,37] much smaller sulfur particles and thinner polymer shell were obtained in this study, which would facilitate both the lithium ionic transportation and the electrochemical availability efficiency of sulfur owing to the poor conductivity of sulfur.

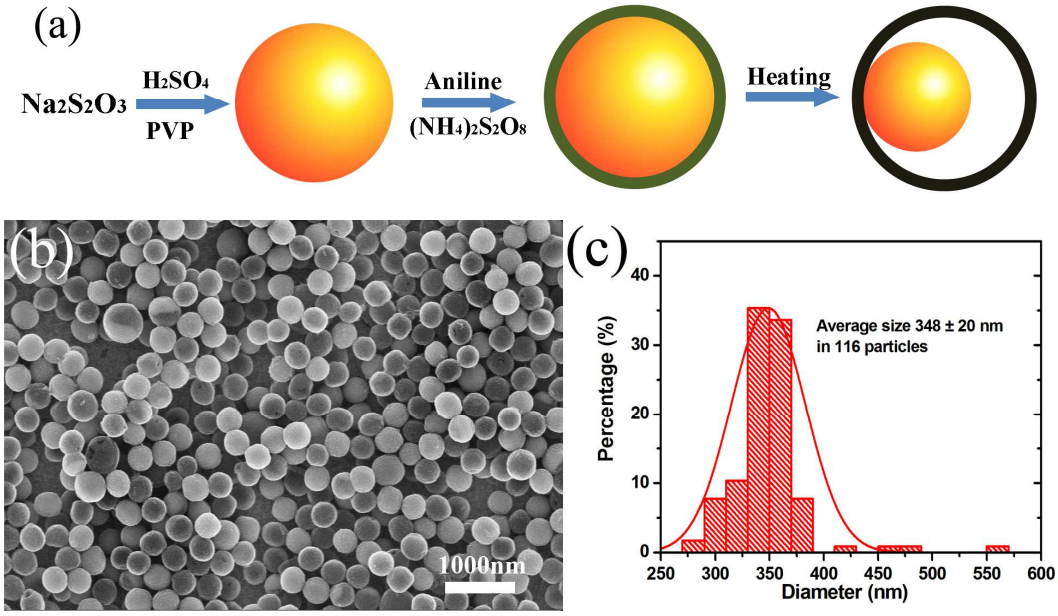

Figure 1. (a) Two step synthesis route for a S-Pani composite, with yellow sphere representing sulfur and dark green shell representing polyaniline and the black shell representing vulcanized polyaniline. (b) SEM images of S-Pani core-shell composite using H_2SO_4 as the acid source and (c) the particle size distribution.

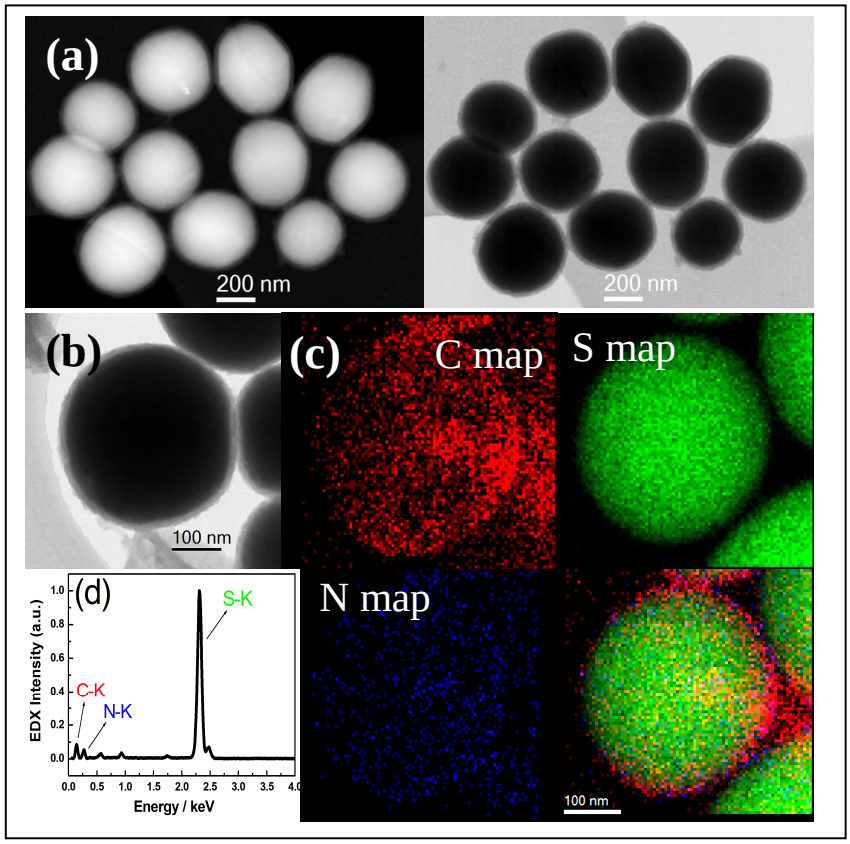

Figure 2. (a) HAADF and BF STEM images of S-Pani core-shell structure. (b) Magnified image of a single S-Pani core-shell particle and (c) the corresponding EDX elemental mapping of carbon, sulfur, nitrogen, along with an overlay of those three maps, showing the enrichment of carbon and nitrogen on the shell. (d) EDX spectrum of S-Pani core-shell composite.

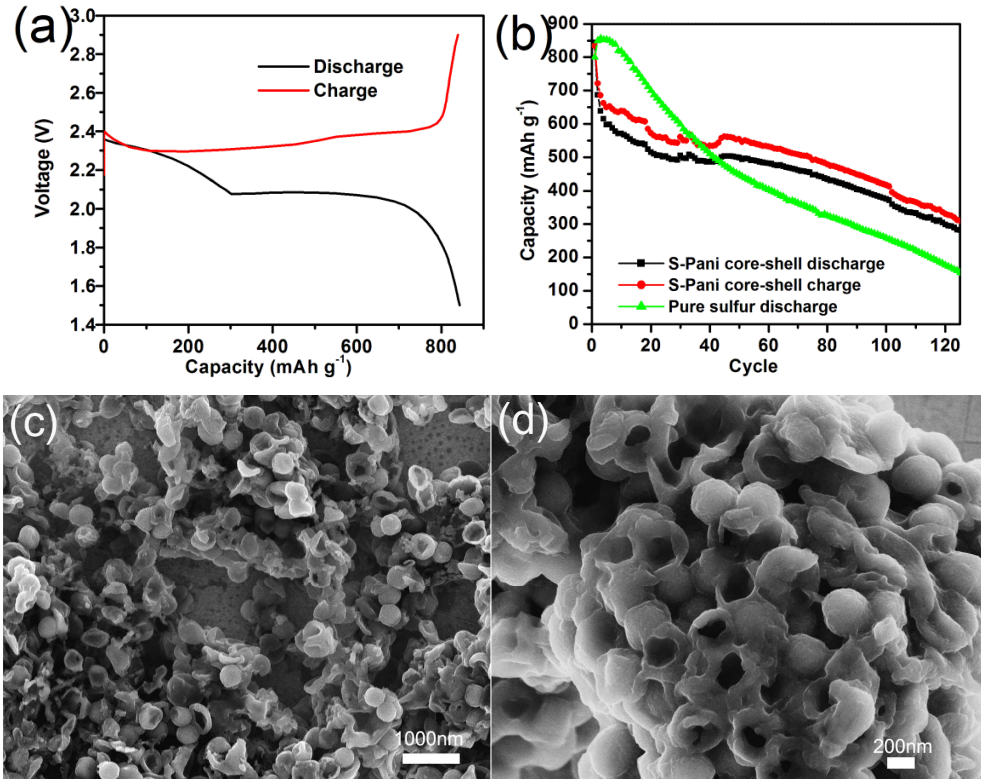

Figure 3. (a) Charge/discharge profiles and (b) Charge/discharge capacities *vs* cycle number for a S-Pani core-shell cathode at a rate of 0.2C (1C=1672 mA g^{-1}). The capacity values were calculated based on the mass of sulfur. The large scale (c) and magnified (d) SEM images of S-Pani core-shell structures after running 5 cycles in the coin cell.

We prepared cells, in which the S-Pani core-shell composite was used as cathode, lithium foil as the anode and 1.0M lithium bis-trifluoromethanesulfonylimide (LiTFSI) in a mixed solvent of 1,3-dioxolane and 1,2-dimethoxyethane (DOL/DME, 1:1, v/v) containing $LiNO_3$ (1 wt%) as the electrolyte. S-Pani was mixed with carbon black (Super P) and water soluble binder sodium alginate (80:15:5 by weight) to prepare the cathode film.[38] Here, water soluble binder was employed to avoid unwanted dissolution of sulfur or even the damage of the nano-structures. As shown in Figure 3a, two well-defined discharge plateaus were observed, which could be assigned to the multi-step reduction mechanism of elemental sulfur, as reported previously.[6-8] The first plateau, centered around 2.35V, was generally attributed to the reduction of the S_8 ring and the formation of S_8^{2-}. The discharge plateau at 2.08V was ascribed to the further reduction of the higher polysulfides (Li_2S_n, $4 \leq n \leq 8$) to the lower polysulfides (Li_2S_n, $n \leq 3$). Within the first 20 cycles, the capacity showed clear fading with cycling, followed by a relatively stable capacity from the 20th to the 50th cycle. These features were similar to the previous reports,[22,36] where only first 50 cycles were presented. In longer cycling, the capacity dropped heavily from 510 mAh g^{-1} to 280 mAh g^{-1} after 125cycles, indicating that the core-shell structure was not effective in preventing the long-term loss of sulfur into the electrolyte during the redox processes. In comparison, a control electrode based on pure sulfur suffered from a much faster capacity fade, yielding a capacity of only 124 mAh g^{-1} after 125 cycles. These results indicate that although the core-shell structure provides a protective coating, it's integrity is not preserved during the volumetric expansion and polysulfides eventually escape during the discharge process. The SEM image of the S-Pani core-shell composite after running 5 cycles in coin cell gave visualized evidence, in which, around half of the particles were broken or shrunk (shown in Figure 3 c and

d). All these above results indicated that the polyaniline shell could not effectively accommodate the large volumetric expansion during the lithiation process, especially in the long term and repeating discharge-charge processes.

In order to provide more space to allow for the volume expansion of sulfur particles during lithiation, it is desirable to develop a S-Pani yolk-shell nanocomposite with polyaniline shells and tunable buffer voids. In this respect, the strategy of leaching sulfur out of the core-shell structures through partial dissolution of sulfur in toluene has been reported.[30] However, if the toluene can leach out the sulfur, it is also plausible that the electrolyte solvent DOL/DME could leach out the polysulfides during the discharge-charge process. To verify this, we tried to prepare the S-pani yolk-shell nanocomposites by leaching them with toluene/ethanol. As predicted, all of the core-shell structures were broken and the resulting half-bowl structures were observed, as shown in images of the Figure 4a. The STEM image exhibited that there was almost no sulfur left in the half bowl structures (Figure 4b), which indicates that nano-size sulfur was easily dissolved out under these conditions and the polyaniline shells were subsequently collapsed.

From recent studies on polyaniline doped sulfur for Li/S electrode composites, polyaniline could react with sulfur at high temperature to form a cross-linked structure, which significantly improved the cycling performance.[39,40] With this knowledge in mind, the S-Pani core-shell composites were heated at 180°C in a sealed tube filled with argon for 12 hours, with the expectation that elemental sulfur would react with polyaniline shell to form a three-dimensional, cross-linked S-Pani yolk-shell structure with both inter- and/or intra-chain sulfide and/or disulfide bonds interconnection through *in-situ* vulcanization.[39] Such a S-Pani yolk-shell

structure could potentially help to provide buffer void space for the volumetric expansion of the polysulfides during lithiation and physically confine the elemental sulfur and the polysulfides.

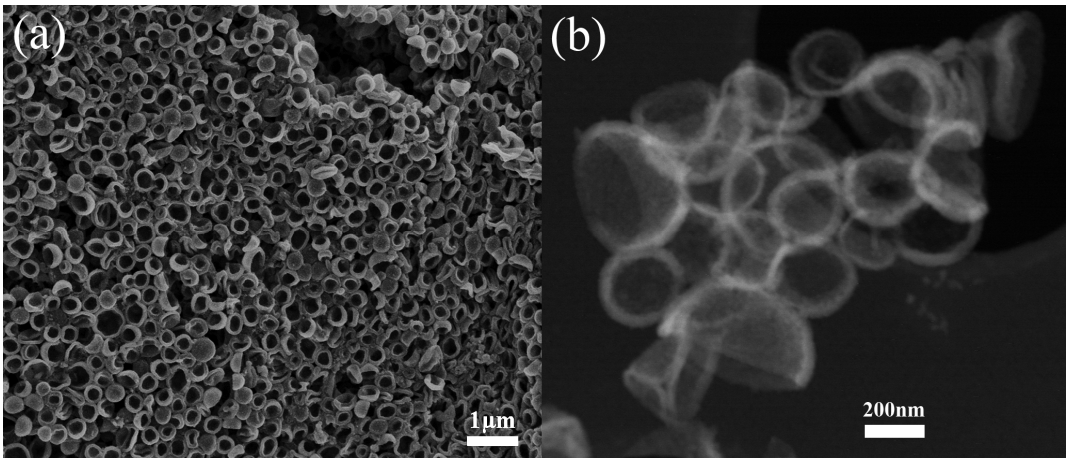

Figure 4. (a) SEM and (b) HAADF-STEM images of S-Pani core-shell structure after leaching in toluene/ethanol.

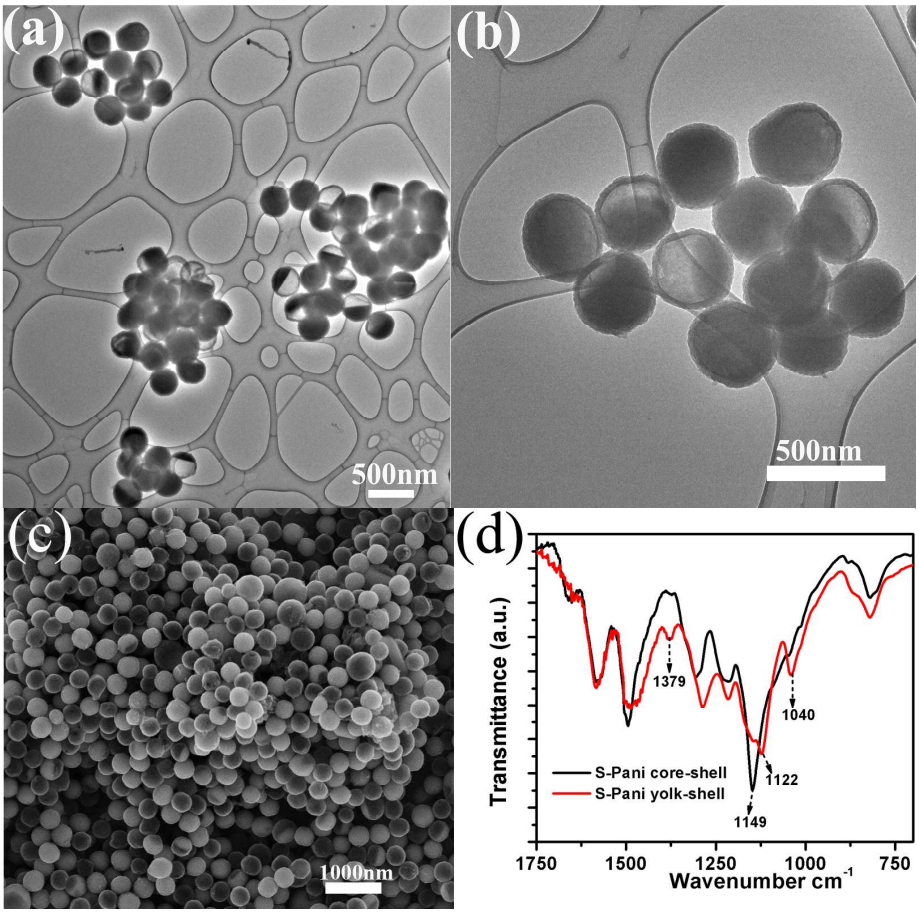

Figure 5. (a) Large scale TEM image and (b) magnified TEM image and (c) SEM image of S-Pani yolk-shell structures after heat-treatment. (d) FTIR spectra of S-Pani core-shell and yolk-shell structures.

Transmission electron microscopy (TEM) and SEM images of S-Pani after heat treatment exhibited uniform, yolk-shell structures without any broken shell, as shown in Figure 5. The intact polymer shell was well preserved and partially hollowed yolk-shell structures of the S-Pani can clearly be observed. The void space appeared as either an empty area or lower intensity area due to the two-dimensional projection nature of the TEM images.[41] The ability of sulfur vapor to diffuse out through the polyaniline shell indicates the porous nature of polyaniline shells, which can be ascribed to the cross aggregation of polyaniline chains. Unlike what the S-Pani core-shell structure did in the toluene/ethanol, the polyaniline shell did not shrink with the diffusing out of the sulfur in the heating treatment, suggesting that the mechanical strength of polyanilne shell was enhanced during the heating vulcanization. It can be attributed to the cross-linked sulfide and/or disulfide bonds interconnection among polyaniline chains. To verify it experimentally, Fourier transformed infrared (FTIR) spectra of S-Pani core-shell and heat treated yolk-shell structures were recorded and shown in Figure 5d. Both the C=C stretching vibration at 1497 cm^{-1} from the benzenoid rings and the C-N stretching vibrational bands at 1307 cm^{-1} shifted to lower wave numbers, owing to the substitution of H atoms on benzenoid rings by S atoms. Three peaks at 1379, 1122 and 1040 cm^{-1} arose in the heat treated S-Pani yolk-shell composites, which could be assigned to the vibration of C-S.[42-44] The intensity of the C-H vibrational band in the vicinity of 1149 cm^{-1} significantly weakens, further confirming the replacement of H atoms on aromatic rings by S atoms.[39] And the heat treated S-Pani yolk-shell composites showed a blacker color compared with the dark green of S-Pani core-shell composites, as shown in the Figure S5 of SI. Different to the orthorhombic sulfur of S-Pani core-shell composite, the XRD of heat

treated S-Pani yolk-shell composite indicated that it contained two types of sulfur, the sulfur (orthorhombic) and Rosickyite (monoclinic), as shown in the Figure S6. This indicates the formation of Rosickyite after heat treatment, giving rise to a polymorph of sulfur. These features confirm that elemental sulfur reacted with the unsaturated bonds of polyaniline during the heat treatment, through a well-known vulcanization reaction. The sulfur content was found to be about 58% in the heat treated yolk-shell composites according to the TGA result in the Figure S7 of SI, which was around 46% in the whole electrode films considering 20% of carbon black and binder. The formation of the yolk-shell structure could be attributed to the vulcanizing reaction and partial evaporation of the elemental sulfur during the heating treatment.

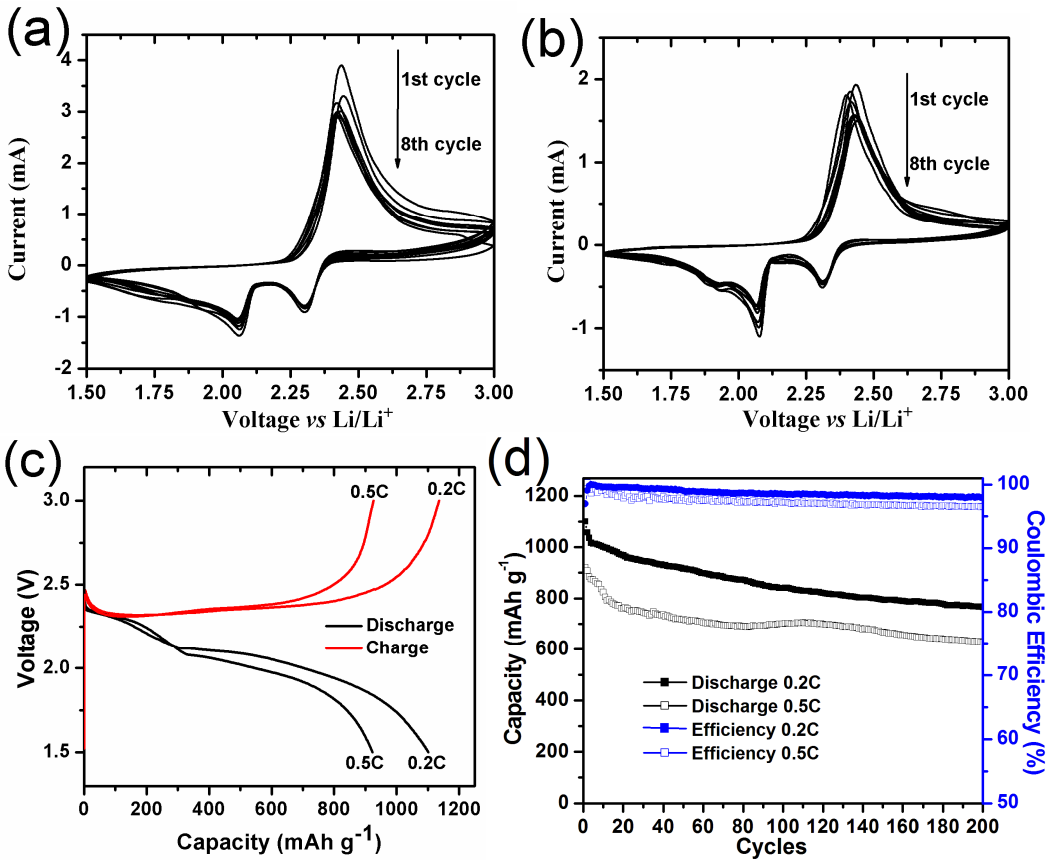

Figure 6. Typical CV curves of S-Pani yolk-shell cathode at a sweep rate of 0.05 mV s^{-1}(a) and 0.02 mV s^{-1}(b); Charge/discharge profiles and capacities *vs* cycle number for S-Pani yolk-shell composite cathodes at a rate of 0.2C (c) and 0.5C (d).

Cyclic voltammograms (CVs) of a Li-S cell with a heat treated S-Pani yolk-shell cathode was obtained at a scan rate of 0.05 mV s^{-1} and 0.02 mv s^{-1}(Figure 6a and 6b). Two reduction peaks around 2.35 and 2.08 V were observed and could be assigned to the multi-step reduction mechanism of elemental sulfur, as reported previously.[6-8] Compared with typical CV curves of Li-S cell, the reduction peak of the heat treated S-Pani yolk-shell cathode at 2.08V was a little smaller and a shoulder centered at 1.9V could be clearly observed, especially at a slow scan rate. Also, the reduction peak at 1.9V could be observed in every reduction cycle of the CV curves from the Figure 6a and 6b, indicating that the reduction at 1.9V was reproducible. This reduction peak could be attributed to the reduction of disulfide bonds connected with polyaniline through the vulcanization.[40] Figure 6c shows the discharge-charge profiles of coin cells using heat treated S-Pani yolk-shell composites as the cathode materials at different current densities. Different to two clear discharge plateaus of the S-Pani core-shell composite electrode, two less well defined discharge plateaus centered around 2.35 and 2.08V were observed for heat treated S-Pani yolk-shell composites, which was in highly agreement with the CV curves of Figure 6a.[39,40] As illustrated in Figure 6c, the heat treated S-Pani yolk-shell composites showed an initial capacity of 1101 and 920 mAh g^{-1} under different current densities of 0.2 and 0.5 C, respectively. Although there was an initial capacity drop, the capacity tended to stabilize after about 10 cycles at both 0.2 C and 0.5 C (Figure 6d). Compared to the S-Pani core-shell electrode described earlier, the heat treated yolk-shell composite electrode exhibited significantly improved capacity retention with cycling, which could be ascribed to the combined contributions from buffer space and stabilized shell through vulcanization. After cycling for 200 cycles, a discharge capacity of 765 mAh g^{-1} was obtained at 0.2 C, which corresponded to a 69.5% capacity retention. At a

higher current density of 0.5 C, a stable cycling performance was observed with a capacity around 628 mAh g^{-1} and a 68.3% capacity retention after running 200 cycles. The relatively lower cycling performance at 0.5 C can be attributed, at least in part, to the lower Coulombic efficiency at this current density. The improved cycling stability verifies that the yolk-shell structure can help to immobilize the polysulfides and mitigate capacity fading. To further investigate the stability of the yolk-shell structure during the cycling of coin cell, a cell was disassembled after running 5 cycles and the composite was regained after rinsing with water. As shown in the Figure 7, the intact polyaniline shells were still preserved, which suggests that the shell of vulcanized polyaniline can accommodate the volumetric expansion during the charge/discharge process. During the discharge process, the elemental sulfur was first reduced due to it's relatively higher reducing potential. With the reducing of elemental sulfur, that is, the lithiation process, the volume of the sulfur/sulfide species was increased to near twice, which will fill the void space within the shell. After that, the disulfide bonds among polyaniline chains were reduced and the shell should not shrink much due to the volumetric increase of the inside sulfide species during lithiation. In subsequent charge process, the sulfide anions on the polymer chains could be re-oxidized to form disulfide again and recover the cross-linked polyaniline shell. So, theoretically, these processes should not destroy the yolk-shell structure. Experimentally, the CV gave reproducible reduction shoulder at 1.9V, which indicate these processes were reversible. In addition, the SEM and TEM images of the yolk-Shell structure after running 5 cycles gave visible evidence that the structure was well preserved.

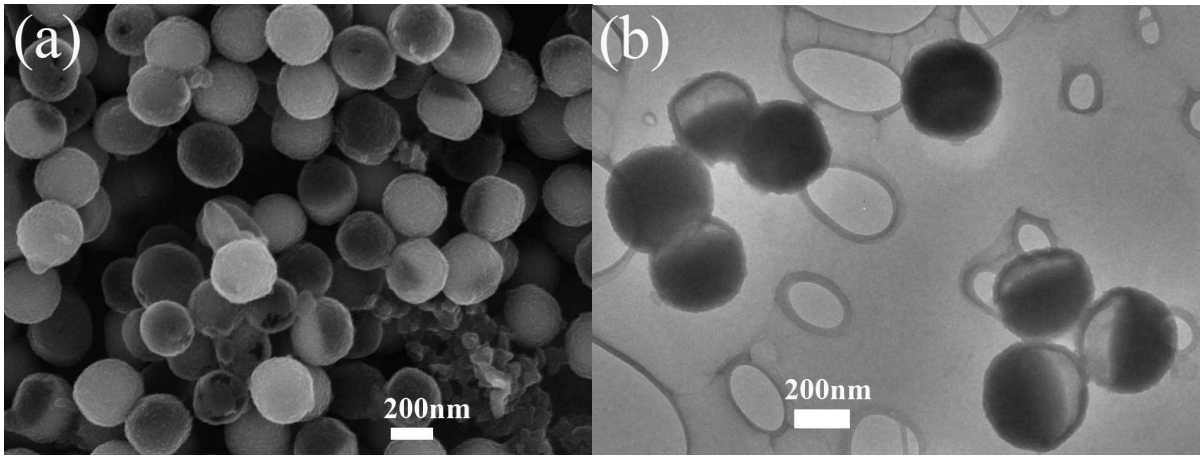

Figure 7. The SEM (a) and TEM (b) images of S-Pani yolk-shell structures after the 5th charge in the coin cell. Small particles are the carbon black particles.

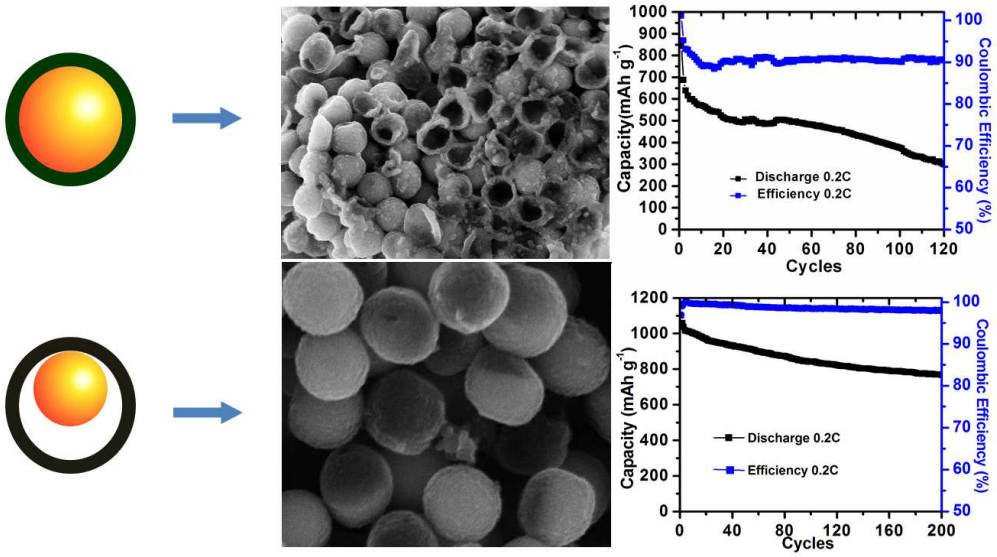

Figure 8. Schematically comparison of the S-Pani core-shell and yolk-shell SEM images after running 5 cycles in cells and the long term cycling performance.

The significantly improved cyclability could be ascribed to the sufficient buffer space in the yolk-shell structures, which allowed for the volume expansion of sulfur. After the heating treatment, the sulfur weight content dropped from 82% to 58%, as shown in the TGA data of Figure S4 and S7 of SI, which indicated that more than 2/3 of sulfur was evaporated out or reacted with the polyaniline shells based on the assumption that the weight of polyaniline did not change. Since the weight of polyaniline shells should actually increase by some degree during the vulcanization, the evaporated sulfur would be around or less than 2/3. These data indicate that the volume of empty space within the yolk-shell nanostructures was estimated to be around or near twice of the sulfur, which would be enough to accommodate the 80% volumetric expansion during the discharge process without causing the shell to crack.[18] Apparently, these values were supported by the TEM images of Figure 5, in which, more than half of the space within the shell was void. Experimentally, the integrity of polyaniline shells was still well preserved after running 5 cycles in coin cell, as shown in the Figure 8, further confirming that the void buffer space of the yolk-shell structures successfully accommodated the volumetric expansion. By contrast, most polyaniline shells of the core-shell composite were cracked after running 5 cycles in coin cell, as shown in the Figure 8. All these above features, from different sides, verified that internal void space in the yolk-shell nanostructures was sufficient to accommodate the volume expansion of polysulfides during lithiation, thus maintaining the intact shells to minimize the polysulfide dissolution and maximize the capacity retention. One thing we should point out is that although this yolk-shell composite delivered much improved cycling stability compared with the core-shell composite, slow capacity degradation could still be observed. And the efficiency was just around 97%~98%, which indicates that the dissolution of

polysulfides and the subsequent shuttling effect still did not completely vanish in this condition. In addition, the sulfur ratio in the yolk-shell composite was only around 58%, which limited the real capacity based on the composite. But owing to the low cost of widely available polyaniline and the easily scaled up heating process that could give uniform distribution of leaching percentage across the entire array of nanoparticles, it is potentially scalable for industry manufacturing.

Section 8.4. Conclusion

In summary, polyaniline coated sulfur with core-shell and yolk-shell structures have been prepared and investigated to immobilize lithium polysulfides as the cathodes of Li-S cells. Compared with the core-shell composite, the as-synthesized S-Pani yolk-shell composite delivered obviously improved cycling stability. The vulcanized soft polymer shells and yolk-shell structures developed in this study successfully encapsulated the sulfur and polysulfide species within the polymer shell and accommodated the volumetric expansion associated with the lithiation, owing to the presence of internal void space. While slight capacity fading was still observed, we believe that these results provide important insights and novel methodology to confine the sulfur and polysulfides for the future application of Li-S batteries.

Supporting Information

Experimental details for the material preparation, characterization, and device testing, along with additional supporting data. This material is available free of charge via the Internet at http://pubs.acs.org.

REFERENCES

1 Whittingham, M. S. *Chem. Rev*. **2004**, *104*, 4271-4301.

2 Aricò, A. S.; Bruce, P. G.; Scrosati, B.; Tarascon, J.-M.; Schalkwijk, W. V. *Nat. Mater.* **2005**, *4*, 366-377.

3 Guo, Y.; Hu, J.; Wan, L. *Adv. Mater*. **2008**, *20*, 2878-2887.

4 Bruce, P. G.; Freunberger, S. A.; Hardwick, L. J.; Tarascon, J.-M. *Nat. Mater.* **2012,** *11*, 19-29.

5 Manthiram, A.; Fu, Y.; Su, Y.-S. *Acc. Chem. Res.*, **2013**, *46*, 1125-1134.

6 Yamin, H.; Gorenshtein, A.; Penciner, J.; Sternberg, Y.; Peled, E. *J. Electrochem. Soc*. **1988**, *135*, 1045-1048.

7 Peled, E.; Sternberg, T.; Gorenshtein, A.; Lavi, Y. *J. Electrochem. Soc*. **1989**, *136*, 1621-1625.

8 Jin, B.; Kim, J. U.; Gu, H. B. *J. Power Sources* **2003**, *117*, 148-152.

9 Jayaprakash, N.; Shen, J.; Moganty, S. S.; Corona, A.; Archer, L. A. *Angew. Chem. Int. Ed.* **2011**, *50*, 5904-5908.

10 Liang, C.; Dudney, N. J.; Howe, J. Y. *Chem. Mater*., **2009**, *21*, 4724-4730.

11 Zhang, C.; Wu, H.; Yuan, C.; Guo, Z.; Lou, X. W. *Angew. Chem. Int. Ed.* **2012**, *51*, 9592-9595.

12 Ji, X.; Lee, K. T.; Nazar, L. F. *Nat. Mater.* **2009**, *8*, 500-506.

13 Zhang, B.; Qin, X.; Li, G. R.; Gao, X. P. *Energy Environ. Sci*., **2010**, *3*, 1531-1537.

14 Ji, X.; Evers, S.; Black, R.; Nazar, L. F. *Nat. Commun*. **2011**, *2*, 325.

15 Schuster, J.; He, G.; Mandlmeier, B.; Yim, T.; Lee, K. T.; Bein, T.; Nazar, L. F. *Angew. Chem. Int. Ed.* **2012**, *51*, 3591-3595.

16 Xin, S.; Gu, L.; Zhao, N.; Yin, Y.; Zhou, L.; Guo, Y.; Wan L. *J. Am. Chem. Soc.*, **2012**, *134*, 18510-18513.

17 Han, S.-C.; Song, M.-S.; Lee, H.; Kim, H.-S.; Ahn, H.-J.; Lee, J.-Y. *J. Electrochem. Soc.* **2003**, *150*, A889-A893.

18 Yang, Y.; Yu, G.; Cha, J. J.; Wu, H.; Vosgueritchian, M.; Yao, Y.; Bao, Z.; Cui, Y. *ACS Nano*, **2011**, *5*, 9187-9193.

19 Yin, L.; Wang, J.; Yang, J.; Nuli, Y. *J. Mater. Chem.* **2011**, *21*, 6807-6810.

20 Wu, F.; Chen, J.; Li, L.; Zhao, T.; Chen, R. *J. Phys. Chem. C*, **2011**, *115*, 24411-24417.

21 Wu, F.; Chen, J.; Chen, R.; Wu, S.; Li, L.; Chen, S.; Zhao, T. *J. Phys. Chem. C*, **2011**, *115*, 6057-6063.

22 Fu, Y.-Z.; Manthiram, A. *J. Phys. Chem. C* **2012**, *116*, 8910-8915.

23 Su, Y.-S.; Manthiram, A. *Nat. Commun*. 2012, 3. 1166.

24 Wang, L.; Wang, D.; Zhang, F.; Jin, J. *Nano Lett*. **2013**, *13*, 4206-4211.

25 Yin, L.; Wang, J.; Lin, F.; Yang, J.; Nuli, Y. *Energy Environ. Sci*., **2012**, *5*, 6966-6972.

26 Guo, J.; Xu, Y.; Wang, C. *Nano Lett*. **2011**, *11*, 4288-4294.

27 Guo, J.; Yang, Z.; Yu, Y.; Abruña, H. D.; Archer, L. A. *J. Am. Chem. Soc.*, **2013**, *135*, 763-767.

28 Zheng, G.; Zhang, Q.; Cha, J. J.; Yang, Y.; Li, W.; She, Z. W.; Cui, Y. *Nano Lett*. **2013**, *13*, 1265-1270.

29 Lu, S.; Cheng, Y.; Wu, X.; Liu, J. *Nano Lett*. **2013**, *13*, 2485-2489.

30 Seh, Z. W.; Li, W.; Cha, J. J.; Zheng, G.; Yang, Y.; McDowell, M. T.; Hsu P.-C.; Cui, Y. *Nat. Commun.* **2013**, *4*, 1331.

31 Schneider, H.; Garsuch, A.; Panchenko, A.; Gronwald, O.; Janssen, N.; Novák, P. *J. Power Sources* **2012**, *205*, 420-425.

32 Ji, L.; Rao, M.; Zheng, H.; Zhang, L.; Li, Y.; Duan, W.; Guo, J.; Cairns, E. J.; Zhang, Y. *J. Am. Chem. Soc.*, **2011**, *133*, 18522-18525.

33 Wang, H.; Yang, Y.; Liang, Y.; Robinson, J. T.; Li, Y.; Jackson, A.; Cui, Y.; Dai, H. *Nano Lett.*, **2011**, *11*, 2644-2647.

34 Jang, J.; Ha, J.; Lim, B. *Chem. Commun*., **2006**, 1622-1624.

35 Liu, Y. D.; Park, B. J.; Kim, Y. H.; Choi, H. J. *J. Mater. Chem*., **2011**, *21*, 17396-17402.

36 Li, G.; Li, G.; Ye, S.; Gao, X. *Adv. Energy Mater.* **2012**, *2*, 1238-1245.

37 Duan, L.; Lu, J.; Liu, W.; Huang, P.; Wang, W.; Liu, Z. *Colloids and Surfaces A*: *Physicochem*. *Eng*. *Aspects* 2012, *414*, 98-103.

38 Kovalenko, I.; Zdyrko, B.; Magasinski, A.; Hertzberg, B.; Milicev, Z.; Burtovyy, R.; Luzinov, I.; Yushin, G. *Science* **2011**, *334*, 75-79.

39 Xiao, L.; Cao, Y.; Xiao, J.; Schwenzer, B.; Engelhard, M. H.; Saraf, L. V.; Nie, Z.; Exarhos, G. J.; Liu J. *Adv. Mater.* **2012**, *24*, 1176-1181.

40 Zhang, S.; Zhang, L.; Wang, W.; Xue, W. *Synthetic Met.* **2010**, *160*, 2041-2044.

41 Gu, M.; Li, Y.; Li, X.; Hu, S.; Zhang, X.; Xu, W.; Thevuthasan, S.; Baer, D. R.; Zhang, J.; Liu, J.; Wang, C. *ACS Nano*, **2012**, *6*, 8439-8447.

42 Yu, X.; Xie, J.; Yang, J.; Huang, H.; Wang, K.; Wen, Z. *J. Electroanal. Chem.* **2004**, *573*, 121-128.

43 Aurbach, D.; Pollak, E.; Elazari, R.; Salitra, G.; Kelley, C. S.; Affinito, J. *J. Electrochem. Soc.* **2009**, *156*, A694-A702.

44 Diao, Y.; Xie, K.; Xiong, S.; Hong, X. *J. Electrochem. Soc.* **2012**, *159*, A1816-A1821.

CHAPTER 9

INFILTRATING SULFUR IN A HIERARCHICAL ARCHITECTURE MWCNT@MESO C CORE-SHELL NANOCOMPOSITES FOR LITHIUM-SULFUR BATTERIES[*†]

Section 9.1. Introduction

Numerous effects has been focused on developing new materials for Li-ion batteries (LIBs), however, limited by the intercalation chemistry of the materials, LIBs cannot meet the increasing demand for higher the energy/power density for applications in hybrid electric vehicles or efficient storage for renewable energy. It is of urgent to explore new materials with high specific energy. Element sulfur (S), with a high theoretical specific capacity of 1675 mA h g^{-1},[1-5] and high specific energy density of 2600 Wh kg^{-1}(when coupled with a Li metal electrode), which is about five times higher than conventional LIBs (410 Wh kg^{-1})[6, 7]. In addition to the high capacity, sulfur as a cathode material also has the advantages of natural abundance, cheap and environmentally friendly,[8] makes Li/S batteries a promising candidate for the next-generation rechargeable batteries.

---

[*] Produced with permission from Deli Wang, Yingchao Yu, Weidong Zhou, Hao Chen, David A. Muller, Francis J. DiSalvo, Hector D. Abruña. *Physical Chemistry Chemical Physics*, 2013,15,9051 Copyright © 2013 Royal Society of Chemistry

[†] D.W. synthesized the sample, Y.Y. performed the microscopy imaging. D.W. and Y.Y. designed and analyzed the battery testing. W.Z. and H.C. helped to perform the synthesis as well as analyzing data. D.A.M., H.D.A. and F.J.D. guided the work.

However, the insulating nature of sulfur and the solubility of lithium polysulfide intermediates in the electrolyte limit the widespread practical use of Li/S batteries technology. One of the ways to overcome the sulfur cathode challenges is to use carbon materials as hosts to improve the conductivity of sulfur and alleviate the diffusion of lithium polysulfide into the electrolyte. Many efforts have been made to prepare various structure and morphology of carbon materials including carbon nanotubes,[9-13] mesoporous carbon,[1, 14-18] carbon nanofibers,[19-21] hollow carbon,[3, 22] graphene/oxides,[23, 24] etc. Multi wall carbon nanotubes (MWCNTs) have been used as carbon matrix and electric conductor for sulfur cathode because of their high conductivity and unique structure. It is reported the cyclability of the Li/S batteries could be improved by combining sulfur with MWCNTs.[13] However, the low surface area (typically less than 200 m^2/g) and pore volume of CNTs limit their capability to accommodate much sulfur. Mesoporous carbons (Meso Cs) with higher surface area and inter connected pore networks have attracted much attention for application in Li/S batteries. For example, by confining sulfur in mesoporous carbon, the S/C composites show a high initial discharge capacity of 1320 mA h g^{-1} and a slow capacity fading over 20 cycles at a current density of 168 mA g^{-1}.[1] However, the electronic conductivity of mesoporous carbon is much lower than other graphite-based materials due to its disordered amorphous nature. Inspired by these previous work, by combining the advantages of MWCNTs and Meso Cs, the hierarchical architecture of MWCNT@Meso C nanocomposites with high surface area and good electronic conductivity might serve as good carbon matrix for Li/S batteries.

Herein, we report the rational design and synthesis of a hierarchical architecture MWCNT@Meso C with a core-shell configuration as an improved confined matrix for the sulfur cathode. In this MWCNT@Meso C core-shell structure, the mesoporous carbon shell serves as carbon matrix to trap sulfur, while the high aspect ratio MWCNT core facilitate the electron transport.

Section 9.2. Materials and Methods

Synthesis of MWCNT@meso C composites. The coating of mesoporous carbon on MWCNTs was conducted using MWCNT@meso SiO_2 composites as a hard template. The MWCNT@meso SiO_2 composites were firstly synthesized according to a sol-gel coating method.[33, 34] In a typical synthesis, 200 mg MWCNTs were dispersed in a CTAB containing EtOH/H2O mixture solution. After sonicating for 1 h, 4 mL ammonia was immediately added into above mixture, and then TEOS (2 mL in 80 mL EtOH) was added and the mixture was stirred under magnetic stirring for 12 h. The mixture was then centrifuged and washed with EtOH and pure water. After vacuum drying, the surfactants in the mixture were removed by ion exchange method (4 g NH_4NO_3 in 240 mL acetone) to obtain a core-shell structured MWCNT@meso SiO_2 composite.

The as-prepared MWCNT@meso SiO_2 composites were then used as a hard template, furfuryl alcohol as a carbon source and oxalic acid as a catalyst to synthesize MWCNT@meso C composites. Typically, 300 mg MWCNT@meso SiO_2 composites were added in an EtOH solution containing 450 mg furfuryl alcohol and 3 mg oxalic acid. After sonicating for half an hour, the mixture was placed in a sealed Teflon container. The hydrothermal reaction was carried out at 80 ^oC for 48 h in order to completely fill the

nanopores of SiO_2 with carbon source. The MWCNT@meso C composites were then obtained after being pyrolyzed at 150 ^oC for 3 h and carbonized at 900 for 2 h. Finally, the silica in the composites was etched in a NaOH solution to obtain MWCNT@meso C composites.

Infiltrating S in MWCNT@meso C composites. Sulfur was infiltrated in the MWCNT@meso C composites by an impregnation-heating method. Firstly, 120 mg sulfur were dissolved in THF under magnetic stirring at 40 ^oC, and 80 mg MWCNT@meso C as carbon matrix were dispersed in it. After ultrasonic blending for 30 min, the suspension was heated atb 40 ^oC under magnetic stirring to allow the solvent to evaporate and to form slurry. The slurry was dried in a vaccum oven at 40 ^oC. After being ground in an agate mortar, the powder was then transferred to a Schlenk / vacuum line and sealed under vacuum. The sample was heated to 200 ^oC for 5 hours to infuse sulfur into the mesoporous carbon host. S/MWCNT composites were also synthesized using the same procedure for comparison.

Characterization. The samples were characterized by powder X-ray diffraction using a Rigaku® Ultima VI diffractometer, operated at 40 kV and 44 mA, and diffraction patterns were collected at a scanning rate of 5 ^{o}/min and with a step of 0.02 ^{o}. TEM was performed using a Shottky-field-emission-gun Tecnai F20 operated at 200 kV. The electron energy loss spectroscopic maps were acquired on a 100 kV 5th-order aberration-corrected scanning transmission electron microscope (Nion UltraSTEM).

Electrochemical measurements. The electrochemical measurements were carried out with CR 2032 coin cells assembled in an argon-filled glove box with lithium metal as anode. The cathodes consisted of 90 wt% active materials and 10 wt% polytetrafluoroethylene as a binder, which were rolled into a thin film. After drying under vacuum at 40 ^{o}C, the film was cut into a circular electrode with an area of 0.71 cm^2. The cut film was then pressed onto a nickel foam as cathode for Li/S battery. Using lithium foil as the anode, the electrodes were separated by a separated material (Celgard 2320). The electrolyte is 1.0 M $LiN(CF_3SO_2)_2$ (LiTFSI) in a mixture of dimethoxyethane (DME) and 1,3-dioxolane (DOL) with 1 : 1 v/v.

Galvanostatic charge/discharge of the coin cells were tested using Arbin battery testing system with a constant discharge current density of 100 mAg^{-1} and charge current density of 100 mAg^{-1}. at a cut-off potential of 1.5–3.0 V under room temperature. All the capacities were normalized to the mass of the sulfur in the active materials. Cyclic voltammetry (CV) testing of the cells were performed on a Solartron electrochemistry working station at a scan rate 0.05 mV s^{-1}

Section 9.3. Results and Discussions

The MWCNT@Meso C core-shell composites were prepared by using sol-gel coating method followed by nanocasting. As shown in Scheme 1, the porous SiO_2 was first coated outside of MWCNT using TEOS as Si source with the aid of cationic surfactant CTAB. The MWCNT@Meso SiO_2 composites were obtained by removing CTAB via an ion-exchange procedure. The MWCNT@Meso SiO_2 nanocomposites then

served as a “hard template” which were soaked with furfural alcohol and oxalic acid. After carbonizing at high temperature and removing of SiO_2, mesoporous C coated MWCNT nanocomposites were obtained. These core-shell structures can be seen clearly from STEM images (Figure 1). Before coating, the diameter of MWCNTs is about 20 nm (Figure a and a’). After coating with a thin SiO_2 layer, the diameter increased by 10 nm, corresponding to a 5 nm thick SiO_2 layer on the MWCNTs surface (Figure b and b’). Figure 1c and c’ show a pair of dark and bright-field STEM images of MWCNT@Meso C. Compared with original MWCNT, the 1-D tubular structures with the retained morphology are reserved, while the surface seems coarser than those of pristine MWCNTs.

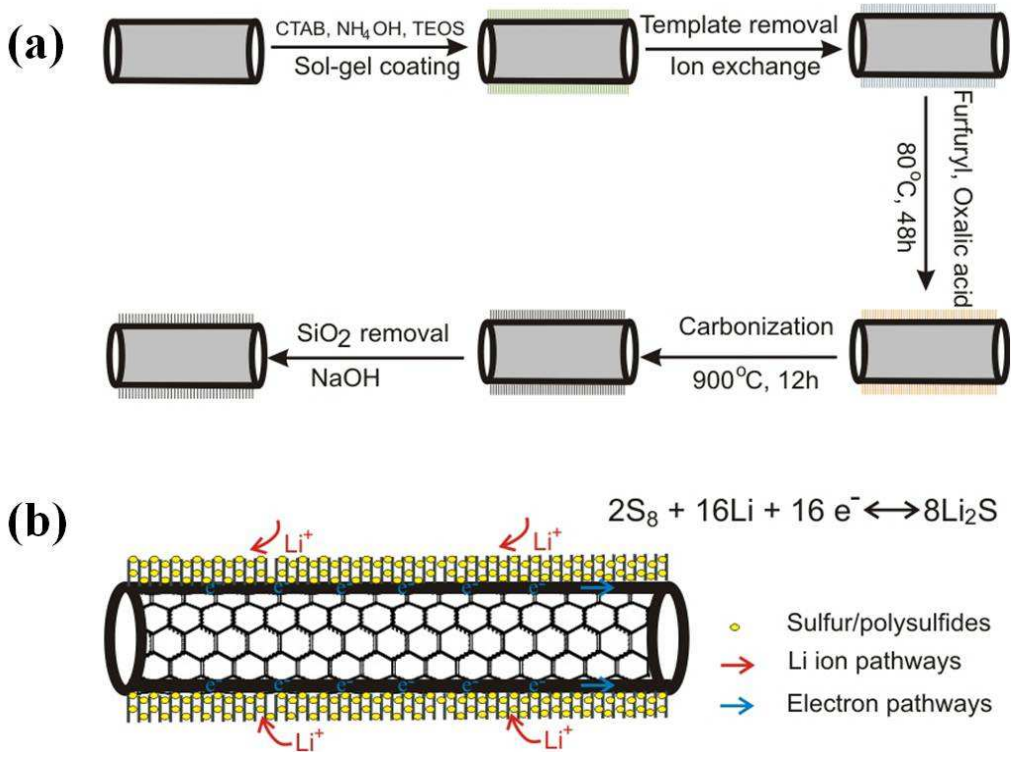

Scheme 1. (a) Synthesis procedure of MWCNT@Meso C core-shell composites; (b) Sulfur infiltrated MWCNT@Meso C core-shell composites as cathode materials for Li/S batteries.

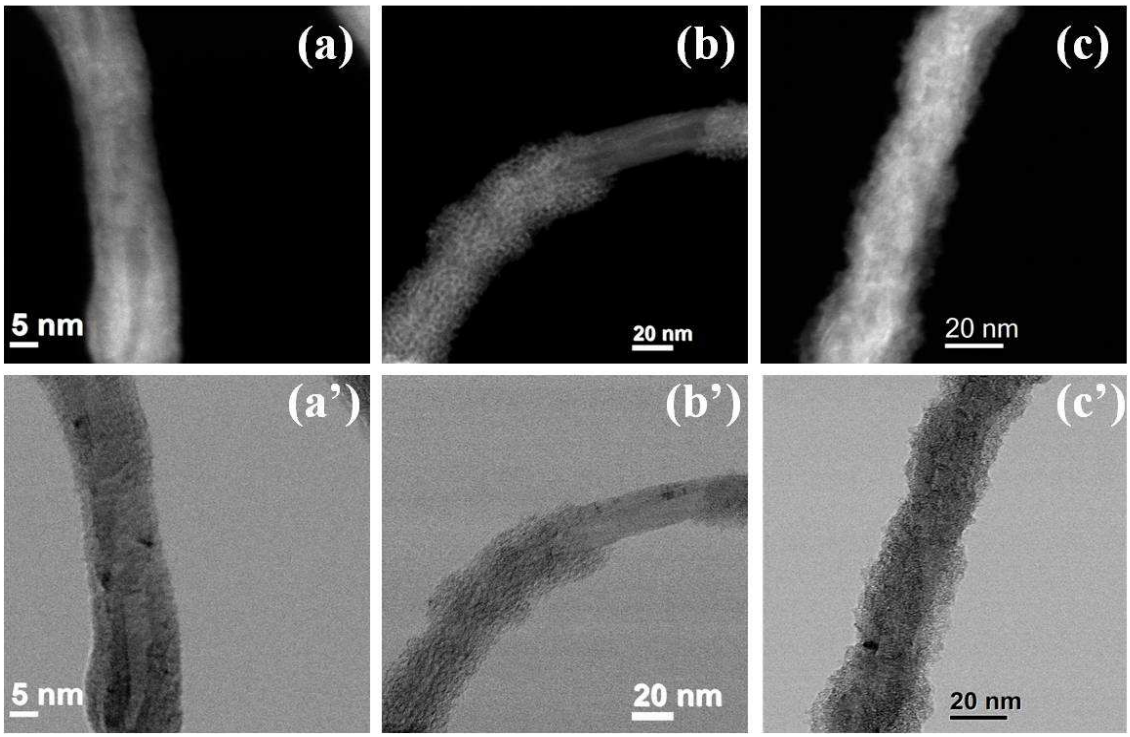

Figure 1. Dark field(a, b and c) and bright field (a', b' and c') STEM images of pristin MWCNT(a,a'), SiO_2 coated MWCNT (b, b'), and mesoporous catbon coated MWCNT (c, c').

Infiltrating sulfur into the MWCNT@meso C core-shell nanocomposites was performed by impregnating followed by vacuum heating method. Specifically, sulfur was first dissolved in THF solution, certain amount of MWCNT@meso C nanocomposites were then dispersed in it. After evaporating solvent and drying in a vacuum oven, the mixture was placed into a quartz tube, which was then transferred to a Schlenk / vacuum line and sealed under vacuum. The sample was then heated to 200 ^{o}C for 5 hours to infuse sulfur into the mesoporous carbon host. S/MWCNT composites were also synthesized using the same procedure for comparison.

Figure 2 show the powder X-ray diffraction (XRD) patterns of sulfur, MWCNT, S/MWCNT, and S/MWCNT@meso C. Pure sulfur shows a typical reflection of a-orthorhombic type of sulfur (S8, JCPDS#08-0247). By combining sulfur with MWCNTs, the diffraction pattern changed to β -monoclinic type of sulfur after impregnation-heating treatment. For S/MWCNT@meso C, the graphitic diffraction peaks of MWCNTs at around 25 ^{o} and 44 ^{o} are still reserved after sulfur infiltration, while the diffraction peaks of sulfur are much weaker or disappeared, indicating sulfur exists as small nanoparticles and dispersed well in the MWCNT@meso C structure.[5, 25, 26] The actual loading of sulfur in S/MWCNT@meso C composites determined using thermogravimetric analysis (TGA) is about 60wt% (Figure 2b), which is close to the nominal ratio.

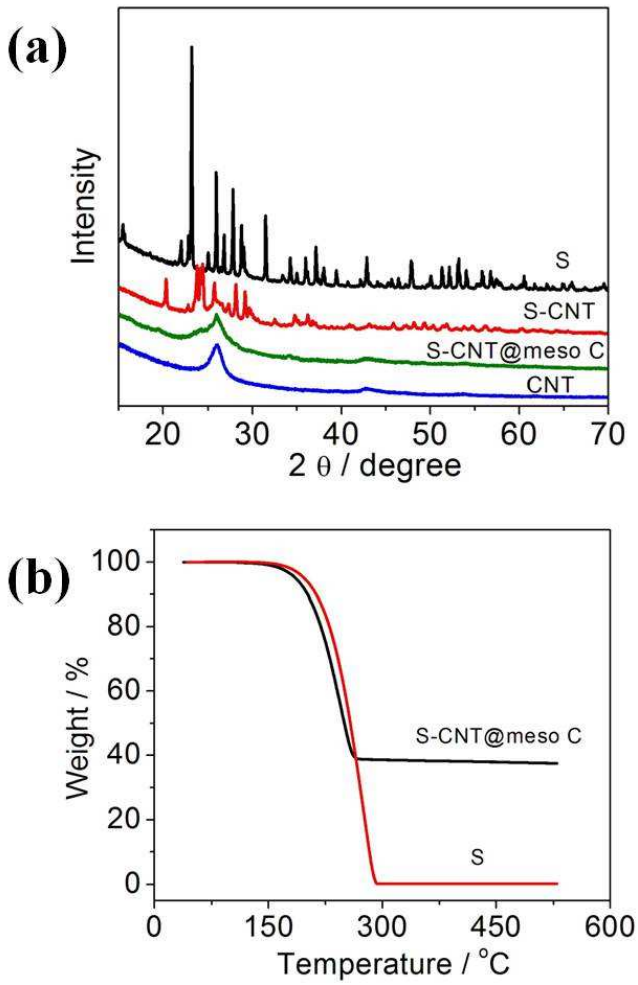

Figure 2. (a) XRD patterns of sulfur, MWCNT, S/MWCNT, and S/MWCNT@meso

Further evidence of sulfur exists in the MWCNT@meso C composite was provided by TEM images and EELS spectrum. As shown in Figure 3a, the EELS spectrum of sulfur $L_{2,3}$ edge was obviously observed. The dark-field STEM image of S/MWCNT@meso C composites (Figure 3b) coupled with the elemental mapping analysis of carbon and sulfur (Figures 3c and d), indicating sulfur dispersed homogenously in the carbon matrix with no obvious aggregation. We can also see from the line profiles that sulfur distributed only on the surface of MWCNT, which is in the matrix of mesoporous carbon (Figure 3e).

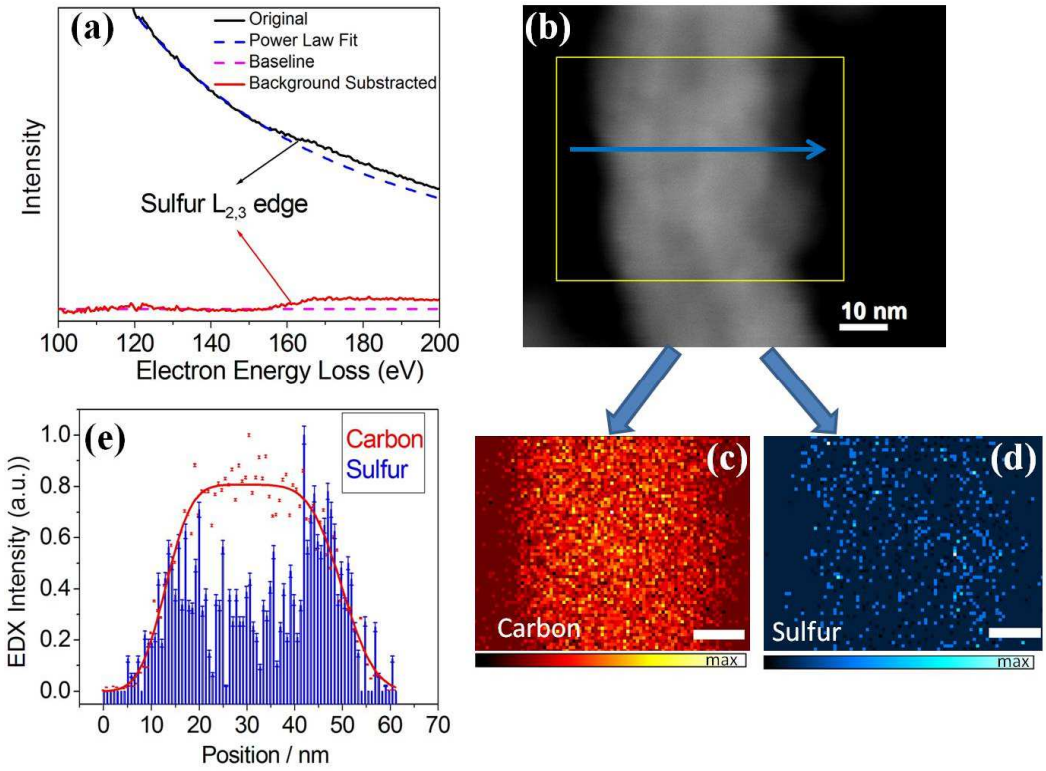

Figure 3. Dark field (DF)-STEM image of S/MWCNT@meso C composite (a) and the corresponding elemental mapping for carbon (b) and sulfur (c), the scale bars are 10 nm; (d) Line profiles of carbon and sulfur composition across the MWCNT in figure a (the white arrow indicates the scan direction); (e) EELS spectrum of sulfur.

The overall electrochemical properties could be improved using this unique structure of S/MWCNT@meso C nanocomposite as cathode materials for Li/S batteries. As previously illustrated in scheme 1b, the outer layer mesoporous carbon shell not only serves as hosts to trap sulfur/polysulfides, but also provides pathway for Li ion transportation, while the inter layer MWCNT core provides electron pathway. Cyclic voltammetry (CV) was firstly carried out to study the kinetic processes of sulfur reduction and polysulfide oxidation of S/MWCNT@meso C nanocomposite. As shown in Figure 4a, there are two peaks in the first cathodic scan, indicating that during discharge the electrochemical reduction of sulfur occurs in two stages. According to the mechanism for sulfur electrochemical reduction, the peak at a potential of around 2.3 V is related to the open ring of cyclic S_8 to long chain lithium polysulfides (Li_2S_n, $4<n<8$).[27-30] The following peak at a potential of about 2.0 V is associated with further reduction of higher-order lithium polysulfides to insoluble Li_2S_2 and Li_2S.[29-32] The first cathodic peak shifts positively in the following cycles. It is probably due to the electrochemical reaction of sulfur needs to overcome the strong absorb energy with the conductive matrix during the first discharge process. Notably, there are no obvious potential or current changes of cathodic peaks in the subsequent cycles, indicating the stable performance of the composite after the first cycles. In the anodic scan, a bigger oxidation peak at a potential of around 2.4 V, followed by a smaller peaks at a potential of around 2.5 V, indicating the charging process also occurs in two stages. The bigger oxidation peak corresponds to the formation of lithium polysulfides from lithium sulfulfides. The smaller peak ascribe to the continuing oxidation of lithium polysulfides to elemental sulfur. And this peak gradually disappears after the first cycle.

The electrochemical performance of the S/MWCNT@meso C nanocomposites was further investigated by galvanostatic charging/discharging the materials in a coin cell. Figure 4b shows typical charge/discharge profiles of S/MWCNT@meso C nanocomposites with a cut-off voltage window of 1.5-3.0 V. Two voltage plateaus appeared at around 2.3 V and 2.0 V in discharge curves, indicating two-step reaction of sulfur with lithium during discharge process, which matches well with the CV curves. In the first cycle, the discharge capacity is 1248 mA h g^{-1} (based on the mass of sulfur). The discharge capacity dropped to 1053 mA h g^{-1} in the second cycle and stabilized at around 1000 mA h g^{-1} during 10 cycles, which is 80% of initial capacity. The capacity starts to decrease after 10 cycles and retained about 640 mA h g^{-1} after 50 cycles. The S/MWCNT@meso C nanocomposites shows remarkable performance enhancement compared with that of S/MWCNT as shown in Figure 4c. Although S/MWCNT cathode shows an initial discharge capacity of 1223 mA h g^{-1}, the capacity kept decreasing and the capacity dropped to 118 mA h g^{-1} after 50 cycles, which is only 10% retaining. However, for S/MWCNT@meso C cathode, there are 51% capacity remained after 50 cycles. The performance improvement could be attributed to the bi-functional effects of MWCNT@meso C as carbon matrix, in which mesoporous carbon traps sulfur/polysulfides and MWCNTs provides electron pathways. The rate capability of S/MWCNT@meso C is demonstrated in Figure 4d. The cell delivered an initial capacity of 1250 mA h g^{-1} at a current density of 0.1 A g^{-1}. As the discharge current density increasing, the discharge capacity gradually decreases and remains at around 720 mA h g^{-1} at a current density of 2 A g^{-1}.

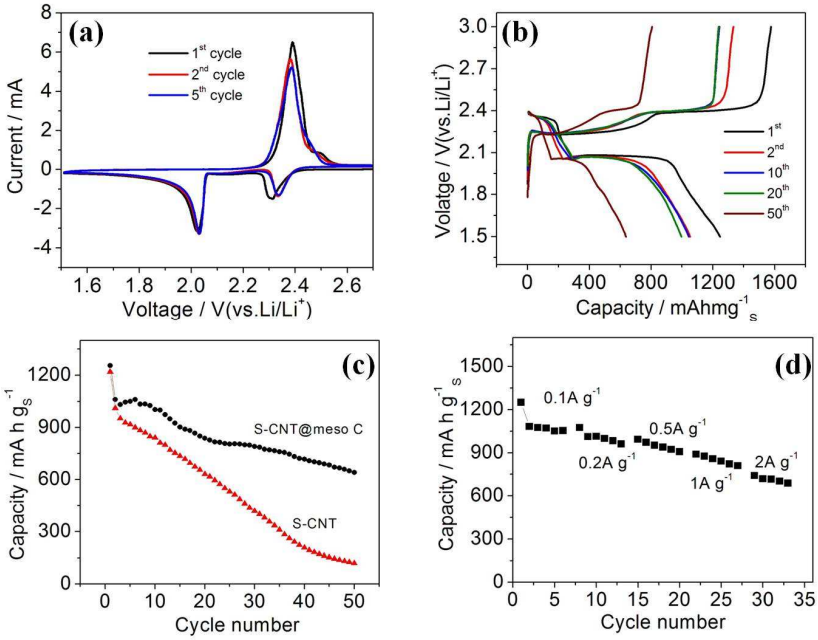

Figure 4. (a)Cyclic voltammogram of the S/MWCNT@meso C nanocomposites in a coin cell at a scan rate of 0.05 mV/s; (b) Charge-discharge profiles of S/MWCNT@meso C at a current density of 0.1 A/g; (c) Cycling performance of S/MWCNT@meso C and S/MWCNT cathodes at a current density of 0.1 A/g; (d) Rate capabilities of S/MWCNT@meso C.

Section 9.4. Conclusion

In conclusion, we have successfully synthesized a hierarchical architecture MWCNT@meso C with a core-shell structure. By infiltrating sulfur in the mesoporous carbon as cathode materials for Li/S battery, the unique S/MWCNT@meso C nanocomposites show an enhanced electrochemical performance. The improved overall electrochemical performance can be attributed to a bi-functional effect of MWCNT@meso C as carbon matrix. First, the mesoporous carbon with higher surface area traps sulfur/polysulfides, while MWCNT core provides electronic pathways. This is only a preliminary result we have obtained using this core-shell structure as carbon matrix for confining sulfur. We are trying to tune some parameters of the shell to optimize the overall electrochemical performance, such as the thickness and the pore size of the mesoporous carbon shell, etc. Anyway, this novel structure may provide some reference information for material design, especially for carbon matrix to trap sulfur in Li/S batteries.

REFERENCES

1. Ji, X.; Lee, K. T.; Nazar, L. F. *Nature Materials* **2009,** 8, (6), 500-506.

2. Cao, Y.; Li, X.; Aksay, I. A.; Lemmon, J.; Nie, Z.; Yang, Z.; Liu, J. *Physical Chemistry Chemical Physics* **2011,** 13, (17), 7660-7665.

3. Jayaprakash, N.; Shen, J.; Moganty, S. S.; Corona, A.; Archer, L. A. *Angewandte Chemie-International Edition* **2011,** 50, (26), 5904-5908.

4. Wang, H.; Yang, Y.; Liang, Y.; Robinson, J. T.; Li, Y.; Jackson, A.; Cui, Y.; Dai, H. *Nano Letters* **2011,** 11, (7), 2644-2647.

5. Elazari, R.; Salitra, G.; Garsuch, A.; Panchenko, A.; Aurbach, D. *Advanced Materials* **2011,** 23, (47), 5641-5644.

6. Park, M.-S.; Yu, J.-S.; Kim, K. J.; Jeong, G.; Kim, J.-H.; Jo, Y.-N.; Hwang, U.; Kang, S.; Woo, T.; Kim, Y.-J. *Physical Chemistry Chemical Physics* **2012,** 14, (19), 6796-6804.

7. Ellis, B. L.; Lee, K. T.; Nazar, L. F. *Chemistry of Materials* **2010,** 22, (3), 691-714.

8. Peramunage, D.; Licht, S. *Science* **1993,** 261, (5124), 1029-1032.

9. Chen, J.-j.; Jia, X.; She, Q.-j.; Wang, C.; Zhang, Q.; Zheng, M.-s.; Dong, Q.-f. *Electrochimica Acta* 55, (27), 8062-8066.

10. Doerfler, S.; Hagen, M.; Althues, H.; Tuebke, J.; Kaskel, S.; Hoffmann, M. J. *Chemical Communications* **2012,** 48, (34), 4097-4099.

11. Chen, J.-j.; Zhang, Q.; Shi, Y.-n.; Qin, L.-l.; Cao, Y.; Zheng, M.-s.; Dong, Q.-f. *Physical Chemistry Chemical Physics* **2012,** 14, (16), 5376-5382.

12. Guo, J.; Xu, Y.; Wang, C. *Nano Letters* 11, (10), 4288-4294.

13. Yin, L.; Wang, J.; Yang, J.; Nuli, Y. *Journal of Materials Chemistry* **2011,** 21, (19), 6807-6810.

14. Demir-Cakan, R.; Morcrette, M.; Nouar, F.; Davoisne, C.; Devic, T.; Gonbeau, D.; Dominko, R.; Serre, C.; Ferey, G.; Tarascon, J.-M. *Journal of the American Chemical Society* **2011,** 133, (40), 16154-16160.

15. Chen, S.-R.; Zhai, Y.-P.; Xu, G.-L.; Jiang, Y.-X.; Zhao, D.-Y.; Li, J.-T.; Huang, L.; Sun, S.-G. *Electrochimica Acta* 56, (26), 9549-9555.

16. Li, X.; Cao, Y.; Qi, W.; Saraf, L. V.; Xiao, J.; Nie, Z.; Mietek, J.; Zhang, J.-G.; Schwenzer, B.; Liu, J. *Journal of Materials Chemistry* 21, (41), 16603-16610.

17. Liang, X.; Wen, Z.; Liu, Y.; Zhang, H.; Huang, L.; Jin, J. *Journal of Power Sources* **2011,** 196, (7), 3655-3658.

18. Liang, C.; Dudney, N. J.; Howe, J. Y. *Chemistry of Materials* **2009,** 21, (19), 4724-4730.

19. Ji, L.; Rao, M.; Aloni, S.; Wang, L.; Cairns, E. J.; Zhang, Y. *Energy & Environmental Science* 4, (12), 5053-5059.

20. Elazari, R.; Salitra, G.; Garsuch, A.; Panchenko, A.; Aurbach, D. *Advanced Materials* 23, (47), 5641-5644.

21. Zheng, G.; Yang, Y.; Cha, J. J.; Hong, S. S.; Cui, Y. *Nano Letters* **2011,** 11, (10), 4462-4467.

22. Zhang, C.; Wu, H. B.; Yuan, C.; Guo, Z.; Lou, X. W. D. *Angewandte Chemie-International Edition* **2012**, DOI: 10.1002/anie.201205292.

23. Evers, S.; Nazar, L. F. *Chemical Communications* **2012,** 48, (9), 1233-1235.

24. Li, N.; Zheng, M.; Lu, H.; Hu, Z.; Shen, C.; Chang, X.; Ji, G.; Cao, J.; Shi, Y. *Chemical Communications* **2012,** 48, (34), 4106-4108.

25. Li, N. W.; Zheng, M. B.; Lu, H. L.; Hu, Z. B.; Shen, C. F.; Chang, X. F.; Ji, G. B.; Cao, J. M.; Shi, Y. *Chemical Communications* 48, (34), 4106-4108.

26. Zhang, B.; Qin, X.; Li, G. R.; Gao, X. P. *Energy & Environmental Science* **2010,** 3, (10), 1531-1537.

27. Elazari, R.; Salitra, G.; Garsuch, A.; Panchenko, A.; Aurbach, D. *Advanced Materials* **2011,** 23, (47), 5644.

28. Ji, L.; Rao, M.; Zheng, H.; Zhang, L.; Li, Y.; Duan, W.; Guo, J.; Cairns, E. J.; Zhang, Y. *Journal of the American Chemical Society* **2011,** 133, (46), 18522-18525.

29. Rao, M.; Li, W.; Cairns, E. J. *Electrochemistry Communications* **2012,** 17, 1-5.

30. Guo, J.; Xu, Y.; Wang, C. *Nano Letters* **2011,** 11, (10), 4288-4294.

31. Cheon, S. E.; Ko, K. S.; Cho, J. H.; Kim, S. W.; Chin, E. Y.; Kim, H. T. *Journal of the Electrochemical Society* **2003,** 150, (6), A796-A799.

32. Barchasz, C.; Molton, F.; Duboc, C.; Lepretre, J.-C.; Patoux, S.; Alloin, F. *Analytical Chemistry* **2012,** 84, (9), 3973-3980.

33. Zhang, M.; Wu, Y.; Feng, X.; He, X.; Chen, L.; Zhang, Y. *Journal of Materials Chemistry* **2010,** 20, (28), 5835-5842.

34. Qian, X.; Lv, Y.; Li, W.; Xia, Y.; Zhao, D. *Journal of Materials Chemistry* **2011,** 21, (34), 13025-13031.

CHAPTER 10

AMYLOPECTIN WRAPPED GRAPHENE OXIDE/SULFUR FOR IMPROVED CYCLABILITY OF LITHIUM-SULFUR BATTERY[*†]

Section 10.1. Introduction

There is currently a great deal of interest in the development of high energy and power density and long life rechargeable batteries for transportation and grid applications. Much attention has been focused on lithium ion batteries (LIBs) due to their potentially high energy density and low cost. The typical cathode materials most widely used in commercial LIBs are $LiCoO_2$, $LiMn_2O_4$ and $LiFePO_4$. However, they are limited by their relatively high cost, as in the case of cobalt, and low energy density.[1-3] Although the theoretical capacities can reach to 300mAh g^{-1}, the maximum practical capacities obtained are typically less than 200mAh g^{-1}. Compared with the relatively large capacity of current anodes, the use of cathodes based on transition metals puts a theoretical limit on LIB systems for large scale energy storage. Lithium-sulfur (Li/S) batteries, represent one of the most promising candidates for next generation LIBs owing to their high theoretical capacity of 1673mAh g^{-1}, which is about five times that of current commercial cathodes.[4] Although the voltage of Li/S cells is around 2.1~2.3V (relative to Li/Li^+), the very high capacity and low cost overcome these limitation. However, despite their

---

[*] Produced with permission from Weidong Zhou , Hao Chen , Yingchao Yu , Deli Wang , Zhiming Cui , Francis J. DiSalvo , and Héctor D. Abruña. (2013) *ACS Nano*, 7, 10, 8801. Copyright © 2013 American Chemical Society

[†] W.Z. and H.C. synthesized the sample, Y.Y. performed the microscopy imaging. D.W. and Z.C helped to perform the synthesis. H.D.A. and F.J.D. guided the work.

attractive properties, Li/S batteries suffer from poor cyclability, which is mainly attributed to the dissolution of intermediate lithium polysulfide products Li_2S_n ($4 \leq n \leq 8$), volumetric expansion and the poor conductivity of sulfur and polysulfide species.[5-7] In order to address these challenges, various methods have been reported including the use of mesoporous carbon,[8-16] graphene oxide,[17,18] carbon nanotube,[19-21] sulfur-coating polymer composites.[22-24] Among these, mesoporous carbon-based materials with pore size of less than 5nm show attractive performance. However, the preparation of mesoporous carbon usually involves the use of highly toxic hydrofluoric acid to remove the hard template.[8-16] And from the mixing of mesoporous carbon and sulfur, if the sulfur could diffuse into the small pores of the mesoporous carbon, the sulfur could also diffuse out during long cycling, considering the fact that the sulfur can still be accessed by electrolyte for long terms. Although the weak interactions between sulfur and mesopores could alleviate the dissolution of polysulfides in a short term, the polysulfides should still be dissolved and diffuse out eventually. This is likely the reason why extended cycle life (>100 cycles) tests with stable capacity retention and high Coulombic efficiency were rarely reported for this type of Li/S composites. In addition, the mesoporous carbon/sulfur composites are constructed through the diffusion of sulfur vapor or liquid sulfur into the nano-pores of mesoporous carbon, which limits the sulfur loading in the electrode composite. Another innegligible phenomenon in Li/S batteries is that polyvinylidene fluoride (PVDF) dissolved in N-methyl-2-pyrrolidone (NMP) was generally employed as the binder. However, NMP could dissolve the sulfur, which will destroy the pre-constructed nanostrucutures and the evaporation of NMP under vacuum could also cause related environmental problems.[25] To overcome these limitations, more feasible methods need to be explored to immobilize the lithium polysulfides at lower cost and can be easily scaled up in industry.

Section 10.2. Materials and Methods

According to the recent studies, graphene-oxide(GO) doped sulfur in Li/S electrode composite show promising improvement for the cycling stability of the corresponding batteries.[17,18] GO consists of a basal plane decorated mostly with epoxide and hydroxyl groups, in addition to carbonyl and carboxyl groups, which are located at the edges.[26-29] These groups in grapheme-oxide play important role for immobilizing the otherwise free lithium polysulfides.[17] However, the stable charge-discharge process of pure GO coated sulfur composite can only be observed at initial 30cycles, followed by an obvious capacity fading. When a PEG surfactant coated sulfur was wrapped with GO, the capacity dropped from initial 1000mAh g^{-1} to 550 mAh g^{-1} after 20 cycles.[18] These capacity fading probably because the superficial sulfur cannot be fully trapped and the open channels among the GO layers provide large space for polysulfides to escape. To further immobilize the polysulfides, a soft polymer should be employed to wrap the GO/S composite and construct a 3-dimensional network for better immobilizing the polysulfide species and accommodating the volumetric expansion during cycling. The polymer had better interact with the marginal hydroxyl and carboxyl group of the GO for binding the margins of adjacent GO layers to avoid the polysulfide diffusing out of the GO layers. In the meantime, it should be both insoluble and non-redox active in the LIBs potential window.

With this consideration in mind, a natural polymer, amylopectin was pitched on here because sufficient hydroxyl units of amylopectin will interact with the hydroxyl group of GO through hydrogen bonding interaction to form cross-linked 3-dimensional

structure, helping to bind the GO layers and accommodate the volumetric expansion, and it is environmentally benign.[30-33] Recently, gelatin and β-cyclodextrin were tested as aqueous binders of the Li-S batteries for the immobilization of polysulfides, which gave improved cyclability in the initial 50 cycles.[34,35] Water soluble brown algae was also harnessed as a binder to build silicon nanopowder–based lithium ion batteries and gave improved performance.[36] Herein, the reasonable combination of amylopectin wrapped GO-Sulfur as electrode composite for improvement of sulfur electrode stability was investigated. As expected, with the assistance of this structure, the cycling stability of the sulfur electrode was enhanced significantly compared with the unwrapped GO-Sulfur composite. This cross-linked build-up, constructed through the intermolecular interactions, provides new opportunities to mitigate the diffusion of lithium polysulfide species and improves the cycling stability of Li/S batteries.

A control sample of amylopectin doped sulfur without GO (but contained carbon black) was first prepared to test the electrochemical properties. Sulfur and carbon black were first heated to 155^0C for 12 hours to obtain a homogeneously mixed material. The mixture was dispersed in an aqueous amylopectin solution under sonication and excess ethanol was then added slowly to yield the black precipitation of amylopectin coated sulfur (S-Amy) composite. According to the thermogravimetric analysis (TGA) curve of the obtained black powder, in Figure S1 of the Supporting Information(SI), around 56% sulfur and 14% amylopectin were contained in the composite. It was then ground in the presence of 5% polytetrafluoroethylene (PTFE) to lower the stiffness of amylopectin, giving the electrode films with an average sulfur mass loading of 4.0 mg cm^{-2}. Coin cells were fabricated to test the electrochemical performance of the S-Amy composite using

lithium foil as the anode and 1.0M lithium bis-trifluoromethanesulfonylimide (LiTFSI) in a mixed solvent of 1,3-dioxolane and 1,2-dimethoxyethane (1:1, v/v) as the electrolyte.

Preparation of S-Amy composite electrode: In a typical electrode making process of S-Amy, 50mg sulfur and 25mg carbon black were first heated at 155^0C for 12 hours to obtain a homogeneous material. The mixture was dispersed in 100ml aqueous solution of 15mg amylopectin under sonication and 300ml ethanol was then added slowly to yield the precipitation of amylopectin coated sulfur-carbon black composite. The above precipitation and polytetrafluoroethylene (PTFE) were well ground in a mortar with the addition of isopropanol and then were roll-pressed to produce an electrode film, which was heated at 50^0C for 12 hours under vacuum before using to make the coin cell. The coin cells were fabricated in an argon-filled glove box using lithium metal as the counter electrode and a microporous polyethylene separator. The control experiment of pure sulfur coin cell was also fabricated according to the same procedure, except that the cathode composite was made from 50% of elemental sulfur, 40% of carbon black and 10% of PTFE binder.

Synthesis of GO-S-Amy composite: 60mg GO was well dispersed in 100ml water through 1 hour sonication to obtain a black homogeneous suspension. For sulfur particles synthesis, 2.0g of $Na_2S_2O_3$ was first dissolved in 400ml of 1% PVP aqueous solution. 6ml concentrated hydrochloric acid was added to the above solution, and then the system was kept at room temperature for 40min with magnetic stirring to get white gel solution of sulfur particles. The suspension of GO was then added into the sulfur gel solution under vigorous magnetic stirring. After 20min, the product of GO-S was collected by centrifuge

and further washed twice with water. 10mg amylopectin was suspended in 100ml water and then heated to 80^0C for 1 hour to get a transparent solution. Fresh prepared 70mg of GO-S and 15mg carbon black were added to the above solution and stirred for 30min under sonication for intensive mixing. The resulting suspension was poured into 300ml ethanol, filtered and dried to get a black powder. The obtained powder and 5% PTFE were well ground in a mortar with the addition of isopropanol and then were roll-pressed to produce an electrode film, which was heated at 50^0C for 12 hours under vacuum before using to fabricate the coin cell. The GO-S-Amy coin cell was fabricated according to the similar procedure as S-Amy coin cell.

Section 10.3. Results and Discussions

A cyclic voltammetry (CV) of a Li/S cell with the S-Amy cathode was obtained at a scan rate of 0.05mV s^{-1}, and was shown in Figure S2 of the SI. Two well-defined reduction peaks at 2.35 and 2.08V were observed, which could be assigned to the multistep reduction mechanism of elemental sulfur, as reported previously.[8-24] The reduction peak centered around 2.35V is generally attributed to the reduction of the S_8 ring and the formation of S_8^{2-}. The reduction peak at 2.08V is associated with further reduction of the higher polysulfide species (Li_2S_n, $4<n<8$) to the lower polysulfide species (Li_2S_n, $n\leq2$). The broad oxidation peak around 2.3-2.5V is associated with the oxidation of polysulfides to the neutral elemental S_8.[9]

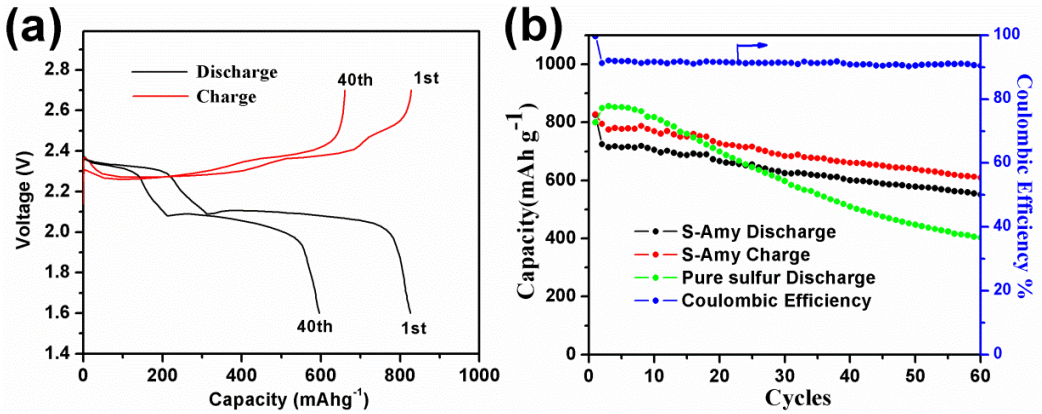

Figure 1. a) Charge/discharge profiles and b) Charge/discharge capacities *vs* cycle number for S-Amy cathode at a rate of C/8. 1C was corresponded to a current density of 1600mA/g and the capacity values were calculated based on the mass of sulfur.

Figure 1a depicted the first and 40th discharge/charge profiles of the S-Amy electrode at a rate of C/8 in a rechargeable lithium cell. Two flat discharge plateaus located at 2.35 and 2.08V were clearly observed, in good agreement with the CV results. As shown in Figure 1b, the S-Amy electrode showed an initial discharge capacity of 825 mAh g^{-1} followed by a gradual decrease during subsequent cycles. Compared with the cycling performance of the pure sulfur electrode, although the pure sulfur cathode exhibited a higher capacity in initial 15cycles, it exhibited a much faster capacity fade especially after 30 cycles. The relatively slow capacity fading of S-Amy electrode indicates that the addition of amylopectin can alleviate the diffusion of the lithium polysulfides into the electrolyte and therefore suggests that the amylopectin could be adopted as an additive for Li/S batteries.[34-36] On the other hand, the coulombic efficiency of the S-Amy electrode stabilized at a little over than 90% and the capacity still faded obviously, which indicate there still be some polysulfide dissolution and shuttling of the polysulfide species.[37]

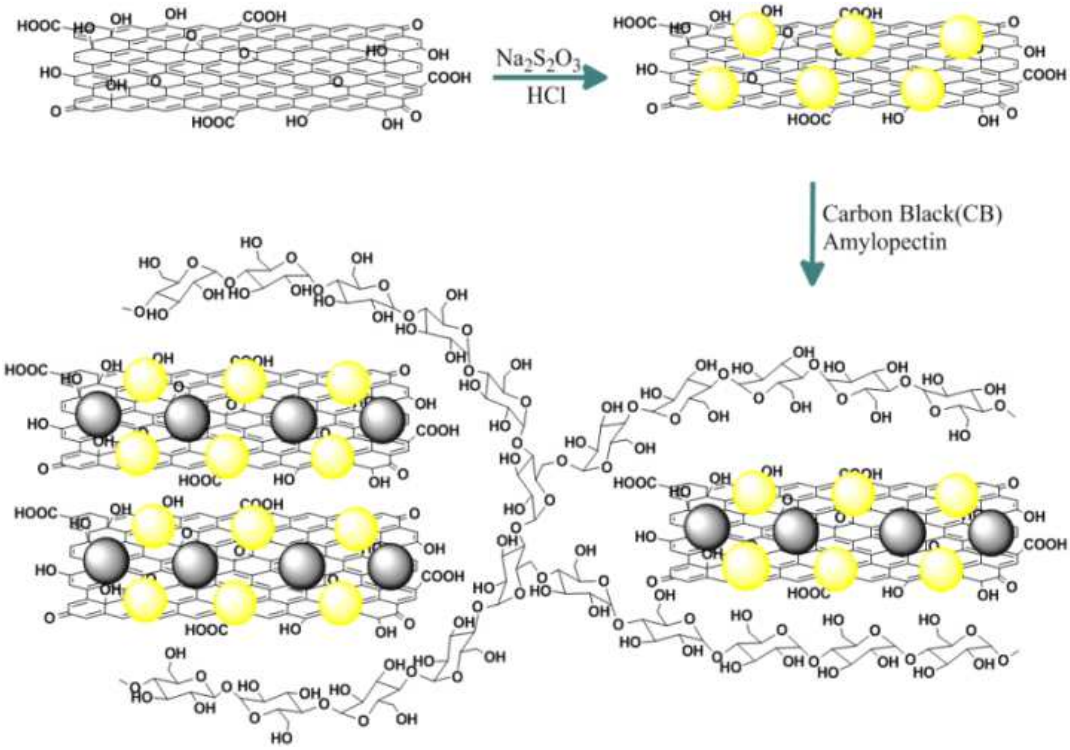

Scheme 1. Schematic two step synthesis route for a GO-S-Amy composite, with yellow balls representing sulfur and black balls representing carbon black.

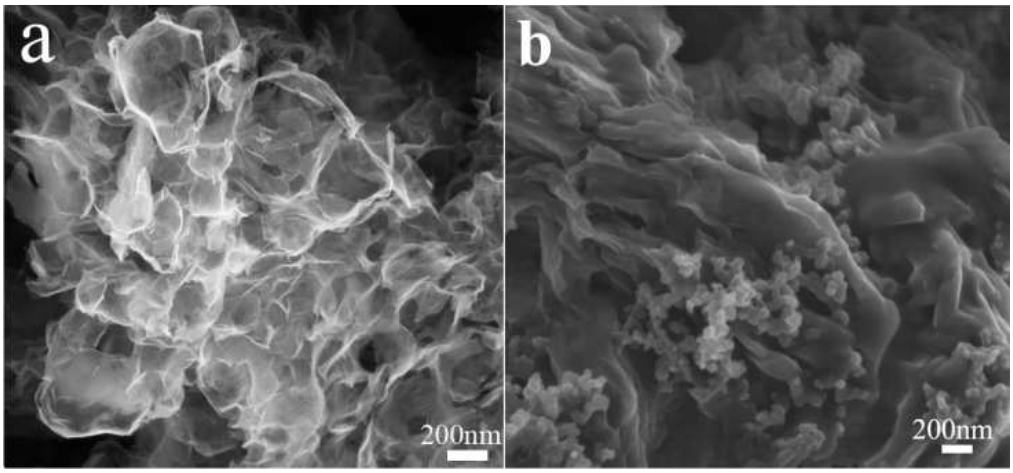

Figure 2. SEM images of GO (a) and GO-S-Amy (b) composite.

The amylopectin wrapped Graphene Oxide-Sulfur(GO-S-Amy) composite was subsequently prepared through a quite sample dissolution-precipitation method. In our approach (Scheme 1), typical Hummers GO was employed in the electrode composite.[29] The GO was first dispersed in the solution of sodium thiosulfate under sonication to form a homogenous suspension. Sulfur particles could then be synthesized and precipitated homogeneously among GO layers by reacting sodium thiosulfate with hydrochloric acid. As shown in the TGA curve of Figure S3 in the SI, around 72 wt% of sulfur was incorporated in the GO-S composite. The as prepared GO-S and carbon black were dispersed in an aqueous solution of amylopectin through sonication. Excess ethanol was then slowly added to give the GO-S-Amy floccus precipitation, which was employed to make the electrode film after drying in vacuum. According to the TGA results of Figure S4 in the SI, the final sulfur content in the whole electrode was around 52% accounting 5% PTFE binder added during the preparation of the electrode film. This approach is much simpler and economical when compared with the widely used procedure of long time or repeated sublimation for infusion of elemental sulfur into porous carbons. Also, such a process is environmentally benign and highly reproducible, and can be straightforward to scale up in industry.

Figure 2 exhibits the scanning electron microscopy (SEM) images of the GO and GO-S-Amy composite. Compared with the well defined flake structure of GO, amorphous and aggregated nano-sheets with carbon black particles on the surface were observed for the GO-S-Amy composite, which could be attributed to the interaction between amylopectin and GO. In the scanning transmission electron microscopy (STEM) images of GO-S-Amy composite, sulfur particles with a diameter of around 500nm could

be clearly observed, as shown in Figure 3a and 3b. Elemental maps of sulfur and carbon (Figure 3) confirmed that the bright particles in Figure 3b were sulfur particles, along with overlaying carbon signals from GO sheets. Compared with the SEM image of Figure 2b, the sulfur particles should have been confined among the GO layers, because there was no sulfur particle could be observed on the surface from the SEM image. Energy-dispersive X-ray (EDX) microanalysis exhibited strong sulfur peak, which is around three times of carbon, as shown in Figure 3f. The relative content of sulfur in GO-S-Amy should be higher considering that the contribution of amylopectin and the carbon film on the STEM grid was also included in the EDX intensity of carbon. In the case of unwrapped GO-S, the sulfur particles could not be observed in the STEM images, as shown in Figure 4, which can be attributed to the high vacuum of STEM and high vapor pressure of the sulfur.[38, 39] Although elemental sulfur could still be detected in the sulfur map, the EDX intensity of sulfur is obviously smaller compared with the carbon, which suggests most of the sulfur in GO-S was evaporated in the high vacuum of STEM. These features, from one side, verify the amylopectin effectively wrapped the sulfur in GO-S-Amy.

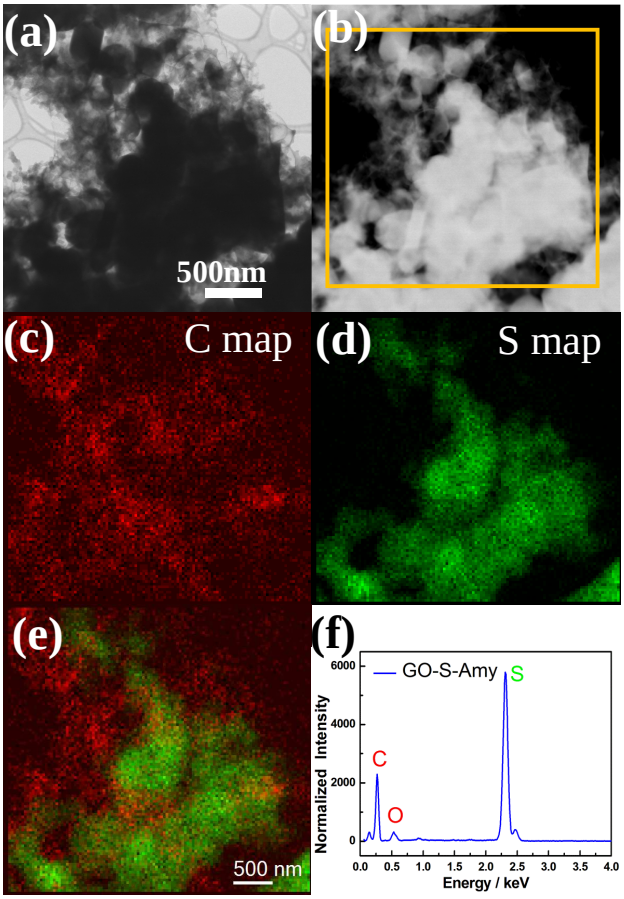

Figure 3. STEM images of GO-S-Amy in bright field (a) and dark field (b). Elemental mapping of the region shown in yellow square of (b) for carbon (c), sulfur (d) along with (e) an overlay of those two maps. (f) EDX spectrum of GO-S-Amy composite.

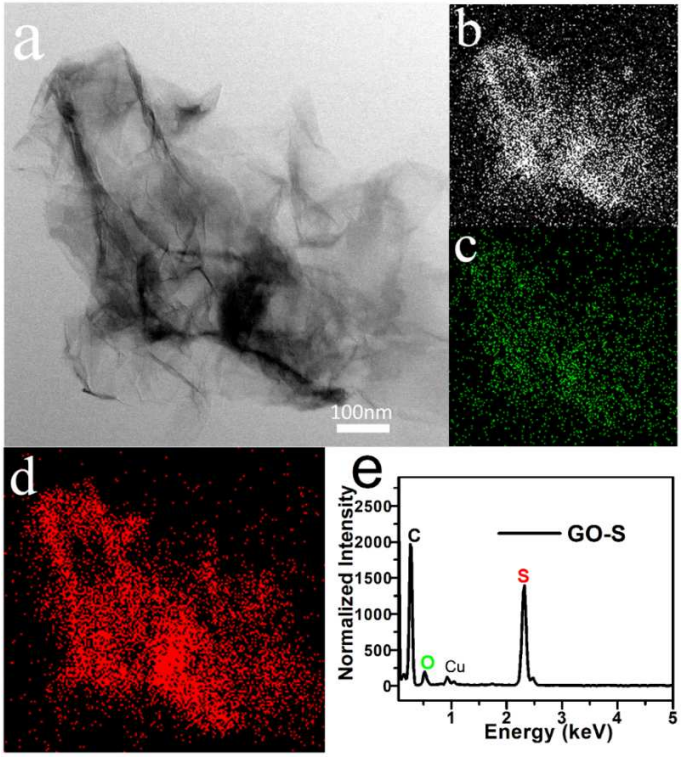

Figure 4. STEM bright field image of the GO-S composite (a) and the corresponding elemental mapping for carbon (b), oxyen (c) and sulfur (d). (e) EDX spectrum of GO-S composite.

The obtained dry GO-S-Amy composite was employed to make the electrode films with several typical sulfur mass loadings of 2.0mg cm^{-2}, 4.0mg cm^{-2} and 6.0mg cm^{-2} through control the thickness of electrode films. Figure 5 shows the CV and cycling performance of coin cells using GO-S-Amy as the cathode with a suffer loading of 4.0mg cm^{-2}. Two well defined reduction peaks centered around 2.3 and 2.03V were clearly observed, similar to the CV of the S-Amy electrode described above. During the initial 10 cycles, the redox curves become sharper gradually suggesting reversibility actually improved with cycling. As illustrated in Figure 5b, the GO-S-Amy electrodes showed initial capacities of 817, 650 and 596 mAh g^{-1} under different C rates of C/8, 5C/16 and C/2, respectively. Although there was an initial drop, the capacity stabilized after about 5 cycles at both low and high current densities, as observed in Figure 5c. Afterward, there was a much more gradual decrease in capacity. A control sample of GO-S without amylopectin coating exhibited a stable cyclability during the first 25 cycles followed by a significant capacity fading. Relative to the amylopectin free GO-S electrode, the GO-S-Amy electrode exhibited much improved capacity retention with long cycling, which was ascribed to the cross-linked structures of GO wrapped amylopectin and polysulfides. After a long-term cycling of 175 cycles, a discharge capacity of 441 mAh g^{-1} was obtained at 5C/16, which corresponded to a 68% capacity retention ratio as shown in Figure 5d. At the higher current density of C/2, much more stable cycling performance was observed with a stable capacity around 430mAh g^{-1}, which did not decay significantly after 100 cycles. The relatively better cycling performance at C/2 can be attributed to the weaker shuttle effect at higher current density.[6] The improved cycling stability verifies the fact that amylopectin wrapped GO-sulfur structure can help to

immobilize the polysulfides and reduce the capacity fading, which was in agreement with the successful confinement of sulfur under high vacuum of STEM. The branched amylopectin could the wrap and bind GO layers effectively through its cross-linked 3-dimension structure and supramolecular interaction, which closes the open channels among GO layers and minimizes the diffusion of the polysulfides. As a result, electrodes employing the amylopectin wrapped GO-Sulfur exhibited better cycling stability.

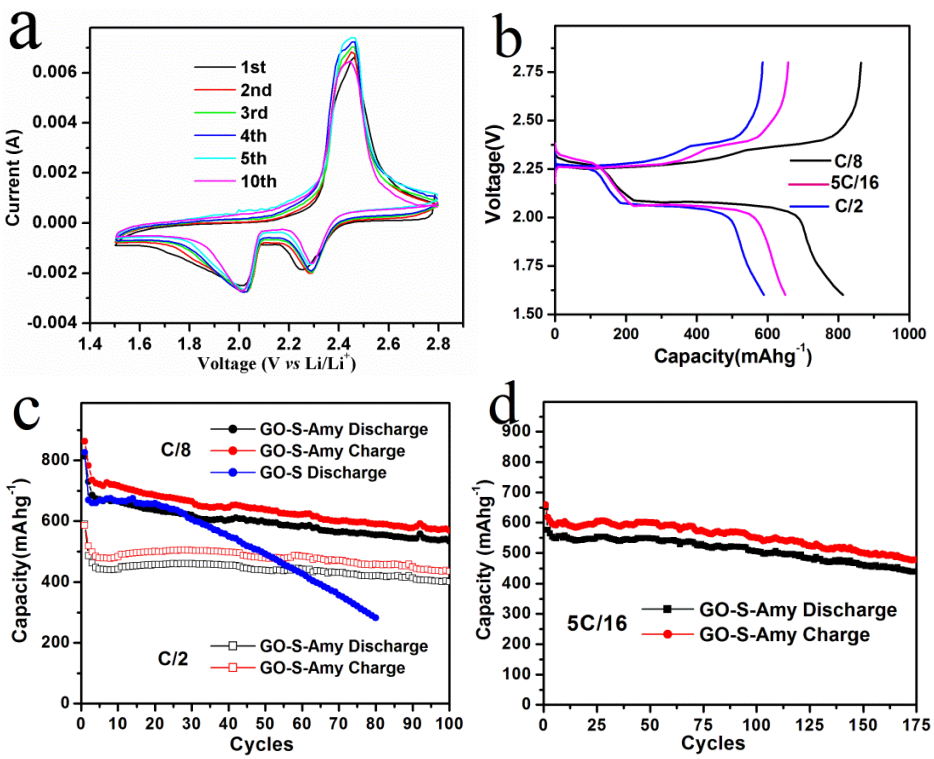

Figure 5. a) Typical CV of GO-S-Amy cathode at a sweep rate of 0.1 mV s^{-1}; b) First cycle charge/discharge profiles for the GO-S-Amy cathodes at current densities of C/8, 5C/16and C/2; c) and d) Charge/discharge capacities *vs* cycle numbers of GO-S and GO-S-Amy at different current densities.

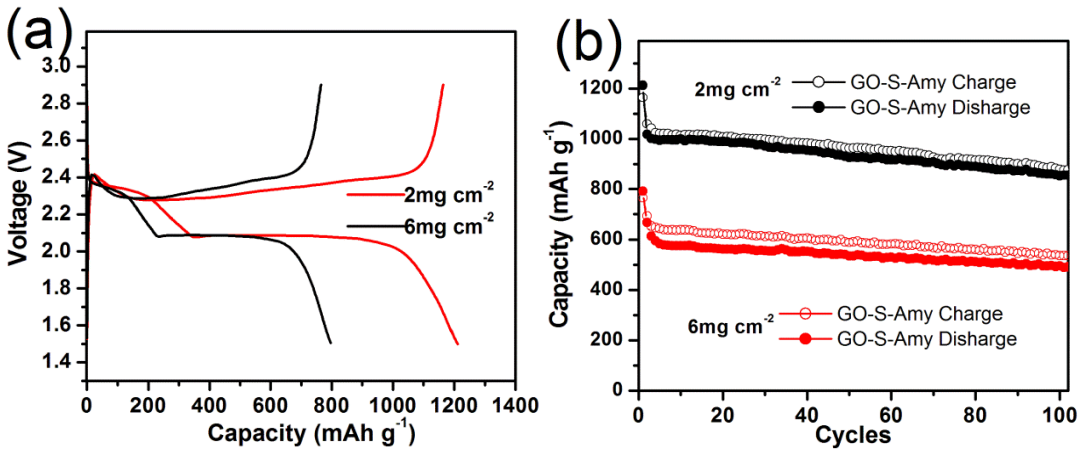

Figure 6. a) First cycle charge/discharge profiles for the GO-S-Amy cathodes with the sulfur loadings of 2mg cm^{-2} and 6mg cm^{-2} at C/8; b) Charge/discharge capacities *vs* cycle numbers of GO-S-Amy at different sulfur loadings.

Figure 6 shows the CV and cycling performance of the GO-S-Amy composite electrodes with different sulfur loadings of 2mg cm^{-2} and 6mg cm^{-2} at C/8. Obviously, the lower suffer loading of 2mg cm^{-2} GO-S-Amy cathode delivered higher discharge capacity and efficiency in this condition. From the Figure S6 of SI, the coulombic efficiencies of the electrode with different sulfur loadings of 2mg cm^{-2}, 4mg cm^{-2} and 6mg cm^{-2} at C/8 were around 98, 94 and 91, respectively. Here, lower capacity at higher suffer loading can be attributed to the poorer ionic transportation and contact in thicker electrode film. We should point out that although this composite showed better cycling stability compared with the pure sulfur and un-wrapped GO-S, slow capacity degradation could still be observed. Besides, the efficiency was just around 98% even in low suffer loading of 2mg cm^{-2}, which indicates that the dissolution of polysulfides and the subsequent shuttling effect are still not completely vanished in this condition. But the low cost of materials and the easy scaled up preparation process give the competitive advantage for this structure.

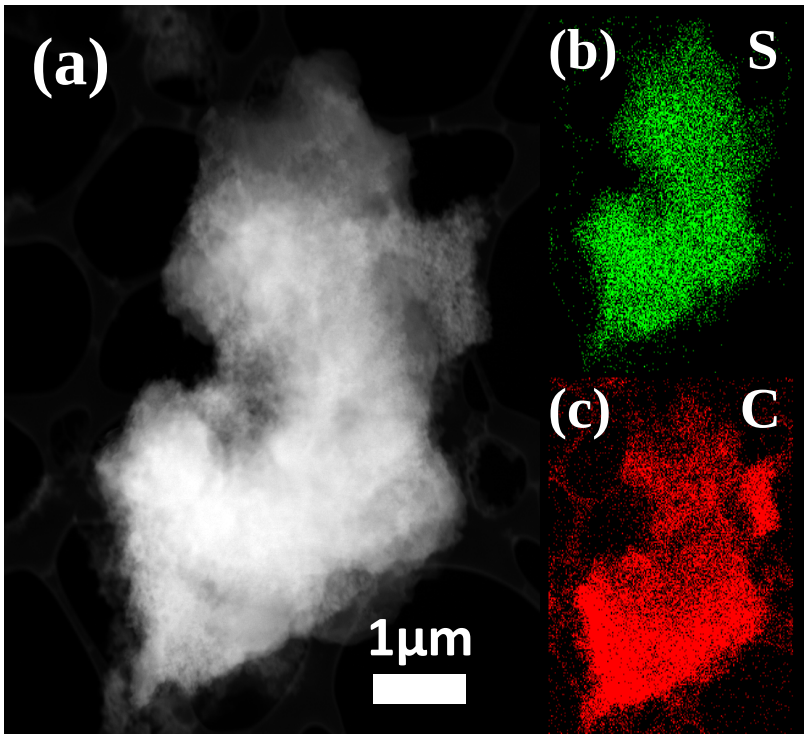

Figure 7. STEM dark field image of GO-S-Amy composite after 50th discharge in cell (a) and corresponding elemental mapping for sulfur (b) and carbon (c).

To further investigate the structure of the GO-S-Amy composite during the long cycling, a cell was opened after 50th full discharge in cell and the electrode was peeled off from the current collector and re-dispersed in THF under sonication. As shown in the STEM images and EDX mapping of Figure 7, the sulfur particles were disappeared and the elemental sulfur dispersed homogeneously among the GO layers, owning to the precipitation of a thin layer of discharge products (Li_2S_2 and/or Li_2S). It is also noticeable that the building-in of GO-S was still maintained after running 50 cycles, which indicates the stability of this structure. The fourier transform infrared spectroscopy (FTIR) spectra of the 50th discharged cathode exhibited obvious peaks at 1580 cm^{-1}, 1426 cm^{-1} and 850 cm^{-1}, as shown in the Figure S8 of the SI, suggesting the formation of S-Li or O-Li.[38,40] The summit of broad band between 3600 and 2600 cm^{-1} resulting from the O-H groups of GO-S-Amy (after 50th discharge) shifted towards short wavenumber compared with the GO-S-Amy, which indicates the presence of the hydrogen bonds in discharged GO-S-Amy composite. Meanwhile, an obvious shoulder at 2535 cm^{-1} could be ascribed to the S-H stretching vibration, which suggested the presence of the balance between O-H and S-H. These observations, including the STEM and FTIR, suggest that the GO-S-Amy composite forms a stable cross-linked structure through the supramolecular interactions, which can accommodate the charge/discharge reactions and preserve the structure in long cycling.

Section 10.4. Conclusion

In conclusion, a natural polymer, amylopectin wrapped graphene oxide - sulfur nanocomposite has been prepared and investigated for immobilizing the lithium polysulfides in the cathode of Li/S cells. With the help of this 3-dimensionally cross-linked structure, the Li/S battery exhibited much improved cycling stability and columbic efficiency compared with the conventional sulfur electrodes. From the comparison of STEM images and EDX data, the branched amylopectin successfully confined the sulfur particles among the GO layers, which helps to tether the polysulfides during the charge/discharge processes. Different sulfur loading electrodes were tested and compared as well, lower sulfur loading electrode show better capacity and efficiency relative to higher sulfur loading electrode. While slight capacity fading presents in these and premier studies, we believe that these results provide reliable insights and novel concepts for future Li/S batteries.

Supporting Information. Experimental details and characterization are included. This material is available free of charge *via* the Internet at http://pubs.acs.org.

REFERENCES

1 Whittingham, M. S. Lithium Batteries and Cathode Materials. *Chem. Rev*. **2004**, *104*, 4271-4301.

2 Aricò, A. S.; Bruce, P. G.; Scrosati, B.; Tarascon, J.-M.; Schalkwijk, W. V. Nanostructured Materials for Advanced Energy Conversion and Storage Devices. *Nat. Mater.* **2005**, *4*, 366-377.

3 Guo, Y.; Hu, J.; Wan, L. Nanostructured Materials for Electrochemical Energy Conversion and Storage Devices. *Adv. Mater*. **2008**, *20*, 2878-2887.

4 Bruce, P. G.; Freunberger, S. A.; Hardwick, L. J.; Tarascon, J.-M. Li–O_2 and Li–S Batteries with High Energy Storage. *Nat. Mater.* **2012**, *11*, 19-29.

5 Mikhaylik, Y.; Kovalev, I.; Schock, R.; Kumaresan, K.; Xu, J.; Affinito, J. High Energy Rechargeable Li-S Cells for EV Application: Status, Remaining Problems and Solutions. *ECS Transactions*, **2010**, *25*, 23-34.

6 Yamin, H.; Gorenshtein, A.; Penciner, J.; Sternberg, Y.; Peled, E. Lithium Sulfur Battery Oxidation/Reduction Mechanisms of Polysulfides in THF Solutions. *J. Electrochem. Soc*. **1988**, *135*, 1045-1048.

7 Peled, E.; Sternberg, T.; Gorenshtein, A.; Lavi, Y. Lithium-Sulfur Battery: Evaluation of Dioxolane-Based Electrolytes. *J. Electrochem. Soc.* **1989**, *136*, 1621-1625.

8 Jayaprakash, N.; Shen, J.; Moganty, S. S.; Corona, A.; Archer, L. A. Porous Hollow Carbon@Sulfur Composites for High-Power Lithium–Sulfur Batteries. *Angew. Chem. Int. Ed.* **2011**, *50*, 5904-5908.

9 Liang, C.; Dudney, N. J.; Howe, J. Y. Hierarchically Structured Sulfur/Carbon Nanocomposite Material for High-Energy Lithium Battery. *Chem. Mater*., **2009**, *21*, 4724-4730.

10 Xiao, L.; Cao, Y.; Xiao, J.; Schwenzer, B.; Engelhard, M. H.; Saraf, L. V.; Nie, Z.; Exarhos, G. J.; Liu J. A Soft Approach to Encapsulate Sulfur: Polyaniline Nanotubes for Lithium-Sulfur Batteries with Long Cycle Life. *Adv. Mater.* **2012**, *24*, 1176-1181.

11 Zhang, C.; Wu, H.; Yuan, C.; Guo, Z.; Lou, X. W. Confining Sulfur in Double-Shelled Hollow Carbon Spheres for Lithium–Sulfur Batteries. *Angew. Chem. Int. Ed.* **2012**, *51*, 9592-9595.

12 Ji, X.; Lee, K. T.; Nazar, L. F. A Highly Ordered Nanostructured Carbon–Sulphur Cathode for Lithium–Sulphur Batteries. *Nat. Mater*. **2009**, *8*, 500-506.

13 Yang, Y.; Yu, G.; Cha, J. J.; Wu, H.; Vosgueritchian, M.; Yao, Y.; Bao, Z.; Cui, Y. Improving the Performance of Lithium–Sulfur Batteries by Conductive Polymer Coating. *ACS Nano*, **2011**, *5*, 9187-9193.

14 Ji, X.; Evers, S.; Black, R.; Nazar, L. F. Stabilizing Lithium–Sulphur Cathodes Using Polysulphide Reservoirs. *Nat. Commun*. **2011**, *2*, 325.

15 Schuster, J.; He, G.; Mandlmeier, B.; Yim, T.; Lee, K. T.; Bein, T.; Nazar, L. F. Spherical Ordered Mesoporous Carbon Nanoparticles with High Porosity for Lithium–Sulfur Batteries. *Angew. Chem. Int. Ed.* **2012**, *51*, 3591-3595.

16 Xin, S.; Gu, L.; Zhao, N.; Yin, Y.; Zhou, L.; Guo, Y.; Wan L. Smaller Sulfur Molecules Promise Better Lithium–Sulfur Batteries. *J. Am. Chem. Soc.*, **2012**, *134*, 18510–18513.

17 Ji, L.; Rao, M.; Zheng, H.; Zhang, L.; Li, Y.; Duan, W.; Guo, J.; Cairns, E. J.; Zhang, Y. Graphene Oxide as a Sulfur Immobilizer in High Performance Lithium/Sulfur Cells. *J. Am. Chem. Soc.*, **2011**, *133*, 18522-18525.

18 Wang, H.; Yang, Y.; Liang, Y.; Robinson, J. T.; Li, Y.; Jackson, A.; Cui, Y.; Dai, H. Graphene-Wrapped Sulfur Particles as a Rechargeable Lithium–Sulfur Battery Cathode Material with High Capacity and Cycling Stability. *Nano Lett.*, **2011**, *11*, 2644-2647.

19 Han, S.-C.; Song, M.-S.; Lee, H.; Kim, H.-S.; Ahn, H.-J.; Lee, J.-Y. Effect of Multiwalled Carbon Nanotubes on Electrochemical Properties of Lithium/Sulfur Rechargeable Batteries. *J. Electrochem. Soc.* **2003**, *150*, A889-A893.

20 Yin, L.; Wang, J.; Yang, J.; Nuli, Y. A Novel Pyrolyzed Polyacrylonitrile-sulfur@MWCNT Composite Cathode Material for High-rate Rechargeable Lithium/Sulfur Batteries. *J. Mater. Chem.* **2011**, *21*, 6807-6810.

21 Wu, F.; Chen, J.; Li, L.; Zhao, T.; Chen, R. Improvement of Rate and Cycle Performence by Rapid Polyaniline Coating of a MWCNT/Sulfur Cathode. *J. Phys. Chem. C*, **2011**, *115*, 24411-24417.

22 Wu, F.; Chen, J.; Chen, R.; Wu, S.; Li, L.; Chen, S.; Zhao, T. Sulfur/Polythiophene with a Core/Shell Structure: Synthesis and Electrochemical Properties of the Cathode for Rechargeable Lithium Batteries. *J. Phys. Chem. C*, **2011**, *115*, 6057-6063.

23 Manthiram, A.; Fu, Y.; Su, Y.-S. Challenges and Prospects of Lithium–Sulfur Batteries. *Acc. Chem. Res.*, **2013**, *46*, 1125–1134.

24 Seh, Z. W.; Li, W.; Cha, J. J.; Zheng, G.; Yang, Y.; McDowell, M. T.; Hsu P.-C.; Cui, Y. Sulphur–TiO_2 Yolk–Shell Nanoarchitecture with Internal Void Space for Long-cycle Lithium–Sulphur Batteries. *Nat. Commun.* **2013**, *4*, 1331.

25 Schneider, H.; Garsuch, A.; Panchenko, A.; Gronwald, O.; Janssen, N.; Novák, P. Influence of different electrode compositions and binder materials on the performance of lithium–sulfur batteries. *J. Power Sources* **2012**, *205*, 420-425.

26 Stankovich, S.; Dikin, D. A.; Piner, R. D.; Kohlhaas, K. A.; Kleinhammes, A.; Jia, Y.; Wu, Y.; Nguyen, S. T.; Ruoff, R. S. Synthesis of Graphene-based Nanosheets *via* Chemical Reduction of Exfoliated Graphite Oxide. *Carbon* **2007**, *45*, 1558-1565.

27 Szabó, T.; Berkesi, O.; Dékány, I. DRIFT Study of Deuterium-Exchanged Graphite Oxide. *Carbon* **2005**, *43*, 3186-3189.

28 Lerf, A.; He, H.; Forster, M.; Klinowski, J. Structure of Graphite Oxide Revisited. *J. Phys. Chem. B*, **1998**, *102*, 4477-4482.

29 Hummers, W. S.; Offeman, R. E. Preparation of Graphitic Oxide. *J. Am. Chem. Soc.* **1958**, *80*, 1339-1339.

30 Lawrence, D. S.; Jiang, T.; Levett, M. Self-Assembling Supramolecular Complexes. *Chem. Rev.*, **1995**, *95*, 2229-2260.

31 Brunsveld, L.; Folmer, B. J. B.; Meijer, E. W.; Sijbesma, R. P. Supramolecular Polymers. *Chem. Rev.*, **2001**, *101*, 4071-4098.

32 Amendola, V.; Esteban-Gómez, D.; Fabbrizzi, L.; Licchelli, M. What Anions Do to N−H-Containing Receptors. *Acc. Chem. Res*. **2006**, *39*, 343-353.

33 Beletskaya, I.; Tyurin, V. S.; Tsivadze, A. Yu.; Guilard, R.; Stern, C. Supramolecular Chemistry of Metalloporphyrins. *Chem. Rev*., **2009**, *109*, 1659-1713.

34 Wang, J.; Yao, Z.; Monroe, C. W.; Yang, J.; Nuli, Y. Carbonyl-β -Cyclodextrin as a Novel Binder for Sulfur Composite Cathodes in Rechargeable Lithium Batteries. *Adv. Funct. Mater.* **2013**, *23*, 1194–1201.

35 Huang, Y.; Sun, J.; Wang, W.; Wang, Y.; Yu, Z.; Zhang, H.; Wang, A.; Yuan, K. Discharge Process of the Sulfur Cathode with a Gelatin Binder. *J. Electrochem. Soc*., **2008**, *155*, A764-A767.

36 Kovalenko, I.; Zdyrko, B.; Magasinski, A.; Hertzberg, B.; Milicev, Z.; Burtovyy, R.; Luzinov, I.; Yushin, G. A Major Constituent of Brown Algae for Use in High-Capacity Li-Ion Batteries. *Science* **2011**, *334*, 75-79.

37 Mikhaylik Y. V.; Akridge, J. R. Polysulfide Shuttle Study in the Li/S Battery System. *J. Electrochem. Soc.* **2004**, *151*, A1969-A1976.

38 Aurbach, D.; Pollak, E.; Elazari, R.; Salitra, G.; Kelley, C. S.; Affinito, J. On the Surface Chemical Aspects of Very High Energy Density, Rechargeable Li–Sulfur Batteries. *J. Electrochem. Soc.* **2009**, *156*, A694-A702.

39 Ferreira, A. G. M.; Lobo, L. Q. The Low-Pressure Phase Diagram of Sulfur. *J. Chem. Thermodynamics* **2011**, *43*, 95-104.

40 Diao, Y.; Xie, K.; Xiong, S.; Hong, X. Insights into Li-S Battery Cathode Capacity Fading Mechanisms: Irreversible Oxidation of Active Mass during Cycling. *J. Electrochem. Soc.*, **2012**, *159*, A1816-A1821.

CHAPTER 11

CONCLUSION

The work presented here encompasses the use of a broad range of advanced electron microscopy approaches for understanding electrochemical energy storage and conversion systems.

It has been demonstrated, particularly in Chapter 2, that the 3-D electron tomography method enables the identification of hundreds of electrocatalyst nanoparticles with one-to-one correspondence before and after electrochemical aging[1]. It allows us to track, in three-dimensions (3-D), the trajectories and morphologies of each Pt-Co nanocatalyst particles on a fuel cell carbon support. The use of atomic-scale electron energy loss spectroscopic imaging enables the correlation of performance degradation of the catalyst with changes in particle/inter-particle morphologies, particle-support interactions and the near-surface chemical composition. We found that, aging of the catalysts under normal fuel cell operating conditions (voltage scans from +0.6 V to +1.0 V for 30,000 cycles) gives rise to coarsening of the nanoparticles, mainly through coalescence, which, in turn, leads to the loss of performance. The observed coalescence events were not due to carbon support degradation, but to the migration of nanoparticles on the support during voltage cycling. This method provides detailed insights into how nanocatalyst degradation occurs in proton exchange membrane fuel cells (PEMFCs), and suggests that minimization of particle movement can potentially slow down the coarsening of the particles, and the attendant performance degradation.

Moving from the *ex-situ* to *in-situ* characterization, we report a study using high-resolution scanning transmission electron microscopy coupled with an *in-situ* thermal annealing stage of surfactant-free, mono-dispersed superparamagnetic PtFe (cubic) alloy nanoparticles (≈ 2 nm in diameter) stabilized in a KCl matrix.[2] *Ex-situ* experiments confirmed that annealing produces PtFe (tetragonal) ordered intermetallic nanoparticles with a mean diameter of 5 nm, and the *in-situ* study revealed that the mechanism of nanoparticle growth is dominated by particle-particle coalescence, although Ostwald ripening is also implicated in a few cases. In addition, to determine the time dependent evolution of the size distribution of an ensemble of over 400 nanoparticles, analysis of the *in-situ* data also allowed tracking of individual nanoparticles, distinguishing coalescence from Ostwald ripening, nanoparticle by nanoparticle. This approach has provided valuable insights into changes in crystal structure and sintering that occur during the thermal annealing of Pt-Fe nanoparticles.

In Chapter 4, we apply the *in-situ* characterization techniques into the liquid phase, where the electrochemical reactions become feasible.[3] We describe an approach that enables imaging the nanoscale distribution of ions during electrochemical charging of a battery in a transmission electron microscope liquid flow cell. We use valence electron energy-loss spectroscopy to track both solvated and intercalated ions, with electronic structure fingerprints of the solvated ions identified using an *ab initio* non-linear response theory. Equipped with the new electrochemical cell holder, nanoscale spectroscopy and theory, we have been able to determine the lithiation state of a $LiFePO_4$ electrode and surrounding aqueous electrolyte in real time with nanoscale resolution during electrochemical charge and discharge. We follow lithium transfer

between electrode and electrolyte and image charging dynamics in the cathode. We observe competing delithiation mechanisms such as core-shell and anisotropic growth occurring in parallel for different particles under the same conditions. This technique represents a general approach for the *operando* nanoscale imaging of electrochemically active ions in the electrode and electrolyte in a wide range of electrical energy storage systems.

This *in-situ* STEM characterization technique cannot only be applied to electrochemical energy systems, but also be applied to the study of nanoparticle metamorphosis. In Chapter 5, high-temperature in-situ electron microscopy and X-ray diffraction revealed that Au and Fe_2O_3 particles fuse in a fluid fashion at temperatures far below their size-reduced melting points. With increasing temperature, the fused particles undergo a sequence of complex structural transformations from surface-alloy to phase segregated and ultimately core-shell structures. The combination of in-situ electron microscopy and spectroscopy provides new insights into fundamental thermodynamic and kinetic aspects governing the formation of heterogeneous nanostructures. The observed structural transformations present an interesting analogy to thin film growth on the curved surface of a nanoparticle. Using single particle observations, we constructed a phase diagram illustrating the complex relationships among composition, morphology, temperature, and particle size.

Learning from the information of *in-situ* TEM study, we have been able to develop better catalysts for fuel cell systems. In Chapter 6, a promising electrocatalyst prototype of low Pt mole fraction, intermetallic nanoparticles of Cu_3Pt, has been prepared

using a simple impregnation-reduction method, followed by a post heat-treatment.[4] Two dealloying methods (electrochemical and chemical) were implemented to control the atomic-level morphology and improve performance for the oxygen reduction reaction. The morphology and elemental composition of the dealloyed nanoparticles were characterized at Ångstrom resolution using an aberration-corrected scanning transmission electron microscope equipped with an electron energy loss spectrometer. We found that the electrochemical dealloying method led to the formation of a thin Pt skin of ca. 1 nm in thickness with an ordered Cu_3Pt core structure, while chemical leaching gave rise to a 'spongy' structure, with no ordered structure being preserved. A 3-D tomographic reconstruction indicated that numerous voids were formed in the chemically dealloyed nanoparticles. Both dealloying methods yielded enhanced specific and mass activities toward the ORR and higher stability relative to Pt/C. The 'spongy' nanoparticles exhibited better mass activity with a slightly lower specific activity than the electrochemically dealloyed nanoparticles after 50 potential cycles. In both cases the mass activity was still enhanced after 5,000 potential cycles.

To better improve the performance of fuel cells, we have looked beyond Pt-metal disordered alloys and described a new class of Pt-Co nanocatalysts comprised of ordered Pt_3Co intermetallic cores with a 2-3 atomic-layer thick platinum shell.[5] In Chapter 7, these nanocatalysts exhibited over 200% increase in mass activity and over 300% increase in specific activity when compared to the disordered Pt_3Co alloy nanoparticles as well as Pt/C. To date, this mass activity for the ORR is the highest among the Pt-Co systems reported in the literature under similar testing conditions. Stability tests showed a minimal loss of activity after 5,000 potential cycles and the ordered core-shell structure was

maintained virtually intact as established by atomic-scale elemental mapping. The high activity and stability are attributed to the Pt-rich shell, and the stable intermetallic Pt_3Co core arrangement. These ordered nanoparticles provide a new direction for catalyst performance optimization for next-generation fuel cells.

Applying the studies from *in-situ* TEM characterization, I have also explored the field of lithium-sulfur batteries. In Chapter 8, we reported the synthesis of a polyaniline-sulfur yolk-shell nanocomposite through a heating vulcanization of a polyaniline-sulfur core-shell structure.[6] We observed that this heating treatment was much more effective, than chemical leaching, to prepare uniform yolk-shell structures. Compared with its sulfur-polyaniline core-shell counterparts, the yolk-shell nanostructures delivered much improved cyclability owing to the presence of internal void space inside the polymer shell to accommodate the volume expansion of sulfur during lithiation. The yolk-shell material exhibited a stable capacity of 765 mAh g^{-1} at 0.2 C after 200 cycles, representing a promising future for industrial scale Li-S batteries.

In Chapter 9, we present a hierarchical architecture MWCNT@ meso C core-shell nanostructure as carbon matrix for effective trapping sulfur/polysulfides as cathode materials for Li/S batteries.[7] The unique structure of MWCNT@Meso C core-shell nanocomposites were prepared by using a sol-gel coating method followed by nanocasting. By infiltrating sulfur into the matrix, the S/MWCNT@Meso C core-shell nanocomposites delivered an initial discharge capacity of 1248 mA h g^{-1}. The capacity was stabilized at about 640 mA h g^{-1} after 50 cycles, which is much higher than that for S/MWCNT. This material exhibited excellent rate capability even at a discharge current

density of 2 A g^{-1}. The improvement in electrochemical performance is attributed to the synergetic effect of MWCNTs cores which provide electronic pathways, while mesoporous carbon shells with relatively high surface area, trap sulfur/polysulfides and provide Li^+ ion pathways.

In Chapter 10, we move more closely to the actual application of lithium sulfur battery system. An amylopectin wrapped graphene oxide-sulfur composite was prepared to construct a 3-dimensionally cross-linked structure through the interaction between amylopectin and graphene oxide, for stabilizing lithium sulfur batteries.[8] With the help of this cross-linked structure, the sulfur particles could be confined much better among the layers of graphene oxide and exhibited significantly improved cyclability, compared with the unwrapped graphene oxide-sulfur composite. The effect of the electrode mass loading on electrochemical performance was investigated as well. In the lower sulfur mass loading cells, such as 2mg cm^{-2}, both of the capacity and efficiency were cleraly better than those of the higher sulfur mass loading cells, such as 6mg cm^{-2}.

Each of the examples above represents the functional and mechanistic insights that the *in-situ* electron microscopy has provided understandings of electrochemical energy storage and conversion systems. Both the *ex-situ* and *in-situ* investigations of Pt-Co nanoparticles confirmed the same degradation mechanisms; that coalescence and carbon support play important roles in fuel cell catalysts degradation. The study using the *in-situ* liquid cell provides a representative of electrochemical behavior of platinum nanoparticles inside an electron microscope. The structure of lithium-sulfur battery composite materials demonstrates their distinct character as stable and high-performance

battery materials and has generated active research in the mechanistic details of the complex chemistry. Given the tremendous efforts to elucidate the impact of modern electrochemical energy materials, more fascinating research and collaborations are ongoing across the fields of chemistry, physics and material science in this new era of renewable energy research.

REFERENCES

1. Yu, Y.; Xin, H. L.; Hovden, R.; Wang, D.; Rus, E. D.; Mundy, J. A.; Muller, D. A.; Abruna, H. D. *Nano Letters* **2012,** 12, (9), 4417-4423.

2. Chen, H.; Yu, Y.; Xin, H. L.; Newton, K. A.; Holtz, M. E.; Wang, D.; Muller, D. A.; Abruna, H. D.; DiSalvo, F. J. *Chemistry of Materials* **2013,** 25, (8), 1436-1442.

3. Holtz, M. E.; Yu, Y.; Gunceler, D.; Gao, J.; Sundararaman, R.; Schwarz, K. A.; Arias, T. A.; Abruña, H. D.; Muller, D. A. *Nano Letters* **2014,** 14, (3), 1453-1459.

4. Wang, D.; Yu, Y.; Xin, H. L.; Hovden, R.; Ercius, P.; Mundy, J. A.; Chen, H.; Richard, J. H.; Muller, D. A.; DiSalvo, F. J.; Abruna, H. D. *Nano Letters* **2012,** 12, (10), 5230-5238.

5. Wang, D.; Xin, H. L.; Hovden, R.; Wang, H.; Yu, Y.; Muller, D. A.; DiSalvo, F. J.; Abruna, H. D. *Nature Materials* **2013,** 12, (1), 81-87.

6. Zhou, W.; Yu, Y.; Chen, H.; DiSalvo, F. J.; Abruna, H. D. *Journal of the American Chemical Society* **2013,** 135, (44), 16736-16743.

7. Wang, D.; Yu, Y.; Zhou, W.; Chen, H.; DiSalvo, F. J.; Muller, D. A.; Abruna, H. D. *Physical Chemistry Chemical Physics* **2013,** 15, (23), 9051-9057.

8. Zhou, W.; Chen, H.; Yu, Y.; Wang, D.; Cui, Z.; DiSalvo, F. J.; Abruna, H. D. *Acs Nano* **2013,** 7, (10), 8801-8808.